An Optical Study of Young Stellar Clusters

Nicola Da Rio

Max-Planck-Institut für Astronomie

Dissertation in Astronomy

submitted to the

Combined Faculties of the Natural Sciences and Mathematics

of the Ruperto-Carola-University of Heidelberg, Germany

for the degree of

Doctor of Natural Sciences

Put forward by

Master Phys. Da Rio Nicola

born in: Udine (Italy)

Oral examination: December 13^{th}, 2010

An Optical Study of Young Stellar Clusters

Referees: Prof. Dr. Thomas Henning
Prof. Dr. Ralf Klessen

Abstract

In the first part of this thesis a new analysis of the Orion Nebula Cluster, one of the most studied star-forming regions in the Galaxy, is presented. Based on multi-band optical photometry and spectroscopy obtained with the *Wide-Field Imager* (WFI) at the ESO/MPI 2.2-m telescope at La Silla Observatory, I study the systematic effects that bias the derivation of stellar parameters of pre-main sequence (PMS) stars. I derive the new H-R diagram of the entire region, and assign masses and ages to all the members. The age is found to be $\sim 2-3$ Myr, older than previously estimated. I also confirm the presence of an age spread, and show how the previously found mass-age correlation can be affected by the sample incompleteness and uncertainties in the evolutionary models.

In the second part of this thesis, I carry out a research on the low-mass stellar population of the young stellar cluster LH 95 in the Large Magellanic Cloud, based on deep optical photometry with the *Advanced Camera for Surveys* (ACS) onboard the *Hubble Space Telescope*; the deepest ever obtained toward this galaxy, down to $V \simeq 28$ mag. I isolate the PMS cluster population, and derive the first extragalactic Initial Mass Function (IMF) down to the subsolar regime. It shows a flattening below 1 $M_{\odot}$, in agreement with the Galactic IMF once results are corrected for unresolved binarity. I study the age distribution of LH 95, introducing a statistical method to derive average age and age-spreads accounting simultaneously for unresolved binarity, differential extinction, variability, accretion and crowding of PMS stars. The best-fit solution for LH 95 suggests an age of ~ 4 Myr with a gaussian age spread of $\sigma \sim 1.2$ Myr. Finally, I study the early-type high-mass stellar population of the cluster, through ground based spectroscopy obtained with the *Fiber-fed Extended Range Optical Spectrograph* (FEROS) at the ESO/MPI 2.2-m telescope at La Silla Observatory, and photometry from the 1-m telescope at Siding Spring Observatory. The derived stellar masses are combined with my results on the low-mass IMF of the cluster for the study of the most complete extragalactic IMF ever performed.

Zusammenfassung

Im ersten Teil dieser Dissertation wird eine neue Analyse des Orion Nebula Cluster, eine der am meisten studierten Sternentstehungregionen der Galaxis, präsentiert. Basierend auf optischer Photometrie und Spektroskopie in verschiedenen Bändern, aufgenommen mit dem *Wide-Field Imager* (WFI) am ESO/MPI 2.2-m Teleskop des La Silla Observatoriums, untersuche ich die systematischen Effekte, die die Ableitung stellarer Parameter von Vorhauptreihensternen (PMS) beeinflussen. Ich leite ein neues H-R Diagram der gesamten Region her und ordne allen Mitgliedern Masse und Alter zu. Das Alter wurde auf $\sim> 2-3$ Myr bestimmt, älter als zuvor angenommen. Ich bestätige die Existenz einer Altersstreuung und zeige, wie die vorherige Masse-Alter-Korrelation durch Unvollständigkeit des Samples und Unsicherheiten in den Entwicklungsmodellen beeinflusst werden kann.

Im zweiten Teil der Dissertation führe ich eine Untersuchung der massearmen Sternenpopulation des jungen Sternhaufen LH 95 in der Großen Magellanschen Wolke durch. Diese basiert auf tiefer optischer Photometrie mit der *Advanced Camera for Surveys* (ACS) an Bord des *Hubble Space Telescope*, die tiefste bisher erreichte innerhalb der Großen Magellanschen Wolk, mit Helligkeiten bis zu $V \simeq 28$ mag. Ich isoliere die PMS-Population des Sternhaufens und leite die erste extragalaktische Anfangsmassenverteilung (IMF) ab, die bis in den subsolaren Bereich reicht. Diese zeigt eine Abflachung unterhalb von 1 $M_{\odot}$, in Übereinstimmung mit der galaktischen IMF sobald die Ergebnisse für nicht aufgelöste Mehrkörpersysteme korrigiert wurden. Ich untersuche die Altersverteilung von LH 95 und führe dabei eine statistische Methode ein, um Durchschnittsalter und Altersstreuungen abzuleiten, die simultan nicht aufgelöste Mehrkörpersysteme, differentielle Extinktion, Variabilität, sowie Akkretion und Crowding der PMS-Sterne einbezieht. Die am besten passende Lösung für LH 95 läßt auf ein Alter von $\sim$ 4 Myr schliessen mit einen Gauß'schen Altersstreuung von $\sigma \sim 1.2$ Myr. Abschließend untersuche ich die massereiche Sternpopulation des Sternhaufen mit Hilfe von erdgebundener Spectroskopie, die mit dem *Fiber-fed Extended Range Optical Spectrograph* (FEROS) am ESO/MPI 2.2-m Teleskops des La Silla Observatoriums aufgenommen wurde, sowie Photometrie des 1-m Teleskops des Siding Spring Observatoriums. Die abgeleiteten Massen der Sterne sind, kombiniert mit den Ergebnissen der Untersuchung der IMF der massearmen Sterne des Sternhaufens, die kompletteste Untersuchung einer extragalaktischen IMF, die bisher durchgeführt wurde.

Ai miei genitori e alla nonna Olga

Table of Contents

Introduction

The star formation process determines the conversion of gas to stars, and the outcome are stars with a range of masses. The distribution of the stellar masses in a given volume of space in a stellar system at the time of their formation is known as the Initial Mass Function (IMF) of the system (Salpeter, 1955; Scalo, 1986; Kroupa, 2002; Chabrier, 2003). Together with the time modulation of the star formation process, known as the star formation rate, it dictates the evolution and fate of stellar systems up to entire galaxies. The vast majority of stars are not formed in isolation, but as part of stellar associations and clusters (Lada & Lada, 2003), where hundreds or even thousands of stars along the entire mass spectrum are found, from the most massive OB-type members, down to low-mass stars ($0.08 < M/\mathrm{M}_{\odot} \lesssim 2$) and Brown Dwarfs ($M \leq 0.08$ $\mathrm{M}_{\odot}$). One of the important debates concerning the star formation within a cluster is whether the process takes place rapidly, on dynamical time-scales, or is a quasi-static process in which protostellar cores take many free-fall time-scales to contract (e.g., Tan et al., 2006; Elmegreen, 2007). The observational study of young stars in a star forming region is fundamental to improve our understanding of such problem, constraining the rapidity with which stars are formed. In fact, whereas the high-mass population of these regions is the direct sign of the youthfulness of these systems, the low-mass pre-main sequence (PMS) members preserve a record of the complete recent star formation history of the star-forming region over long periods, since their evolution towards the main–sequence is extremely slow and can last for many tens of Myr. Moreover, young (few Myr old) clusters are usually not dynamically evolved nor have had time to disperse; thus the mass distribution of their members reflects that at the time of formation, i.e., their IMF. As a consequence, the study of the low-mass PMS population in young clusters is fundamental to improve our understanding of the star formation processes and the IMF.

In the Galaxy, observational studies of young stars have been carried out throughout the last decades in several stellar systems, from nearby, loose stellar associations, such as

the young population of Taurus-Auriga dark cloud (e.g., Joy, 1949; Bertout, 1989; Kenyon & Hartmann, 1995), to the most massive young clusters (e.g., Westerlund, 1961; Brandl et al., 1999; Brandner et al., 2008; Portegies Zwart et al., 2010). One of the most studied star forming regions in our Galaxy is the Orion Nebula (M42, NGC 1976), with its associated young stellar cluster (Orion Nebula Cluster, ONC). Its interest is due to the fact that the ONC is the nearest site of recent massive star formation and is therefore regarded as a prototype of dense star forming regions. At a distance of $\sim$ 400 pc from the Sun (Sandstrom et al., 2007; Menten et al., 2007; Hirota et al., 2007), the region is projected on the northwestern side of the Orion A giant molecular cloud, but contrary to the majority of star forming regions in the Galaxy (Lada & Lada, 2003), it is only slightly extinguished. This is due to the presence of the most massive members of the young stellar population, θ^1Ori-C in the Trapezium cluster in particular, whose ultra-violet emission has carved an ionized cavity in the molecular material which now engulfs most of the young cluster. The high extinction provided by the background molecular cloud (up to $A_V \simeq 100$ mag, Bergin et al. 1996), the position of this region at the anticenter of the Galaxy ($l \simeq 209\,\mathrm{deg}$), and the high projected distance from the galactic plane ($b \simeq -19\,\mathrm{deg}$) conspire to provide a rather low foreground and background stellar contamination, enabling us to perform extinction-limited studies of a young, nearly coeval, relatively rich and uncontaminated pre-main sequence (PMS) cluster ($1 - 3 \times 10^4$ stars aged $\sim 1 - 3$ Myr, Hillenbrand et al., 2001). The ONC has been repeatedly studied both at visible wavelengths (e.g., Herbig & Terndrup, 1986; Prosser et al., 1994; Hillenbrand, 1997; Robberto et al., 2004) and in the near-IR (e.g Ali & Depoy , 1995; Hillenbrand et al., 1998; Hillenbrand & Carpenter, 2000; Lucas & Roche, 2000; Luhman et al., 2000; Slesnick et al., 2004; Robberto et al., 2010) with increasing field coverage and sensitivity, probing the cluster well into the substellar regime.

The derivation of the stellar parameters of PMS stars is particularly challenging: in the optical, these stars show significant excesses caused by on-going accretion from the disk (Appenzeller & Mundt, 1989), which also vary with time. Large star spots on the stellar surface, caused by the magnetic structure of these objects, further alters the observed fluxes, and causes additional variability on timescales of the order of days (Herbst et al., 2002). In the infrared, the presence of circumstellar disks produces an excess, whose intensity and spectral energy distribution depends on the geometrical properties of the disk-star system. Young stellar systems are usually partially embedded in their parental cloud (Lada & Lada, 2003), generally spatially non-uniform. The extinction from the dust

contained in this material redden the observed colors, and must be estimated and properly removed for each star. Furthermore, additional uncertainties affect all the steps needed to pass from observational quantities (magnitudes, colors, spectra) to physical parameters of the stars (temperatures, masses, ages). Specifically, the transformation of spectral types to effective temperatures is quite uncertain (Cohen & Kuhi, 1979; Luhman, 1999). Moreover, the modeling of the evolution of young stars, in terms of effective temperature and radius for a given stellar mass as a function of time, still presents several uncertainties, and different families of evolutionary models (D'Antona & Mazzitelli, 1994; Baraffe et al., 1998; Palla & Stahler, 1999; Siess et al., 2000) are not in agreement with each other. This leads to additional uncertainties in the estimation of the masses and ages from the measured properties of the stars. Moreover, observational studies of young stellar populations in Galactic star-forming regions and clusters are affected by contamination from foreground and background field populations; this requires accurate determination of memberships, for example through an analysis of the proper motions (e.g., Jones & Walker, 1988; Rochau et al., 2010), or based on other indicators of youthfulness of the stars, e.g, the lithium abundance (e.g., Palla et al., 2007), or X-ray emission (e.g., van den Berg et al., 2002).

The Large and Small Magellanic Clouds (LMC, SMC), the dwarf metal-poor companion-galaxies to our own, are well-suited environments for the study of *resolved* star formation at low metallicity. Indeed, both galaxies are characterized by an exceptional sample of star-forming regions, where hydrogen has been already started to be ionized by the UV-winds of massive stars, the HII regions (Henize, 1956; Davies et al., 1976). A plethora of young stellar associations and clusters are embedded in these regions (e.g., Bica & Schmitt, 1995; Bica et al., 1999), giving evidence of recent (or current) clustered star formation. Recently (Gouliermis et al., 2006a, 2007), the first detection of low-mass PMS stars in young star clusters of the Magellanic Clouds (MCs), which was made possible by the high spatial resolution and sensitivity of the Hubble Space Telescope, opened a new field of studies of such populations outside our Galaxy. This advancement did not only extend the studies of young star forming regions outside the Milky Way, but also offered particular advantages. Observations of young clusters in the MCs are much less affected by the dust extinction which typically limits observational studies in the disk of our Galaxy. Moreover, the negligible distance spread of the stars within the MCs simplifies the membership assignment and the removal of the field population contamination, since it can be assumed that all the stars detected photometrically lie at the same distance from

us (Caldwell & Coulson, 1986; Cole, 1998). This guarantees that, by simply obtaining a color-magnitude diagram (CMD) of both a young cluster and a neighboring field of the MCs, the population of young members in the low-mass regime can be isolated from the contamination of background and foreground evolved populations. Unfortunately, despite these advantages, the far distance of the MCs does not allow us, with contemporary instrumentation, to perform studies comparable with what is possible for nearby Galactic star-forming regions. For instance, individual optical and near-IR spectroscopy or X-ray monitoring of low-mass PMS stars in the MCs is yet not practical. Photometric studies of such stars require either space-based or adaptive optics supported ground-based observations. Furthermore, at present, observations of young stars in the MCs are limited to the low-mass stars, with a detection limit which can hardly reach the hydrogen burning limit, while the detection brown dwarf in these regions is still not feasible.

As a consequence, *the study of PMS systems in the Galaxy and in the MCs is complementary*. On one hand, an extensive study of nearby PMS stars is fundamental to improve our understanding of the behavior of these objects, reducing the always present aforementioned uncertainties. On the other hand, what we learn from Galactic young regions is critical to interpret the observations of young stellar associations and clusters in the MCs, in order to answer the open questions concerning the early phases of stellar evolution in these galaxies, and also, thanks to the numerous star forming regions observable in these galaxy, to study star formation processes in general.

This thesis is been developed and carried out based on this approach. In the first part (Chapter 1), I present a new analysis of the stellar population of Orion Nebula Cluster, based on multi-band photometry as well as spectroscopy. Besides of improving our knowledge of this region by better evaluating – and occasionally correcting with respect to previous works – measured properties such as the IMF, the cluster age, the mass-age relation, etc., I also study several effects which bias the derived stellar parameters, such as the assumed intrinsic colors for young stars and the color effect caused by ongoing accretion. These results are then applied in the second part of this thesis, in which I analyze the stellar population of the young association LH 95 in the Large Magellanic Cloud. In Chapter 2, thus, I use deep HST/ACS $V-$ and $I-$equivalent photometry to derive the IMF of the region down to $\sim 0.4\mathrm{M}_{\odot}$. In Chapter 3 I study, with the same observational material, the mean age and age distribution of the system, introducing a new statistical method to disentangle both physical and observational biases that affect the observed fluxes of PMS stars with single-epoch photometry. Finally, in Chapter 4 I

focus on the massive population of LH 95, investigated through both spectroscopy and photometry, and its connection to the low-mass PMS stellar content of the cluster. A conclusive summary and future perspectives of this research are then presented at the end of the thesis.

Part I

The Orion Nebula Cluster

Chapter 1

A Multi-Color Optical Survey of the ONC - The New HR diagram[1]

1.1 Introduction

The Orion Nebula Cluster (ONC), at a distance of $\sim$ 400 pc from the Sun (Menten et al., 2007), is the closest site of recent massive star formation. It contains several thousands (Hillenbrand et al., 2001) of stars and brown dwarfs from the smallest stellar masses to O-type stars (Hillenbrand, 1997). Its particular position, well above the galactic plane, together with the high background extinction from the parental cloud, and the low foreground extinction, provide significant advantages for the observational studies of its stellar population.

Despite these advantages, observational studies of the ONC are not without difficulties. The nebulosity which surrounds the ONC population and the presence of circumstellar material (disks and envelopes) cause highly non-uniform extinction among the members which must be corrected for each individual star. Furthermore, on-going accretion, variability due to star spots or stellar instabilities, influence the observed optical colors, which may vary with time. In principle, an observational effort including simultaneous multi-band photometry over a large wavelength range and adequate temporal sampling to account for variability effects may overcome these difficulties, disentangling the non-photospheric emission from complete spectral energy distributions (SEDs). Even in the presence of perfect measurements of photometry, and with consideration of the above effects, uncertainties remain in the conversions between colors and magnitudes to temperatures and luminosities, which differ from those of main sequence stars especially for

[1]**The research presented in this chapter has been published in two refereed papers: Da Rio et al. (2009b) and Da Rio et al. (2010a)**

late spectral types.

The combination of these uncertainties makes the construction of an accurate H-R diagram (HRD) based on photometry alone for the PMS population misleading. The construction of the HRD is more robust when photometry is complemented with spectroscopy, since spectral types can easily be determined even though moderate extinction, and the accretion excess can be directly identified from the line emissions or measurement at high dispersion of spectral veiling. Nonetheless, also in this case, the uncertainty in the spectral type-$T_{\rm eff}$ relation and, in addition, the difficulty of obtain spectra in a crowded field with bright, variable background emission limit the accuracy in deriving the stellar parameters. From the point of view of constructing the HRD of the ONC, the most complete work remains that of Hillenbrand (1997, hereafter H97). Using compiled plus new VI photometry and optical spectroscopy, H97 derived the extinction for $\sim$ 1000 stellar (i.e., above the H-burning mass) members and used the dereddened photometry to place the stars in the HRD. This made it possible to derive the stellar ages and masses through the comparison with PMS evolutionary models.

The Hubble Space Telescope Treasury Program on the Orion Nebula Cluster (HST GO-10246, P.I. M. Robberto) carried out multicolor visible photometry of the ONC with the highest possible spatial resolution and sensitivity, in order to obtain the most accurate estimates of stellar parameters. The Hubble observations have been complemented by ancillary ground based observations, necessary because of the limitations of the HST data in regard to source saturation and variability. Source saturation with HST was unavoidable given the long exposures (approximately 340 s) used to reach high signal-to-noise on the faintest ONC members. This time is long enough that point sources in Orion brighter than $I \simeq 17.6$ mag saturate in the F775W and F850LP filters (I and z-band equivalent) of ACS/WFC. This roughly corresponds to masses at the hydrogen burning limit, assuming for the cluster a 1 Myr age and 414 pc distance (Menten et al., 2007). Concerning variability, the choreography of the HST Treasury Program observations did not enable a given field to be imaged in all filters in a single visit. Since most sources in the ONC present variability (Herbst et al., 2002), which is typical for T Tauri stars for both accretion processes (Classical T Tauri Stars, CTTS) and rotation of spotted surface stars (Weak-line T Tauri stars, WTTS), this adds a source of uncertainty, especially if the variability is wavelength dependent.

To supplement the HST observations, ground-based data have been taken simultaneously from CTIO (near infrared) and La Silla (optical) on two nights in 2005 January.

The Near Infrared J, H, and K data and results are presented in Robberto et al. (2009). At La Silla, we used the Wide Field Imager (WFI) at the ESO-MPI 2.2 m telescope to image the same field in the U, B, V, and I bands, as well as in the Hα line and in a medium resolution filter at 6200 Å. For stars earlier than late K type, this filter samples the R-band in a region free from major nebular lines, whereas for M-type stars and substellar objects it turns out be centered on a TiO absorption feature whose strength depends on the spectral type, growing towards the latest M types. In Figure 1.1 we show an example of three standard spectra taken from the Bruzual-Persson-Gunn-Striker spectral atlas (Gunn & Stryker, 1983), showing how the absorption band coincides with the filter profile. A photometric study which includes narrow-band measurements at 6200 Å might therefore be helpful for constraining the spectral type of cool stars, as well as disentangling the temperature-reddening degeneracy in the observed broad-band colors. In what concerns the Hα photometry, it can be used to assess membership, and derive mass accretion rates through an absolute estimate of the accretion luminosity.

In this chapter we present the optical photometry of the ONC obtained in $UBVI$, Hα and in the 6200$\mathring{A}$ medium-band filters using the Wide Field Imager (WFI) at the 2.2m MPG/ESO telescope on La Silla. We then use these data to construct the HRD for the intermediate- (1 $M_\odot \lesssim M \lesssim$ 8 $M_\odot$) and low-mass (0.08 $M_\odot \lesssim M \lesssim$ 1 $M_\odot$) end of the stellar population. As in H97, we complement the optical photometry with spectroscopy, extending the spectral catalog of that work with new spectral types from slit spectroscopy, and also from narrow-band photometry. This allows us to improve over H97 extending the completeness of the sample of members placed in the HRD. The use of multi-color photometry provides advantages in estimating the contributions of both accretion luminosity and reddening to the observed colors. However, this is possible only together with an independent estimate of $T_{\rm eff}$. For late-type stars it is not enough to rely on stellar photometry, in particular on the V and I bands alone, due to the degeneracy between reddening and $T_{\rm eff}$ (H97). In principle, multi-band photometric observations can help in breaking the degeneracy (Romaniello et al., 2002), but the presence of non-photospheric emission, such as, for example, the U and B excesses due to accretion, limits the accuracy of the results. The most reliable method to break the temperature-reddening degeneracy remains to obtain an independent estimate of the effective temperature of the stars by means of spectroscopy. Thus we derive the stellar parameters only for the sub-sample with available $T_{\rm eff}$ estimates.

We describe the observations (Section 1.2), their reduction and calibration (Section

1.3) and photometry. In particular, the photometric catalog, the corresponding color-magnitude diagram and the completeness of our sample are described in Section 1.4. In Section 1.5 we focus on the 6200$\mathring{A}$ medium band photometry, from which we derive a spectrophotometric index correlated with the spectral type. In Section 1.5.1 we derive the line excesses in the Hα line. In Section 1.6 we study the color-color diagrams for all sources in the catalog in comparison with intrinsic colors computed from synthetic photometry; this allows us to test and correct empirically the models in order to derive the intrinsic, photospheric, colors valid for the ONC. In Section 1.7 we isolate the subsample for which a measurement of $T_{\rm eff}$ is available, either from optical spectroscopy or narrow-band photometry, and using this subsample, in Section 1.8 we derive the new HRD of the ONC, and discuss the age distribution, the mass function, and the correlation between ages and masses using two families of PMS evolutionary models.

.

1.2 The observations

The Wide Field Imager (WFI) is a focal reducer-type camera mounted at the Cassegrain focus of the 2.2-m MPG/ESO telescope at La Silla. The camera features an array of 8 2k×4k pixel CCDs, arranged in a 4×2 mosaic. The optics deliver a field of view of 34 × 33 arcmin with 0.238 arcsec per pixel scale. The WFI CCDs have a typical read noise of 4.5 e^- pix^{-1} and a gain of 2.2 e^- ADU^{-1}.

We selected the ESO877, ESO878, ESO843, and ESO879 broad-band filters, roughly corresponding to the standard U, B, V, and I bands (note that the ESO879 I band is centered at a wavelength higher than the standard $I_{\rm C}$ band, see Figure 1.2), and the medium-band MB#620/17_ESO866 and narrow-band NB#Halpha/7_ESO856 filters. We refer in this work to the MB#620/17 filter as the *TiO band*.

In Table 1.1 we summarize the characteristics of the WFI bands we use. For each band the effective throughput is calculated multiplying the filter passbands[2] by the average CCD quantum efficiency[3] (Q.E.). The averaged flux of Vega for each band

$$\int f_{\rm Vega} S_\lambda \, {\rm d}\lambda / \int S_\lambda {\rm d}\lambda \tag{1.1}$$

[2]http://www.eso.org/lasilla/instruments/wfi/inst/filters/

[3]http://www.eso.org/lasilla/instruments/wfi/inst/filters/WFI-Filters-2006-09-18.tar.gz

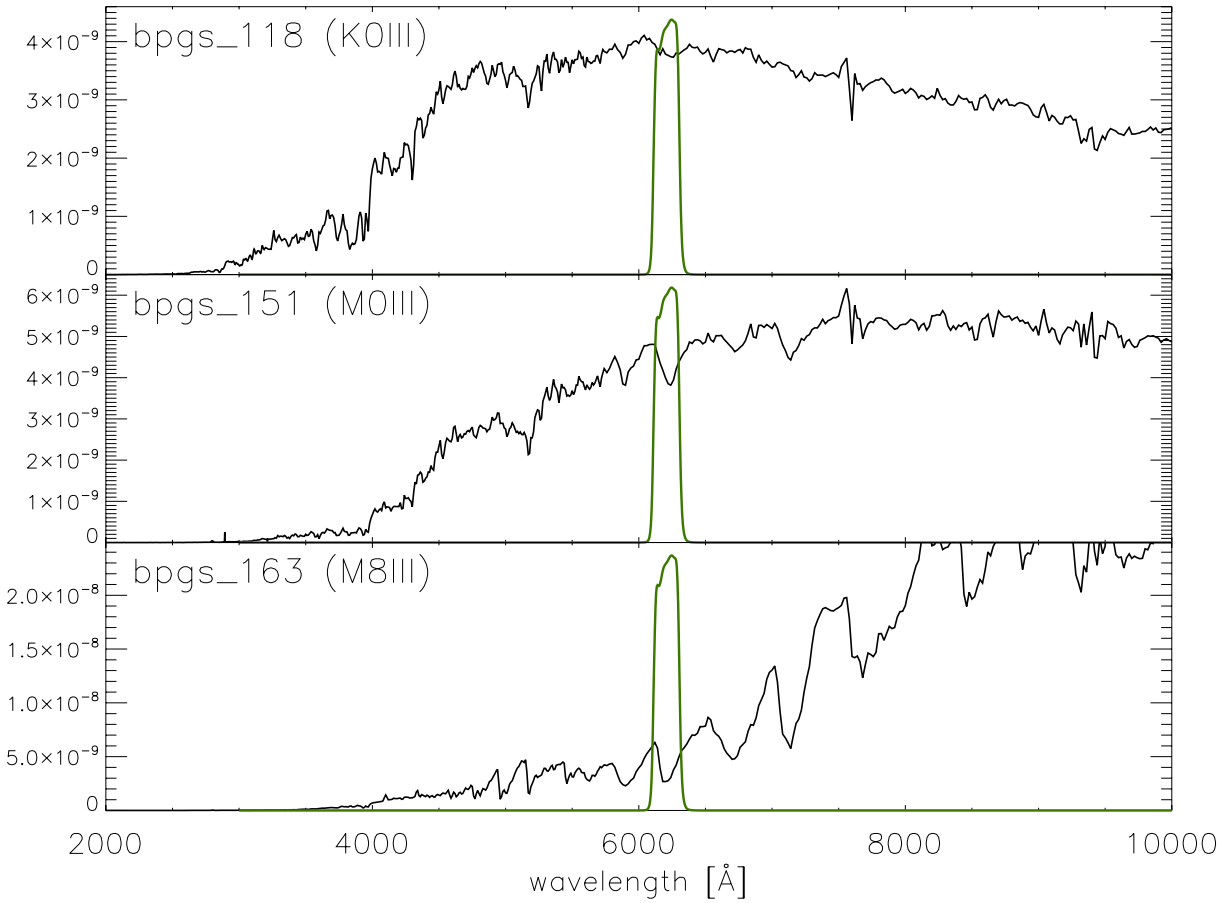

Figure 1.1 The medium-band MB#620/17_ESO866 filter response curve plotted over three standard spectra of giant stars (luminosity class III) of the Bruzual-Persson-Gunn-Striker catalog: *46LMI* (spectral type K0), *HD116870* (M0) and *Z Cyg* (M8). The TiO band mapped by this filter is stronger for late spectral types.

is presented in column 5 of Table 1.1, where S_λ is the band throughput and $f_{\rm Vega}$ a calibrated spectrum of Vega (Bohlin, 2007). This quantity, multiplied by the equivalent width (column 3), provides the zero-points of the photometric systems. For each band, this is the flux in erg s^{-1} cm^{-2} from a zero magnitude source when the filter throughput is normalized to have 100% response at the peak.

Our target field was observed in service observing mode on the nights of 2005 January 1 and 2 (hereafter indicated as Night A and Night B, respectively). The same observing strategy was adopted on both nights: for each filter we took 5 dithered exposures of 280 s ("Deep") and 30 s ("Medium"), plus one single 3 s short exposure ("Short"). The five dithered exposures made it possible to eliminate the gaps between CCDs in the

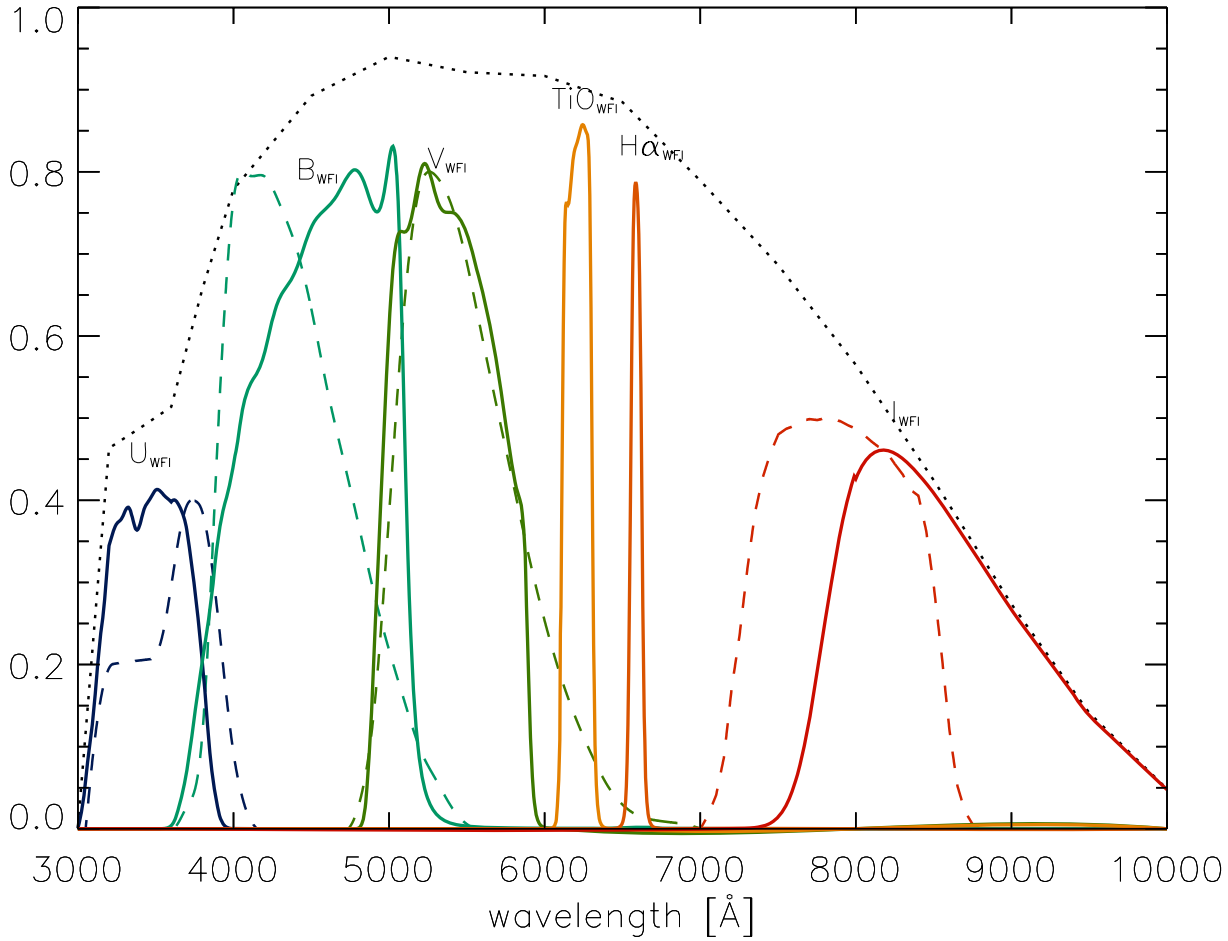

Figure 1.2 Band profiles for the six filters used in our observations (solid curves). The upper dotted line in black traces the CCD quantum efficiency; dashed lines in color represent the standard Johnson U, B, V and Cousins $I_{\rm C}$ bands. The ESO879 I band is centered at a significantly higher wavelength ($\sim$ 8269 Å) than its Cousins counterpart.

Table 1.1 Effective wavelength, FWHM, E.W. and Vega zero-points for the WFI photometric bands used

Band	$\lambda_{\rm eff}$ (Å)	FWHM (Å)	E.W. (Å)	Vega Flux erg s^{-1}cm^{-2}Å^{-1}
U	3470	668	639	$3.40 \cdot 10^{-9}$
B	4541	1139	1058	$5.88 \cdot 10^{-9}$
V	5375	884	791	$3.86 \cdot 10^{-9}$
I	8620	1354	1431	$9.50 \cdot 10^{-10}$
TiO	6217	193	190	$2.47 \cdot 10^{-9}$

final mosaics, whereas the different exposure times increase the dynamic range of measured magnitudes. The final size of the mosaics, trimmed to the largest common area, is approximately 35 × 34 arcmin. Absolute photometric calibration was obtained by comparison with the Landolt SA 98 field (Landolt, 1992), observed twice each night at low and high airmass. The average seeing was better in Night A than in Night B (respectively 1.2″and 1.8″).

1.3 Data reduction

1.3.1 Images and source catalogue

The data were reduced using a version of *alambic*, the ESO/MVM (Multi-Vision Model) image reduction system (Vandame , 2004) as part of the EIS project for basic reduction of imaging data for a number of ESO imaging instruments. To speed up the data processing, we installed the package and ran the pipeline parallel version on a server cluster at the Space Telescope Science Institute.

The package automatically performs all the common image reduction steps: removal of instrument effects (bias removal, flat field normalization), computation and removal of fringing (only present in I-band exposures), bad-pixel-map creation, and normalization of gain levels between different CCD chips.

Alambic also performs both relative and absolute astrometric calibration and distortion correction of the images to enable alignment and stacking of dithered frames. This step is achieved by retrieving an astrometric reference catalog, by default the GSC2 catalog, from the ESO archive. Since the GSC2 catalog turns out to be deficient in the Orion Nebula region, we used instead the 2MASS J-band catalog, which therefore represents our absolute astrometric standard. The near-IR 2MASS catalog does not trace well the distribution of sources at our shortest wavelengths; thus, an iterative process has been carried out: the J-band reference catalog has been used for absolute astrometric calibration of TiO and I bands. For the V band we bootstrapped from these two bands, extracting from the TiO and I calibrated images a secondary photometric catalog; the resulting V catalog was then used to perform astrometric calibration of B band images, and finally the B catalog was used for the U exposures. The final coordinates of bright blue sources detectable in all images have been checked to assess the accuracy of the procedure, which typically provides coordinates that agree to within one pixel between different bands. A

better astrometric calibration is not needed for our purposes, considering that the average FWHM for the point-spread function (PSF) in the data is ~ 1.5 arcsec, or 6 pixels. After astrometric calibration, all final images with the same filter and exposure time have been coadded using SWarp, a package included in the TERAPIX package (Bertin et al. , 2002).

For the four U,B,V,I broad bands PSF photometry has been performed using the Daophot II package (Stetson, 1987) on all the broad-band filter images. Unlike aperture photometry, which we used instead for the narrow band filters -, PSF photometry resolves and measures with good accuracy the luminosity of stars in highly crowded areas, such as the Trapezium region. We computed the PSF function for every image, using a set of reference stars located over the entire frame, and then refined this with an iterative sigma-clipping algorithm that rejected the candidates with excessive χ^2. PSF fitting was then performed on all the sources extracted with peak above 3σ of the local mean sky background, evaluated for every image using the SExtractor tool (Bertin et al. , 2002). We did not attempt to recover saturated sources, relying instead on the frames with shorter exposure times; only a small number of stars turned out to be saturated even in the 3s exposures too, and are therefore not present in our final catalog.

For each field and filter, we merged the photometric catalogs obtained with the different exposure times on the basis of the absolute positions of the sources, using the DAOMASTER package (Stetson, 1987). Systematic differences in magnitude between different frames (mostly due to airmass variations) have been corrected assuming that the fundamental instrumental magnitude is the one measured on the short (3s) exposures. The instrumental magnitudes of stars well measured in different images have been averaged.

For every filter and exposure time we eventually kept only the sources detected in both nights, in order to reduce contamination from spurious detections, which turns out to be not negligible due to the deep threshold (3σ) chosen for source identification. We have matched the photometry in the six bands using again DAOMASTER, keeping only those that present a counterpart in two adjacent bands, starting from the reddest ones (i.e., sources found in V and I; then B, V and I; then U, B, V and I). This is because we expect the observed SEDs to increase with wavelength in the visible range for all the faint, red end of the population; in other words, faint sources may be present only at the longer wavelengths, remaining invisible at the shortest ones; on the other hand, bright sources have been detected in all filters, if not saturated. For the Hα and TiO (6200Å) bands we performed aperture photometry, evaluating and correcting the

aperture correction to be applied using the brightest sources in the sample. These data have been first independently matched, keeping only stars detected in both filters on both nights to eliminate the eventual spurious detection, and afterwards have been measured and matched to the broadband catalog.

To ensure that our catalog is free from any additional spurious detections, we checked our final list of bona-fide candidates by visually inspecting their appearance in every filter. The data relative to the two nights have not been merged, thus in the final catalog the photometry of each source has two entries. However, given the better sky conditions in Night A, we will concentrate our analysis to the data taken on this night.

1.3.2 Absolute Calibration

Broad-band photometry

Traditionally, the absolute calibration of optical photometry is achieved by determining the transformation between the instrumental and the Johnson-Cousins photometric systems. This method assumes a linear or polynomial dependance of the magnitude offset for a given band as a function of a color index. This relation should be derived from a number of standard stars observed under the same conditions. In this work we chose not to perform a color correction, but instead we define a new photometric system based on the actual throughput of our passbands. This turns out to be an advantage, considering that there are several sources of uncertainty regarding the color correction to be applied. The main reasons of concern are the following.

First, as shown in Figure 1.7, our set of observed PMS stars includes some with very high color indices, up to $V - I \sim 6$. This is due to the combination of low $T_{\rm eff}$ for the low mass objects and high A_V in the region. The standard stars observed in the field SA98 reach only color terms up to $V - I \simeq 2$. There is no reason to assume that the linear transformation extracted from these standard stars can be extrapolated to the very red PMS stars. In fact, typical standard stars do not provide any information about the color corrections at extremely red color.

Second, in general the strengths of spectrum features that characterize stars of different $T_{\rm eff}$ depends on several other parameters besides temperature, such as surface gravity and metallicity. In continuum-dominated SEDs, as for early-type stars, these parameters have little effect in the computation of the integrated colors, but for late-type stars, whose SEDs are increasingly dominated by broad, strong molecular absorption bands (mostly TiO and

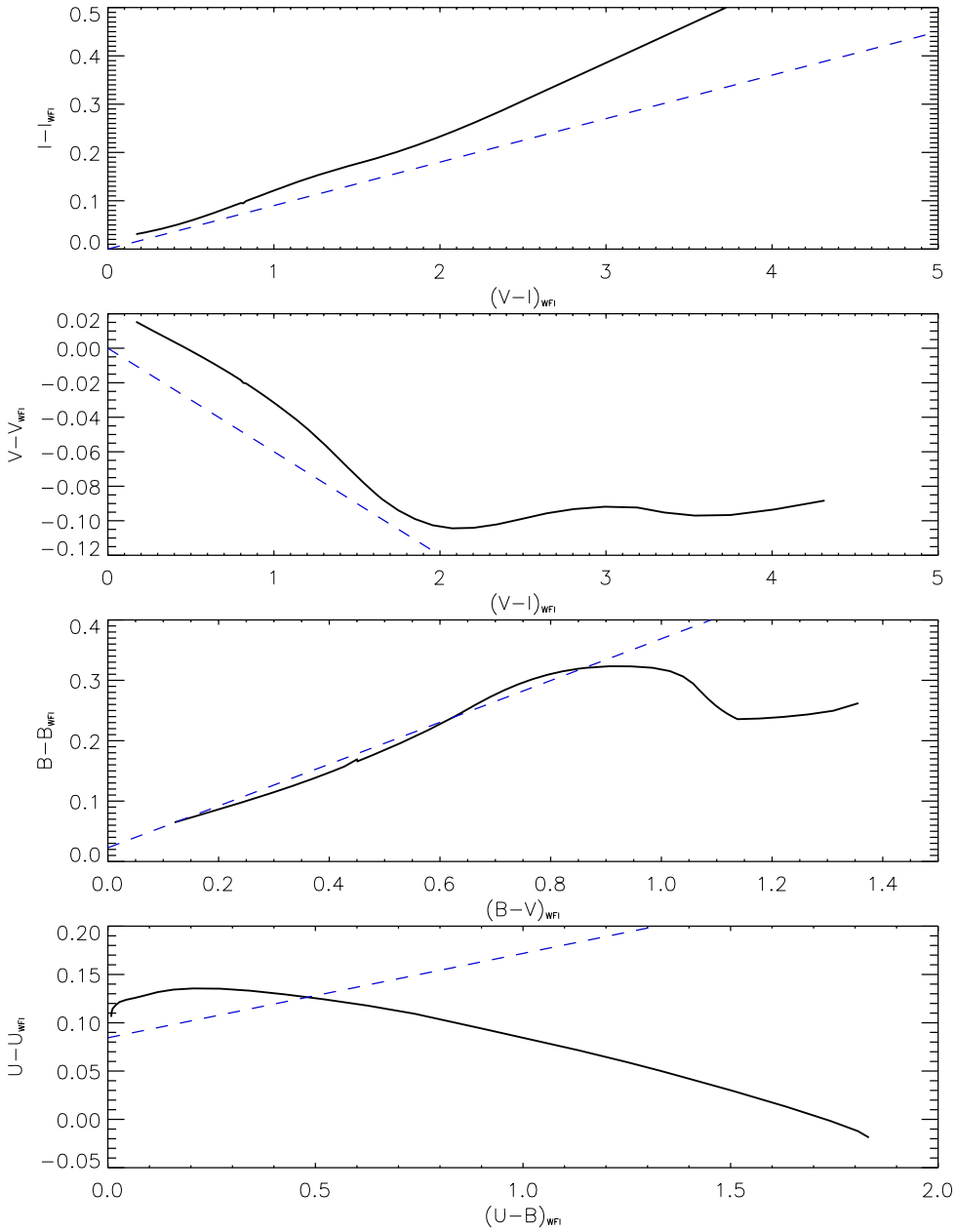

Figure 1.3 Transformations between the WFI instrumental photometric system and the standard Johnson-Cousins system. The dashed line refers to the linear relations obtained from standard field observation (extrapolating the filters color terms comparing the observed colors with tabulated standard magnitudes spanning a more limited range in color); the solid line is the result of synthetic photometry using NextGen models with $\log g = 3.5$ and $2600 \leq T_{\rm eff} \leq 8200$ K. B and U bands show high differences due to non linearity of the color correction.

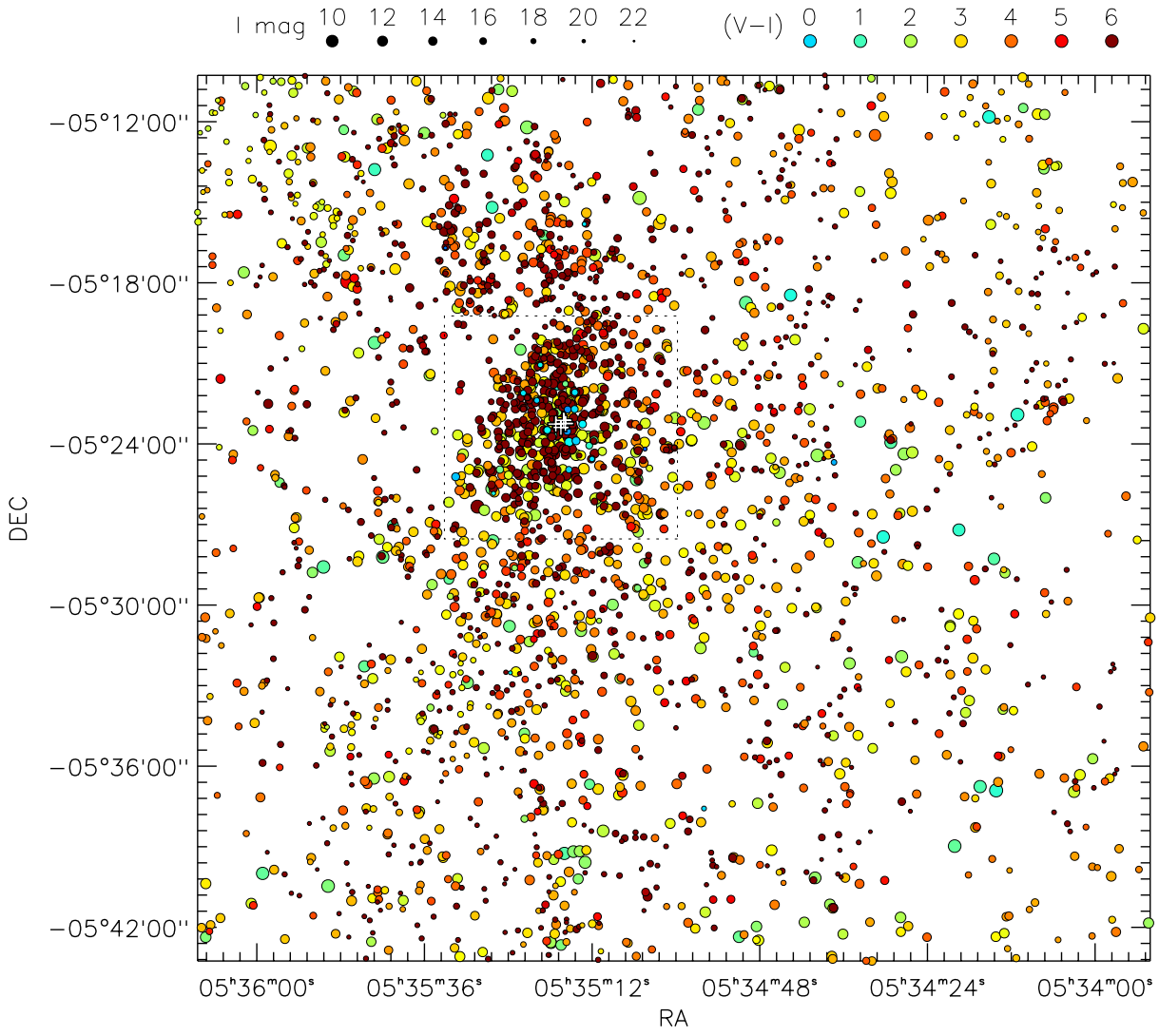

Figure 1.4 Point-like sources selected in the final catalogue with at least V and I magnitude detected for both night A and B. The size of the dots increases with I magnitude, and the colors represent the $V - I$ values as shown in the legend. The position of the four stars of the Trapezium cluster is shown with crosses. The dotted contour delimits the central area of 1pc of size centered on the star $\theta_1 c$ of the trapezium cluster. The zoomed spatial distribution within such a region is shown in Figure 1.5.

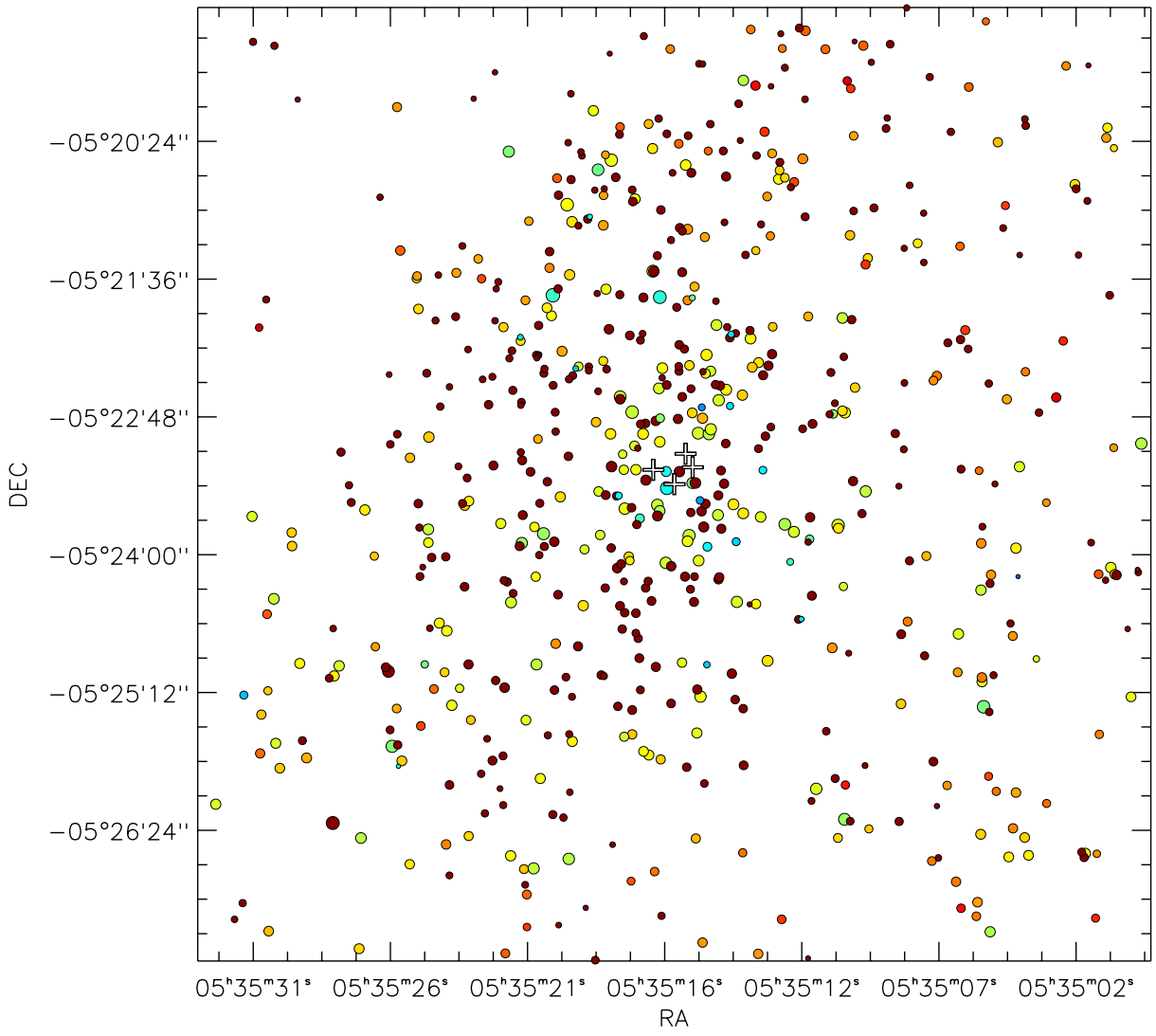

Figure 1.5 Same as Figure 1.4, for the inner area (1 pc of size) centered on the star $\theta_1 c$

VO), magnitudes are sensitive to changes in the strength of these features resulting from differences in the physical parameters, and so are the colors and color corrections. Thus, besides our lack of knowledge about the shape of the color corrections for red objects (see above), these correction are not unique for all the ONC members.

In order to assess the first point we performed a test extracting synthetic photometry from a set of stellar atmosphere models. We used the NextGen models (Hauschildt et al., 1999), choosing a set of spectra with $2600 \leq T_{\rm eff} \leq 8200$ K and $\log g = 3.5$.[4] Synthetic photometry has been derived using the Gensynphot software included in the Chorizos package (Maíz-Apellániz, 2004). We defined the WFI bands by multiplying the filter transmissions by the CCD quantum efficiency curves, quantities that are well known for the WFI instrument, and then computed the zero-points of this newly defined VegaMag photometric system using the calibrated Vega spectrum distributed with the Chorizos package. The measured instrumental magnitudes, therefore, are already expressed in this photometric system except for constant zero-points depending on the observing conditions. These offsets in fact coincide with the zero-points derived from standard field observations according to the standard method for photometric calibration (when we consider the color term relative to the calibrated magnitudes of the standard stars). This fact is clear considering the standard transformation, for instance, to calibrate an instrumental B-band photometry. We have that $(B - B_{WFI,\rm Ins}) = ZP + CC \cdot (B - V)$, where $B_{WFI,\rm Ins}$ is corrected in order to be valid for the airmass of the science observation in this band, from the two repetitions of standard field observations which were originally taken at low and high airmass each night. The intercept $(B - V) = 0$ corresponds to a Vega-type star, and in this case we have that $B - B_{WFI,\rm Ins} = ZP$. Furthermore, in the VegaMag convention, all the colors must be zero for a Vega-type star, so $(B - B_{WFI,\rm VegaMag}) = 0$. From these two expressions, finally, $(B_{WFI,\rm VegaMag} - B_{WFI,\rm Ins}) = ZP$. The same method used for all the bands results in an absolute calibration of the photometry in the instrumental-VegaMag photometric system.

We then computed the synthetic magnitudes for stars with different $T_{\rm eff}$ (i.e., different colors) in both the instrumental and the Johnson-Cousins photometric systems, determining the color-correction relations. The results are shown in Figure 1.3 for the four broad-band filters used. In every case the nonlinearity of these transformations is evident for high color terms; this effect affects dramatically the B band, with shifts up to few

[4] This value of $\log g$ is approximately one tenth of the solar value, and, according to the tables of H97 is a good enough approximation along all the temperature ranges in the ONC.

tenths of magnitude from the linear color correction relation at high $B-V$.

While in principle it could be possible to apply the simulated color correction law, these are sensitive not only to the stellar parameters, but also to the accuracy of the synthetic atmosphere models. Unfortunately the uncertainties present in all these grids, especially in the temperature range of the M-type stars, are still limiting factors for an accurate evaluation of the integrated colors (see Baraffe et al., 1998). Therefore, it is clear that keeping our catalog in the instrumental system removes most of the uncertainties related to the absolute photometric calibration, and, as we are going to show later on, preserves the capability of studying the stellar parameters through direct comparison of the observations with theoretical models. Our treatment of the color effects at high color terms and low surface gravity (in both band transformations and bolometric correction) represents a major improvement over the H97 analysis.

Narrow-band photometry

Due to the lack of standard star reference photometry in the two narrow bands in our dataset (the 6200Å TiO band and the Hα band), a traditional zero-point calibration approach cannot be followed; thus, we calibrated these data as follows.

First, the photometry of the two nights has been cross-calibrated, matching identical stars and determining the global average offset of night B versus night A, this step allows us to clean the sample from spurious detections. Then the magnitudes have been converted to units of flux (counts s^{-1}). We computed the ratio between the actual efficiencies (measured ADU / flux) between the TiO band and the Hα filter, taking into account the differences in the filter passbands, the quantum efficiency $QE(\nu)$, of the WFI CCDs, airmass – deriving the atmospheric extinction at 6200 Å linearly from the ones measured in V and I – and photon energy. In this way we derived *a priori* that, considering the observations of night A, a constant flux observed in both filters (in terms of Jy) corresponds to a number of ADUs in the Hα images ~ 2.70 lower that in the TiO images. Therefore, correcting for this factor, we *relatively* calibrate the Hα photometry on the TiO one. The subsequent absolute calibration of the latter, therefore, calibrates the Hα as well.

The problem is therefore to find the magnitude offset to apply to the TiO photometry in order to express our data in standard VegaMag. By definition this offset is such that a for a Vega-type star all the colors are zero, for instance $(V_{WFI}-TiO)=0$ or $(TiO-I_{WFI})=0$. Unfortunately our sample lacks a significant number of such objects,

requiring to use stars of later type to improve the precision of the calibration. If we consider the most abundant M-type stars in our catalog, however, the behavior of the measured flux in TiO is strongly affected by the absorption feature shown in Figure 1.1. We consider therefore the intermediate temperature stars (G and early K spectral types), isolated in our sample by matching our photometric catalog with the spectroscopy of Hillenbrand (1997). A first order estimate of the calibration to be applied to the TiO photometry could be to impose that, for these stars, the magnitude at 6200nm is equal to the linear interpolation of the V and I magnitudes, assumed at a wavelength equal to the average wavelength of the band profiles (see Table 1.1). We investigate the correctness of this assumption using synthetic photometry on a grid of atmosphere models. We consider the NextGen (Hauschildt et al., 1999) grid, for solar metallicity and surface gravity $\log(g/g_{\odot}) = 3.5$, an average value for PMS stars. In the temperature range we selected - for which the uncertainty of the theoretical spectra is negligible (Baraffe et al., 1998) -, the models predict that the TiO magnitude is on constantly 0.17 mag brighter than the assumed linear interpolation, and therefore we applied this offset in order to calibrate the TiO photometry. Once the photometry in VegaMag is calibrated, we are able to express it into physical flux, calculating the zero-point of the band of $3.175150 \cdot 10^6$ mJy by means of integration of a reference Vega spectrum using the *STSDAS Synphot* software. Given that we calibrate the Hα photometry in units of flux relatively to the TiO, the same zero point, as explained above, is therefore the same also for the absolute calibration of the Hα photometry.

1.4 The Source Catalog

The final catalog includes 2,621 point-like sources detected in I band, 1,523 of which have both V and I magnitudes, 1,134 also B magnitudes and 431 have U magnitudes. Narrow band photometry is available for 1040 stars. As mentioned above, the catalog itself provides for each star 2 distinct photometric values for nights A and B, respectively; however, given the poor sky conditions of night B, we present only the results from the observations during the first night.

In Figure 1.4 we present the distribution on the sky of the detected sources. The general structure of the cluster, elongated in the north-south direction as already described

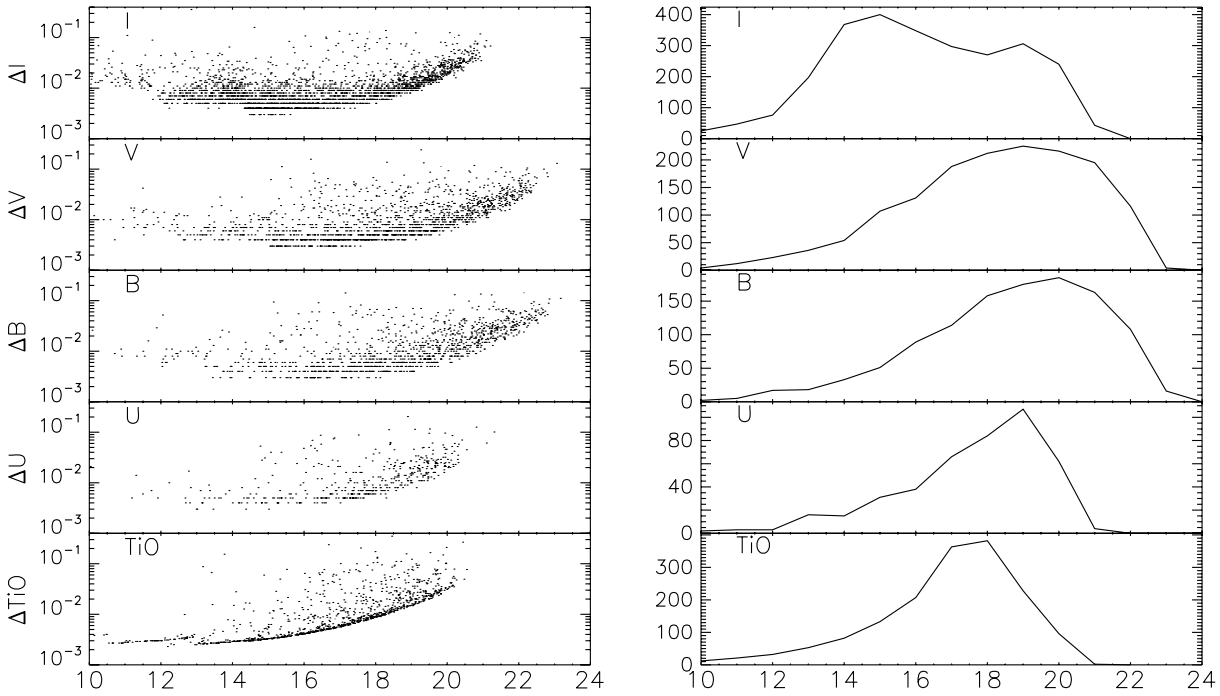

Figure 1.6 *Left panel*: photometric errors for the five bands observed. *Right panel*: luminosity functions. The double peak in the I band is reasonable due to contamination by background stars.

in Hillenbrand & Hartmann (1998), is evident. In this figure we also highlight different luminosities with the dot size and the $(V - I)$ indexes with colors.

Figure 1.6a shows the photometric errors as a function of luminosities for the UBVI+TiO filters. The visible multiple trends in the distribution of photometric errors are due to the superposition of deep, medium and short exposures. Bright stars are likely to be measured only in short exposures being saturated in the long ones, and their photometric error turns out relatively high. Figure 1.6b presents the observed luminosity functions in the 5 bands.

In Figure 1.7 we present the color-magnitude diagram for the four broad-band filters. We use different symbols for the stars having all the four broad-band magnitudes are available, only B, V, and I, or only V and I. Given the red colors of the ONC members, the faint stars lack signal at the shorter wavelengths.

We estimated the completeness limit of our survey, comparing our luminosity functions (LFs) in V band with the one derived from the HST/ACS catalog (M. Robberto et al. 2010, in preparation) in the $V-$ equivalent filter F555W. The HST survey is characterized by a considerably fainter detection limit. In order to allow for a consistent comparison,

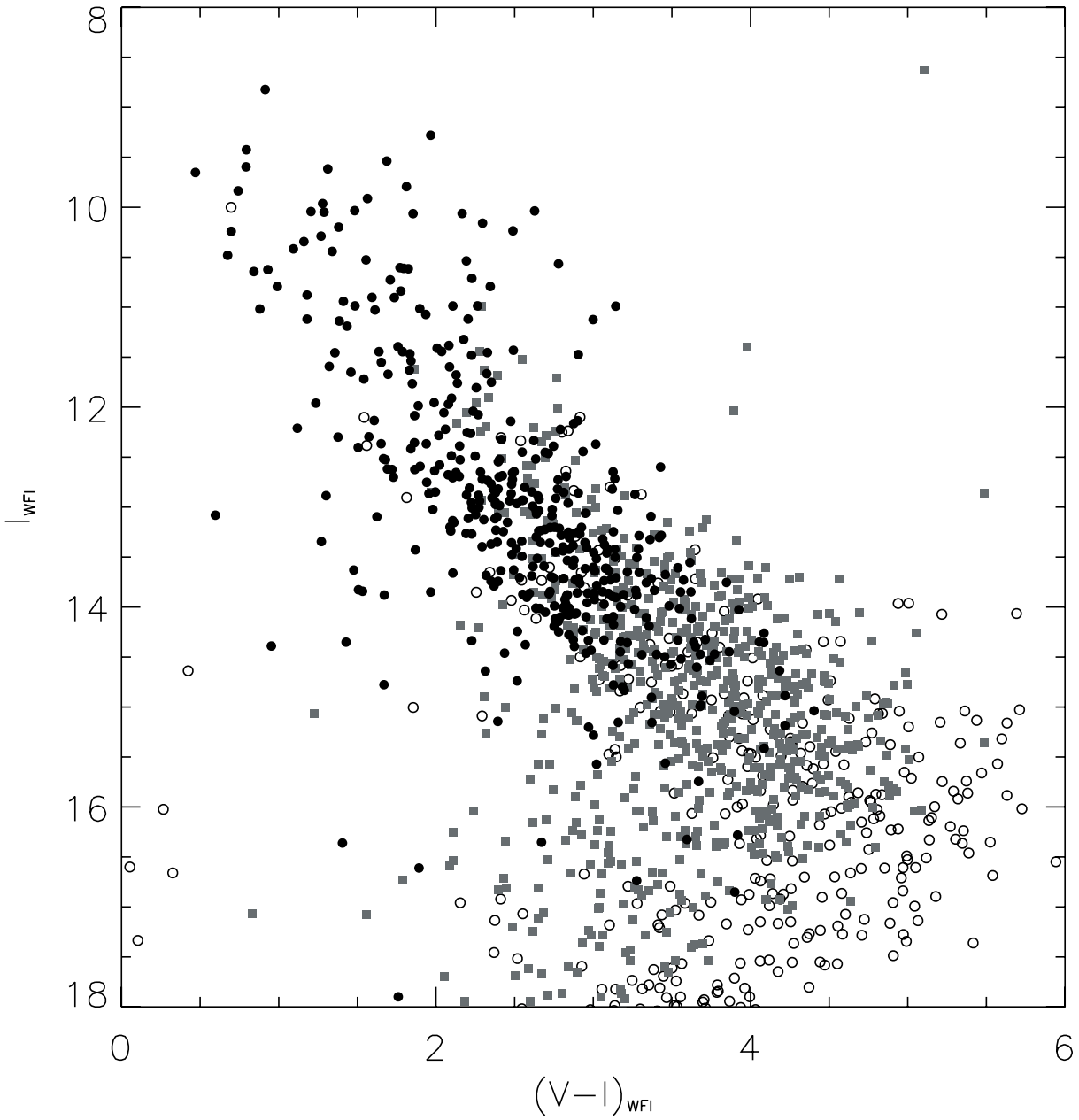

Figure 1.7 Instrumental color-magnitude diagram for the sources present in our catalog: filled circles are objects with all U, B, V, and I measures, squares are sources lacking U, and open circles are objects with only V and I magnitudes.

we considered only sources present in the common field of view. This, which is about 55% of the $\sim$ 1100 arcmin^2 total WFI FOV and contains about 70% of the WFI sources we detected, is wide enough to be well representative of the whole observed area, covering both the central part of the cluster, more affected by crowding, and the loose periphery. The ratio between LF counts, as a function of the V magnitude, directly provides our completeness function in this band. It is shown in Figure 1.8. At the bright end of the distribution the deep ACS catalog is deficient of sources with respect to WFI, due to saturation and to the presence of non stellar sources (e.g proplyds or circumstellar halos) which may contaminate our lower resolution of ground based catalog. At the faint end, the ratio of sources detected with WFI to $\sim 50\%$ at $V \simeq 20.8$, which we therefore consider as representative of our completeness limit for the source detected in both $V-$ and $I-$band.

Our catalog, presenting for each star coordinates, calibrated magnitudes and photometric errors in U, B, V, I, and TiO band is given in Table 1.2 (including only photometry derived from night A observations, used in this work). We matched our catalog with the one of Hillenbrand (1997), and the last column of Table 1.2 reports (if present) the ID number of the latter.

In principle, the photometry from the second night could have been used to estimate the stellar variability and to provide a better characterization of the uncertainty associated to photometry. However, the poor seeing conditions of the second night strongly affect also the accuracy of the photometry. This is because in a field like the Orion Nebula source confusion and non uniformity of the nebular background have a stronger influence on the photometric accuracy when the PSF is larger. If we limit ourselves to the brightest part of the photometric catalog, where these uncertainties have lower impact, we see that the standard deviation of the difference in magnitudes between the two night, for the bright 50% of the population, is 0.17 mag in the $I-$band, 0.30 mag in $V-$band and $B-$band, 0.35 mag in $U-$band, on a time baseline of about 24 hours. This is compatible with what found by Herbst et al. (2002), who report that more than 50% of the cluster members display a $I-$band variability larger than 0.2 magnitudes over periods of a few days.

The reported coordinates are the positions measured on the reduced images in I band, whose field distortion has been corrected by means of a polynomial warping using the 2mass astrometry as a reference for all the matched sources. We estimate the precision of our astrometry comparing our positions with those of the H97 catalog and with the HST/ACS photometry. In the comparison with H97, the standard deviation of the coordinate offsets is $0.24''$ in RA and $0.22''$ in Dec, while with respect to the HST photometry

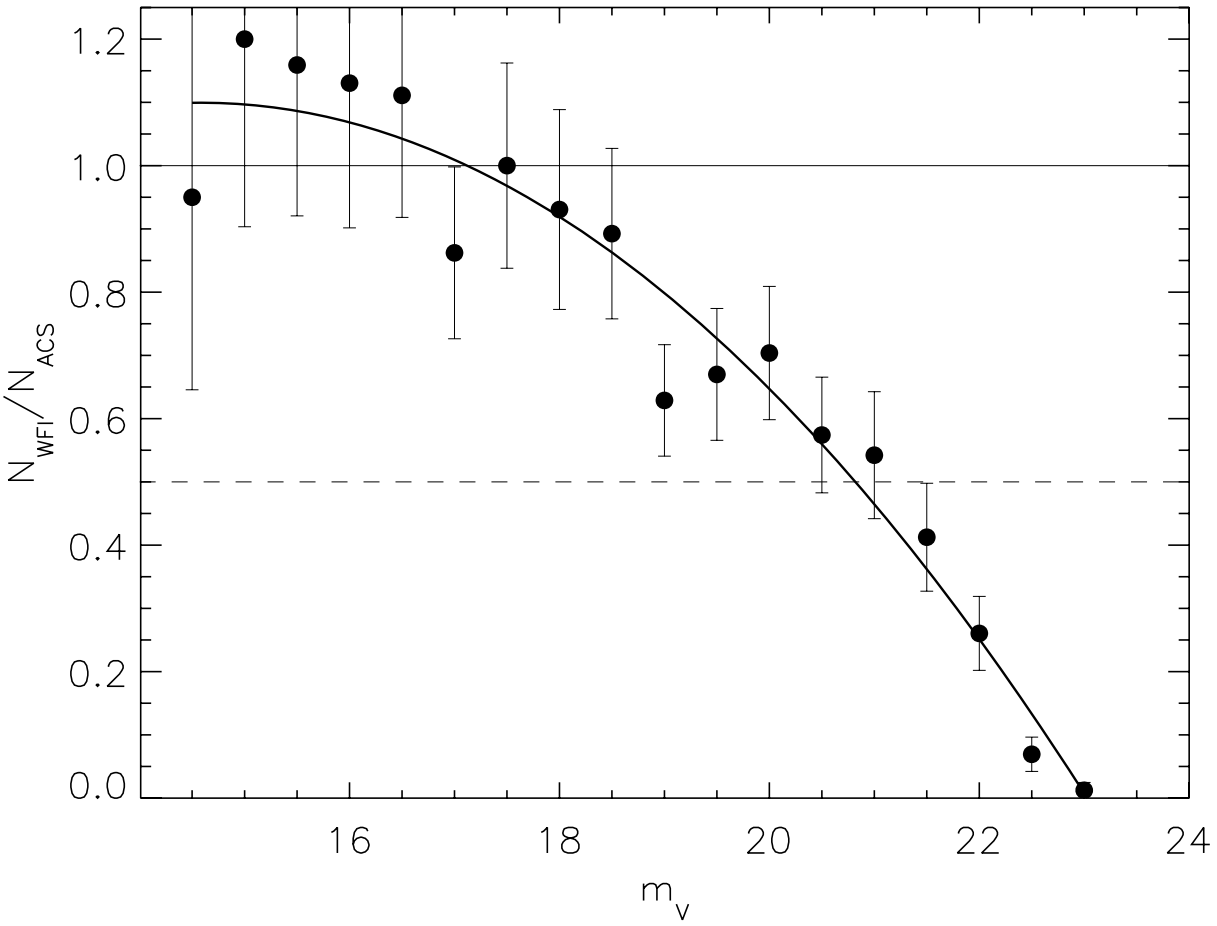

Figure 1.8 Completeness function for the V band. Dots represent the measure ratio between the number of sources counted in bins spaced 0.5 magnitudes in the WFI and the HST/ACS catalog respectively, considering only the common FOV of the two surveys. A polynomial fit of the second order is overlayed. The apparent systematic completeness greater than unity in the bright end is due to source saturation of the ACS imaging.

they decrease to $0.13''$ and $0.11''$ respectively. Given that the astrometric precision of the ACS catalog is much less than 1 pixel ($0.05''$), the latter dispersions are a good estimate of the uncertainty of our astrometry. Therefore, we consider the astrometric precision of our WFI catalog to be $\sim 0.13''$, which therefore improves by a factor of 2 over H97.

The Hα catalog, expressed in terms of non photospheric flux excess, is presented independently (see Section 1.5.1).

It is worthwhile to estimate the improvement in the optical characterization of ONC stars of our sample with respect to the one of H97. The two catalogs cover a similar extension on the sky, but the latter, counting 1576 sources with respect to our 2621 stars, is centered on the Trapezium cluster whereas our observations are centered about $6'$ to the south-west. If we consider only stars detected in the common area of the two catalogs, we have 2246 stars from WFI data and 1463 from H97, 926 of which are with known spectral types. We highlight that in the presented catalog we do not recover all the H97 sources in the common area, but we lose about 90 stars. This is mostly due for saturation in the WFI observations, but we also found for small sparse groups of stars evidences of systematic shifts in the coordinates between our coordinates and the H97 ones, large enough to fail our matching algorithms and probably due to erroneous coordinates in the literature. We do not consider those stars among the matched ones (last column of Table 1.2)

1.5 The TiO spectrophotometric index

The depth of the TiO spectral feature shown in Figure 1.1 can be used to classify late-type stars. To this purpose, we have defined a index, [TiO], using the V, I and TiO luminosities.

Our [TiO] index represents, roughly speaking, the "lack" of flux, in magnitudes, measured in the TiO feature, and is defined as the difference between the linear interpolation at 6200 Å of the V and I magnitudes and the apparent magnitude in the TiO band:

$$\begin{aligned} [TiO] &= m_{TiO,interp} - m_{TiO} \\ &= \left(V_{\mathrm{WFI}} - (V-I)_{\mathrm{WFI}} \cdot \frac{\lambda_{\mathrm{TiO}} - \lambda_V}{\lambda_I - \lambda_V} \right) - m_{TiO} \end{aligned} \tag{1.2}$$

where λ_V, λ_I and λ_{TiO} are the central wavelengths of the three filters, as reported in Table 1.1.

Table 1.2. WFI photometric catalog relative to Night A observations.

ID	RA (J2000.0)	Dec (J2000.0)	U	ΔU	B	ΔB	V	ΔV	TiO	ΔTiO	I	ΔI	H97 ID
1	05 35 47.01	-05 17 56.9	···	···	16.093	0.004	13.728	0.004	12.097	0.003	8.626	0.027	992
2	05 35 20.71	-05 21 44.4	9.886	0.008	10.041	0.009	9.736	0.008	9.540	0.004	8.822	0.021	660
3	05 35 05.20	-05 14 50.3	13.260	0.007	12.141	0.011	11.246	0.017	10.535	0.003	9.280	0.036	260
4	05 34 14.16	-05 36 54.1	11.081	0.005	10.697	0.009	10.219	0.010	9.929	0.004	9.425	0.016	···
5	05 35 21.31	-05 12 12.7	13.057	0.004	12.043	0.052	11.225	0.015	10.646	0.003	9.538	0.018	670
6	05 35 28.41	-05 26 20.1	···	···	···	···	···	···	9.601	0.004	9.552	0.016	831
7	05 34 11.11	-05 22 54.6	11.199	0.014	10.900	0.008	10.388	0.010	10.130	0.004	9.596	0.018	···
8	05 34 49.97	-05 18 44.6	12.583	0.004	11.496	0.010	10.928	0.010	10.474	0.004	9.616	0.023	108
9	05 35 16.72	-05 23 25.2	9.928	0.021	10.075	0.026	10.122	0.012	9.908	0.006	9.652	0.019	···
10	05 34 39.75	-05 24 25.6	14.065	0.004	12.535	0.010	11.606	0.008	10.906	0.003	9.794	0.021	45
···	···	···	···	···	···	···	···	···	···	···	···	···	···

Note. — Only a portion of the table is shown, for guidance to its content. The Hα photometry is presented separately in Table 1.5. All the magnitudes are given the VegaMag instrumental system. The last column reports the corresponding ID of the source in the catalog of Hillenbrand (1997), if present.

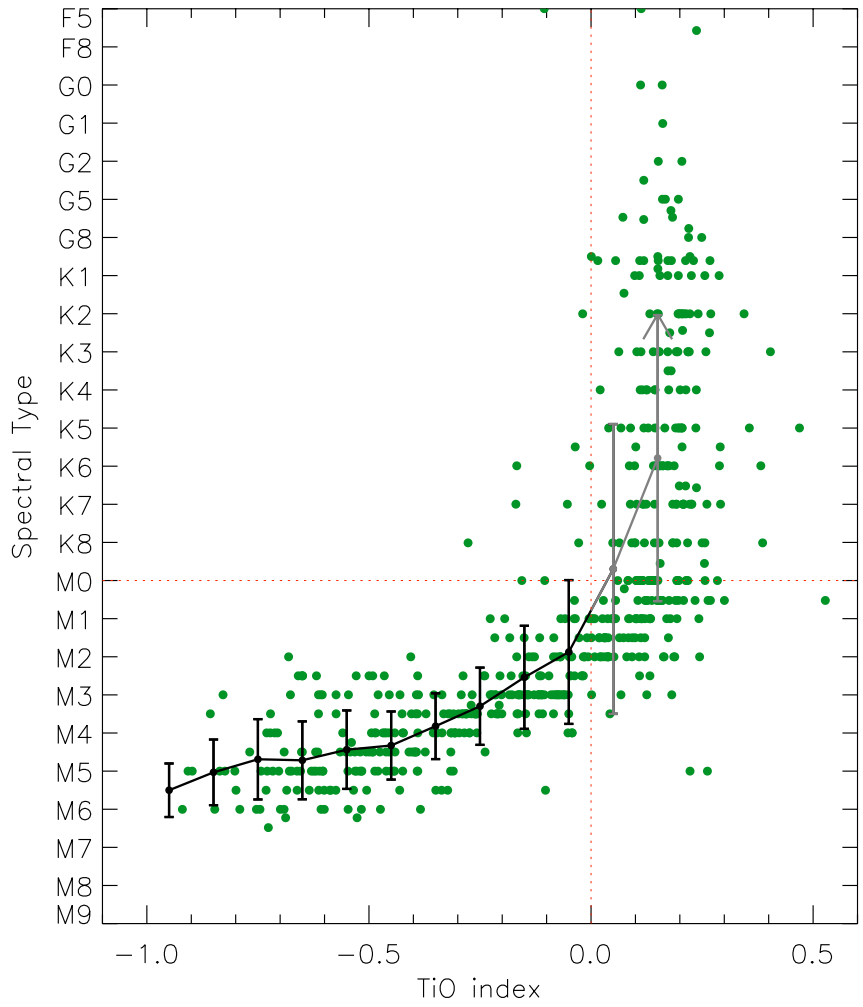

Figure 1.9 The spectral type versus [TiO] index relation showing all the 583 stars for which H97 spectral types and TiO photometric index are available, 298 of which are with [TiO]<0. The law we derived for M-type stars with low photometric errors ($\Delta m_{\rm TiO} \leq 0.03$) is overplotted (black line).

In Figure 1.9 we plot our [TiO] index versus the spectral type extracted for all the stars available from Hillenbrand (1997). This sample counts 583 stars. For M-type stars, the depth of the TiO feature measured by means of narrow-band photometry increases moving towards higher types, and is up to one magnitude fainter than the linear interpolation between V and I. In this spectral range, therefore, there is a definite correlation between [TiO] and spectral type, whereas for earlier classes it assumes a roughly constant value of $\simeq 0.1 - 0.2$ mag. This limits its use to M type stars and possibly brown dwarfs, which are not included in the H97 list.

By isolating within our catalog the stars with small photometric errors ($\Delta m_{\rm TiO} < 0.03$), we derived a quantitative relation between the TiO index and spectral type, extracted a moving average, as shown in Figure 1.9, and shown in Table 1.3. The 1σ uncertainty is also reported, showing that our relation is accurate to better than 1 spectral sub-class for M3-M6 types and better than 2 spectral sub-classes for M0-M2 types.

We investigated the sources of scatter evident in the figure looking for dependencies on other parameters. While assuming equal metallicity for the ONC members is quite legitimate, an age spread for the ONC members leads to a distribution of surface gravity for stars of a given mass, given that the stellar radius changes during PMS evolution. Specifically, we consider the tabulated values of $\log g$ derived in Hillenbrand (1997) using D'Antona & Mazzitelli (1994) evolutionary models on their H-R diagram. The latter was obtained from spectral types converted into $T_{\rm err}$ according to Cohen & Kuhi (1979) and bolometric corrections applied to reddening corrected $V - I$ photometry. In Figure 1.10 we present the surface gravity distribution, and presenting the H97 stars in the $T_{\rm eff}$ vs $\log g$ in comparison with PMS isochrones of different ages, we show that the measured age spread in the ONC is the main cause of a wide distribution of surface gravity in our sample.

We divided our stars in two samples, of low and high surface gravity, and we found that variations in surface gravity introduce a systematic offset in the TiO index versus spectral type relation. In Figure 1.11 we show the result of isolating stars with $\log g < 3.5$ and $\log g > 3.5$ in cgs units (the threshold being the average value of $\log g$ in our sample). We subtracted the "predicted" spectral type from the [TiO] index using our law tabulated in Table 1.3 to the "actual" one, and for each of the two subsamples we computed the average of these residuals (Figure 1.11, bottom panel). This is not zero in the two cases, suggesting a real dependance of the behavior of our index on the stellar surface gravity.

We then carried out a statistical test of the average of two subsets, assuming a gaussian

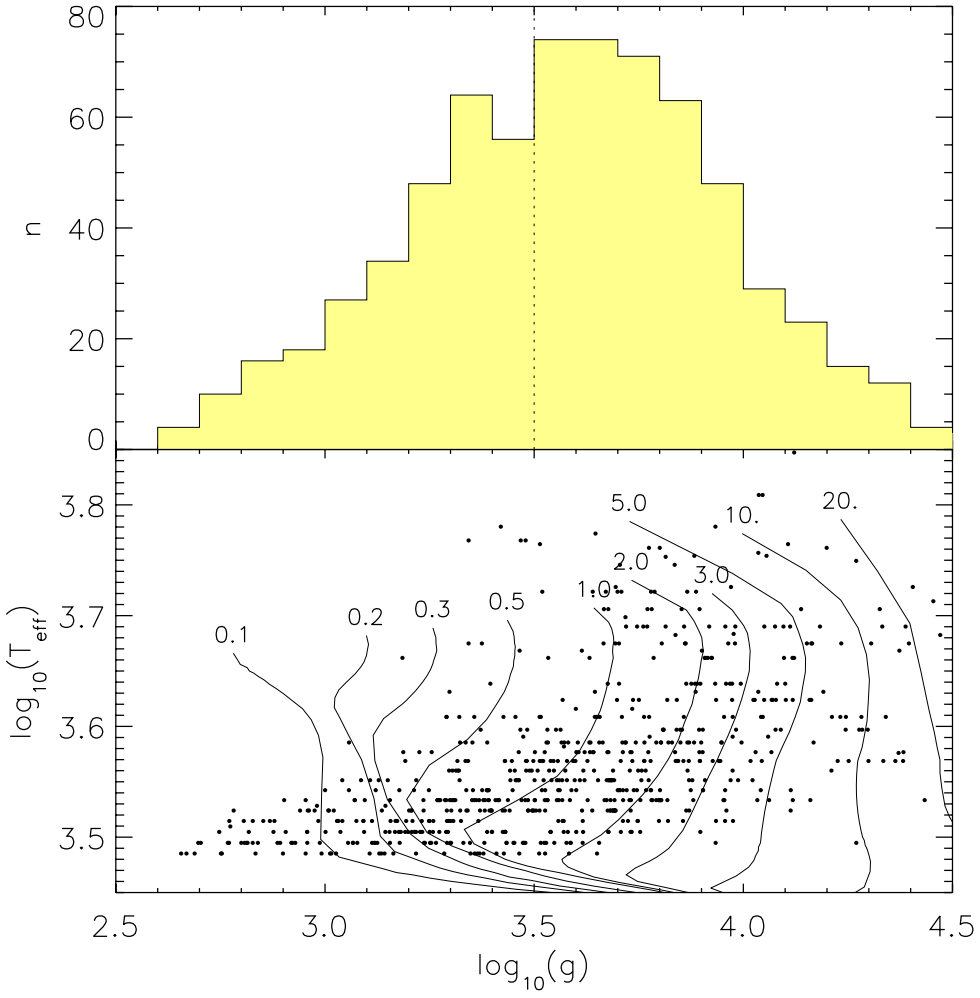

Figure 1.10 *Upper panel:* the distribution of $\log g$ (cgs units) from Hillenbrand (1997), limited to the sample of stars used to derive our [TiO] - spectral type relation. *Lower panel*: $T_{\rm eff}$ vs $\log g$ from the same work. Isochrones from 0.1 Myr to 20 Myr from evolutionary models of D'Antona & Mazzitelli (1994) are overlayed highlighting that the derived broad distribution of $\log g$ comes from the interpretation of the H-R diagram spread as due to an age distribution.

Table 1.3. Empirical TiO versus spectral type relation

TiO index	Sp Type	σ [types]
-0.95	M5.5	0.7
-0.85	M5.0	0.9
-0.75	M4.7	1.1
-0.65	M4.7	1.0
-0.55	M4.4	1.0
-0.45	M4.3	0.9
-0.35	M3.8	0.9
-0.25	M3.3	1.0
-0.15	M2.5	1.4
-0.05	M1.9	1.9
0.05	<M3.5	···
0.15	<M0.5	···

distribution, and comparing the shift between the two mean values from zero with the relative rms. In other words, we computed the probability P that the two distributions are statistical representations of the same distribution considering the estimator z as follows:

$$z = \frac{m_1 - m_2}{\sqrt{\frac{\sigma_1^2}{N_1} + \frac{\sigma_2^2}{N_2}}} \tag{1.3}$$

where $m_1 - m_2 = 1.1$ spectral sub-types is the difference between the two mean values (shown in Figure 1.11b by the dashed and dotted lines), σ_1 and σ_2 are the standard deviations of the two sets, and N_1 and N_2 are the total number of stars in each set. We derived $z = 5.9$, corresponding to a probability (for the gaussian hypothesis) of about $2 \cdot 10^{-9}$. This proves that the behavior of the TiO index is dependent on surface gravity, and, for a given value of the index, the higher the surface gravity, the lower the derived spectral type. The difference of the averages of $\log g$ in the two subsets is equal to 0.53 dex. We derive a shift in the [TiO] vs $\log T_{\rm eff}$ relation of 2 subtypes per unit of $\log g$ with respect to our empirical law tabulated in Table 1.3, valid for the average value $\log g = 3.5$.

[t!]

The dependence of the [TiO] index on surface gravity is intriguing, but its interpretation is not necessarily trivial. In fact, as the depth of the TiO feature is influenced by

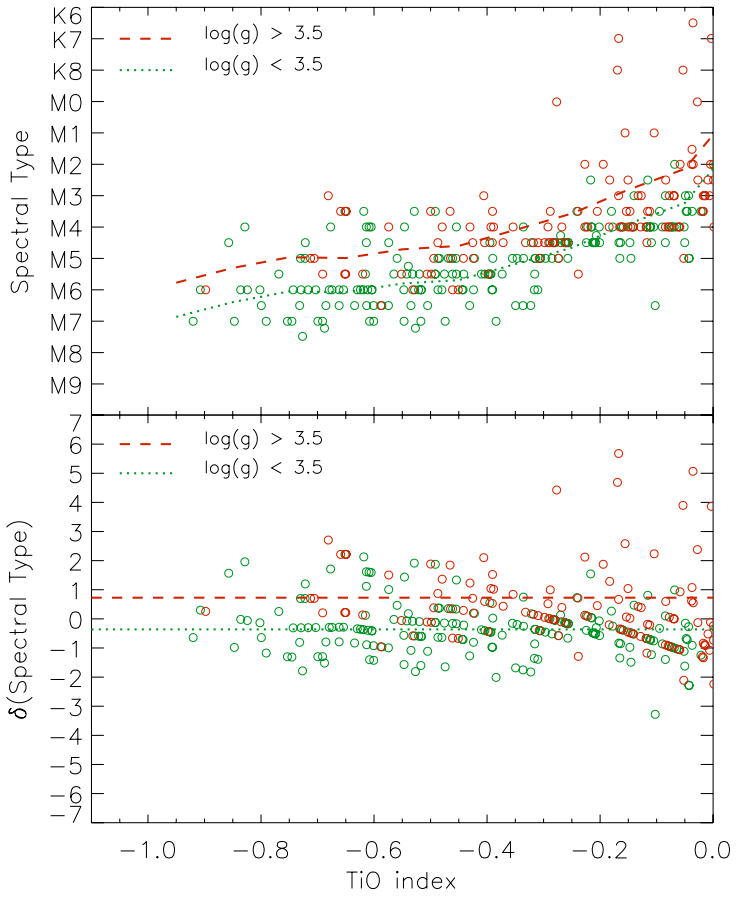

Figure 1.11 *Upper panel:* the relation for values of TiO indices for the case of $\log g > 3.5$ and < 3.5 in cgs units. *Bottom panel:* the displacement in units of spectral types with respect to the global dependence of Table 1.3, showing the average in the 2 cases.

stellar surface gravity, also the behavior or the $V-$ and $I-$ band of cold stars depend on the luminosity class of the star, and therefore on the stellar parameter $\log g$. Moreover, the younger is a low-mass PMS star, the lower is its surface gravity (because of its larger radius); the dependance we found could be, therefore, introduced by different ages in the considered mass range. For instance, mass accretion, which is typically higher for young pre-main sequence objects introduces veiling in the stellar spectrum, which decreases the relative depth of the spectral absorption features, causing a star of a given temperature to have a shallower TiO feature at younger ages.

In any case, neither age nor surface gravity is known for stars of the ONC for which the spectral type is not determined. This implies that using our [TiO] - spectral type relation to classify M-type stars cannot be refined by the aforementioned consideration

about surface gravity. Therefore, we leave a detailed analysis of the sources of this effect in the [TiO] index to a future work, considering, for the moment, only the global relation expressed in Table 1.3.

Using this, we compute the value of [TiO] for all stars not included in the H97 spectral catalog for which our V,I and TiO band photometry is available. Selecting only sources with [TiO]< 0. We derive the spectral type and its uncertainty for 217 additional stars. The results are tabulated in Table 1.4.

Table 1.4: New M-type stars classified from the [TiO] index

	ID *	RA (J2000.0)	Dec (J2000.0)	[TiO] (mags)	Spectral Type	σ
1	1306	05 36 00.49	-05 41 10.9	-0.145	M2.5	1.4
2	608	05 35 59.48	-05 37 09.6	-0.478	M4.4	0.9
3	1642	05 35 59.25	-05 33 00.4	-0.541	M4.4	1.0
4	630	05 35 57.51	-05 39 51.3	-0.080	M2.1	1.7
5	1571	05 35 57.35	-05 25 15.6	-0.457	M4.3	0.9
6	758	05 35 55.97	-05 42 26.3	-0.225	M3.1	1.1
7	1084	05 35 54.49	-05 26 45.6	-0.241	M3.2	1.0
8	1370	05 35 52.90	-05 25 43.9	-0.068	M2.0	1.8
9	732	05 35 52.20	-05 39 24.7	-0.001	M0.8	2.8
10	746	05 35 51.76	-05 17 39.4	-0.393	M4.0	0.9
11	815	05 35 48.71	-05 42 14.4	-0.369	M3.9	0.9
12	660	05 35 47.65	-05 37 38.8	-0.322	M3.7	0.9
13	304	05 35 46.42	-05 41 00.7	-0.400	M4.1	0.9
14	1233	05 35 44.58	-05 32 55.9	-0.321	M3.7	0.9
15	515	05 35 43.44	-05 40 55.0	-0.049	M1.9	1.9
16	938	05 35 42.66	-05 40 42.2	-0.462	M4.3	0.9
17	1404	05 35 42.61	-05 26 33.7	-0.550	M4.4	1.0
18	778	05 35 41.30	-05 38 32.9	-0.382	M4.0	0.9
19	890	05 35 41.23	-05 38 29.4	-0.410	M4.1	0.9
20	999	05 35 41.13	-05 42 51.1	-0.472	M4.4	0.9
21	379	05 35 40.83	-05 32 01.8	-0.311	M3.6	0.9
22	1258	05 35 37.06	-05 37 37.2	-0.569	M4.5	1.0
23	1390	05 35 36.55	-05 40 25.1	-0.510	M4.4	1.0
24	562	05 35 36.35	-05 31 37.8	-0.461	M4.3	0.9
25	629	05 35 35.95	-05 38 42.7	-0.334	M3.7	0.9
26	594	05 35 35.61	-05 29 36.5	-0.492	M4.4	1.0
27	549	05 35 35.14	-05 21 23.6	-0.115	M2.3	1.5
28	1271	05 35 35.02	-05 41 01.4	-0.307	M3.6	0.9
29	1322	05 35 34.64	-05 27 15.0	-0.692	M4.7	1.0
30	1038	05 35 34.61	-05 15 52.7	-0.442	M4.3	0.9
31	879	05 35 34.37	-05 26 59.6	-0.814	M4.9	0.9
32	293	05 35 34.21	-05 27 18.2	-0.334	M3.7	0.9
33	947	05 35 33.59	-05 15 23.2	-0.045	M1.8	2.0
34	734	05 35 33.41	-05 39 21.3	-0.186	M2.8	1.2
35	545	05 35 33.31	-05 39 24.9	-0.086	M2.1	1.7
36	664	05 35 33.11	-05 17 34.0	-0.525	M4.4	1.0
37	1313	05 35 32.88	-05 39 19.1	-0.748	M4.7	1.1
38	1459	05 35 32.60	-05 40 12.4	-0.684	M4.7	1.0

Table 1.4 – continued from previous page

39	1116	05 35 31.75	-05 16 39.9	-0.038	M1.6	2.1
40	838	05 35 31.68	-05 42 46.0	-0.239	M3.2	1.1
41	814	05 35 31.56	-05 16 36.9	-0.978	M5.6	0.7
42	1108	05 35 31.53	-05 15 23.6	-0.140	M2.5	1.4
43	657	05 35 30.70	-05 18 07.1	-0.050	M1.9	1.9
44	1011	05 35 30.63	-05 15 16.3	-0.789	M4.8	1.0
45	460	05 35 30.42	-05 34 38.6	-0.564	M4.5	1.0
46	364	05 35 29.80	-05 16 06.4	-0.038	M1.6	2.1
47	1517	05 35 29.67	-05 30 24.7	-0.301	M3.6	0.9
48	794	05 35 28.77	-05 41 34.0	-0.230	M3.1	1.1
49	1009	05 35 28.28	-05 37 19.6	-0.644	M4.7	1.0
50	487	05 35 27.66	-05 42 55.2	-0.307	M3.6	0.9
51	432	05 35 27.20	-05 30 24.7	-0.518	M4.4	1.0
52	638	05 35 26.72	-05 16 45.1	-0.405	M4.1	0.9
53	780	05 35 26.45	-05 30 16.4	-0.358	M3.9	0.9
54	939	05 35 25.53	-05 34 04.7	-0.067	M2.0	1.8
55	823	05 35 25.33	-05 25 29.4	-0.354	M3.8	0.9
56	725	05 35 25.22	-05 29 51.6	-0.461	M4.3	0.9
57	284	05 35 24.64	-05 11 58.3	-0.253	M3.3	1.0
58	484	05 35 24.47	-05 11 58.0	-0.469	M4.3	0.9
59	644	05 35 24.09	-05 21 32.7	-0.499	M4.4	1.0
60	948	05 35 23.50	-05 34 23.4	-0.435	M4.3	0.9
61	1054	05 35 22.68	-05 16 14.0	-0.072	M2.0	1.8
62	341	05 35 22.61	-05 14 11.2	-0.143	M2.5	1.4
63	1015	05 35 22.24	-05 18 08.8	-0.735	M4.7	1.0
64	1337	05 35 22.07	-05 28 55.6	-0.341	M3.8	0.9
65	667	05 35 21.97	-05 17 04.9	-0.560	M4.5	1.0
66	743	05 35 21.88	-05 17 03.4	-0.428	M4.2	0.9
67	1347	05 35 21.63	-05 17 19.1	-0.288	M3.5	1.0
68	713	05 35 21.62	-05 26 57.5	-0.474	M4.4	0.9
69	560	05 35 21.62	-05 34 58.4	-0.333	M3.7	0.9
70	420	05 35 21.25	-05 42 12.3	-0.151	M2.5	1.3
71	795	05 35 21.15	-05 18 21.3	-0.378	M4.0	0.9
72	415	05 35 20.93	-05 40 14.3	-0.521	M4.4	1.0
73	739	05 35 20.56	-05 20 43.2	-0.084	M2.1	1.7
74	1314	05 35 19.86	-05 31 03.7	-0.178	M2.8	1.3
75	770	05 35 19.81	-05 22 21.6	-0.084	M2.1	1.7
76	491	05 35 19.79	-05 30 37.5	-0.563	M4.5	1.0
77	836	05 35 19.75	-05 39 35.6	-0.235	M3.2	1.1
78	1246	05 35 19.56	-05 27 35.6	-0.030	M1.4	2.3
79	408	05 35 19.48	-05 36 51.8	-0.276	M3.4	1.0
80	1486	05 35 19.32	-05 16 09.9	-0.198	M2.9	1.2
81	414	05 35 18.83	-05 14 45.6	-0.211	M3.0	1.1
82	1185	05 35 18.49	-05 42 30.7	-0.516	M4.4	1.0
83	1104	05 35 18.46	-05 39 19.8	-0.522	M4.4	1.0
84	454	05 35 18.29	-05 28 46.1	-0.143	M2.5	1.4
85	1070	05 35 17.97	-05 16 45.1	-0.095	M2.2	1.6
86	523	05 35 17.93	-05 25 33.8	-0.186	M2.8	1.2
87	666	05 35 17.66	-05 23 41.0	-1.033	M5.9	0.6
88	433	05 35 17.53	-05 40 48.3	-0.248	M3.3	1.0
89	552	05 35 17.43	-05 30 25.3	-0.119	M2.3	1.5
90	468	05 35 17.34	-05 42 14.6	-0.076	M2.0	1.7
91	707	05 35 17.15	-05 41 53.8	-0.492	M4.4	1.0

Table 1.4 – continued from previous page

92	723	05 35 17.00	-05 15 44.2	-0.396	M4.1	0.9
93	950	05 35 16.81	-05 39 17.0	-0.582	M4.5	1.0
94	68	05 35 16.75	-05 24 04.2	-0.007	M0.9	2.7
95	686	05 35 15.95	-05 16 57.5	-0.222	M3.1	1.1
96	709	05 35 15.94	-05 41 11.4	-0.441	M4.3	0.9
97	1588	05 35 15.49	-05 22 42.9	-0.048	M1.8	1.9
98	642	05 35 15.48	-05 35 11.9	-0.157	M2.6	1.3
99	375	05 35 15.30	-05 39 56.1	-0.329	M3.7	0.9
100	936	05 35 14.63	-05 16 46.1	-0.510	M4.4	1.0
101	912	05 35 13.75	-05 34 54.9	-0.401	M4.1	0.9
102	576	05 35 13.65	-05 28 46.2	-0.189	M2.8	1.2
103	693	05 35 13.56	-05 27 57.2	-0.482	M4.4	0.9
104	1130	05 35 13.31	-05 37 15.8	-0.792	M4.8	1.0
105	1274	05 35 13.17	-05 36 18.0	-0.218	M3.1	1.1
106	1078	05 35 12.94	-05 28 49.8	-0.241	M3.2	1.0
107	1648	05 35 12.40	-05 24 03.7	-0.317	M3.6	0.9
108	681	05 35 12.26	-05 20 45.2	-0.246	M3.3	1.0
109	917	05 35 12.04	-05 14 14.6	-0.179	M2.8	1.3
110	662	05 35 11.77	-05 21 55.5	-0.470	M4.4	0.9
111	942	05 35 11.72	-05 23 51.9	-0.471	M4.4	0.9
112	706	05 35 11.65	-05 31 01.1	-0.485	M4.4	0.9
113	1222	05 35 11.23	-05 41 36.1	-0.191	M2.8	1.2
114	721	05 35 11.17	-05 19 35.8	-0.397	M4.1	0.9
115	1168	05 35 11.07	-05 41 56.3	-0.624	M4.6	1.0
116	915	05 35 10.90	-05 22 46.4	-0.169	M2.7	1.3
117	984	05 35 10.41	-05 19 52.4	-0.186	M2.8	1.2
118	482	05 35 10.13	-05 22 32.6	-0.056	M1.9	1.9
119	808	05 35 09.27	-05 16 56.0	-0.098	M2.2	1.6
120	690	05 35 08.29	-05 24 34.9	-0.613	M4.6	1.0
121	827	05 35 08.03	-05 36 14.1	-0.628	M4.7	1.0
122	1272	05 35 07.09	-05 42 33.3	-0.299	M3.6	0.9
123	941	05 35 06.91	-05 26 00.5	-0.722	M4.7	1.0
124	1064	05 35 06.83	-05 42 35.4	-0.283	M3.5	1.0
125	898	05 35 06.42	-05 27 04.7	-0.741	M4.7	1.1
126	1348	05 35 05.75	-05 35 22.1	-0.739	M4.7	1.0
127	413	05 35 05.69	-05 25 04.1	-0.346	M3.8	0.9
128	1123	05 35 05.67	-05 43 04.6	-0.594	M4.6	1.0
129	945	05 35 05.61	-05 18 24.8	-0.378	M4.0	0.9
130	513	05 35 05.13	-05 20 24.4	-0.130	M2.4	1.5
131	1753	05 35 03.79	-05 24 54.4	-0.435	M4.3	0.9
132	1403	05 35 02.99	-05 38 40.5	-0.613	M4.6	1.0
133	1209	05 35 02.69	-05 32 24.9	-0.597	M4.6	1.0
134	1150	05 35 01.71	-05 27 09.8	-0.802	M4.9	1.0
135	1035	05 35 01.32	-05 18 21.3	-0.436	M4.3	0.9
136	503	05 35 01.16	-05 29 55.2	-0.243	M3.2	1.0
137	1540	05 34 59.18	-05 41 12.5	-0.296	M3.5	0.9
138	1572	05 34 57.36	-05 32 43.1	-0.031	M1.5	2.3
139	522	05 34 57.23	-05 42 02.7	-0.052	M1.9	1.9
140	1152	05 34 53.48	-05 40 03.9	-0.525	M4.4	1.0
141	1603	05 34 53.07	-05 26 27.7	-0.619	M4.6	1.0
142	1224	05 34 52.67	-05 21 25.2	-0.395	M4.0	0.9
143	1067	05 34 52.36	-05 25 00.7	-0.940	M5.5	0.7
144	626	05 34 52.34	-05 30 07.9	-0.384	M4.0	0.9

Table 1.4 – continued from previous page

145	331	05 34 51.74	-05 39 24.0	-0.106	M2.2	1.6
146	735	05 34 50.86	-05 39 29.2	-0.482	M4.4	0.9
147	1363	05 34 50.21	-05 35 39.0	-0.789	M4.8	1.0
148	1138	05 34 48.45	-05 31 07.2	-0.336	M3.7	0.9
149	1543	05 34 47.73	-05 26 32.1	-0.434	M4.2	0.9
150	1510	05 34 47.66	-05 31 11.7	-0.331	M3.7	0.9
151	1562	05 34 46.87	-05 30 19.7	-0.501	M4.4	1.0
152	481	05 34 45.87	-05 41 09.6	-0.212	M3.0	1.1
153	307	05 34 42.73	-05 28 37.5	-0.154	M2.6	1.3
154	1366	05 34 42.48	-05 22 46.2	-0.623	M4.6	1.0
155	1242	05 34 42.19	-05 33 03.5	-0.217	M3.0	1.1
156	1243	05 34 41.96	-05 21 32.0	-0.654	M4.7	1.0
157	1160	05 34 41.72	-05 36 48.7	-0.509	M4.4	1.0
158	1211	05 34 39.11	-05 34 02.3	-0.739	M4.7	1.0
159	969	05 34 38.19	-05 35 49.5	-0.437	M4.3	0.9
160	181	05 34 36.54	-05 36 17.1	-0.008	M1.0	2.7
161	661	05 34 35.76	-05 40 09.4	-0.155	M2.6	1.3
162	702	05 34 35.68	-05 35 52.1	-0.180	M2.8	1.3
163	1230	05 34 35.60	-05 37 24.0	-0.597	M4.6	1.0
164	655	05 34 33.72	-05 40 22.7	-0.595	M4.6	1.0
165	858	05 34 32.23	-05 41 48.4	-0.400	M4.1	0.9
166	1155	05 34 30.24	-05 17 01.2	-0.550	M4.4	1.0
167	1052	05 34 30.11	-05 40 15.2	-0.618	M4.6	1.0
168	979	05 34 29.34	-05 33 39.7	-0.128	M2.4	1.5
169	1121	05 34 28.96	-05 23 48.1	-0.636	M4.7	1.0
170	1391	05 34 28.56	-05 30 32.4	-0.409	M4.1	0.9
171	570	05 34 27.80	-05 42 10.2	-0.025	M1.3	2.4
172	401	05 34 27.53	-05 28 28.4	-0.425	M4.2	0.9
173	565	05 34 26.75	-05 41 57.3	-0.194	M2.9	1.2
174	995	05 34 25.78	-05 35 46.5	-0.411	M4.1	0.9
175	949	05 34 25.54	-05 37 02.3	-0.350	M3.8	0.9
176	907	05 34 24.05	-05 42 22.1	-0.295	M3.5	0.9
177	688	05 34 21.23	-05 35 34.7	-0.502	M4.4	1.0
178	902	05 34 18.68	-05 37 08.1	-0.451	M4.3	0.9
179	1708	05 34 18.37	-05 22 54.9	-0.297	M3.5	0.9
180	256	05 34 17.48	-05 31 58.6	-0.138	M2.5	1.4
181	525	05 34 17.43	-05 30 35.2	-0.189	M2.8	1.2
182	1418	05 34 17.26	-05 22 36.8	-0.022	M1.3	2.4
183	1489	05 34 17.15	-05 37 11.8	-0.269	M3.4	1.0
184	388	05 34 17.14	-05 38 16.8	-0.237	M3.2	1.1
185	1053	05 34 16.95	-05 30 53.2	-0.811	M4.9	0.9
186	1294	05 34 15.09	-05 23 00.0	-0.309	M3.6	0.9
187	615	05 34 13.87	-05 36 35.3	-0.479	M4.4	0.9
188	1017	05 34 13.51	-05 35 38.6	-0.050	M1.9	1.9
189	395	05 34 13.20	-05 33 53.5	-0.131	M2.4	1.5
190	889	05 34 12.71	-05 41 36.4	-0.446	M4.3	0.9
191	1086	05 34 12.33	-05 41 34.7	-0.489	M4.4	0.9
192	864	05 34 12.02	-05 24 19.6	-0.284	M3.5	1.0
193	1113	05 34 11.50	-05 30 19.8	-0.784	M4.8	1.0
194	457	05 34 09.01	-05 24 05.6	-0.065	M2.0	1.8
195	121	05 34 08.22	-05 11 43.0	-0.168	M2.7	1.3
196	641	05 34 07.96	-05 36 17.0	-0.288	M3.5	1.0
197	839	05 34 07.80	-05 22 32.3	-0.216	M3.0	1.1

Table 1.4 – continued from previous page

198	358	05 34 07.46	-05 13 36.4	-0.139	M2.5	1.4
199	1099	05 34 07.22	-05 29 32.4	-0.636	M4.7	1.0
200	1032	05 34 07.13	-05 22 27.0	-0.778	M4.8	1.0
201	1073	05 34 07.12	-05 15 59.3	-0.357	M3.9	0.9
202	1457	05 34 07.02	-05 30 20.0	-0.322	M3.7	0.9
203	1090	05 34 06.86	-05 23 08.3	-0.808	M4.9	0.9
204	1508	05 34 06.78	-05 21 46.8	-0.472	M4.4	0.9
205	1057	05 34 04.64	-05 22 22.4	-0.357	M3.9	0.9
206	918	05 34 04.40	-05 36 26.4	-0.650	M4.7	1.0
207	1257	05 34 03.89	-05 29 51.1	-0.618	M4.6	1.0
208	480	05 34 03.71	-05 22 18.7	-0.236	M3.2	1.1
209	935	05 34 02.91	-05 39 21.1	-0.456	M4.3	0.9
210	1343	05 34 02.67	-05 33 02.9	-0.854	M5.1	0.9
211	647	05 33 57.91	-05 36 26.9	-0.284	M3.5	1.0
212	362	05 33 57.68	-05 40 06.0	-0.098	M2.2	1.6
213	427	05 33 56.77	-05 21 33.4	-0.410	M4.1	0.9
214	946	05 33 56.56	-05 39 04.3	-0.389	M4.0	0.9
215	1241	05 33 53.97	-05 27 34.5	-0.083	M2.1	1.7
216	553	05 33 53.08	-05 35 15.7	-0.471	M4.4	0.9
217	384	05 33 52.11	-05 30 28.3	-0.268	M3.4	1.0

1.5.1 The Hα photometry

T Tauri stars are known to exhibit strong Hα emission, associated, together with UV excess, with ongoing mass accretion from a circumstellar disk to the star. The Hα excess is the most used observational quantity to estimate the mass accretion rates, an important parameter for understanding the evolution of both stars and disks. Here we describe the derived line excess derived from our photometry in the WFI Hα filter.

After having calibrated the Hα photometry into units of Jy, as described in Section 1.3.2, we derive the line excess, following an approach analogous to the one used for the TiO index. We computed the flux at 6563 Å by linear interpolation between the (logarithmic) fluxes in V and I. We computed for all stars the ratio between the measured flux and the interpolated flux; for stars that do not emit in Hα – or for which the line emission is negligible – this ratio should be close to unity. We analyzed the behavior of our assumption of linear interpolation for the photospheric flux by plotting the Hα excess as a function of the TiO index, to highlight eventual trends with spectral class. In other words, it is reasonable to question the hypothesis that a relation of type (V-I) vs (6563$\mathring{A}$-I) is linear along the entire range in colors, especially for late type stars.

Indeed, as seen in Figure 1.12, besides the presence of a large population of stars with a noticeable excess, all the stars without emission lie on a locus which has a weak – but definite – dependence on the TiO index, and therefore on spectral type (see the [TiO] - temperature relation described in Section 1.5). We isolated this curve iterating a sigma-clipping algorithm and considered this flux level as the photospheric baseline. Clearly this baseline is valid on a statistical base, given that the real photospheric flux in proximity of the Hα can have a small dependence on other stellar parameters besides the V and I magnitudes and the [TiO]-derived spectral type, but our estimate remains the best guess relying on our own data.

The line excess, in mJy, does not yet represent the true line emission of the stars, because the filter profile is not centered at $\lambda_{\mathrm{H}\alpha}$ but is displaced 25 Å towards redder wavelengths, and at the line wavelength the filter throughput is about 80% of its peak. While for the photospheric baseline, locally constant, one can approximate the filter throughput as a squared profile, neglecting the true shape of the filter, this local variation of efficiency must be taken into account, increasing the flux excess by a factor of approximately 20%. We investigated the possibility that, in the case of a very broad Hα line in emission, part of the flux could end up in a part of the filter profile characterized by a very low transmission, limiting the accuracy of the correction factor we applied to the flux. However, CTTSs tend to have Hα line emissions with a relatively limited range of broadenings, usually not exceeding $\sim$ 200km/s (4–5$\AA$), (e.g. Alencar & Basri, 2000) much lower than the WFI Hα filter width. In Figure 1.13 we show the filter throughput as a function of wavelength with three examples of $H\alpha$ lines (assumed gaussian for simplicity) overplotted, with a sigma of 100, 200 and 300km/s. It is evident that, even for a relatively high line broadening, the fraction of line flux that ends up in a region of the filter characterized by a very low transparency is negligible, and that, within the line, the throughput can be considered quite linear. Therefore our assumption that the overall transparency of the filter for a Hα line in emission can be considered constant and independent on the line broadening is fairly good, or, at least, not the major source of uncertainty in this result.

We correct for this factor and present our the result in Table 1.5, reporting the excesses both in physical flux and in equivalent width (E.W.)[5], as well as the estimated photospheric continuum level.

[5]For the equivalent width we follow the standard convention, i.e. positive E.W. is associated with an absorption, negative E.W. with an emission.

In Figures 1.14 and 1.15 we present the sky distribution of the sources for which we detect an excess in the Hα flux. A remarkable number of these latter is characterized by a line excess with an equivalent width of more than 50$\mathring{A}$ in modulus.

Unfortunately an accurate evaluation of the uncertainty in the derived Hα emission is limited. Presumably a fraction of the stars can suffer from strong nebular Hα contamination, due to the non uniformity of the latter and the relatively low spatial resolution of the seeing limited ground-based observations. Furthermore, emission from unresolved photoevaporated circumstellar disks can lead to an overestimate of the Hα excess. A qualitative estimate of at least the first bias is possible from the observed scatter in the ratio between the observed flux and the interpolated continuum level for the stars that do not show line excess. For this purpose we considered all the stars with a positive EW (i.e. Hα absorption; these are the points of Figure 1.12 located below the locus where non-emitters should lie (thick line). In an ideal case they should be characterized by a EW$\simeq$ 0, however, their scatter, which presents a standard deviation of 12% and a distribution with tails extended to 50% of the predicted continuum level, can be considered as representative of the overall uncertainty that we associate with the measured excess. A better estimate of the latter will be possible by means of a cross matching with the photometry obtained with the HST/ACS catalog, for all the sources in the common area, which we postpone to a future publication of our group.

These results can be used, together with the ultraviolet excess obtainable from our WFI $U-$band photometry, to study the mass accretion rates.

Table 1.5. Hα excess

	ID	RA (J2000)	Dec (J2000)	E.W. ($\AA$)	E.W. (Hz)	Hα excess (erg/s/cm^2)	Hα excess mJy	Hα cont. (erg/s/cm^2)	Hα cont. mJy
1	911	05 36 07.04	-05 34 18.3	-49.3	-3.43E+012	1.69E-014	0.317	2.63E-014	0.493
2	1219	05 36 05.82	-05 28 02.9	-114.	-7.94E+012	1.55E-014	0.290	1.04E-014	0.195
3	1136	05 36 05.75	-05 18 55.9	-1.84	-1.28E+011	3.10E-016	0.00582	1.29E-014	0.242
4	622	05 36 05.19	-05 21 34.5	6.83	4.75E+011	-2.12E-015	-0.0398	2.38E-014	0.446
5	832	05 36 03.85	-05 30 18.7	-108.	-7.50E+012	5.05E-014	0.948	3.59E-014	0.673
6	1298	05 36 03.47	-05 24 35.9	19.6	1.37E+012	-1.34E-015	-0.0251	5.22E-015	0.0980
7	909	05 36 03.36	-05 24 23.2	3.50	2.44E+011	-1.10E-015	-0.0206	2.40E-014	0.450
8	1111	05 36 02.82	-05 32 54.3	6.15	4.28E+011	-7.32E-016	-0.0137	9.12E-015	0.171
9	887	05 36 02.75	-05 15 27.1	-1.12	-7.79E+010	2.00E-016	0.00375	1.37E-014	0.256
10	1581	05 36 02.59	-05 34 31.3	9.48	6.60E+011	-4.59E-016	-0.00861	3.70E-015	0.0695
...	...	...	...	...	...	...	...	...	...

Note. — Only a portion of the table is shown, for guidance to its content. IDs (second column) are as in Table 1.2.

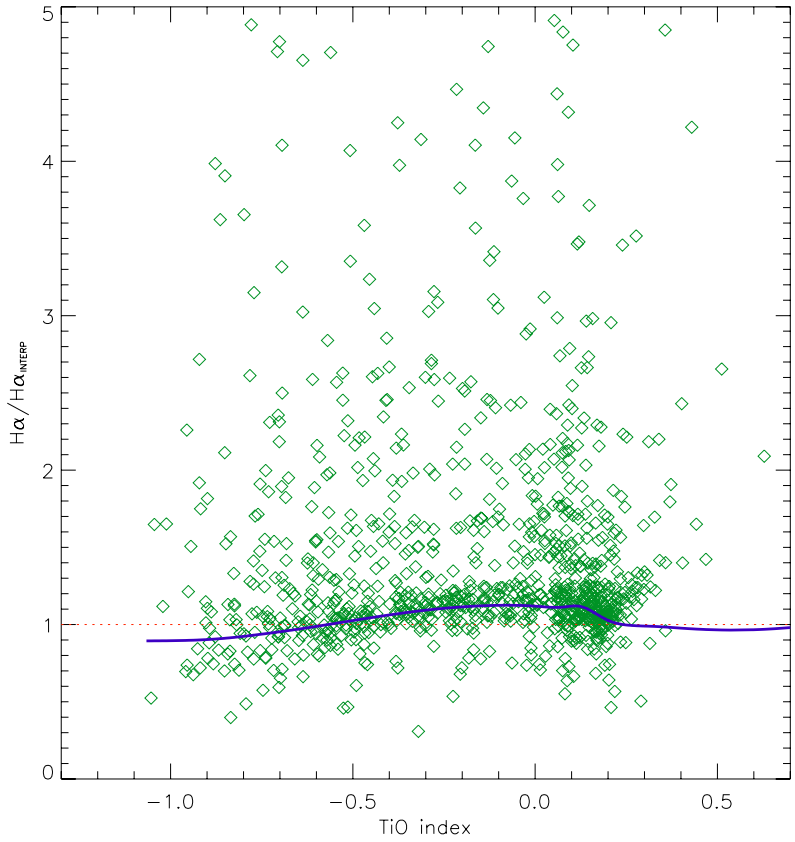

Figure 1.12 Ratio between the measured flux in Hα and the one interpolated between V and I, with respect to the [TiO] index. Although it is almost equal to unity for a significant fraction of stars that do not show excess (which means that the $V - I$ interpolation at 6563 Å is a good approximation for the intrinsic photospheric flux at this wavelength), the TiO index – and its correlation with spectral type – can be used to refine the level of intrinsic stellar flux. The thick solid line, obtained iterating a sigma-clipping robust mean computation technique, represents the zero-emission level at Hα as a function of the TiO index.

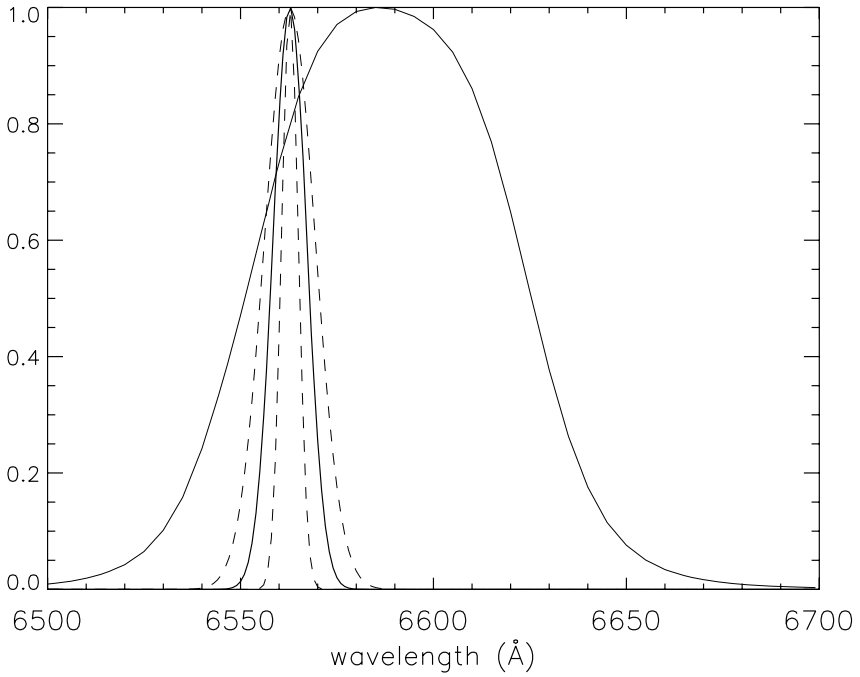

Figure 1.13 The WFI Hα filter profile (broad solid line) is compared to Hα emission lines, assumed gaussian for simplicity, of different widths: 200km/s (thick solid line), 100km/s and 300km/s (dashed lines). The filter central wavelength is located about 25$\mathring{A}$ to the red with respect to $\lambda_{\mathrm{H}\alpha} = 6563\mathring{A}$, where the transparency of the filter is about 80% of its peak. For a typical value of broadening for the Hα emission of CTTS of $\Delta\lambda \lesssim 200$km/s the , and therefore this average value of filter transparency can be reasonably considered independent of the line broadening.

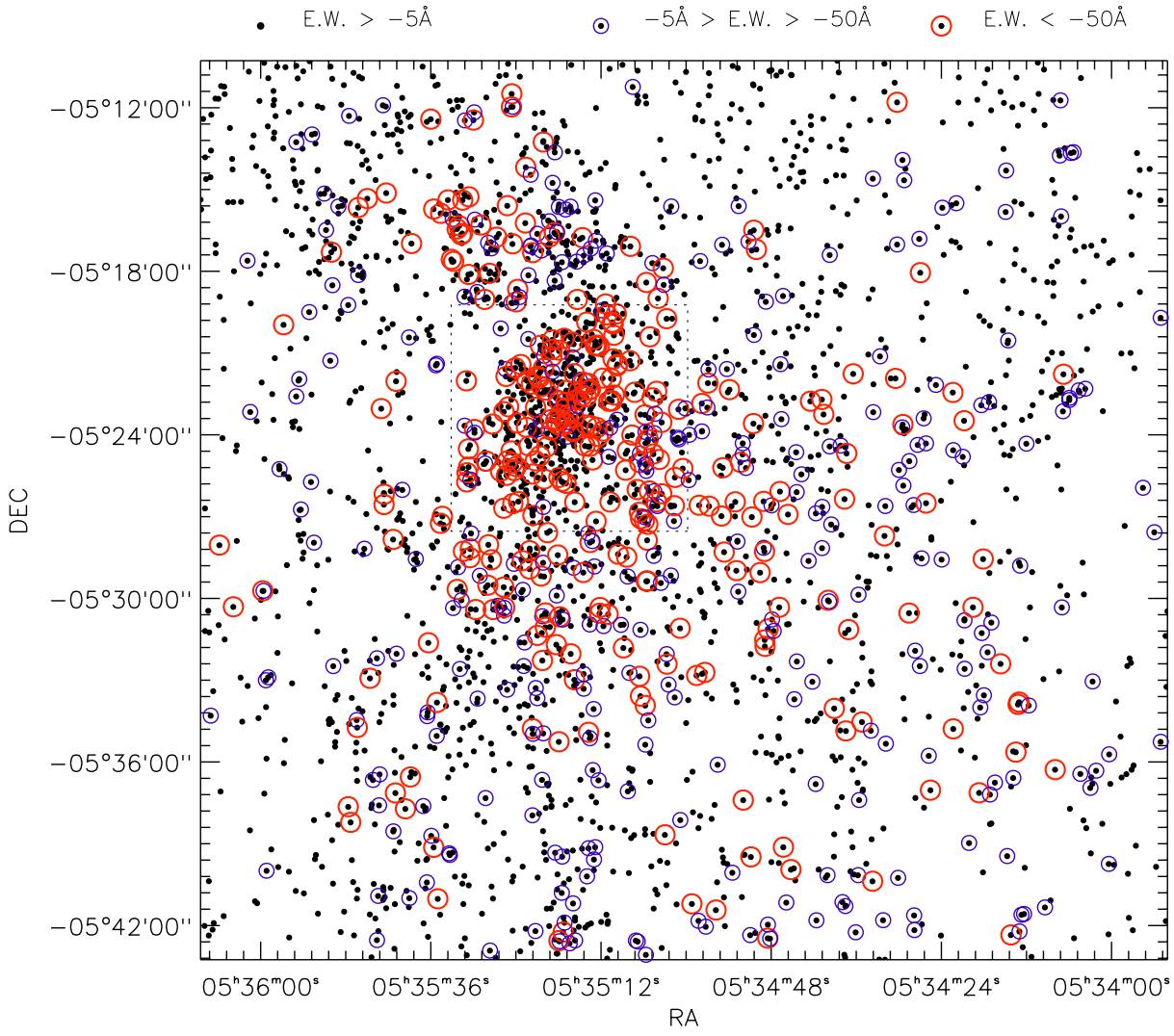

Figure 1.14 Distribution of the stars associated to a Hα excess. Black points have E.W. > -5$\mathring{A}$ and represent absorption and very weak emission sources; 315 stars are characterized by a weak excess - that we defined to be such that the measured equivalent width of the line emission (in absolute value) is between 5$\mathring{A}$ and 50$\mathring{A}$ - (small blue circles), while 323 stars show a strong line excess, exceeding 50$\mathring{A}$ in —E.W.— (large red circles).

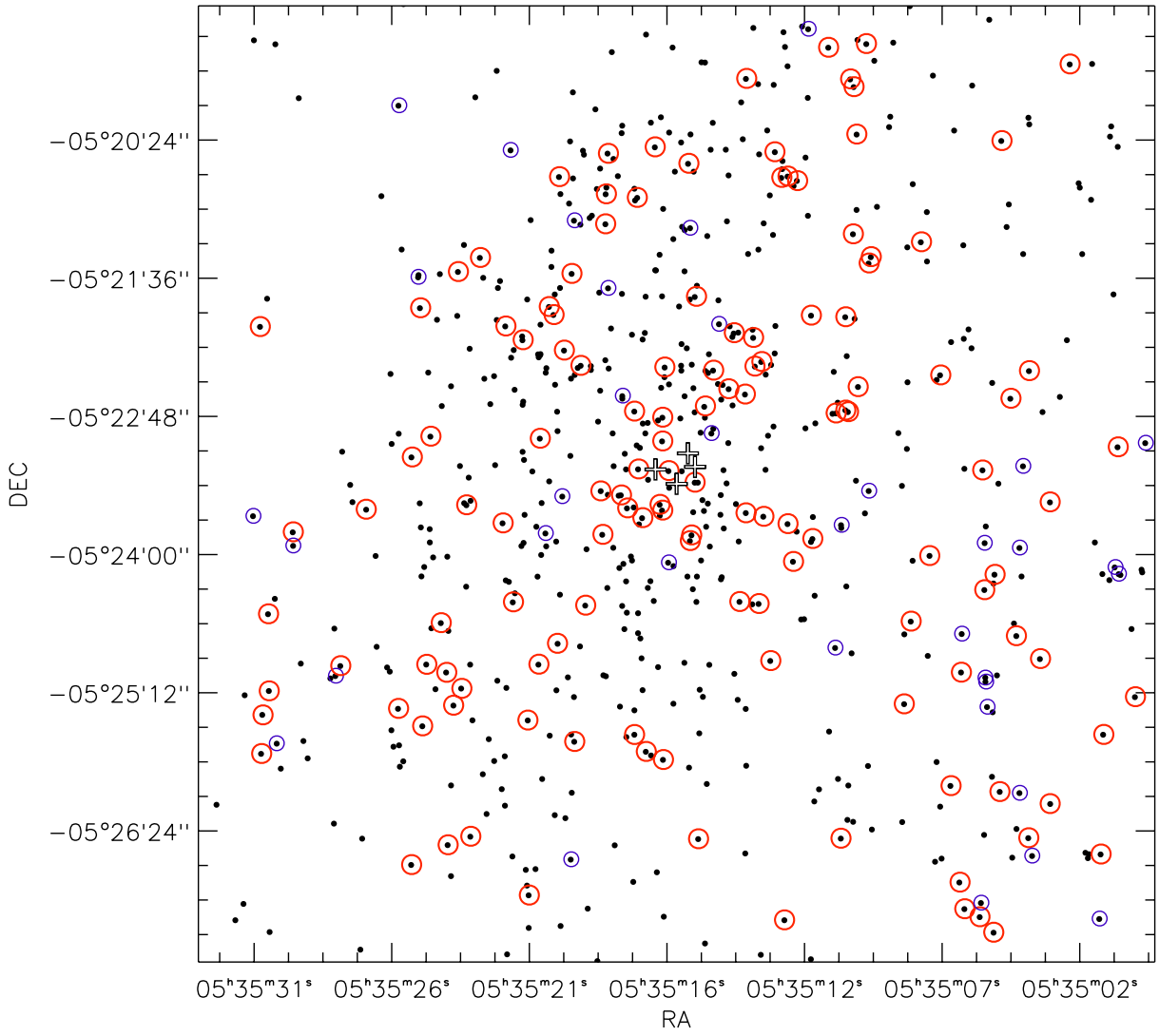

Figure 1.15 Same as Figure 1.15, for the inner (1pc x 1pc) part of the ONC, centered on the trapezium cluster (denoted by crosses).

1.6 Analysis of the photometric colors of the ONC

For a star of a given spectral type, the broad-band colors as well as the integrated flux and bolometric correction (BC), depend in general on the $T_{\rm eff}$, $\log g$ and [Fe/H]. For main sequence and post-main sequence stars the dependence has been investigated both through empirical studies (Flower, 1996; Alonso et al., 1999), relying on stellar templates, and through stellar atmosphere modeling (e.g., Allard & Hauschildt (1995)). For young PMS stars, unfortunately, an extensive empirical study of the intrinsic photospheric colors, and their possible variation compared to MS dwarfs, has never been carried out. This is mostly due to the fact that the observed fluxes for this class of stars are strongly contaminated by excesses caused by accretion activity and circumstellar material; moreover young (few Myr old) PMS populations are usually somewhat embedded into their parental cloud, with extinction differentially affecting the cluster members. As a consequence it is rather difficult to accurately measure the intrinsic photospheric emission of PMS stars.

Further, the effects of non-uniform foreground extinction, those from the amount and composition of any circumstellar dust which affects both the total extinction and the reddening law, and those from the possible presence of on-going mass accretion cause a combination of reddening and blueing effects beyond the uncertainties in the intrinsic colors. The dependence of observed colors on the various physical parameters involved is degenerate. For these reasons, optical photometry alone is insufficient to derive stellar parameters for young stars and additional constraints are needed, for instance an independent estimate of $T_{\rm eff}$ for the star. In order to disentangle or at least constrain the various effects, a precise knowledge of the underlying photospheric emission – i.e., the intrinsic colors – of young stars is required; we focus our discussion here first.

Our multi-band photometry on the ONC can inform us as to the behavior of the optical photospheric colors of young stars. The observed population spans a broad range in $T_{\rm eff}$and also features a range of disk and accretion properties, including diskless and non-accreting objects which can be used to infer intrinsic colors as a function of $T_{\rm eff}$. In this section we compare intrinsic colors predicted using synthetic photometry (Section 1.6.1), with the observed colors of stars in the ONC. This allows us to both test the accuracy of the model predictions, and to constrain empirically those valid for the ONC (Section 1.6.2). Additionally, we use synthetic photometry to model the effects of extinction and mass accretion on the integrated colors. The results of this analysis will be used in Section 1.7 to derive the stellar parameters of the members, for the subsample of the catalog with

available $T_{\rm eff}$estimate.

1.6.1 Synthetic photometry

Given the wide range of stellar spectral types covered by our survey, spanning from early types to late-M stars, we must consider different families of synthetic spectra which cover different ranges of $T_{\rm eff}$. The selection of adequate model atmospheres is particularly critical for late type stars (M-type and later), whose SEDs are dominated by broad molecular absorption features and possibly contain some dust in their atmospheres that can affect the observed spectra and colors.

For intermediate temperatures we used the NextGen models (Hauschildt et al., 1999). This grid of synthetic spectra, computed in the range 3000 K$<T_{\rm eff}<$ 10000 K using the stellar atmosphere code PHOENIX (Hauschildt et al., 1997) is known to reproduce fairly well the optical colors of stars down to the K spectral class. For late-M stars these models are not adequate to reproduce the observational data. Baraffe et al. (1998) show that they are unable to fit solar-metallicity V vs $(V-I)$ color-magnitude diagrams for main sequence populations. The problems set in for $(V-I) \gtrsim 2$, which corresponds to $T_{\rm eff} \lesssim$ 3600 K, and can be attributed to shortcomings in the treatment of molecules. In particular, Allard et al. (2000) illustrate that the main reason for the failure of NextGen spectra in matching the optical properties of late-type stars is the incompleteness of the opacities of TiO lines and water. In that work they present new families of synthetic spectra (AMES-MT models) with updated opacities; the optical colors computed from these models were tested against the VRI photometric catalog of Leggett (1992), finding a fairly good match with the data down to the lowest temperatures. This suggests some confidence in the ability of the AMES models to reproduce the optical colors of main sequence dwarfs, at least in the $V-I$ range. We anticipate that in this section (see Figure 1.18) we will further demonstrate the good agreement between the synthetic ZAMS from AMES models and empirical BVI color scales valid for MS dwarfs. Although it remains to be demonstrated that the AMES models are appropriate also for the lower gravities of the PMS stars, the match for the main sequence gives us some confidence in the use of this grid of spectra.

We therefore use the AMES-MT models for the low temperatures in our set of atmosphere models instead of the NextGen spectra; although this substitution is strictly required only for $T_{\rm eff} \lesssim$ 4000 K, we adopt it for the whole 2000 K$< T_{\rm eff} <$ 5000 K range so

to have a smooth connection with NextGen at intermediate temperatures. For $T_{\rm eff}$> 8000 K we use the Kurucz models (Kurucz, 1993). Due to source saturation, we lack the most luminous members of the ONC in our photometric catalog, and therefore our sample is not populated in the early type end of the population. The metallicity adopted is [M/H]= 0, the only value available for the AMES-MT grid, which is in good agreement with the observations of ONC members (e.g. D'Orazi et al., 2009).

The values of $\log g$ span from 3.0 to 5.5 (in logarithmic scale with g in cgs units) with a step of 0.5 dex. During the PMS phase stellar contraction leads to a decrease of the stellar radius and therefore an increase in $\log g$ according to the relation:

$$\log g = \log \left[\frac{M}{\mathrm{M}_\odot} \left(\frac{R}{R_\odot} \right)^{-2} \cdot g_\odot \right] \tag{1.4}$$

and $g_\odot = 2.794 \cdot 10^4$ g cm s^{-2}. Examples of these relations are shown in Figure 1.16 for Siess et al. (2000) isochrones from 0.5 Myr to the ZAMS.

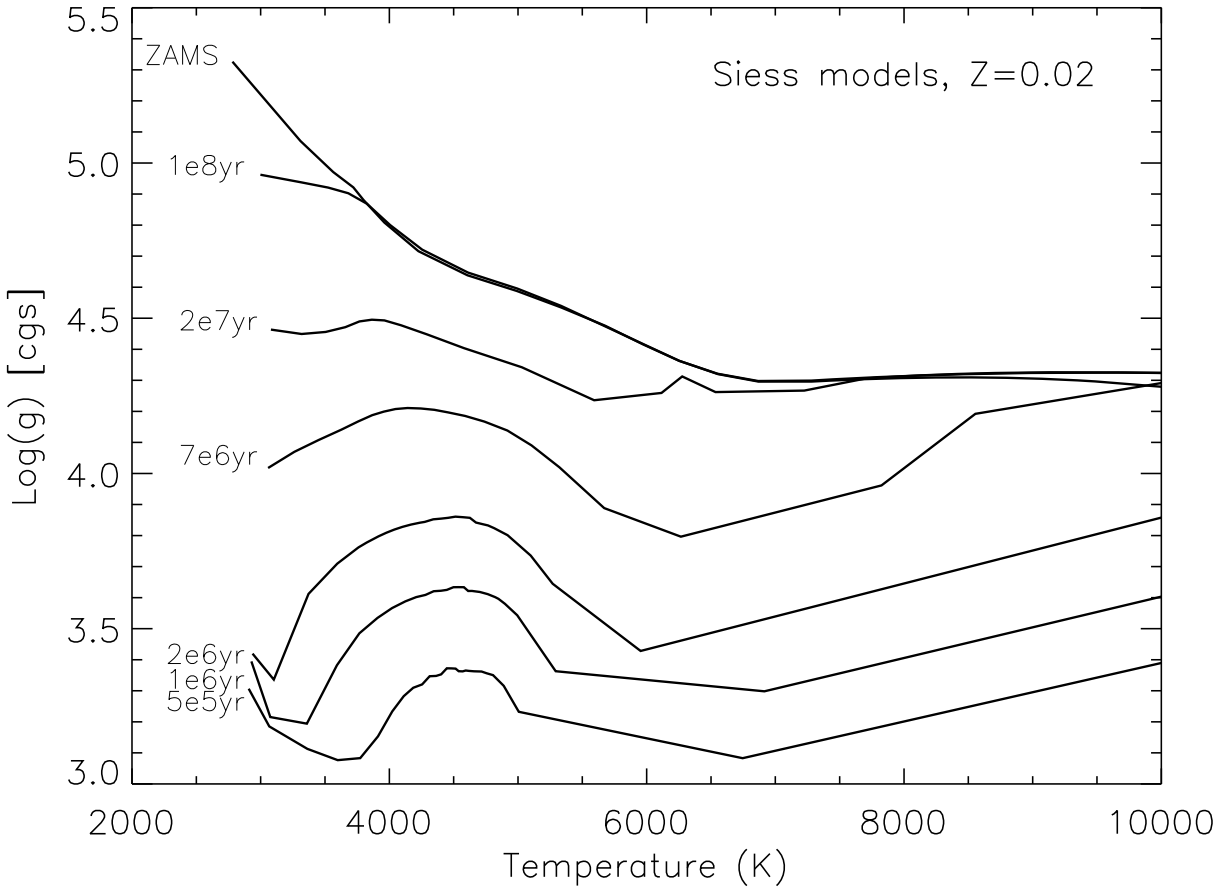

Figure 1.16 $\log g$ vs. $T_{\rm eff}$ relations for a sample of Siess isochrones.

In general increasing ages correspond to increasing surface gravities and for the M-type stars ($T_{\rm eff}\lesssim$4000 K) the difference in $\log g$ can be more than two orders of magnitude during the PMS evolution, changing from $\log g \simeq 3.5$ for a star aged a few Myr to $\log g \simeq 5.5$ for a dwarf M-type stars. For early spectral types the difference is lower, about 1 dex ($\log g \simeq 3.5$ to $\log g \simeq 4.5$). We therefore create, by interpolating within our grid of synthetic spectra, a family of spectra corresponding to each Siess isochrone, as a function of temperature. On this family we perform synthetic photometry to compute absolute magnitudes in the WFI instrumental photometric system, the standard of the photometric catalog presented in Section 1.4.

The absolute magnitude in a photometric band S_λ of a star with a spectral energy distribution F_λ, and stellar radius R is given by

$$M_{S_\lambda} = -2.5 \log \left[\left(\frac{R}{10\mathrm{pc}} \right)^2 \frac{\int_\lambda \lambda F_\lambda S_\lambda 10^{-0.4 A_\lambda} \mathrm{d}\lambda}{\int_\lambda \lambda f^0_\lambda S_\lambda \mathrm{d}\lambda} \right] + ZP_{S_\lambda} \tag{1.5}$$

where f^0_λ is a reference spectrum that gives a known apparent magnitude ZP_{S_λ}; in the VEGAMAG photometric system, which uses the flux of α Lyr as reference, $f^0_\lambda = F_{\lambda,\,\mathrm{VEGA}}$ and the zero-points ZP_{S_λ} vanish according to our definition of WFI VEGAMAG system. We also assume an extinction $A_\lambda = 0$, since we are interested in constructing a general observable grid of evolutionary models for unreddened objects. Eq. (1.5) can be rewritten then as:

$$\begin{aligned} M_{S_\lambda} &= -5 \log \left(\frac{R_\odot}{10\mathrm{pc}} \right) - 5 \log \left(\frac{R_\star}{R_\odot} \right) + B(F_\lambda, S_\lambda) \\ &= 43.2337 - 5 \log \left(\frac{R_\star}{R_\odot} \right) + B(F_\lambda, S_\lambda) \end{aligned} \tag{1.6}$$

where

$$B(F_\lambda, S_\lambda) = -2.5 \log \left(\frac{\int_\lambda \lambda F_\lambda S_\lambda \mathrm{d}\lambda}{\int_\lambda \lambda F_{\lambda,\mathrm{Vega}} S_\lambda \mathrm{d}\lambda} \right) \tag{1.7}$$

The latter term can be directly calculated having the synthetic spectrum for every $T_{\rm eff}$ point of a given isochrone, a calibrated Vega spectrum and the band profile of the WFI photometric filter. The Vega normalization is performed using a recent reference spectrum of Vega (Bohlin, 2007).

In Figure 1.17 we present three observed color-color plots for the ONC in B, V, I and TiO bands, together with the intrinsic colors computed from synthetic photometry using

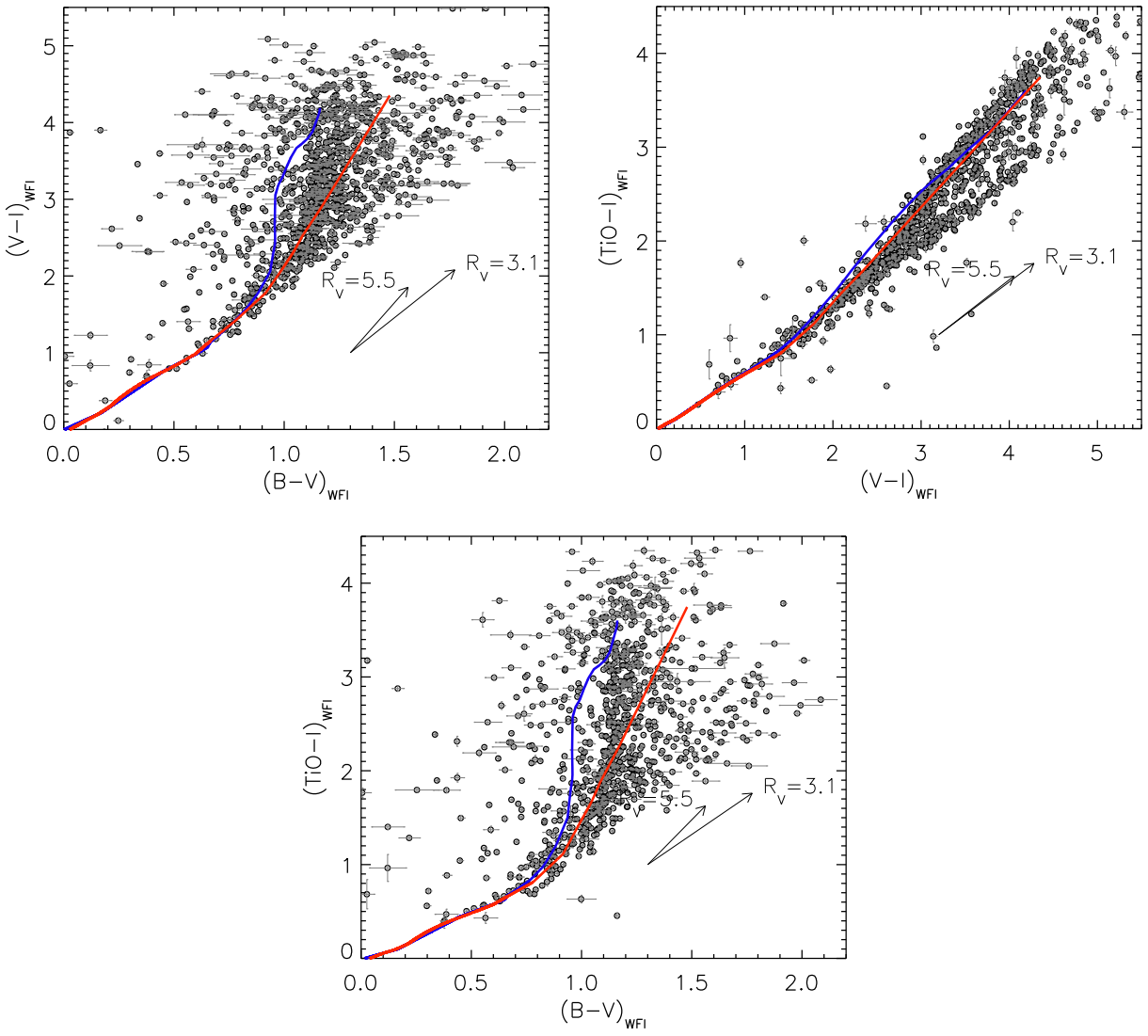

Figure 1.17 Color-color diagrams for the ONC (circles). The solid lines are the loci of intrinsic photospheric emission computed by means of synthetic photometry, assuming a 2 Myr Siess isochrone (blue line) and the Siess ZAMS (red line) to define $\log g$ as a function of $T_{\rm eff}$, for $A_V = 0$. The reddening vectors corresponding to $A_V = 2$ mag for two choices of R_V are reported as a reference.

Table 1.6 Transformation between reddening parameters.

R_V	R_I(WFI) $= \frac{A_I}{E(V-I)}$	R_V(WFI) $= \frac{A_V}{E(V-I)}$
2.0	0.69	1.69
3.1	1.06	2.06
4.3	1.31	2.31
5.5	1.49	2.49
6.0	1.53	2.53

our grid of spectra selecting *logg* values from a Siess et al. (2000) 2 Myr isochrone and for the zero age main-sequence (ZAMS) of the same family. The 2 Myr age is illustrative here, but consistent with the age of ONC derived from an HRD once Siess et al. (2000) evolutionary models and a shorter distance for the ONC are used (though at least twice larger than the value found by H97 using D'Antona & Mazzitelli (1994) evolutionary models). As shown in Hillenbrand et al. (2008), Siess models tend to predict higher ages, relative to other contemporary model isochrones, for a given PMS population in the HRD. Also, using a shorter distance for the ONC increases the age significantly from that derived by H97, by $\sim 50\%$

In the same plot we show the extinction direction, for $A_V = 2$. We have assumed two choices of the extinction law, the "typical" Galactic one, described by a reddening parameter $R_V = A_V/(A_B - A_V) = 3.1$ and the "anomalous" one, considered more appropriate for the ONC (Johnson, 1967; Costero & Peimbert, 1970), whose flatter variation with wavelength is described by a higher value $R_V = 5.5$. Since our photometry is expressed in the WFI instrumental photometric system, we computed the transformation of the reddening parameters R_λ for the WFI bands as a function of R_V, which by definition refers to the Johnson photometric standard. We performed the computation, for several choices of the *standard* reddening parameter $R_V = A_V/E(B-V)$ (in Johnson photometric system) applying the Cardelli et al. (1989) reddening curve on our reference synthetic spectra, and measuring the extinctions in both Johnson and WFI photometric systems. Examples of the transformation between R_V (Johnson) and R_V, R_I (WFI) bands are listed in Table 1.6.

A broad range of optical colors is exhibited by the ONC stars in Figure 1.17. Stars to the far right of the model ZAMS lines are heavily reddened stars, while stars to the far

left, especially along $B-V$ axes, can be explained in terms of highly accreting stars, as we demonstrate in Section 1.23. Stars of intermediate color require detailed interpretation. It is important to recall from above that ZAMS colors are not necessarily applicable to the young stellar population of the ONC. According to the models, the photospheric colors of pre-main sequence stars should vary significantly with age, in particular in BVI colors. From Figure 1.17 it is evident that the model ZAMS is systematically redder in $B-V$ than much our data, in a way that is unexpected from a distribution of accretion rates. The effect is significant for large colors ($V-I \gtrsim 2$), corresponding to $T_{\rm eff} \lesssim 4000$ K, or M-type stars. Apparently the ONC color sequence is the locus seen just to the left of the model ZAMS. This suggests either a problem with the ZAMS relation or that the intrinsic colors of young pre-main sequence stars are bluer than main-sequence dwarfs. We now explore whether the atmosphere models we have selected are appropriate to describe the intrinsic emission of first the ZAMS and then the young ONC stars.

We validate that the models can reproduce the observed colors of main sequence stars by showing in Figure 1.18 the 2Myr model and the ZAMS model computed in the Johnson-Cousins BVI_c bands using our grid of synthetic spectra, as well as empirical colors valid of MS dwarfs, from Kenyon & Hartmann (1995) and VandenBerg & Clem (2003). We test the correctness of the model ZAMS in the standard Johnson-Cousins bands since we don't have at disposal an empirical color scale for MS dwarfs in the WFI photometric system. We stress that due to the differences between Johnson-Cousins and WFI systems, the predicted colors are slightly different than those presented in Figure 1.17a, in particular the $(B-V)$ color is larger than that for our WFI bands; however the qualitative behavior remains unchanged: a young isochrone is significantly bluer than the ZAMS. On the other hand the model ZAMS is compatible with empirical color scales derived for the same photometric system, with offsets much smaller than the difference between the 2 Myr locus and the modeled ZAMS. This confirms that the ZAMS computed by means if synthetic photometry on our grid of atmosphere model is fairly accurate.

1.6.2 Constraining the intrinsic colors for ONC stars

Returning now to the WFI photometric system and Figure 1.17, the question becomes what is the appropriate set of intrinsic photospheric colors to utilize. In general, the non-uniform extinction of the members displaces each star in the direction of a reddening vector, spreading the location of any hypothetical ONC isochrone in color. We assume

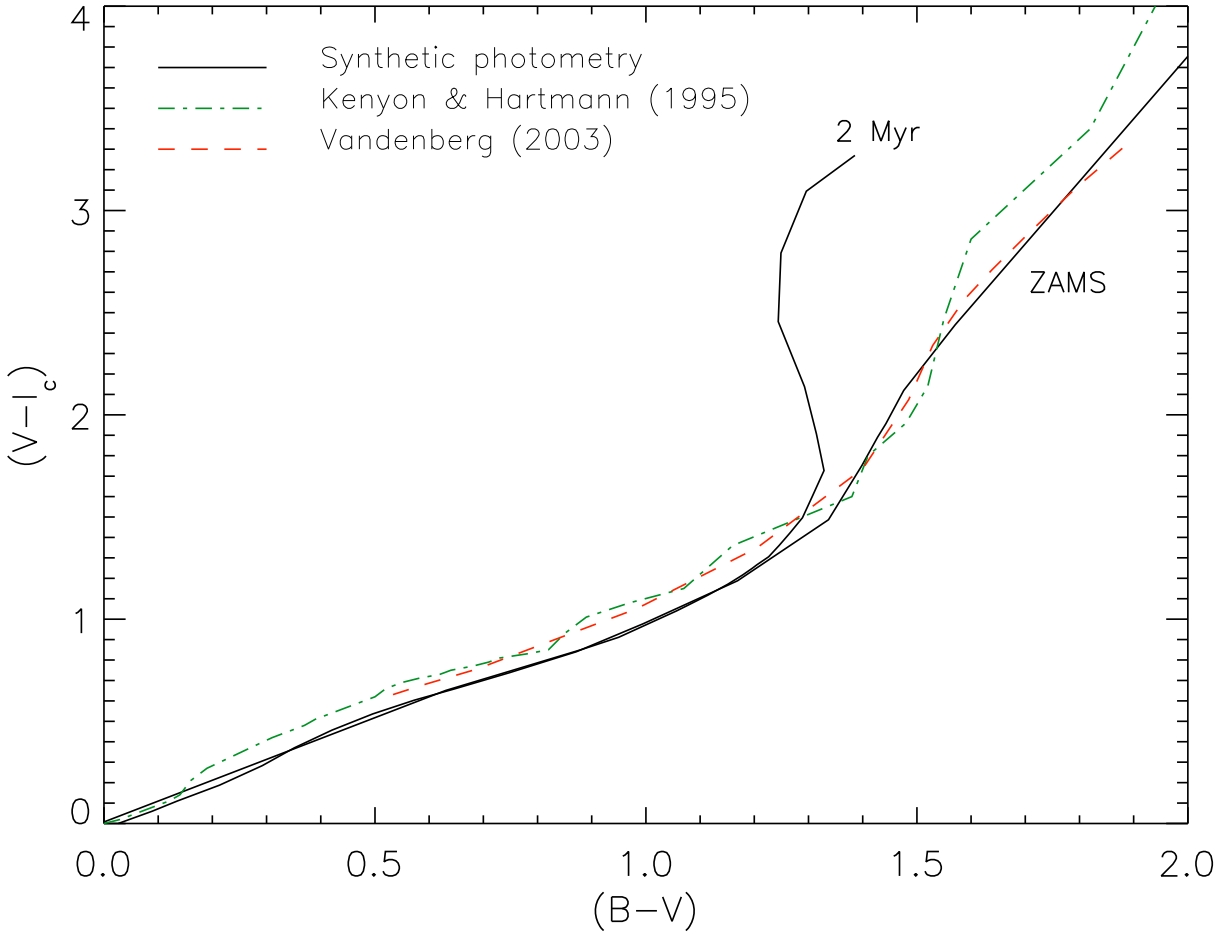

Figure 1.18 Comparison between the intrinsic colors derived by our synthetic photometry for a 2 Myr and the ZAMS (black lines) and the empirical colors valid for MS dwarfs from Kenyon & Hartmann (1995) and VandenBerg & Clem (2003), in the Johnson-Cousins BVI_c bands. The modeled ZAMS, compatible with the empirical counterpart, suggests a fairly good accuracy of the atmosphere models we used, at least for $\log g$ values of dwarfs.

that the reddening distribution is similar for members having different spectral types; this is a fairly good approximation but for the lowest intrinsic luminosities for which high A_V are below the detection threshold. Thus, the fiducial points of the observed distributions for the ONC population are expected to be parallel to any appropriate pre-main sequence model computed for $A_V = 0$, and located at redder colors than the intrinsic photospheric locus (i.e. shifted by a non-negative amount of extinction).

Although reddening from a 1 or 2 Myr isochrone could explain the observed displacement of the observed color locus redward of the model isochrones but blueward of the ZAMS, it is not adequate to simply adopt a model isochrone since one of the goals of

this study is to assess the age and age spread for the ONC population. It is instructive to study the constraints available from our own photometry on the actual intrinsic BVI colors that are appropriate. We define an empirical intrinsic color isochrone in BVI for stars in the ONC by considering a set of stars that are free of both blue excess due to accretion and reddening due to extinction.

From Figure 1.17a,c it is evident that the 2 Myr synthetic colors, when reddened, are more compatible with the observed sequence than the ZAMS locus. However, it is hard to provide a quantitative estimate of this level of agreement. This is because the observed sequence shows a large scattering, mainly due to the differential extinction but, as we will demonstrate in Section 1.23, also because of broad-band excesses caused by stellar accretion. To simplify comparison of the model colors with our data, we isolate stars that:

- are candidate non-accreting objects: we utilize the Hα excesses presented in Section 1.5.1 and we select the sources with no excess.
- have modest extinction: we consider the extinctions from H97, and select sources with $0 < A_V < 0.5$
- are known ONC members: we consider the memberships tabulated in H97, mainly collected from Jones & Walker (1988), and select stars with membership probability $m \geq 98\%$
- have small photometric errors: we restrict errors to < 0.1 mag in all BVI bands.

Restricted in this way, the sample satisfying all of the above criteria contains ~ 21 stars and includes the known ONC members for which the observed fluxes are closest to simple photospheres. By dereddening their colors subtracting the modest extinctions measured in H97, these stars should lie on our color-color diagram along a sequence which represents the intrinsic colors valid for the ONC. This color locus is illustrated in Figure 1.19, where we also overlay the predicted intrinsic colors from synthetic photometry for the ZAMS and the 2 Myr isochrone. While the intrinsic colors of this sample of non-accreting ONC stars are bluer than those along the ZAMS, they are not as blue as the theoretically predicted colors for a 1-2 Myr population.

We thus confirm that the intrinsic colors for the ONC are not in agreement with the dwarf colors, but rather bluer as qualitatively predicted by the 2 Myr isochrone. However, small offsets are still present with respect to the young isochrone that are color-dependent.

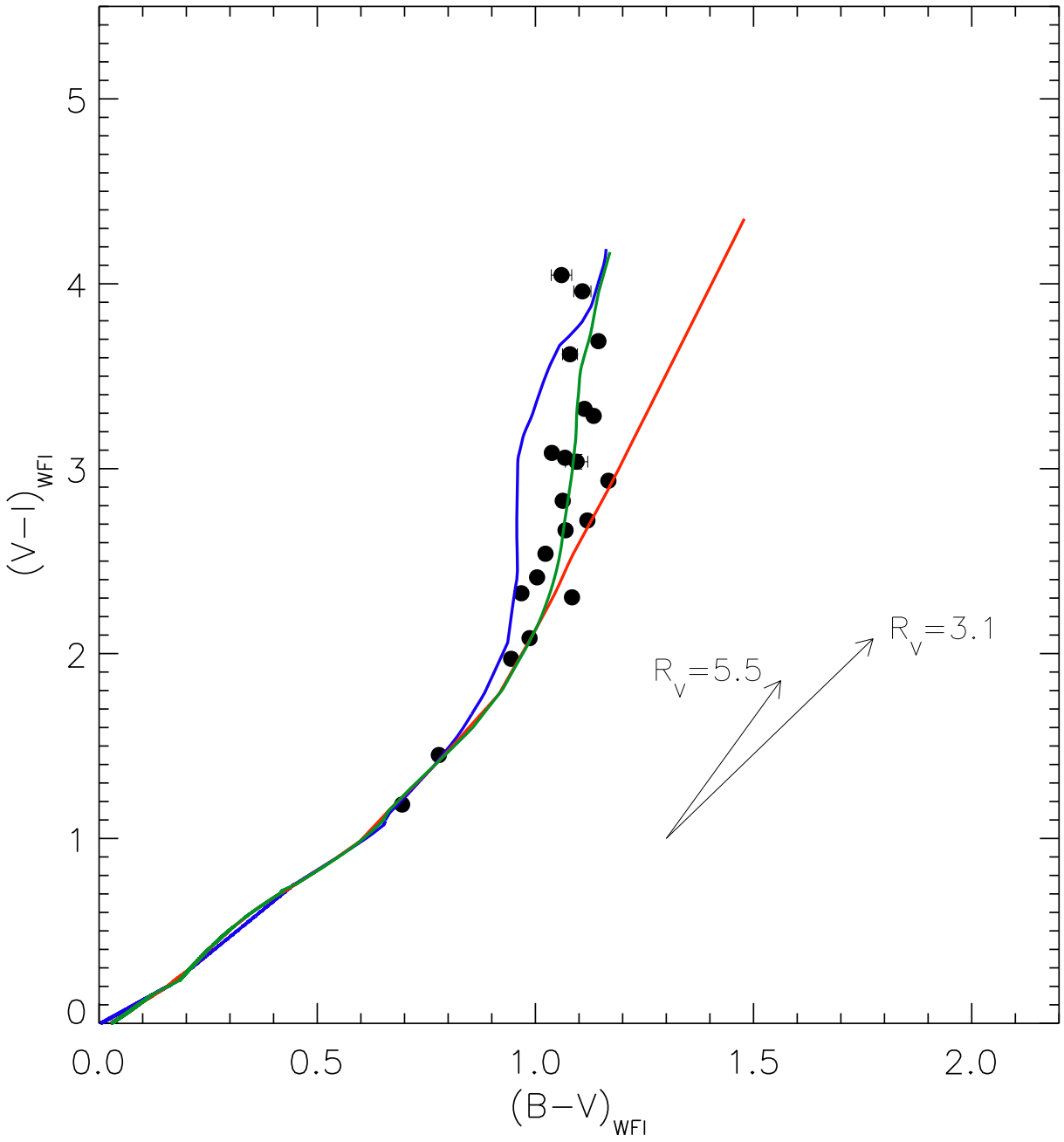

Figure 1.19 BVI color-color plot including only sources with small photometric error (≤ 0.1 mag), membership probability known and $\geq 98\%$, no Hα, excess, modest extinction from H97 ($0.1 < A_V < 0.5$) (dots). The data have been de-reddened based on the extinctions measured from H97. As in Figure 1.17, the red and blue lines represent respectively the synthetic ZAMS and 2 Myr model. The green line is our empirical calibration of the intrinsic colors, intermediate between the two (see text).

In particular, while the 2 Myr model seems appropriate for the coolest stars ($\sim$ 3000 K, corresponding to $(V-I) \sim 4$), the observed separation of the ONC color sequence from the ZAMS locus occurs at slightly larger colors ($V-I \gtrsim 2$) than predicted by the 2 Myr model. We chose therefore to use the empirical data to refine the model isochrone colors so as to best match the data of Figure 1.19. To this purpose we consider the ZAMS intrinsic colors for $T_{\rm eff} \geq$ 3700 K, the 2 Myr synthetic colors for $T_{\rm eff} \leq$ 2900 K, and a linear interpolation between the two for 2900 K$<T_{\rm eff}<$ 3700 K. The result is shown also in Figure 1.19, green line; it is evident how this empirical correction of the intrinsic colors now allows for a good match to the selected sample of non-accreting non-extinguished members of the ONC.

We refer hereafter as the *reference model* these empirically validated intrinsic BVI colors, which can be considered a fairly good approximation of the photospheric fluxes, as a function of $T_{\rm eff}$, for the ONC.

1.6.3 Bolometric corrections

As described above, intrinsic colors for 2 Myr and ZAMS stars were derived by means of synthetic photometry performed on a grid of spectra using the appropriate $\log g$ vs. $T_{\rm eff}$. For the intermediate $\log g$ values between the two models that is needed for our empirical isochrone, we adopt ZAMS values for $T_{\rm eff} \geq$ 3700 K, 2 Myr for $T_{\rm eff} \leq$ 2900 K, and a linear interpolation in between) to provide the empirically constrained set of model spectra that match the optical colors of the ONC.

We can use these *reference spectra* to also compute the bolometric corrections (BC) valid for our filters without relying on relations taken from the literature that, besides requiring color transformations, may not fully apply to pre-main-sequence stars. Clearly, based on our data, we cannot validate the accuracy of the BCs we derive from synthetic photometry. However, based on the evidences we have presented in Section and 1.6.1 and 1.6.2 suggesting that our reference model is adequate to describe the photospheric emission of the ONC stars at optical wavelengths, we are confident that the BCs derived on the same spectra are similarly appropriate.

The bolometric corrections are defined as the difference between the bolometric magnitude of an object, found by integrating the SED across all wavelengths, and the magnitude in a given band:

$$\mathrm{BC} = 2.5 \cdot \log \left[\frac{\int f_\lambda(T) \cdot S_\lambda d\lambda}{\int f_\lambda(T) \cdot d\lambda} \Big/ \frac{\int f_\lambda(\odot) \cdot S_\lambda d\lambda}{\int f_\lambda(\odot) \cdot d\lambda} \right] + C, \tag{1.8}$$

where C is a constant equal to the bolometric correction for the Sun, $BC_{\odot}$, in that particular photometric band. The values of C are irrelevant in our case, since for obtaining the total luminosities in terms of $L/L_{\odot}$ (see Section 1.8 and Eq. 1.9), $BC_{\odot}$ is subtracted and vanishes; thus we impose $C = 0$. The integrals in Eq. 1.8 have been computed for the V and I bands for the reference spectra, and for consistency we considered as a reference solar spectrum a NextGen SED interpolated on the grid for solar values with $T_{\rm eff}$=5780 K, $\log g = 4.43$, and $[M/H] = 0.0$.

The results are shown in Figure 1.20 as a function of temperature. For comparison, we also show these relations computed in the same way but using the surface-gravity values of the Siess ZAMS and the Siess 2 Myr isochrone. As for the colors, important differences arise for $T_{\rm eff} < 4000\ K$, corresponding to M-type stars. In these regime, the difference between the three models is up to 0.15 mag for BC_I and up to 0.6 mag for BC_V. For the derivation of the H-R diagram (see Section 1.8) we utilize only BC_I, and the measured difference of 0.15 mag between the 2 Myr model and the ZAMS translates into an offset of 0.06 dex in $\log L$, amount small enough to be irrelevant for the computation of the stellar parameters. Therefore, we assume the reference model BCs for consistency with the model we use to derive the intrinsic colors, confident that possible uncertainties in the BCs do not affect significantly the result. The major advantage of our approach is that we can compute consistently these quantities for the WFI photometric system which our photometry follows.

1.6.4 Extinction law

We are making an implicit assumption that the extinction in the entire region under study follows the same reddening law. Differences in grain size and composition might be expected, due to the complex structure of the ISM within the Orion Nebula, the non-uniformity of the foreground lid of neutral material and, for a fraction of members, the presence of circumstellar disks in different evolutionary state. Optical photometry alone cannot provide an independent assessment of the most adequate reddening law for each source, given the degeneracy for late-type stars between the observed colors and $T_{\rm eff}$ and the presence of non-photospheric effects. From our color-color plots, however, we can make some general considerations. Whereas the $(V - I)$ vs. $(TiO - I)$ plot of Figure 1.17 does not provide useful information, as the reddening vectors for the two choices of R_V are nearly parallel due to the limited wavelength range spanned, in the $(V - I)$ vs.

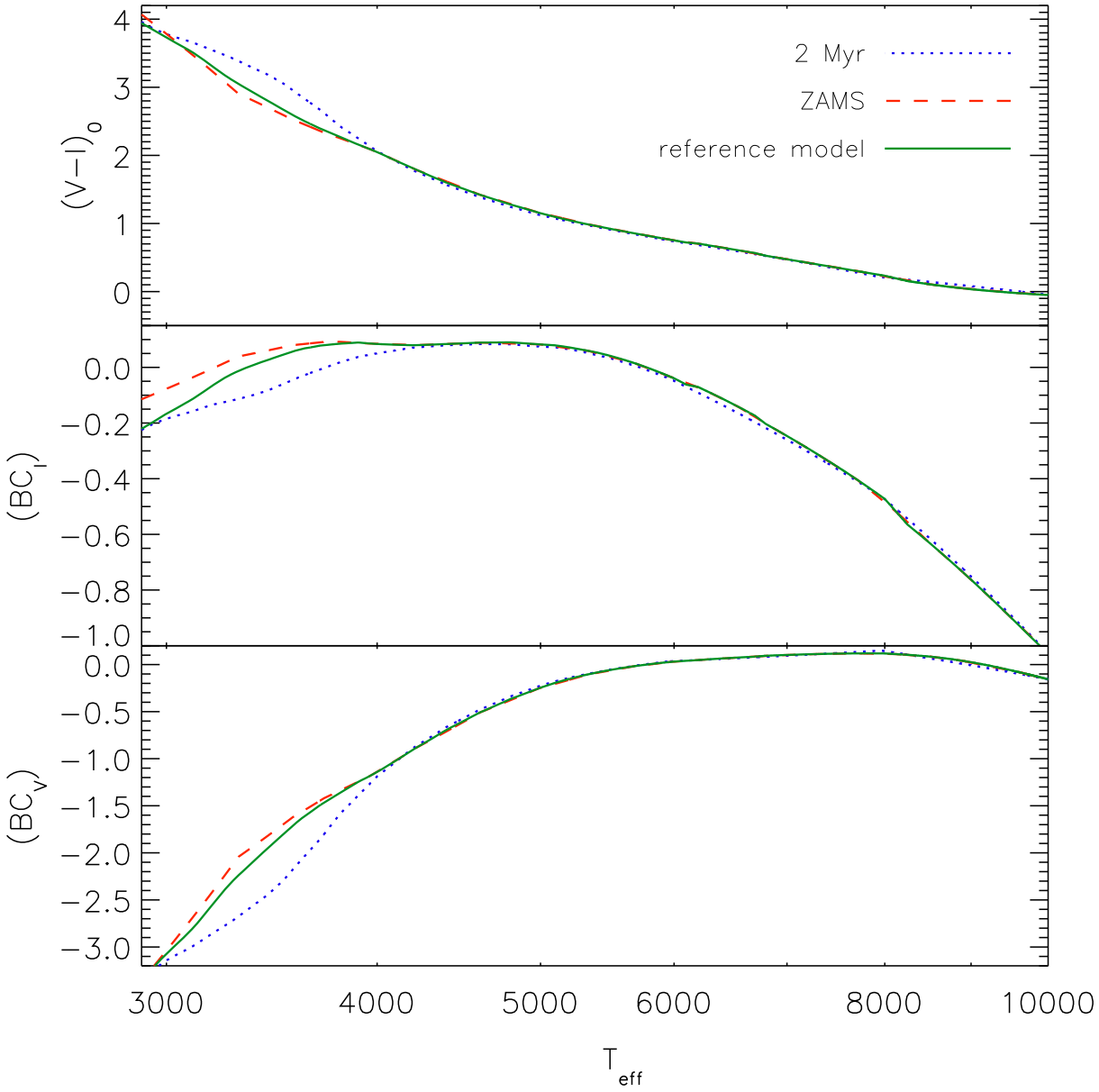

Figure 1.20 *Upper panel:* intrinsic color $(V-I)_0$ as a function of temperature, computed for our 2 Myr isochrone, the ZAMS, and our empirically calibrated reference model, in the WFI instrumental bands. *Middle panel and lower panels:* Bolometric corrections derived in the same way, for the I and V WFI instrumental bands.

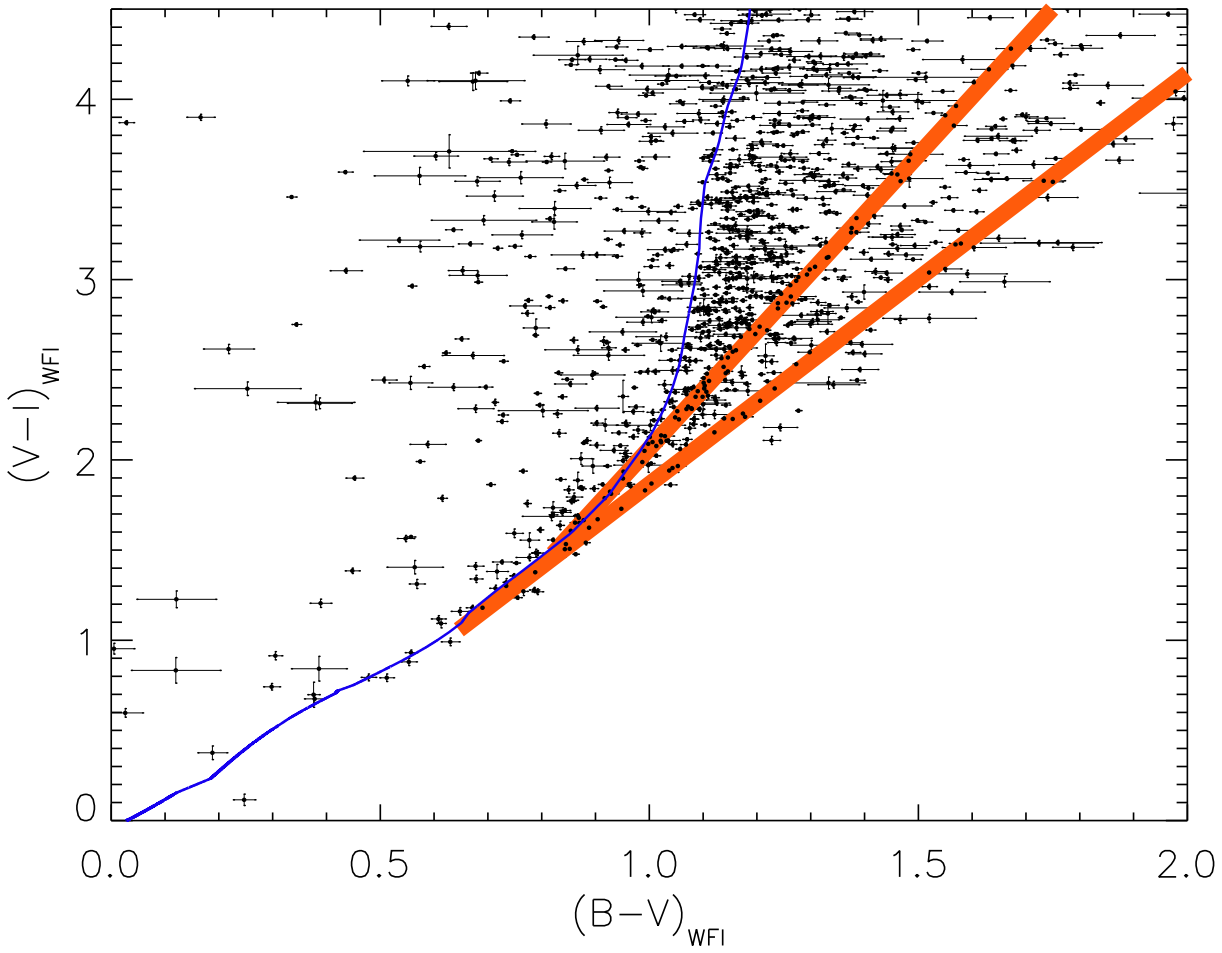

Figure 1.21 $(B-V)$ vs $(V-I)$ plot of the ONC population (dots), with the 2 Myr reference model (solid line). The two thick lines correspond to the reddening direction assuming $R_V = 5.5$ (upper line) and $R_V = 3.1$ (lower line) extinction laws, applied to the tangent points of the model.

$(B-I)$ plot the two reddening vectors are clearly separated. For spectral types K and earlier ($(V-I) < 2$), our template model is nearly parallel to the two reddening vectors (i.e., the above mentioned degeneracy between spectral types and reddening), meaning that all the highly extinguished members within this range should be located in a narrow stripe at higher color terms.

In Figure 1.21 we show the reddening directions for the two values of R_V applied to the tangent points with the reference model. If $R_V = 5.5$ were the correct choice, no stars would be detected to the right from the associated reddening direction, in contrast with our data. On the contrary, the $R_V = 3.1$ reddening limit encompasses almost the entire photometry, with the exception of few scattered stars with high photometric errors

in $(B-V)$. Clearly, the scatter in our data and the photometric errors limit a precise estimate of the actual value of R_V. Nevertheless, we can conclude in an unquestionable way that the typical galactic law is more compatible with our data than the Costero & Peimbert (1970).

Given the uncertainties, and for the purpose of discussing how the choice of R_V affects the scientific results, we perform the analysis presented in the next sections using both values, but we present mostly the results for $R_V = 3.1$, mentioning any systematic changes induced by assuming the higher R_V, where relevant.

1.6.5 Mass accretion

The color-color diagrams of Figure 1.17 show that there is a fraction of stars lying significantly to the left of the models. In this region, according to our reference model, a star of given temperature and positive reddening cannot end up. The fact that the TiO-I vs V-I frame is the "tightest", while the $(TiO-I)$ and $(V-I)$ vs. $(B-V)$ are more scattered suggests that these sources have significant excess in the B band. Moreover, low $(V-I)$ stars are scattered only bluewards with respect to the reference model, confirming the presence of a B-band excess for a subsample of sources with low reddening.

We investigated the possibility that the blue excess is due to accretion luminosity. According to the current paradigm for classical T Tauri stars (CTTS), gas is accreted onto the central star from an accretion disk truncated at a few stellar radii by the stellar magnetic field. From the inner edge of the disk, the material falls along infall columns beamed by magnetic field lines (Koenigl, 1991; Shu et al., 1994; Muzerolle et al., 1998b). Several lines of observational evidence support the magnetospheric model, including: (1) the broad emission lines emitted by the infalling gas, presenting occasionally redshifted absorption components (Calvet & Hartmann, 1992; Muzerolle et al., 1998a); (2) the near-infrared spectral energy distributions (SEDs), consistent with those of disks truncated at small radii (Kenyon et al., 1994; Meyer et al., 1997); (3) the variations in luminosity consistent with the presence of *hot spots*, originating where the accretion flow impacts the stellar surface (Herbst et al., 1994; Gullbring et al., 2000). The presence of ongoing accretion processes in the ONC has been investigated by several studies, e.g., in Rebull et al. (2000) and Robberto et al. (2004) from the U-band excess is used to obtain mass accretion rates, or in Sicilia-Aguilar et al. (2005) and Hillenbrand et al. (1998) using optical spectroscopy.

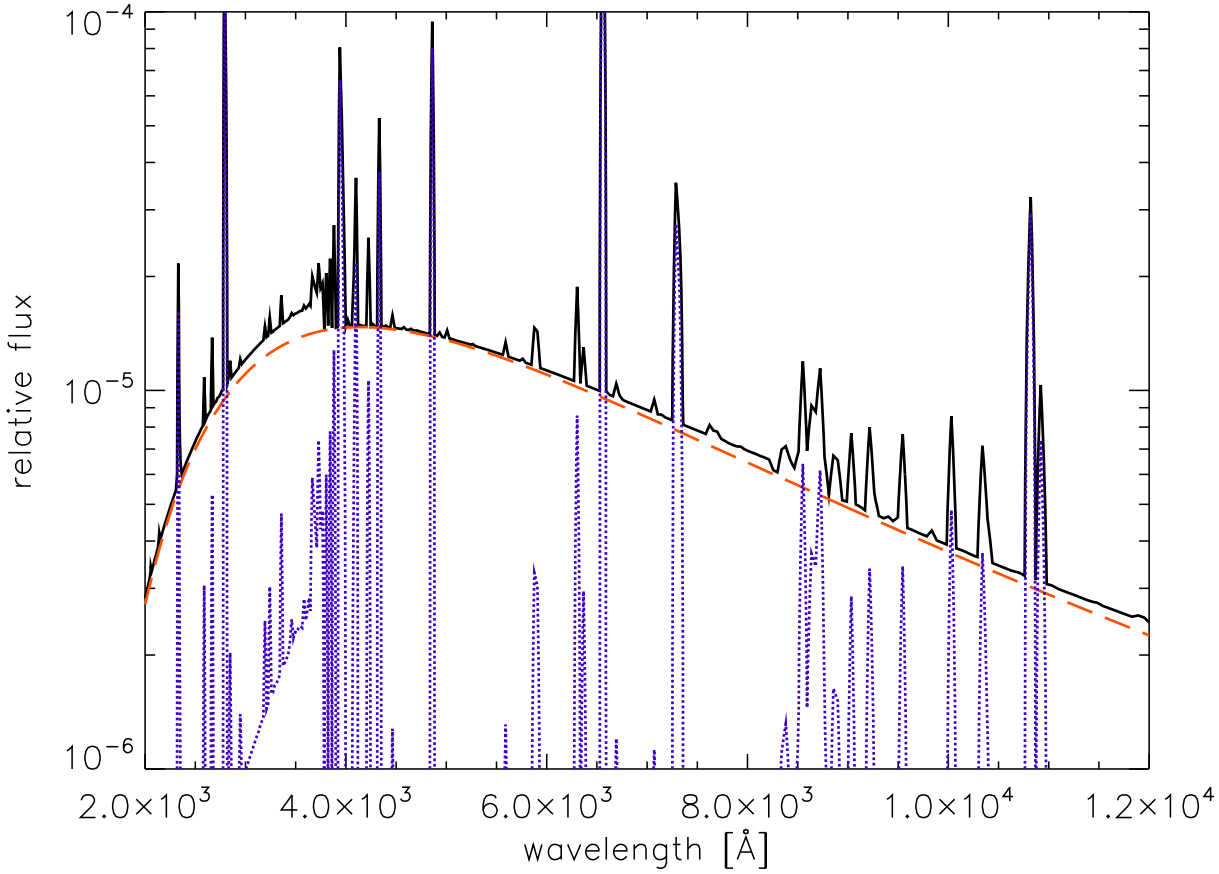

Figure 1.22 Accretion spectrum simulated with CLOUDY. The solid line is the total emission, which is the superposition of an optically thick emission, with $T_{\rm eff}$=7000 K, of the heated photosphere (*dashed line*) and the optically thin emission of ionized gas with density $n = 10^8$ cm^{-3} (dotted line).

In order to verify the possible role of accretion also in our BVI bands, we simulated a typical accretion spectrum to be added to our reference models. According to Calvet & Gullbring (1998), the total accretion column emission can be well approximated by the superposition of an optically thick emission from the heated photosphere below the shock, and an optically thin emission generated in the infalling flow. The SED of the optically thick emission is compatible with a photosphere with $T_{\rm eff}$ = 6000-8000 K, while the optically thin pre-shock column can be modeled by thermal recombination emission. The relative fraction of the two components with respect to the total emission produced by accretion is about 3/4 and 1/4, respectively. We therefore assumed for the optically thick emission a black body with T = 7000 K, whereas for the thin emission we used the version 07.02.01 of the CLOUDY software, last described by Ferland et al. (1998), to reproduce the spectrum of an optically thin slab ($n = 10^8$ cm^{-3}) also at $T \simeq 7,000$ K.

The derived, low resolution, accretion spectrum is shown in Figure 1.22.

We calculated the displacement in the color-color diagrams caused by the presence of ongoing accretion by adding these spectra, with an increasing ratio of $L_{\rm accr}/L_{\rm tot}$, to our reference model. For any given combination, we recalculated the synthetic photometry, deriving the $(B-V)$, and $(V-I)$ colors in the WFI instrumental photometric system. The results (Figure 1.23) show the derived loci for each stellar temperature, all converging to the point representative of the pure accretion spectrum, as well as for fixed $L_{\rm accr}/L_{\rm tot}$ ratios.

The blue excess that is observed for a number of the ONC targets in the $(V-I)$ vs. $(B-V)$ diagram apparently can be explained by an accretion spectrum added to the stellar emission, with typical luminosity well below 10% of the total luminosity of the star. Figure 1.23 clearly shows that small fractions of accretion luminosity have a larger effect on the colors of low-temperature stars, indicating that accretion effects must be taken into account especially in the study of the low-mass end of the ONC.

We have tested how critical is the assumption of a unique accretion spectrum for the modeling of the color excess. When the accretion temperature is set to be 9000 K instead of 7000K (see Figure 1.24), the colors of the pure accretion spectrum (i.e. the location, in the diagram of Figure 1.23 where all the curves join) decrease by 0.15 mag in $(B-V)$ and 0.2 mag in $(V-I)$. This is a small difference already in the limiting case of $L_{\rm accr}/L_{\rm tot}$=1, for much lower accretion, which is the case of the majority of our stars, the position of the accretion curves of Figure 1.23 remains almost unchanged. We conclude that our approximation of applying a unique accretion spectrum to model the stellar colors contamination is enough robust for our purposes.

1.7 Analysis of stars with known spectral type

In the previous sections we have isolated the intrinsic color scale which best fits the photospheric emission of the ONC members. From the intrinsic colors, taking also into account possible color anomalies through the addition of an accretion spectrum, we can determine the extinction A_V and therefore the stellar luminosity. The combination of spectroscopic information with accurate photometry, together with our determination of the intrinsic relations (intrinsic colors and BCs for the young ONC, and the treatment of $L_{\rm accr}$ excess), allow us to build the H-R diagram for the ONC improving over the analysis of previous works.

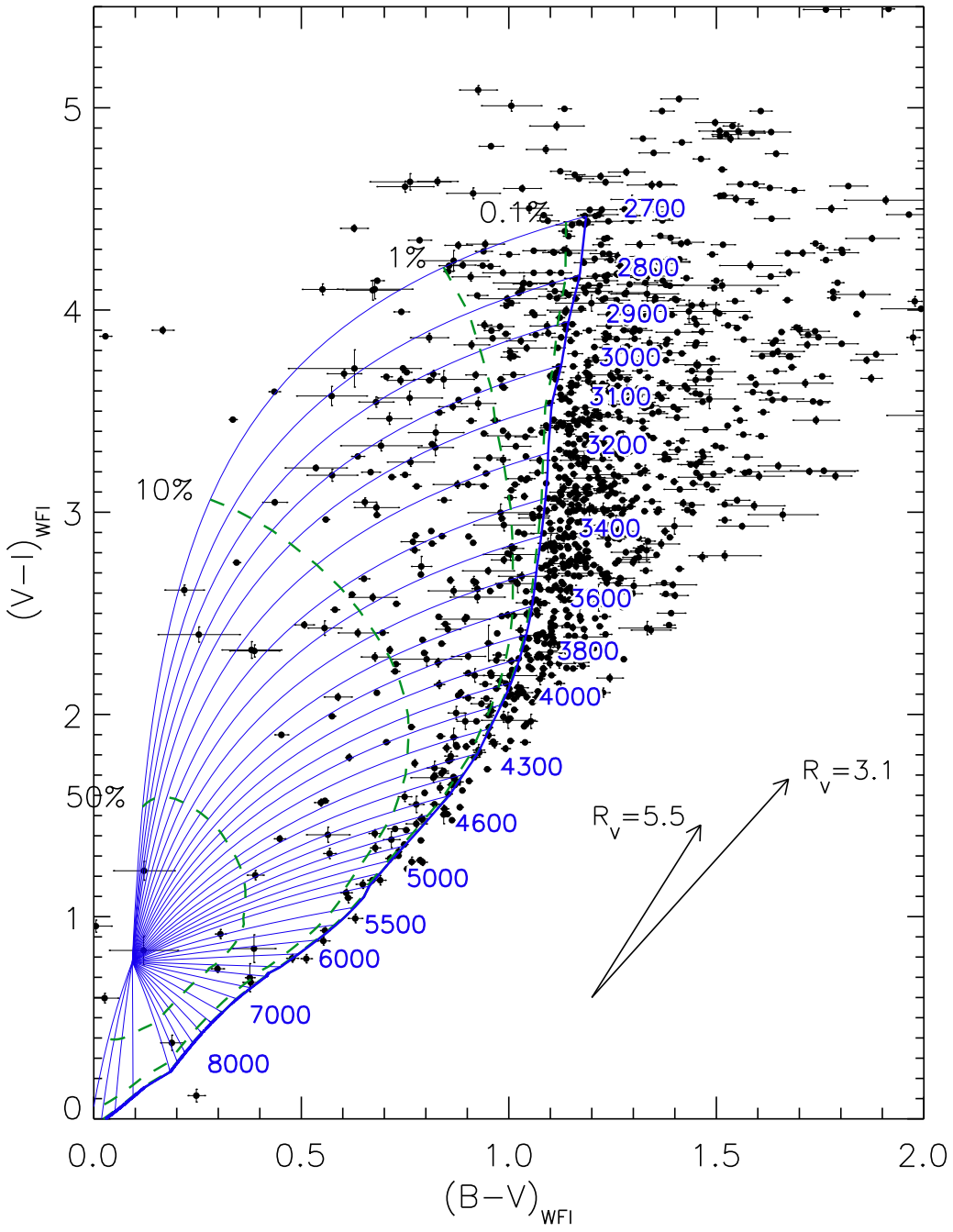

Figure 1.23 *BVI* color-color diagram of our WFI catalog. The thick line represents the synthetic CMD obtained from the reference spectra selected (see sub§1.6.2) for $A_V = 0$ and the pertinent effective temperatures are shown along the curve. Thin blue lines represent the computed displacement, for a star of a given temperature, adding a component of the accretion spectrum (as in Figure 1.22) and increasing the parameter $L_{\rm accr}/L_{\rm tot}$ from 0 to 1. Loci for $L_{\rm accr}/L_{\rm tot} = 0.5$, 0.1, 0.01 and 0.001 are overplotted (*dashed lines*). Reddening vectors corresponding to an extinction of $A_V = 2$ are shown for the two choices of reddening parameter R_V assumed in this work.

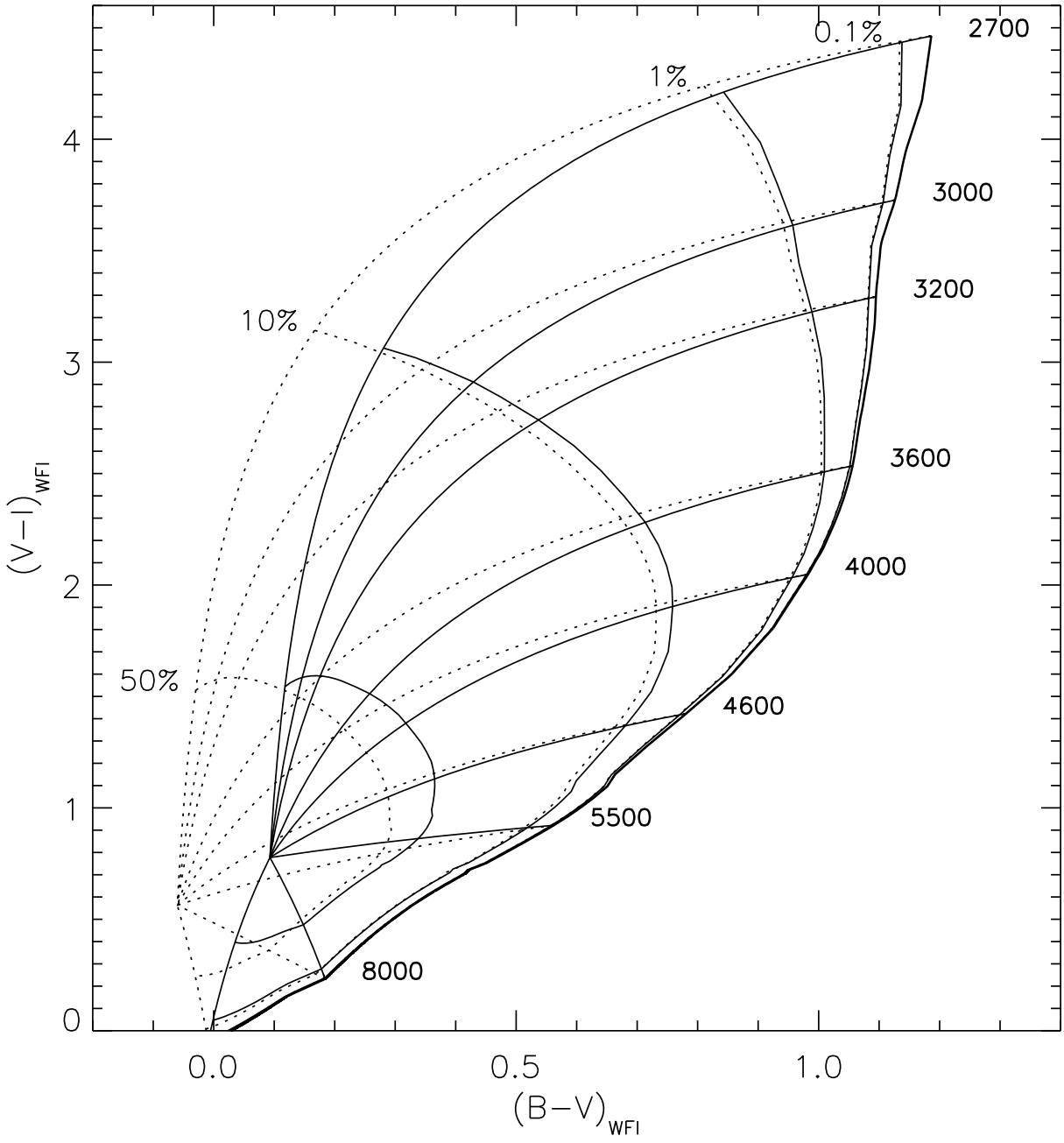

Figure 1.24 Same as Figure 1.23, showing the difference in modeled displacement caused by accretion increasing the accretion temperature from 7000 K (assumed in the case of Figure 1.23, solid lines) to 9000 K (dotted lines).

1.7.1 Spectral types

We take full advantage of the catalog of spectral types in the ONC of H97 to determine the temperatures of as many members as possible. Matching our catalog with the H97 spectroscopy, we isolated 876 sources with available spectral type.

We extend the H97 sample of spectral types using new spectroscopic data. The observations were obtained as part of a follow-up to the study of Stassun et al. (1999) of the larger Orion Nebula star forming region. The spectra were obtained with the WIYN 3.5m multi-object spectrograph at Kitt Peak National Observatory on UT 2000 Feb 11. The instrument setup was the same as described in H97, providing wavelength coverage over the range 5000Å$< \lambda <$ 9000Å with spectral resolution of $R \sim 1000$. Exposure times were 2 hours and the typical signal to noise ratio was ~ 50 per resolution element. Spectral types were determined from the spectra using the same spectral indices described by H97. In particular, for our targets which are principally of K and M type, we found the TiO indices at 6760Å, 7100Å, and 7800Å to be most useful. We calibrated the indices against observations of stars previously classified by H97 as well as with the template library of Allen & Strom (1995). For 85% of the sources a spectral type is assigned with a precision of 1 subtype or less. From these observations, we include the 65 stars that overlap with the WFI FOV.

We also add 182 stars classified in from the TiO spectro-photometric index ([TiO], see section 1.5. These sources are limited in the spectral range M1-M6. Earlier spectral types are not classified with this method because our index correlates with a TiO absorption band present only in M-type stars. On the other hand, for late M-type stars we were limited by the detection limit of the 6200Å narrow-band filter. Given the small range of $T_{\rm eff}$ spanned, this selection effect in $T_{\rm eff}$ corresponds to a selection in masses, since the evolutionary tracks are nearly vertical in the HRD.

Thus, spectral classification is available for 1123 out of 2621 stars with optical photometry. For 121 of them, only $I-$band ground-based photometry is available, and we exclude them from our analysis since the lack of at least one color term makes the derivation of the reddening impossible. The sample of stars with known spectral type and at least V and I magnitudes accounts therefore for 1002 objects, 820 of them with slit spectroscopy (from both H97 and our new spectroscopic survey) and 182 M-type stars classified by means of [TiO] index.

For the stars also present in the H97 catalog, we utilize the membership probability

collected in that work, which is taken from the proper motion survey of Jones & Walker (1988) and assigning a 99% probability to the externally photo-evaporated disks (*proplyds*, Bally et al. 2000; Ricci et al. 2008) located in the vicinity of the Trapezium cluster. Among our 1002 stars, 703 are confirmed members, with a membership probability $P > 50\%$, while 54 are non-members ($P < 50\%$). The distribution of memberships is bimodal, peaking at $P = 99\%$ and $P = 0\%$. This implies that our choice to define the limit at 50% does not influence significantly the selection. In fact selecting only sources with $P > 80\%$ results in selecting only 12 fewer stars. For 245 the membership is unknown, but given the relatively low fraction of confirmed non-members, we expect all but 20-30 of this stars to be ONC members. This contamination, corresponding to 2–3% of the sample is too small to bias our results; therefore we consider the unknown membership stars as *bona fide* members, taking advantage of the inclusion of $\sim 35\%$ more stars in our sample to improve the statistical significance of our results.

1.7.2 Analysis of completeness

In Section 1.4 we obtained the completeness function of our photometric catalog, based on the comparison of the luminosity functions (LFs) derived for WFI with that of the HST/ACS survey on the ONC, characterized by a much fainter detection limit. We refer to this as the *photometric completeness*. Here we compute the completeness function of the sample of stars that have at least both V and I magnitude in our catalog and and available spectral type. We refer to this one as the HRD *subsample completeness.*

The spectroscopic catalog of H97 is shallower than our photometry, with a 50% completeness at $I_c \simeq 17.5$ mag, and our extension from new spectroscopy does not change significantly this limit[6]. On the other hand, the subsample of stars classified with the [TiO] index is about 0.5 mag deeper than in H97, to $I \sim 18$ mag and does not cover the bright end of the cluster, populated by earlier spectral types.

The $V - I$ color limit is essentially set by the photometric completeness at $V-$band. Our $I-$band photometry is much deeper than the $V-$band: all the sources detected in V are also detected in I whereas we detect twice as much sources in I than in V. On the other hand $B-$band is shallower than V, but to provide an estimate of the stellar parameters at least one color (i.e., $(V-I)$) is needed (see Section 1.7.4). As a consequence, the inclusion of a star in the subsample used to derive the stellar parameters, is limited

[6]The new spectra we have presented do not extend the H97 spectral catalog to fainter magnitudes, and are mostly located outside the FOV of H97, in the peripheral regions of our WFI FOV.

by only a) $T_{\rm eff}$ estimates; b) $V-$band photometric detection.

The $V-$band *subsample completeness* function is the product of the *photometric completeness* in V and the fraction of sources, as a function of V magnitude, that have a $T_{\rm eff}$ estimate. We computed the latter simply as a ratio between the LFs in $V-$band of the subsample and the entire catalog. In this way the subsample completeness accounts for both the detection limit of the photometry, and the selection effects from the non-homogeneity of the sub-sample with $T_{\rm eff}$ estimates. In other words, it represents the probability of a star of a given $V-$magnitude to be detected in V and I and to be assigned a spectral type.

In Figure 1.25 we show the HRD subsample completeness function. We fit a polynomial for $V > 13.5$, while we assume the function to be constant, at 83% completeness for $V \leq 14$ given the high statistical uncertainties in the determination of the function.

We include 50% of the sources at $V \simeq 20$ mag and the completeness is zero for $V > 22$ mag. The completeness is lower than 100% for the brightest end of the sample, and this is due both to saturated sources (saturated in I and not present in our catalog) or simply because of the lack of spectroscopy. The higher fraction at $15 \lesssim V \lesssim 18$ mag comes from the classification of M-type stars from the [TiO] photometric index, capable of detecting almost all the sources in this range and therefore providing a more complete spectral typing coverage than spectroscopy.

This completeness is used in the next sections, converted from being expressed in magnitudes to masses and ages, to correct the age distribution and the mass function.

1.7.3 Spectral type-temperature relations

In Section 1.7.1 we have collected the spectral types for part of the sources present in our photometric catalog. These must be converted into $T_{\rm eff}$, because: 1) for deriving intrinsic colors and bolometric corrections (see Section 1.6.3) we rely on synthetic photometry on grids of stellar atmosphere models which are computed in terms of $T_{\rm eff}$; 2) also our model for the displacement of the colors caused by accretion luminosity – which we use in the following sections to disentangle this effect for determining A_V of the members – is based on the same quantities.

To derive the effective temperatures from the available spectral types we use the spectral type vs. temperature relation of Luhman et al. (2003). This relation, qualitatively intermediate between giants and dwarfs for M-type stars, is derived empirically imposing

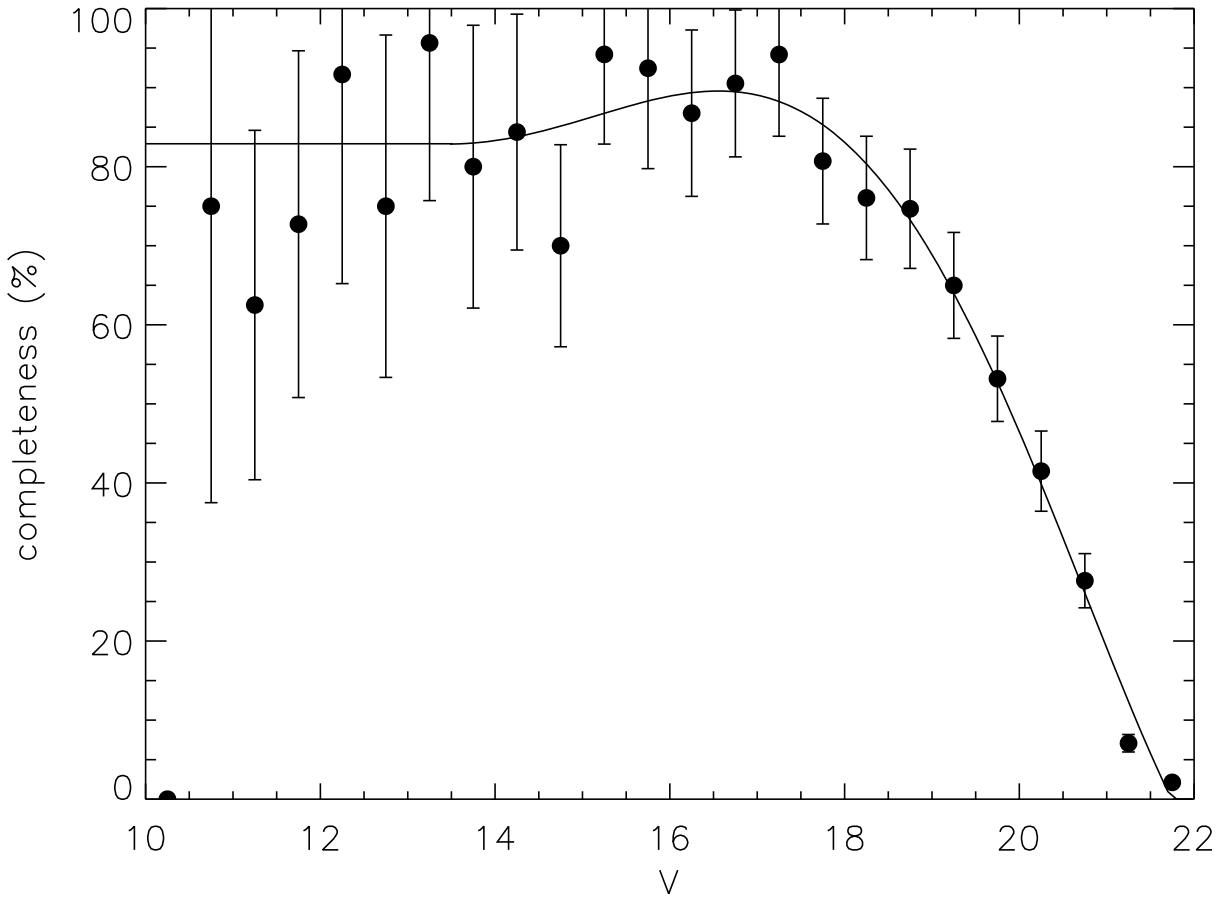

Figure 1.25 The $V-$band completeness of the sub-sample of stars with $T_{\rm eff}$ estimates (dots). The thick line is a 6th order polynomial fit for $V > 13.5$, while the completeness has been assumed equal to a fraction 0.83 for $V \leq 14$.

that all the four members of the presumably coeval multiple system GG Tau are located on the same BCAH98 (Baraffe et al., 1998) isochrone (Luhman, 1999), and uses the relation from Schmidt-Kahler (1982) for types $< M0$. This is different from what used in H97, taken largely from Cohen & Kuhi (1979) (and supplemented with appropriate scales for O-type stars (Chlebowski & Garmany, 1991) and late M-types (Kirkpatrick et al., 1993) and shifted in the K8-M1 range to be smoother). Figure 1.26 compares the spectral type - temperature relations of Luhman with the one of H97. The major differences are for the M spectral types, where Luhman predicts higher $T_{\rm eff}$.

Using the Luhman relation partially solves a problem encountered by H97, the systematic trend of the average extinction as a function of temperature with late type stars

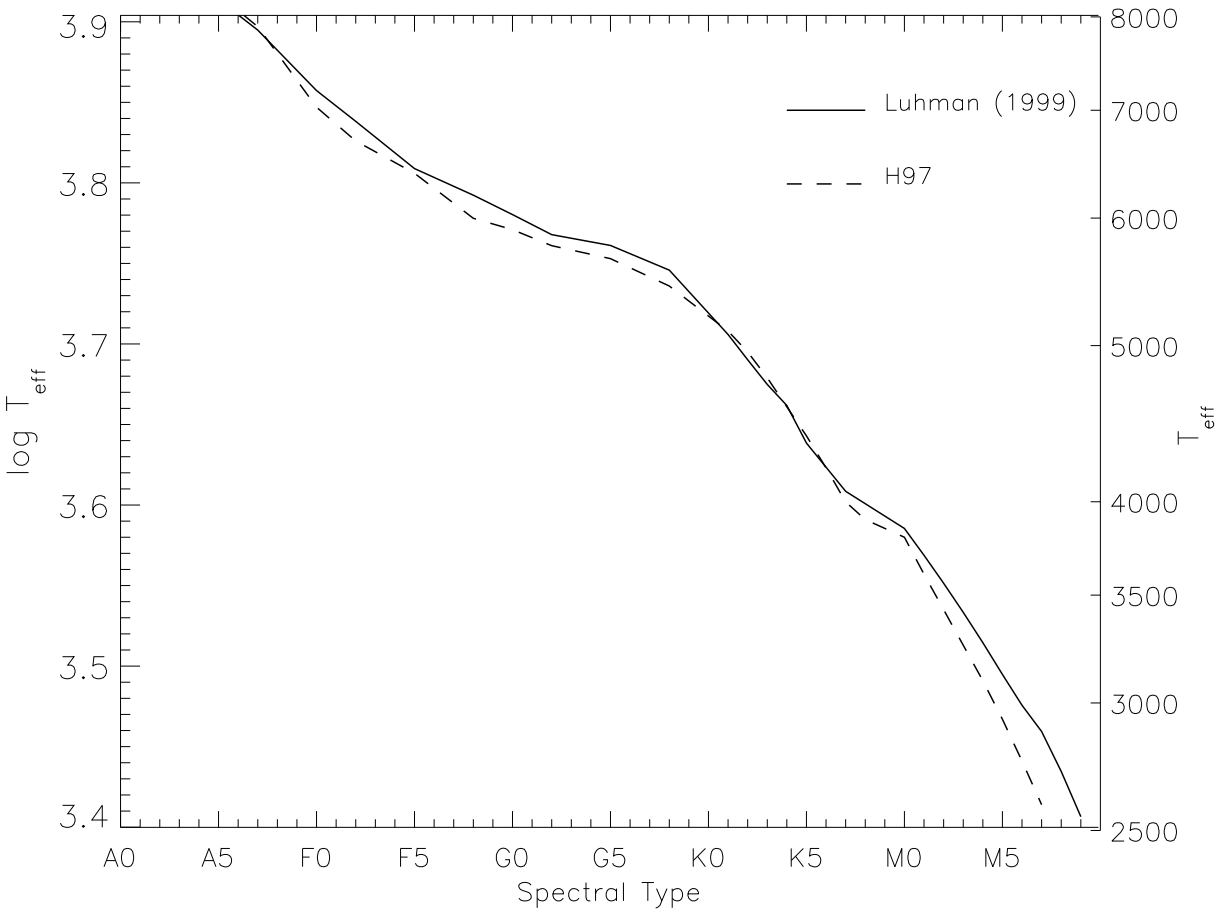

Figure 1.26 Comparison between the spectral type-$T_{\rm eff}$ relations used for this work (Luhman et al., 2003) and the one used on the ONC in H97 that was derived in Cohen & Kuhi (1979). The main differences rise with increasing spectral class, and can be several hundreds of Kelvin for late-M type stars.

appearing bluer than the color predicted according to their spectra type for zero extinction. This effect in H97 was partially due to the temperature–intrinsic color transformation assumed in that paper, which we already improved as described in Section 1.6.2; but only by using the Luhman relation between spectral types and $T_{\rm eff}$ is it possible to remove the correlation between mean reddening and temperature, characterized by systematically lower – even negative – values of A_V moving toward late-M spectral types. The Luhman scale, predicting for a given late spectral type a higher temperature and therefore bluer intrinsic color, reduces the number of sources whose observed colors cannot be matched by adding some reddening. A more detailed analysis on how the choice of the temperature scale affects the derived extinctions is presented in subsection 1.7.5.

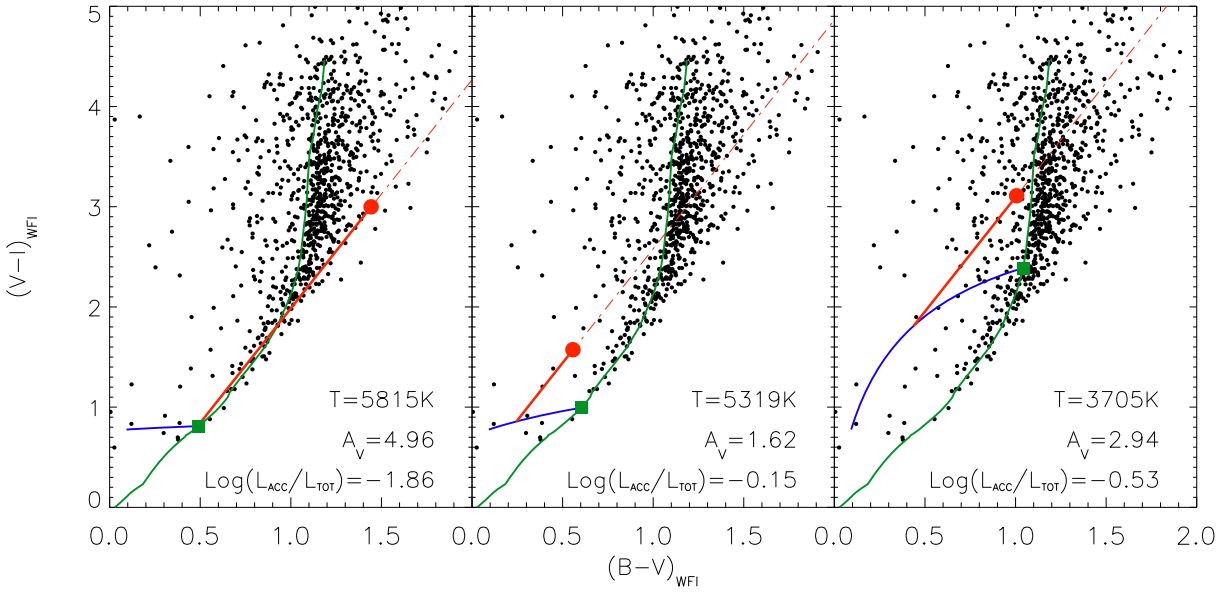

Figure 1.27 Examples of the method applied for the determination of reddening taking into account accretion for three stars in our sample. The ONC sample with available $T_{\rm eff}$ estimates (black dots) is plotted together with our reference model (green line). For each plot, the red circle indicates the observed colors of the considered star, and the green squares the predicted photospheric colors (for $A_V = 0$ and $L_{\rm acc} = 0$) given $T_{\rm eff}$ of the star from its spectral type. The blue curve is the displacement, from the photospheric color, increasing $L_{\rm accr}/L_{\rm tot}$ from 0 to 1 (see Figure 1.23). The intersection of the reddening direction (dash-dot line) applied to the star, and the accretion curve delimits the reddening vector (solid red line). In the three cases we report in the panels the known $T_{\rm eff}$ and the derived extinction and accretion luminosity for the considered star.

1.7.4 Derivation of reddening and accretion

The reddening is defined as the difference between the observed color and the intrinsic one, for example the color excess $E(V-I) = (V-I)_{\rm obs} - (V-I)_0$. The intrinsic color $(V-I)_0$ is usually derived on the basis of an assumed temperature-color relation. In the presence of accretion, however, the source colors are also affected by $L_{\rm accr}$ as shown in Figure 1.23, and since this effect makes the colors bluer, partially compensating the reddening caused by dust extinction, neglecting the accretion may lead to an underestimation of A_V. Furthermore, in our analysis of the color-color diagrams we have accounted explicitly for surface-gravity effects and for accretion effects in all the photometric bands of our photometry. This enables us to assess both reddening and accretion more realistically than past methods, based on optical photometry, which assume that only one or the other of the effects dominates in the bands in which the observations have been obtained.

We have therefore developed a technique that consistently takes both A_V and $L_{\rm accr}$ into

account, providing at the same time an estimate of the accretion luminosity and reddening. Given a star for which $T_{\rm eff}$ is known, our reference model gives its original position in the color-color diagram for zero reddening and accretion; the measured location of the star in the color-color plots will be in general displaced because of these effects. But under the assumption that they are uncorrelated of each other (the differential extinction depends mainly on the position of the star inside the nebula) and since we know how to model them (i.e., we know the reddening vector and we have a model for the accretion providing the displacement curve for all possible values of $L_{\rm accr}/L_{\rm tot}$), we can find the solution that produces the measured displacement with a unique combination of A_V and $L_{\rm accr}/L_{\rm tot}$.

In practice, for each star in the color-color diagram, $(B-V)$ vs. $(V-I)$ we compute the track (like those shown in Figure 1.23) representing the displacement computed for increasing $L_{\rm accr}/L_{\rm tot}$ from 0 to 1 for the exact $T_{\rm eff}$ value of the star. Then we found the intersection between the reddening vector applied to the position of the star and the accretion curve. This provides the exact reddening vector, and its component along the y-axis gives the excess $E(V-I)$. The intersection point also gives a value of $L_{\rm accr}$ for the star, according to our model of the accretion spectrum. In this way, under the assumption that the accretion spectrum we have used is representative of all the stars and the reddening law is the same for all stars, the values of $L_{\rm accr}$ and A_V for each star are uniquely derived. Some examples of this method are plotted in Figure 1.27.

In a few cases this method cannot find a geometrical solution; this happens when the star is too blue or too red in $(B-V)$, so that the extinction line, applied backward to the star, never crosses the curve computed for its temperature. Since the photometric errors are higher in B than in V or I, we attribute this effect to the inaccuracy of the $(B-V)$ color, and therefore we move the point along this axis until the closest intersection condition is found, respectively the tangency condition of reddening line and accretion curve, when the location of the star is too on the left, and the starting point along the accretion curve where $L_{\rm accr}=0$ when it is too on the right.

For some stars the extinction and accretion determination is degenerate. This is the case of Figure 1.27c, where the reddening vector intersects the accretion curve in 2 points, either low A_V and low $L_{\rm acc}$ (the solution shown) or higher A_V and $L_{\rm acc}$. In this cases, which involve only low-$T_{\rm eff}$ stars, we always choose the first scenario.

In a few cases the derived extinction came out negative. This happens when the observed $(B-V)$ is higher and $(V-I)$ is lower than the locus for zero accretion at the star's temperature. For 13% of the sources the B magnitude is not available and A_V is

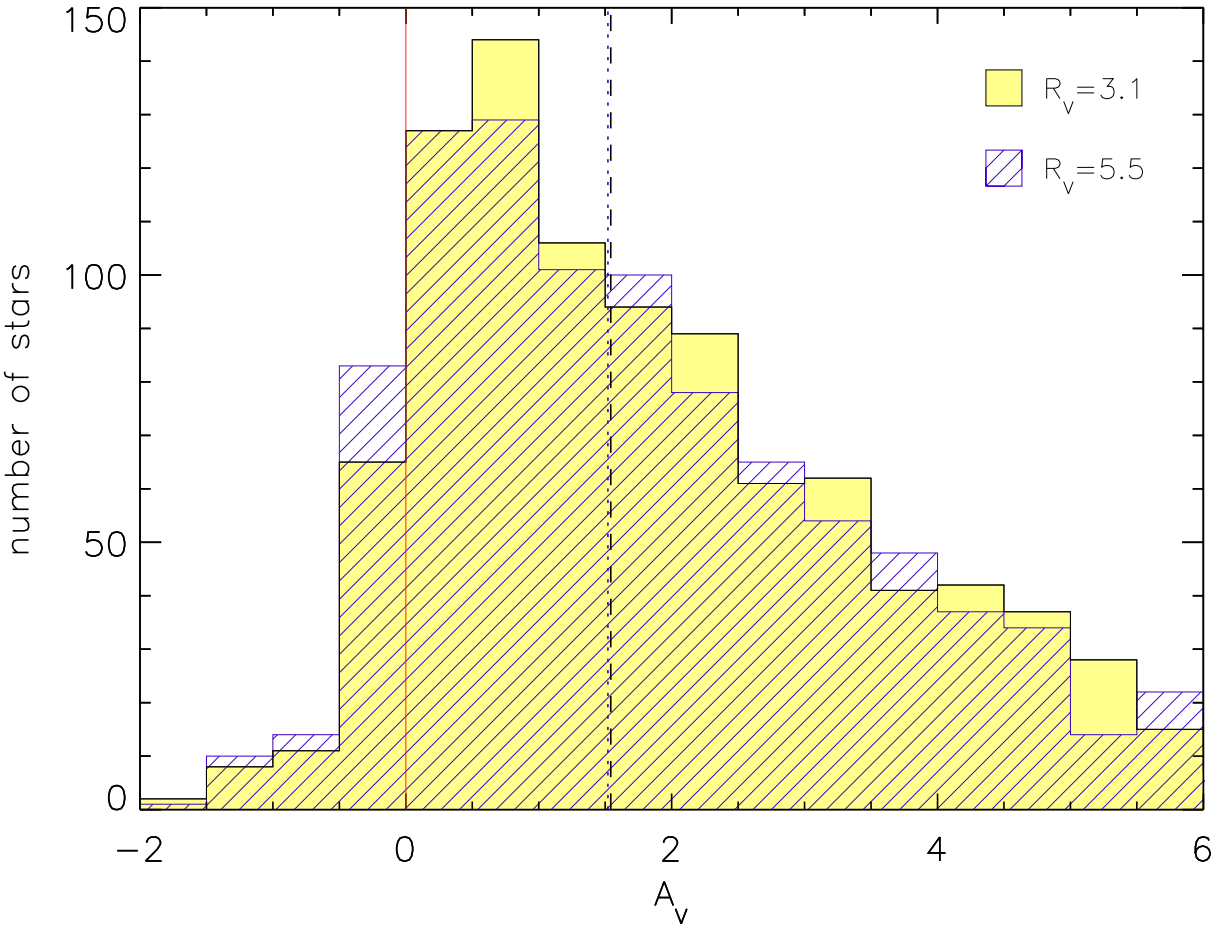

Figure 1.28 Distribution of the extinction measured for the ONC stars, in terms of A_I in the WFI photometric system, for values of $R_V = 3.1$ and 5.5. The dashed line shows the median value for the extinction for $R_V = 3.1$; the dotted line is the median for $R_V = 5.5$.

therefore derived simply from the excess $E(V - I)$.

In Figure 1.28 the distribution of A_V is shown, for the two choices of R_V. There is a small fraction of stars, as mentioned, for which we find a negative extinction. This, reasonably accounted for by the uncertainties, is however significantly smaller than in H97. In these cases we consider the star to have zero extinction for the derivation of the stellar parameters, as in H97. The median of the distribution extinction for the whole sample is at $A_V \simeq 1.5$ mag.

In Figure 1.29 the distribution of $\log L_{\rm accr}/L_{\rm tot}$ is shown, including all the stars for which the value of $L_{\rm accr}$, derived from our geometrical method, is positive and big enough to lead to a displacement in the two color diagrams larger than the photometric error. We find about 60% of the stars showing an excess attributed to accretion, with a relative

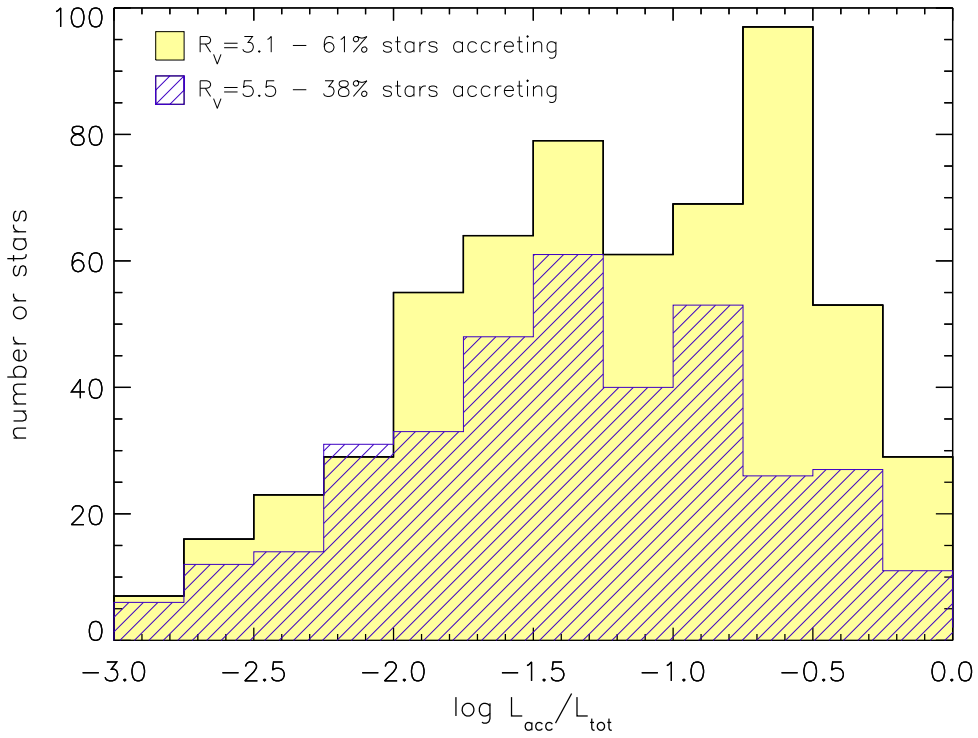

Figure 1.29 Distribution of the accretion luminosities derived, for the two values of R_V.

fraction $L_{\rm accr}/L_{\rm tot}$ peaking at 5–25%. These values are comparable to those seen in the more rapidly accreting Taurus members (Herczeg & Hillenbrand, 2008). Increasing R_V produces a decrease in both the fraction of accreting sources and the measured $L_{\rm accr}$, as a consequence of the steeper de-reddening vector in the B, V, I plot.

We estimate the uncertainties in our determined extinction and accretion luminosity using again the geometrical method in the 2-color diagrams. Given the non-analytical nature of the method, we use a Monte Carlo (MC) approach to compute how the uncertainties in our data (both photometric errors and uncertainty in the spectral types) propagate to the determined values of A_V and $L_{\rm accr}$. For each star we perturb randomly the photometry of each band with their photometric errors, assumed to be gaussian. We also consider the uncertainties in the spectral types from spectroscopy, of ± 1 sub-type, and we assign a temperature within this interval from a flat distribution. We iterate this approach 200 times for each star, deriving each time the $E(V-I)$ and $\log(L_{\rm accr}/L_{\rm tot})$ values. We then analyze the overall variation of the derived results. Our test shows that, on average, $\sigma_{E(V-I)} = 0.12$ mag, with the uncertainty in the spectral typing being the dominant source of uncertainty. Concerning the accretion luminosity fraction $\log(L_{\rm accr}/L_{\rm tot})$,

our MC test shows that the uncertainty can be up to 1 order of magnitude. We conclude that our method is fairly accurate in computing the extinction A_V, a most critical parameter for placing the members in the HRD, but provides only a rough estimate of the accretion luminosities of the sources. Other methods more directly based on accretion indicators (line emission, UV-excess,...) should therefore be used for an accurate analysis of the accretion activity of our sources.

1.7.5 Systematic effects in deriving A_V

In the previous sections we have presented evidences that intrinsic colors valid for MS dwarfs are incompatible with the observed colors of the ONC, suggesting a gravity dependence of the optical color scale for M-type PMS stars. This is also predicted by atmosphere modeling, though with a limited accuracy. Thus we have calibrated the optical colors to best match our ONC data, defining our reference model for colors as a function of $T_{\rm eff}$.

We have presented a method to estimate A_V from 3 photometric bands accounting for possible accretion luminosity, and we have mentioned that we chose a particular spectral type – $T_{\rm eff}$ relation to reduce the number of sources showing negative A_V. Here we analyze in more detail how all these aspects affect the derived reddening distribution.

We have considered all 8 possible combinations of either considering or not considering the 3 described improvements, which is: a) converting the spectral types into $T_{\rm eff}$ using the Luhman et al. (2003) scale or the Cohen & Kuhi (1979) one, used, e.g., in H97; b) using the intrinsic colors in B, V, I band from our reference model or from the $\log g$ values of the ZAMS; c) deriving A_V using the from BVI disentangling accretion as described in Section 1.7.4 or simply neglecting the accretion and the B-band information and basing solely on the excess $E(V-I)$. In the case of the ZAMS model, we have first computed the displacements in the 2-color diagrams caused by accretion luminosity, in a similar way as for our reference model, shown in Figure 1.23.

The results are presented in figure 1.30, as a function of $T_{\rm eff}$ to highlight systematic trends. For guidance, the top-left panel shows the results we use, and the bottom-right one reproduces qualitatively the findings using the same methods and relations as in H97, with a systematical lower A_V toward the latest M-type stars.

It is evident that using the Luhman temperature scale for M-type stars instead of the Cohen & Kuhi relation leads to systematically higher A_V, compensating very well the problem of deriving negative reddenings.

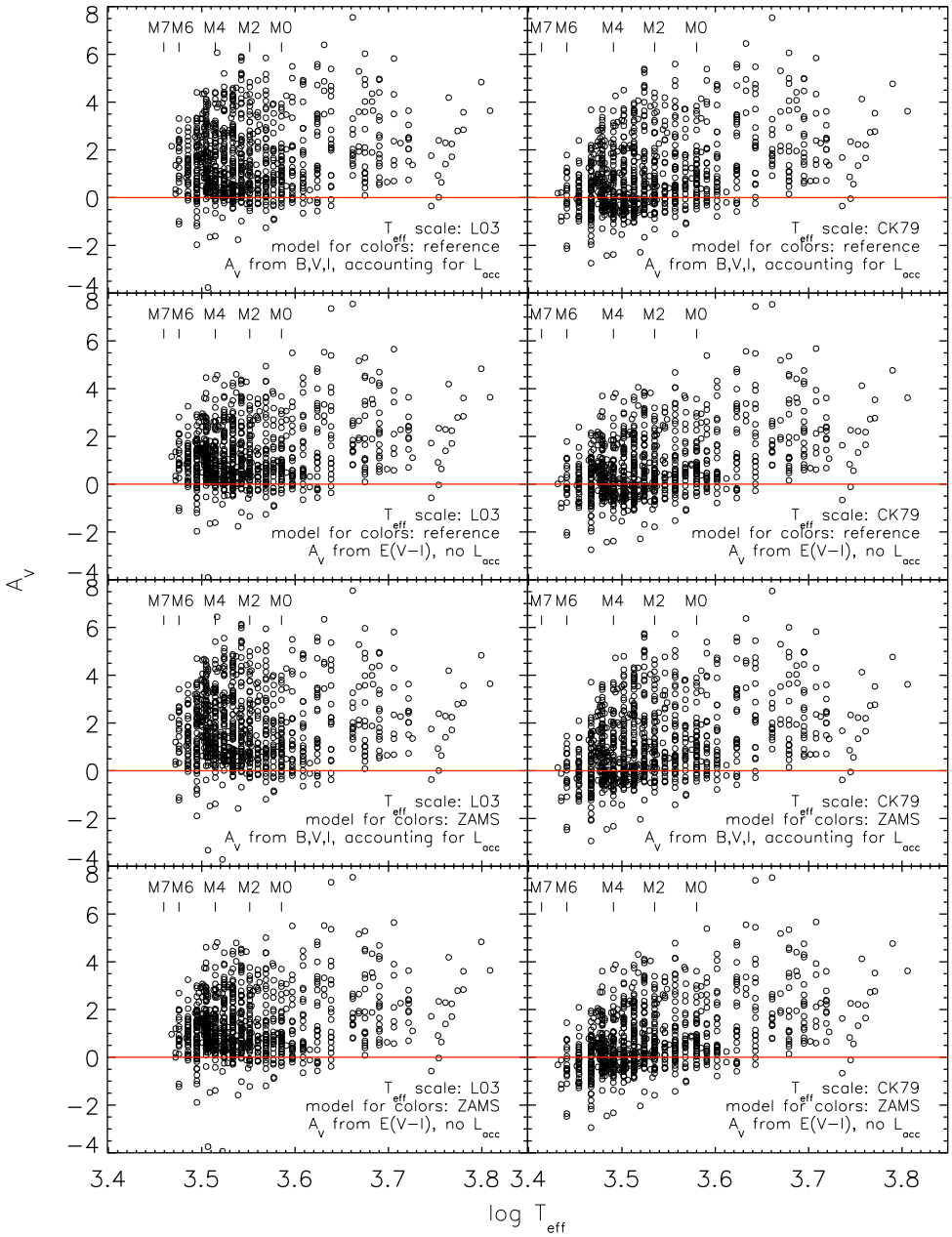

Figure 1.30 A_V vs. $\log(T_{\rm eff})$ plots for the ONC members, for all the combinations of changing: *a)* $T_{\rm eff}$vs. spectral type scale – left panels using the Luhman scale, right panels using the Cohen & Kuhi scale; *b)* intrinsic colors: – rows 1 and 2 using our empirically calibrated reference model, rows 3 and 4 using the result of synthetic photometry constraining $\log g$ from the Siess ZAMS; *c)* method to derive A_V: - row 1 and 3 using our geometrical method to disentangle A_V from $L_{\rm accr}$, row 2 and 4 neglecting B magnitude and deriving A_V from $E(V-I)$.

The differences we observed in the A_V values changing the color scales from ZAMS to our empirical reference model are more modest, and Figure 1.30 alone does not allow to clearly justify the choice of one or another color scale. We remind the reader that the intrinsic colors from the ZAMS model do not reproduce the observed color-color diagrams, (see Figure 1.17), and therefore cannot be considered representative of the observed data. In particular, assuming the dwarfs colors leads to systematically higher accretion luminosities for cool members, predicting almost all M-type stars to have a positive value of $L_{\rm acc}/L_{\rm tot}$.

Finally, if we do not consider the color offsets due to on-going accretion (Figure 1.30, second and fourth rows), the predicted extinctions are underestimated. This is clear from figure 1.23: a positive value of $L_{\rm accr}$ leads to lower intrinsic colors (both $B-I$ and $V-I$), increasing the measured A_V.

1.8 The H-R diagram of the ONC

The Hertzsprung-Russell diagram, representing the total luminosity emanating from the stellar photosphere versus the photospheric effective temperature, is the physical counterpart to the observational color-magnitude diagram. The transformation between the two requires the knowledge of a number of quantities. In our case, having at our disposal $T_{\rm eff}$, we convert the observed magnitudes into total luminosities correcting for accretion and extinction (Section 1.7.4), using our computed bolometric corrections for the WFI photometric system (Section 1.6.3), and considering the solar colors and bolometric magnitude. We therefore compute the luminosity as follows:

$$\begin{aligned}\log\left(\frac{L}{L_\odot}\right) &= 0.4\cdot\left[M_{bol,\odot}-M_{bol,\star}\right] \qquad (1.9)\\ &= 0.4\cdot\left[M_{I_{\rm WFI},\odot}-M_{I_{\rm WFI},\star}+BC_{I_{\rm WFI},\odot}-BC_{I\,{\rm WFI},\star}\right]\\ &= 0.4\cdot\left[M_{V,\odot}-(V-I_{\rm WFI})_\odot-I_{\rm WFI}+\Delta I_{ACC}+\right.\\ &\qquad\left. A_{I_{\rm WFI}}+BC_{I_{\rm WFI}}(T)+DM\right]\end{aligned}$$

where $I_{\rm WFI}$ and $V_{\rm WFI}$ are magnitudes referred to the WFI system, while V is $V_{\rm Johnson}$. The term $\Delta I_{\rm accr}$ (negative) is the I band excess due to the accretion luminosity derived as shown in §1.7.4, directly computed from synthetic photometry on the accretion spectrum normalized to the measured value of $L_{\rm acc}$ of each star, for the 2/3 of the stars showing accretion in their colors. $\Delta I_{\rm\,accr}$ has a mean value of -0.16 ± 0.1 mag, and is clearly zero for the rest of the sample.

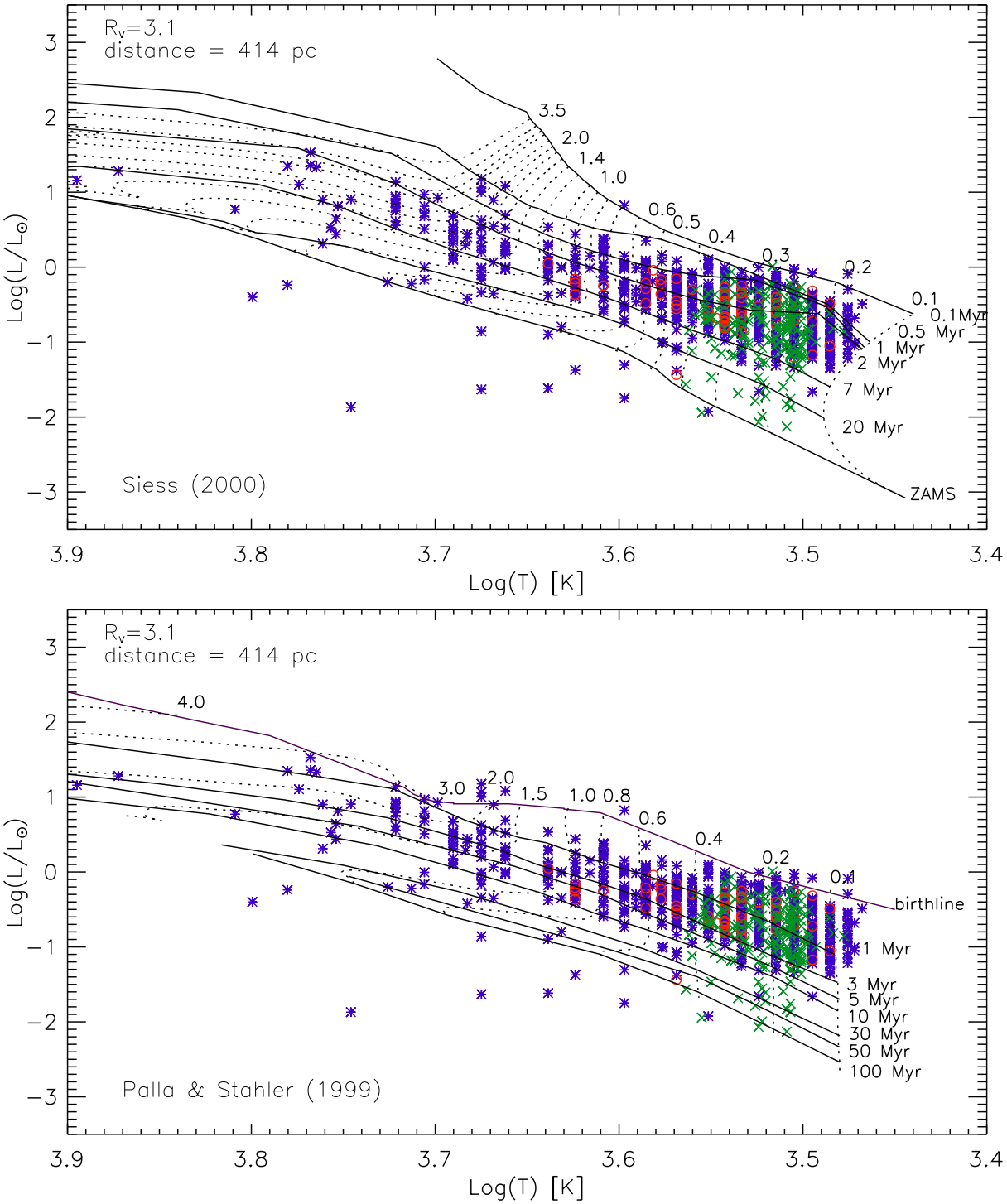

Figure 1.31 Hertzsprung-Russel diagram for the ONC. Isochrones and tracks from Siess et al. (2000) (upper panel) and Palla & Stahler (1999) (lower panel) are overplotted, for masses from $0.1M_{\odot}$ to $3.5M_{\odot}$ and ages from 10^5 years to the ZAMS in the Siess case, and from the birthline to 10^8 Myr for the Palla & Stahler (1999) models. Blue stars are spectral types from H97, excluding sources with a membership probability $< 50\%$. Red circles indicate the additional sources we classify from our spectroscopic survey. Green crosses show the location of the M-type source, for which the temperature is determined from the [TiO] spectrophotometric index.

According to our convention for the bolometric correction, we have $\mathrm{BC}_{I_{\mathrm{WFI}},\odot} = 0$. For the solar values we used $M_{V\odot} = M_{V(\mathrm{Johnson})\odot} = 4.83$ (Binney & Merrifield, 1998) and by means of synthetic photometry on our solar spectrum we find $(V_{\mathrm{Johnson}} - I_{\mathrm{WFI}})_\odot = 0.80$. Regarding the distance of the ONC, recent investigations based on accurate trigonometric parallax measurements (Hirota et al., 2007; Sandstrom et al., 2007; Menten et al., 2007) lead to a revision of the value $d \simeq 470$ pc adopted by H97. Amongst these, we used the most precise estimate $d = 414 \pm 7$ pc (Menten et al., 2007), based on a recent VLBA trigonometric parallax, corresponding to a distance modulus DM= 8.085.

As mentioned in Section 1.7, we have excluded from our sample all the confirmed non-members, and we expect that the remaining contamination from foreground and background sources with unknown membership is relatively low ($\sim$2 – 3% of our sample).

The resulting HRDs, for the standard $R_V = 3.1$ reddening law, are shown in Figure 1.31. We mention that assuming the higher value of $R_V \simeq 5.5$ leads to predicted higher luminosities because, for a given color excess $E(V - I)$ the extinction A_I is higher (see Table 1.6). The upper and lower panels in Figure 1.31 correspond to different PMS evolutionary models; top) the models by Siess, with ages from 10^5 years to the ZAMS; bottom) the models of Palla & Stahler (1999) (ages from 10^6 to 10^8 years), which include the deuterium birthline. Our sample reaches masses as low as 0.1 $\mathrm{M}_\odot$, extending to the intermediate-mass range up to several solar masses.

Figure 1.31 highlights the differences between the two families of evolutionary models in the comparison with our data. Whereas both are generally parallel to the median of the observed sequence, Siess predicts that isochrones of a given age are located at higher luminosities, which implies that the ages predicted for the cluster members are older. Palla & Stahler (1999), on the other hand, predict lower luminosities.

There are a few anomalous stars located in regions of the HRD not covered by the PMS isochrones. Stars located below the ZAMS can be background objects with no membership information. However, there are also some underluminous confirmed members. As explained, e.g., in Kraus & Hillenbrand (2009), this effect seen in other PMS systems is due to the presence of dense circumstellar material (e.g., an edge-on circumstellar disks) which may both a) occult partially the photosphere; and b) scattering a significant amount of stellar flux - more efficiently for short optical wavelengths - along the line of sight. This hypothesis has received recent support from the study of Guarcello et al. (2010). All the sources below the Siess ZAMS or the 100 Myr Palla isochrones are excluded from our further analysis.

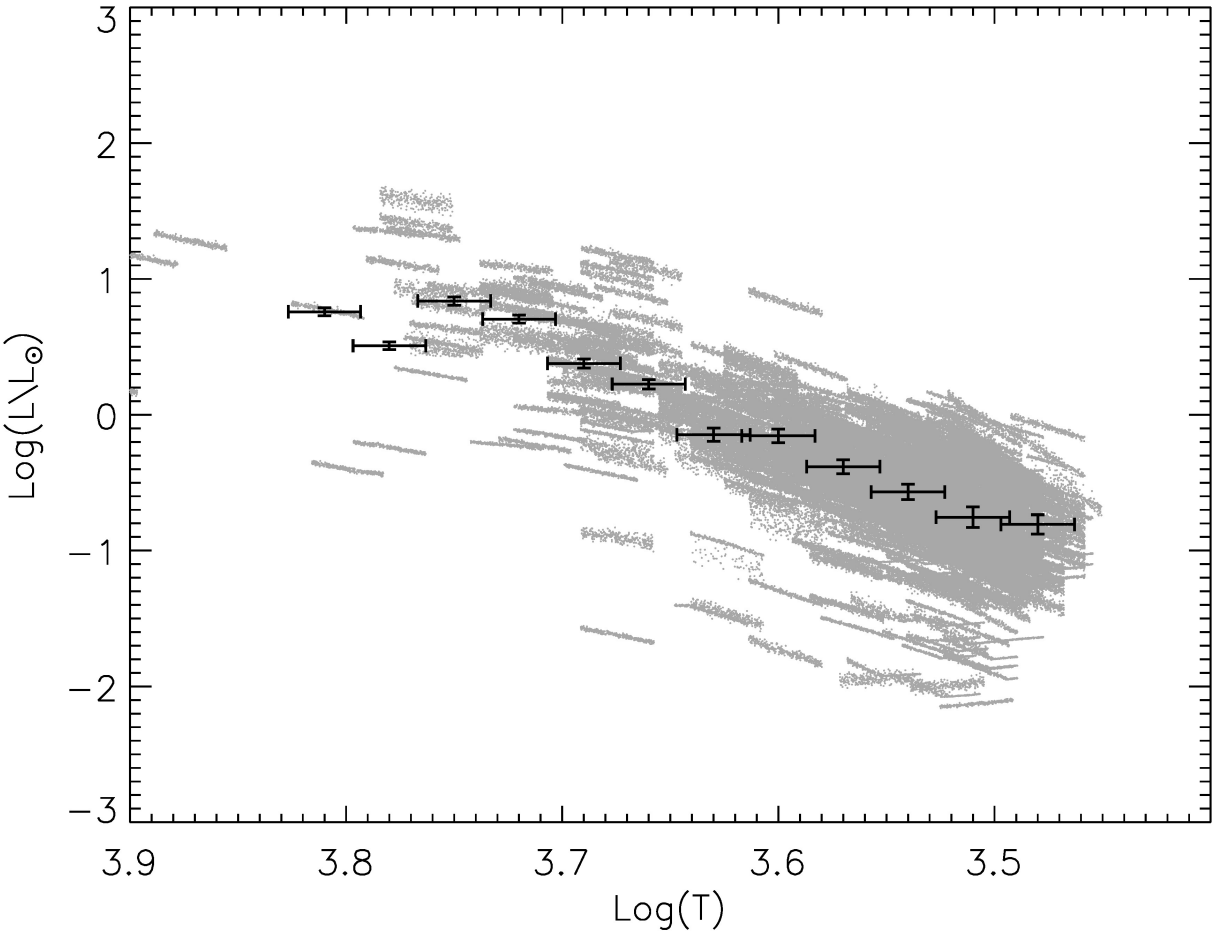

Figure 1.32 Representation of the method we used for determining the average uncertainties that affects our determination of the H-R diagram. For each star we propagate the uncertainties simulating a "cloud" of determined positions in the diagram. The black points with error bars represent the average determined uncertainty in $\log L$ and $\log T$ in 12 bins of surface temperatures.

We assess the overall uncertainty, from the observational errors, in the position of the stars in the HRD, using a Monte Carlo approach similar to that adopted in Section 1.7.4. We consider the uncertainty in the spectral type and the photometric errors, apply these effects randomly a number of times to each star, deriving the final position in the HRD as described above. For each source the methods produces a "cloud" of points in the H-R diagram which represent the real scatter associated with the star. Figure 1.32 shows the result of an iteration. Each star is associated with a stripe of points, whose inclination and shape in general depend on the location of the star in the 2-color diagrams and its temperature. To understand better the general behavior of the resulting uncertainties, we divide stars in bins of $\log(T_{\rm eff})$ and compute the average spread in both $T_{\rm eff}$ and $\log L$ with

respect to the actual position of the stars of Figure 1.31. This is represented with black points and error bars in Figure 1.32. It is evident that the uncertainty in $T_{\rm eff}$, which comes directly from the uncertainty in assigning spectral types, is usually much higher than the spread in $\log(L)$, even if this is influenced by the former (as mentioned in Section 1.7.4, the errors in $T_{\rm eff}$ usually contribute more than the photometric errors in the derivation of A_I, which affects $\log(L)$.

Concerning the luminosities, however, we must stress that there are several sources of uncertainties beyond the measurement errors, which involve both the data analysis and the physical nature of the members. In fact, our determination of A_V and $L_{\rm accr}$ from the BVI photometry relies on the assumption of a unique accretion spectrum in the modeling of the veiling. The SED of the accretion spectrum – and therefore its broad band colors – may actually be different from star to star. As mentioned in Section 1.6.5, these variations should not affect much the extinction, and so $L_{\rm tot}$. We do not have at our disposal a representative sample of calibrated accretion spectra for the ONC, mostly due the bright nebular background against which a flux-calibrated excess would have to be measured relative to the stellar continuum. Therefore we are unable to characterize explicitly the error distribution on the luminosity caused by the accretion spectrum modeling. Other sources of apparent luminosity spread are, moreover, circumstellar emission, scattered light, unresolved companions, variability and accretion history. As a consequence, the errors on $L_{\rm tot}$ shown in Figure 1.32 do not represent the maximum uncertainty, but the minimum error based on the uncertainties of our data that are known. Only a quantitative knowledge of all the sources of luminosity spread could disentangle, therefore, apparent luminosity spread from true age spread. This problem, critical for the understanding of age distribution in the star formation history of young stellar systems (e.g., Hillenbrand et al., 2008; Hillenbrand, 2009; Baraffe et al., 2009) will not be discussed in detail in this work.

We can compare our derived luminosities with the values found by H97, for the sources present in both catalogs. The results, as a function of $T_{\rm eff}$, are shown in Figure 1.33. Besides a modest scattering in the result, most probably due to stellar variability, a definite trend is evident: for $\log T_{\rm eff} > 3.6$, corresponding roughly to K and earlier spectral types, we estimate a lower bolometric luminosity. This is in part caused by the lower distance we adopted for the ONC; however this accounts for only 0.11 dex of $\log L$. The changes we applied to the intrinsic colors and to the temperature scale do not affect critically this range of spectral types; therefore, this systematic effect is largely due to our bolometric

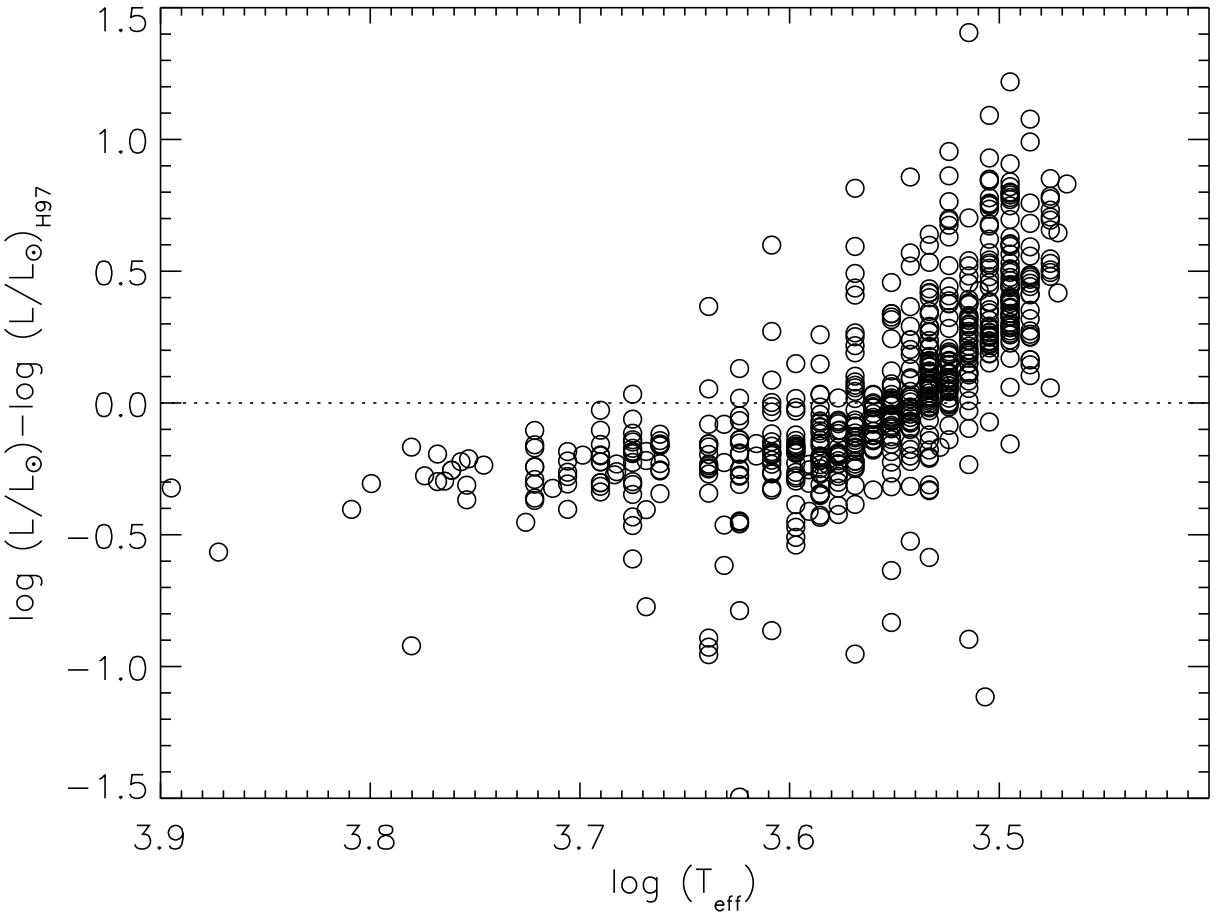

Figure 1.33 Difference between bolometric luminosities derived from our calculations and from Hillenbrand (1997), as a function of $T_{\rm eff}$. The systematic trend is evident: for early type stars we derive a lower value of L, while for M-type stars our luminosities trend toward increasingly higher values toward lower temperatures, relative to H97. A number of differences in the analyses contribute to this trend.

corrections from $I-$band magnitudes. A different type of discrepancy appears for cold stars, where our analysis leads to higher luminosity than in H97. This is mostly due to the higher extinctions compared to H97 that we measure in this range. Since the Luhman temperature scale we adopt predicts higher $T_{\rm eff}$ in this interval, our HRD is shifted both to higher $\log L$ and higher $\log T$ for M-type stars compared to H97, and continue to follow fairly well the isochronal slopes of evolutionary models.

1.8.1 Completeness of the HRD

In section 1.7.2 the completeness of our spectro-photometric catalog is derived as a function of V mag, i.e. for the CMD. This function, however, cannot be directly translated in

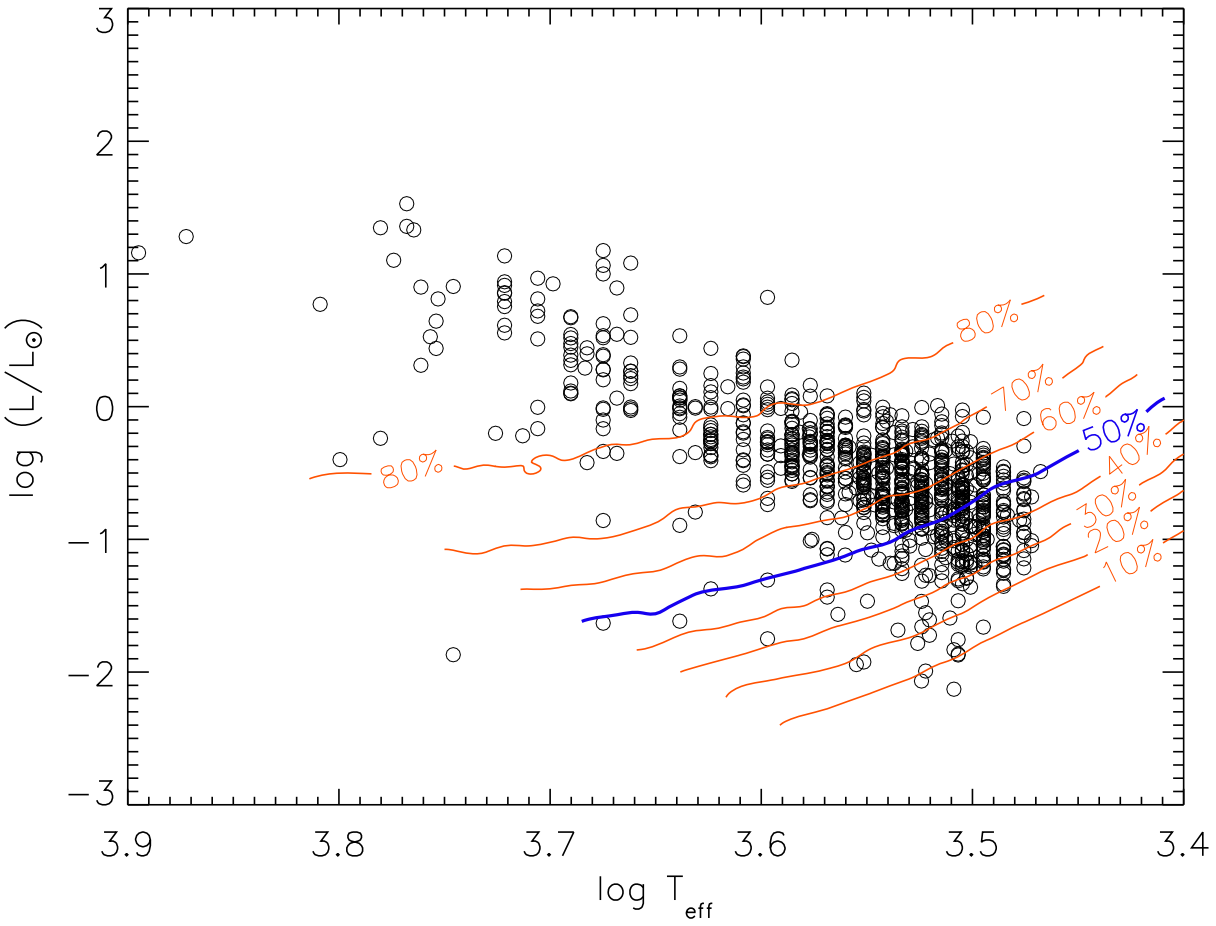

Figure 1.34 Simulated completeness in the HRD

the HRD, because of differential extinction and nonlinearity of intrinsic colors and bolometric corrections. Therefore we developed a statistical simulation that, for each point of the CMD, determines the probability for such star to be observed and present in our spectral type sample.

We proceed as follows. We consider a uniform, dense, cartesian grid of points in the HRD. For each of these points we find its counterpart in the CMD for $A_V = 0$, converting $T_{\rm eff}$ and $\log L$ into $(V-I)_0$ and I_0 using the intrinsic colors of our reference model and applying backward the bolometric correction and the distance modulus. In reality, a star having the considered $T_{\rm eff}$ and $\log L$ of the grid point is not necessarily observed in this position of the CMD, but reddened along the extinction direction of an amount that follows the distribution of A_V inside the nebula. We consider as a representative distribution of A_V the distribution we determined in section 1.7.4 limited for the brightest half (in $\log L$) of the population. This is because the reddening for intrinsically faint stars in our sample is biased toward low values, since such sources with high A_V fall below our detection limit. For each point in the transformed grid in the CMD we utilize a Monte Carlo approach for applying the extinction, creating 1000 simulated reddened stars, with values of A_V drawn from this distribution. Therefore, this set of aligned, simulated stars correspond to the all the positions in the CMD where a star with the considered $T_{\rm eff}$ and $\log L$ can be located, following the true extinction distribution. We assign the completeness computed in Section 1.7.2 to all the 1000 simulated stars according to their position in the CMD. The average of the 1000 values of completeness corresponds statistically to the real probability, for a source with the considered $T_{\rm eff}$ and $\log L$, to be detected in our catalog and assigned a spectral type. Iterating the same method for all the points in the HRD, we populate a 2D distribution of completeness in this plane.

The result is shown in Figure 1.34. Our results show that the completeness decreases toward both low $L/L_\odot$ and low $T_{\rm eff}$.

1.8.2 Distribution in the mass-age plane

Using the models of Siess et al. (2000) and Palla & Stahler (1999), we assign an age and mass to each star. To this purpose, we compute 2D interpolated surfaces with age and mass given as a function of $\log(T_{\rm eff}), \log(L/L_\odot)$. In Table 1.7 we present our results for the stars of our sample.

We analyze our masses and ages, and study their distribution in the mass-age diagram;

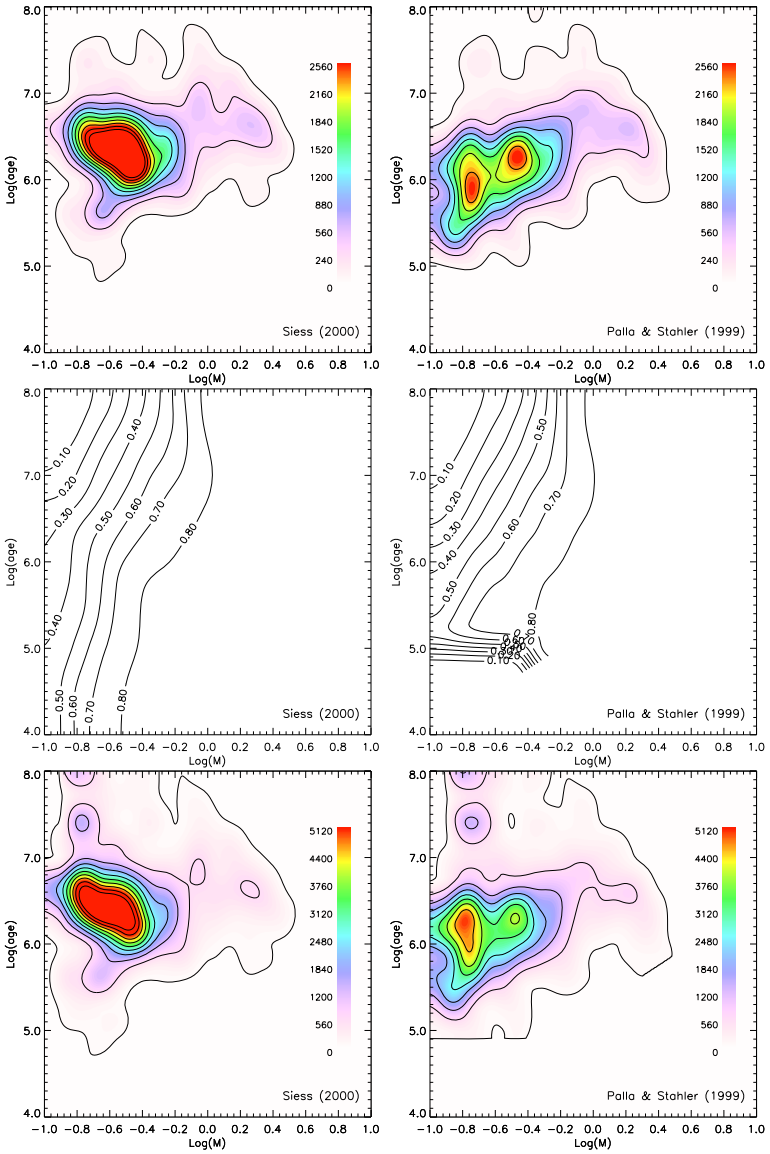

Figure 1.35 *Upper panels:* density map in the plane $\log(age)$ vs. $\log(mass)$ according to our results using Siess et al. (2000) and Palla & Stahler (1999) evolutionary models. Stars are counted into a grid of uniform bins spaced 0.1 in $\log(M)$ and 0.25 in $\log(age)$, and the derived map has been oversampled, interpolated and smoothed with a kernel sized 0.13×0.32. The color scale reported is in units of number of stars per unit of $\log(M)$ and per unit of $\log(age)$. It is evident that in the Siess case the age distribution is uniform (besides a broad age spread at all the masses), but for the Palla & Stahler models there is an evident correlation between age and mass, predicting younger ages for very low mass stars and older for intermediate masses. *Middle panels:* contour plots of the completeness function in the mass-age plane, computed for the evolutionary models of Siess et al. (2000) and Palla & Stahler (1999), and for $R_V = 3.1$, from our simulation. The apparent vanishing completeness in the bottom-left corner of the Palla & Stahler case is due to the lack of information of these evolutionary tracks for young ages and very low masses, but this does not affect our results given that our sample includes no stars in this range. *Bottom panels:* the density maps of the upper panels normalized dividing it by the completeness.

Table 1.7 Positions in the H-R diagram and values of mass and age from Siess (2000) and Palla & Stahler (1999)

							Siess		Palla					
ID	RA	Dec	$\log T_{\rm eff}$	$\log L$	A_V	$\log \frac{L_{\rm acc}}{L_{\rm tot}}$	M	log age	M	log age	Spectral Type	H97 ID	mem [2]	Spectral Type
	J2000	J2000	K	$L_\odot$	mag		$M_\odot$	yr	$M_\odot$	yr	from: [1]		%	
1	5 35 47.02	-5 17 56.91	3.615	2.739	7.263	< -5	...	...	...	...	H97	992	0	K3-M0I ...
2	5 35 20.71	-5 21 44.45	4.251	2.628	2.184	-1.31	...	...	...	...	H97	660	99	B3 ...
3	5 35 05.21	-5 14 50.37	3.768	1.529	2.665	-0.53	2.918	6.326	2.850	5.854	H97	260	97	F8 ...
5	5 35 21.32	-5 12 12.74	3.768	1.359	2.027	-0.79	2.570	6.469	2.450	6.226	H97	670	70	G8: ...
8	5 34 49.98	-5 18 44.61	3.936	1.625	2.511	-0.72	2.342	6.684	2.400	6.434	H97	108	92	A3 ...
10	5 34 39.76	-5 24 25.66	3.662	1.045	0.898	-1.57	1.930	5.669	...	...	H97	45	0	K4 ...
11	5 35 16.97	-5 21 45.42	3.969	1.371	1.345	-0.72	2.155	6.941	2.250	6.695	H97	531	99	A0 ...
15	5 35 05.64	-5 25 19.45	3.699	0.926	0.769	-1.49	2.515	6.209	2.487	5.667	H97	273	99	K0 ...
16	5 35 20.21	-5 20 57.09	3.780	1.348	4.239	-0.22	2.432	6.551	2.400	6.285	H97	640	99	K0 ...
...	...	...	...	...	...	...	...	...	...	...	...	...	...	

Note. — Only results assuming $R_V = 3.1$ are included. Only a portion of the table is shown here for guidance regarding its form and content.)

[1]H97 refers to spectral types from Hillenbrand (1997), NEW to stars classified from our spectroscopy, TiO refers to M-type stars classified from the [TiO] photometric index.

[2]Membership probability, as in H97.

this allows us also to investigate possible correlations between the two quantities.

For this purpose, we produce a number density map in a $\log(age)$ vs. $\log(M)$ plot, counting the stars present into uniform bins of width 0.25 dex in $\log(age)$ and 0.1 dex in $\log(M)$. A boxcar smoothing with a kernel size of 1.3 times the original grid size is applied to smooth out local variations due to statistical noise.

The result is shown in Figure 1.35, upper panels, with density contours highlighted. The outermost solid contour corresponds to 1 star per bin, the second 5, and the third 9, corresponding to poisson uncertainty of 100%, 45%, and 33%. Evidence of correlations should be investigated in the inner part of the map, where the majority of the objects are positioned. Here it is evident that whereas Siess models do not show a global trend, in the Palla & Stahler case the low-mass stars turn out to be systematically younger than the intermediate masses, with an average age changing by more that one dex along our mass range. H97 reported a similar inconsistency in their analysis, based on the evolutionary models of D'Antona & Mazzitelli (1994). The fact that the age-mass correlation is found using Palla & Stahler models while not seen in our results from Siess isochrones could imply that the latter should be considered in better agreement with our data.

However, as discussed in Palla & Stahler (1999), the completeness of the sample can potentially bias the mass-age relation. This is especially true in the very-low mass regime, as seen in Figure 1.34, as older PMS stars have lower luminosity than younger objects and therefore are more likely to be excluded from a stellar sample due to sensitivity limits.

We therefore investigate if the incompleteness of our stellar sample could be responsible for the observed mass-age relation in order to correct the derived results.

We compute the completeness in the mass-age plane following an analogous method as for the HRD (Section 1.8.1), but considering instead of a uniform grid of $\log T_{\rm eff}$ and $\log L$ values, a cartesian grid of masses and ages in the HRD, identical to the one used for Figure 1.35a,b. The result is now model-dependent, since a given mass-age point is located in different positions of the HRD according to the two sets of evolutionary models.

The result is shown in Figure 1.35, middle panels, interpolated and smoothed in the same way as for the density maps. Results confirm that completeness decreases toward lower masses and higher ages, in a qualitatively similar fashion to the observed mass-age correlation found from our data with Palla & Stahler isochrones. Differences between the results obtained with the two sets of evolutionary models are due to the different shape of tracks and isochrones, especially in the low-mass range (see the HRDs of Figure 1.31). The cutoff for the youngest ages in the completeness derived using Palla & Stahler models is due to the lack of the early PMS phases in this family of models.

The "normalized" mass-age map, computed by dividing our preliminary results of Figure 1.35a,b by the completeness map, is shown in the bottom panels of the same Figure. While the shape of the distributions in the mass-age plane and the average age for the ONC do not change by a large quantity, due to the smooth variation of completeness against mass and age, we find that the correlation between mass and age for the Palla & Stahler models reduces significantly, and below 1 $M_{\odot}$ the trend of age with mass is less evident, while, on the contrary, for the Siess models the completeness correction suggests an anti-correlation between ages and masses, hinting for higher predicted ages for low-mass stars.

In the high-mass end of these plots ($M \gtrsim 1 M_{\odot}$) there is still a tendency toward a higher measured average age, but we do not consider this as a solid evidence for a measured mass-age correlation. This for two main reasons: on the one hand, intermediate stars of young ages are not covered by the evolutionary models of Palla & Stahler, and on the other hand for low-mass and high-age fraction of the population the completeness we determined is too low to be correctable using our method. In conclusion, we do not find evidences of an age trend with respect to stellar mass in the ONC, both using Siess and Palla & Stahler evolutionary models.

The apparent over-density evident in the completeness-corrected map at $\log M = 0.8 M_{\odot}$ for $\log(\text{age}) > 7$ is not relevant, being solely due to statistical noise.

1.8.3 The age distribution

In Figure 1.36 we present the measured age distribution and the same after correcting for the completeness $C(\tau)$, for the two families of PMS models, as we now describe. From the 2D completeness functions in the mass-age plane, we can now derive the overall completeness in ages. If $C(M,\tau)$ is the completeness function of mass and age, shown in Figure 1.35e,f, the completeness in ages $C(\tau)$ is just its projection normalized on the density in the mass-age plane:

$$C(\tau) = \frac{\int C(M,\tau)\cdot n(M,\tau)\ \mathrm{d}M}{\int n(M,\tau)\ \mathrm{d}M} = \frac{\int n_{\mathrm{sample}}(M,\tau)\ \mathrm{d}M}{\int n(M,\tau)\ \mathrm{d}M} \tag{1.10}$$

where $n(M,\tau)$ is the completeness-corrected density in the mass-age plane (Figure 1.35e,f) and $n_{\mathrm{sample}}(M,\tau)$ the measured one (Figure 1.35a,b).

The completeness correction does not influence significantly the average ages and the measured age spread; but increases the old age tail of the distributions. In the Siess et al. (2000) case the age distribution peaks at ~ 3 Myr, with a broadening of 0.3 dex while with Palla & Stahler (1999) the peak is at about 2 Myr with a higher broadening of 0.4 dex. However, the broader distribution of the latter in logarithmic scale vanishes in linear units, because of the younger average age. Within 1σ the age of the population spans from 2.5 to 5 Myr for Siess, and from 1.22 to 3.22 Myr for Palla & Stahler. Increasing the slope of the reddening law produces a modest shift toward younger ages ($\lesssim 0.1$ dex)because of the higher luminosities derived. As mentioned in the previous section, the observed age spread does not coincide with a real star formation history, because of the unknown uncertainties in the stellar luminosities. Therefore the distributions shown in Figure 1.36 represents the combined effect of the real age spread and the apparent spread originated by other effects that scatter the measured luminosities. The latter is mainly due to stellar variability and scattered light from circumstellar material, and is probably responsible for the 7–9% (respectively for Palla & Stahler and Siess models) of stars with a measured age exceeding 10 Myr, percentage that increases of $\sim 50\%$ when correcting for completeness. This fraction of old age sources is about 3-5 times higher than the upper limit for the residual contamination from non-members (see Section 1.7).

We stress that the sources of apparent luminosity scattering we have mentioned may be responsible for the tails of the age distribution, but we do not expect the overall width of the age distribution to be significantly overestimated. In particular, our age spread agrees

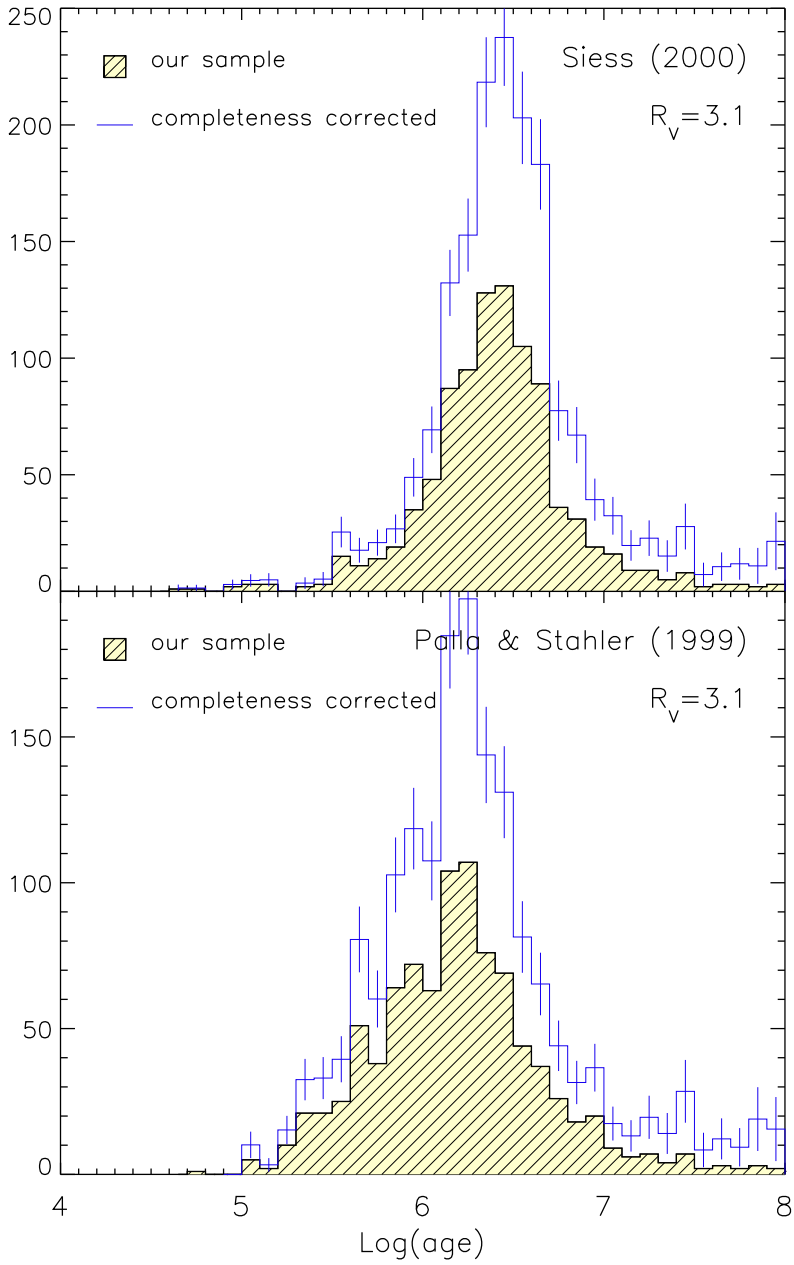

Figure 1.36 Age distribution for the ONC population. *Top panel:* ages derived using the Siess et al. (2000) evolutionary models; *bottom panel:* the same using Palla & Stahler (1999). The filled histograms show the distributions of ages in our sample. The open histograms are the same after correcting for incompleteness, and the statistical uncertainties are shown for each age bin.

with the one measured in the ONC by Jeffries (2007) by means of a statistical analysis of geometrically estimated radii - therefore immune of the effects of hidden binarity, variability, extinction uncertainties. This suggests that a real age spread is the main cause of the observed luminosity spread in the H-RD and that we have not significantly overestimated the width of the age distribution.

1.8.4 The mass function

The mass function (MF) of a system is defined as the number distribution of stars as a function of mass. While a general observational approach measures the so-called *present day mass function* (PDMF), a cornerstone for understanding how stars form is the *Initial Mass Function* (IMF), which is the mass distribution according to which stars are born. For a pre-main sequence population younger than the time required to produce a significant mass segregation, or to evolve the most massive stars into post-MS phase, the observed mass function coincides with the IMF.

The derivation of the IMF from observations always presents several sources of uncertainty, the main ones typically being unresolved companions and completeness. We can assess the completeness of our sample as a function of mass from the 2D completeness in an equivalent way as for the age completeness (eq. 1.10), projecting it on the mass scale:

$$C(M) = \frac{\int n_{\rm sample}(M,\tau)\ \mathrm{d}\tau}{\int n(M,\tau)\mathrm{d}\tau} \tag{1.11}$$

The results, computed for both evolutionary models, are presented in Figure 1.37. In the intermediate-mass regime both evolutionary models provide similar completeness, whereas for lower masses the Palla & Stahler models lead to a systematically lower completeness.

To derive the IMF of the ONC we count the number of stars in equally spaced bins 0.1 dex wide in $\log M$ and normalize the result to the bin width in order to express the IMF in terms of $\xi(M)$ instead of $\xi(\log M)$. We correct the star counts for completeness, interpolating the function shown in Figure 1.37 to the mass values of the IMF.

The two panels of Figure 1.38 show the IMF derived for both Siess and Palla & Stahler evolutionary models. In the same figure, the H97 IMF is overplotted, showing that it follows our distribution for intermediate- and low-mass stars ($M \gtrsim 0.4$ M$_\odot$). The Kroupa (2001) and Salpeter (1955) IMF are shown as well, evidencing the differences with our mass distributions. Specifically, Kroupa under-produces the observed low-mass population and

Table 1.8 Initial mass function for the ONC. //

	Siess		Palla & Stahler	
$\log(M/\mathrm{M}_\odot)$	$\log\xi(M)$	$\sigma\log\xi(M)$	$\log\xi(M)$	$\sigma\log\xi(M)$
-0.95	3.06	0.19	3.66	0.07
-0.85	3.49	0.09	3.81	0.05
-0.75	3.81	0.04	3.92	0.03
-0.65	3.72	0.04	3.48	0.05
-0.55	3.62	0.03	3.38	0.05
-0.45	3.45	0.03	3.30	0.04
-0.35	2.99	0.05	3.00	0.05
-0.25	2.82	0.05	2.83	0.05
-0.15	2.49	0.07	2.58	0.06
-0.05	2.36	0.07	2.29	0.08
0.05	2.07	0.09	2.13	0.08
0.15	1.95	0.09	1.99	0.09
0.25	1.91	0.09	1.84	0.09
0.35	1.59	0.11	1.40	0.14
0.45	1.12	0.19	0.43	0.53

does not exhibit the observed turn-over. Salpeter over-produces the observed number of low mass stars with the effect perhaps even larger than indicated due to the normalization in the mid-masses rather than the high mass end. Table 1.8 provides the value for $\xi(M)$ and the associated uncertainty for the two cases.

As we mentioned in Section 1.8.3, the luminosity spread we measure can be slightly overestimated due to physical and observational biases such as stellar variability, hidden binarity, scattered light, and uncertainties in the positioning of the members in the H-RD. However, since the evolutionary tracks in the H-RD are nearly vertical in the mass range we investigate, and given that, as mentioned, a true age spread is probably the dominant source of luminosity spread, we do not expect that our IMF is significantly affected by these biases.

The two sets of models produce significant differences in the IMF for low-mass stars, $\log(M) \lesssim 0.3\mathrm{M}_\odot$. For both models the IMF shows a flattening at low masses. This feature is real, given our accurate assessment of completeness. However, while for Palla & Stahler the change of slope from the general power-law is relatively modest and in agreement with the Kroupa mass distribution, the Siess model leads to a clear turn-over below 0.2 $\mathrm{M}_\odot$, compensated by an apparent overabundance of stars in the range $0.2\mathrm{M}_\odot < M < 0.3\mathrm{M}_\odot$.

Similar differences in the shape of the IMF below $0.2M_{\odot}$, due to differences between theoretical models, temperature scales and bolometric corrections, were also reported by Hillenbrand & Carpenter (2000).

We tested also the changes when R_V is increased (not shown in the Figure), finding that this does not introduce significant modifications in the shape of the IMF. This is not surprising, considering that the reddening law affects the luminosity of stars, shifting the point in the H-R diagram along the $y-$axis in proportion to the color excesses $E(V-I)$, whereas for most of the stars in this temperature and luminosity range the evolutionary tracks are nearly vertical.

With respect to the IMF presented by Muench et al. (2002), derived from a Monte Carlo best-fit to the observed $K-$band luminosity function, we confirm the power-law increase with slope similar to the $x = -1.35$ value of Salpeter (1955), for masses larger than $M \simeq 0.6$ $M_{\odot}$. However, the break they found at $M \simeq 0.6$ $M_{\odot}$ occurs in our case at lower masses, $M \simeq 0.3$ $M_{\odot}$ or less. This is consistent with the fact that there ONC members are known to present $K-$band excess due to circumstellar material, which biases the fluxes toward brighter values which are erroneously interpreted as higher masses than the underlying stars truly possess.

Thanks to the highest number of sources present in the subsample used to derive the IMF, as well as our completeness correction, we are able to constrain the position of the IMF peak at low stellar masses with a higher confidence than previous works. As discussed in Briceño (2008), the presence of a peak in the stellar distribution at spectral types ∼M3 (corresponding roughly with masses $M \sim 0.3M_{\odot}$) is measured for all the young populations of the Orion complex, suggesting a common origin for all these populations. On the contrary, other star forming regions such as Taurus and IC348 present IMFs increasing down to the hydrogen burning limit, and in the case of Taurus, showing evidences of stellar overabundance at $M \sim 0.6$–$0.8M_{\odot}$. According to our results, we confirm the presence of a peak in the very-low mass regime, but this is located lower masses, closer to $0.2M_{\odot}$.

In conclusion, our analysis shows that especially at the lowest stellar masses, and presumably also in the entire brown dwarf regime, the actual shape of the IMF depends strongly on the model assumptions. Our current understanding of the pre-main-sequence stellar evolution suffers from the lack of a general consensus on the best model to adopt. By combining accurate and simultaneous multicolor photometry with spectroscopy it is possible to derive critical information to constrain the models, as we have tried to show in this chapter. An extension of this analysis in the substellar mass range will be enabled by

the study of the HST ACS photometry (*Robberto et al., 2010, in preparation*) obtained for the HST Treasury Program on the Orion Nebula Cluster, to which this ground-based observational effort also belongs.

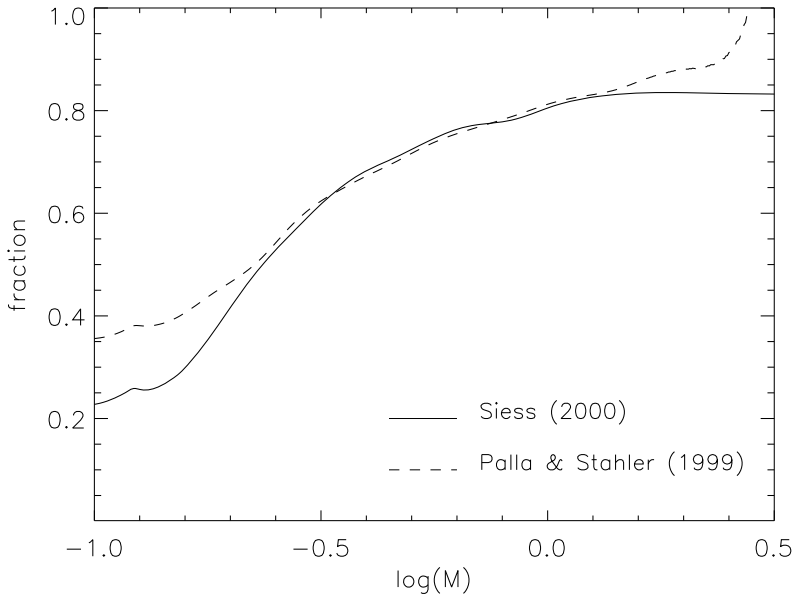

Figure 1.37 Completeness as a function of stellar mass computed for both evolutionary models.

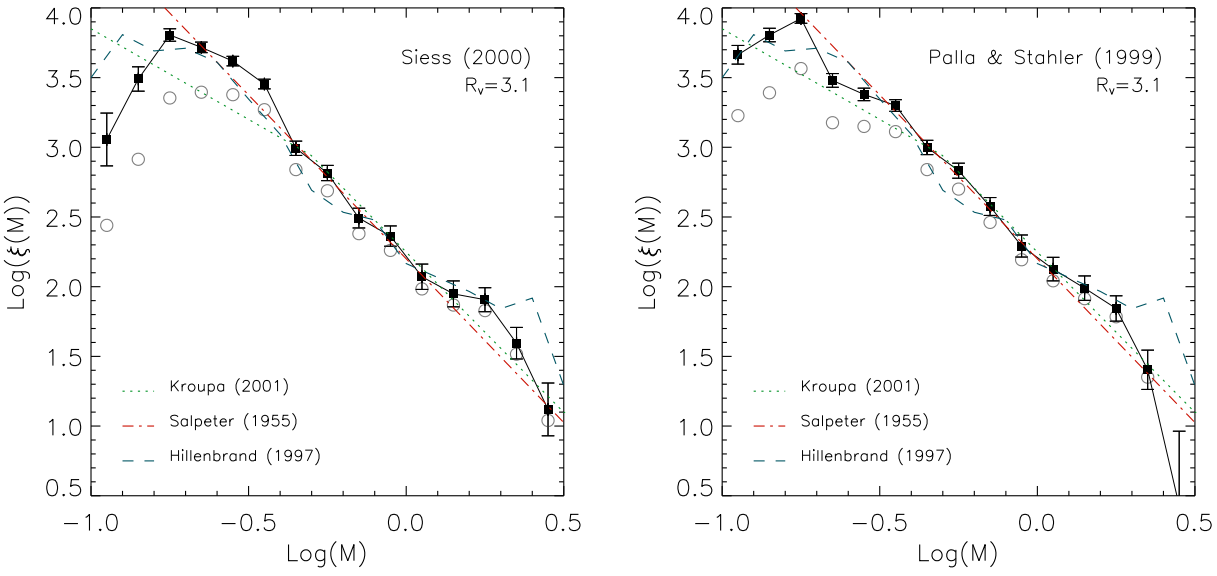

Figure 1.38 Completeness-corrected mass functions derived for the ONC (filled squares) according to the models of Siess et al. (2000) *(left panel)* and Palla & Stahler (1999) *(right panel)*. The open circles are the same without the completeness correction. Units are number of stars per solar mass (i.e., the counts have been normalized to the width of each bin in units solar masses). The mass function for the ONC derived in H97 is superimposed to highlight the differences in the low mass range. The Salpeter (1955) single power law IMF and the IMF of Kroupa (2001) are shown as well.

Part II

The Young Cluster LH 95 in the Large Magellanic Cloud

Chapter 2

The Complete IMF Down to the Subsolar Regime in the Large Magellanic Cloud with HST/ACS Observations[1]

2.1 Introduction

The study of the low-mass populations young stellar associations of the Magellanic Clouds provides important improvements in the understanding extragalactic star formation. The investigation of the star formation processes, and the Initial Mass Function (IMF), together with the time dependency of the formation events, are key points in the characterization of stellar populations in any kind of concentrations, from small clusters to entire galaxies.

Regarding the IMF, several studies have been carried out in the past for the Galaxy (e.g. Salpeter, 1955; Scalo, 1986; Kroupa, 2001; Chabrier, 2003), describing the initial numbers of massive stars ($M \gtrsim 8$ M$_\odot$), stars of intermediate mass (1 M$_\odot \lesssim M \lesssim$ 8 M$_\odot$), low-mass stars (0.08 M$_\odot \lesssim M \lesssim 1$ M$_\odot$) and brown dwarfs ($M \lesssim 0.08$ M$_\odot$). The findings of such investigations support the hypothesis of the universality of the IMF, in the sense that the average IMF measured in a diversity of galactic systems does not show noticeable variations (Kroupa, 2002). This statement turns out to be rather certain for the intermediate- and high-mass stars, while for low-mass stars there could be a dependence of the IMF slope on metallicity, in the sense that metal-rich environments tend to produce more low-mass stars than metal-poor systems (Piotto & Zoccali, 1999; Reylé & Robin,

[1]**The research presented in this chapter has been published, as a refereed paper, in Da Rio et al. (2009a)**

2001), although several IMF measurements are needed to confirm such a systematic effect. In low-mass studies there are several uncertainties present. For example the study of the IMF in metal-poor galactic globular clusters (Piotto & Zoccali, 1999) is significantly limited by the corrections for dynamical evolution effects. Specifically, phenomena such as mass segregation and unknown binarity fraction change dramatically the presently measured mass distribution with respect to the one at the time of the formation of these systems (Marks et al., 2008).

Under these circumstances, ideal environments for the search of a metallicity dependence of the IMF are the Magellanic Clouds. Their stellar populations are characterized by metallicities of $[Fe/H] \simeq 2.5$ to 5 times lower than in the disk of the Milky Way (Luck et al., 1998), but have a similar star formation rate (SFR) (Westerlund, 1997). Furthermore, the low metal abundances of the Magellanic Clouds suggest that their environments − as well as in other galaxies of the Local Group − are closer to the ones at the early ages of the universe, when the peak of star formation occurred ($z \simeq 1.5$, Pei et al., 1999). Moreover, the lower dust-to-gas ratio in the Magellanic Clouds (Koornneef, 1982; Bouchet et al., 1985), in comparison with the Milky Way, assures a lower extinction, reducing the bias introduced by differential reddening, a well known limitation in the study of young stellar populations.

Most of the star formation occurs in dense cores of Giant Molecular Clouds, where one or more large stellar concentrations, known as OB associations (Ambartsumian , 1947), are formed. However, most of the star formation studies in the Milky Way are carried out in smaller fields, like the young Taurus, Lupus and Chamaeleon star-forming regions. Although it has been shown that galactic OB associations host populations of faint, low-mass PMS stars (Preibisch et al., 2002; Sherry et al., 2004; Briceño et al., 2007) their analysis is strongly limited by the contamination of background and foreground evolved populations, requiring detailed measurements of proper motions, time-consuming spectroscopy and multiepoch photometry to define their membership. On the other hand, the study of OB associations in the LMC is less subject to contamination by field populations, due to the limited distance spread (Caldwell & Coulson, 1986; Cole, 1998). However, in order to identify the faint red PMS stellar component of LMC associations, photometry with instruments of high sensitivity and angular resolution is required, due to the larger distance from us.

Recent findings from the *Hubble Space Telescope* (HST) confirm the presence of PMS stars in OB associations of the Magellanic Clouds. Gouliermis et al. (2006a) studied this

case in the LMC association LH 52, using WFPC2 observations in the V- and I-equivalent bands, and they discovered a population of objects in the color-magnitude diagram (CMD) consistent with T-Tauri stars. Subsequently, the *Advanced Camera for Surveys* (ACS) has been used to perform similar studies in other associations of the Magellanic Clouds, such as NGC 346 (Nota et al., 2006; Gouliermis et al., 2006b; Hennekemper et al., 2008; Sabbi et al., 2008) and NGC 602 (Schmalzl et al., 2008) in the Small Magellanic Cloud (SMC). However, these studies could not characterize the subsolar mass function, because of the insufficient detection of such stars.

In a recent paper (Gouliermis et al., 2007) ACS observations enabled one to discover a rich population of PMS stars in the star-forming region LH 95 in the LMC In this chapter, based on those data, we focus on the IMF of these stars, which is reliable for masses down to about 0.3 $M_{\odot}$, considering that our photometry allowed to perform precise completeness corrections for stars with masses down to this limit. In Section 2.2 we describe our photometry and the completeness of our data. In Section 2.3 we apply the decontamination of the observed stellar sample in the area of the association LH 95 from the contribution of the general LMC field for the identification of the stellar members of the system. We also investigate the spatial distribution of the identified pre-main sequence population, in order to define the limits of the main body of the system, and we apply extinction measurements. We make use of evolutionary models in combination with our photometry for the construction of the system IMF of LH 95 in Section 2.5. We discuss our findings in Section 2.6.

2.2 Photometry

In this study we analyze the photometry presented in Gouliermis et al. (2007), derived from deep observations with the Wide-Field Channel (WFC) of ACS onboard *HST* within the GO Program 10566 (PI: D. Gouliermis). Two pointings were observed, one centered on the association LH 95 itself, which we refer to as the "system", and another one about $2'$ to the west on an empty area, typical of the local LMC field. We refer to the latter as the "field". For each pointing observations in two photometric bands were available: F555W and F814W, roughly equivalent to the Johnson V and Cousins I bands respectively. The observations and their photometry are described in detail in Gouliermis et al. (2007). We found about 16000 stars in the system, about 2600 of which lie in the PMS region of the CMD, and about 17000 in the field.

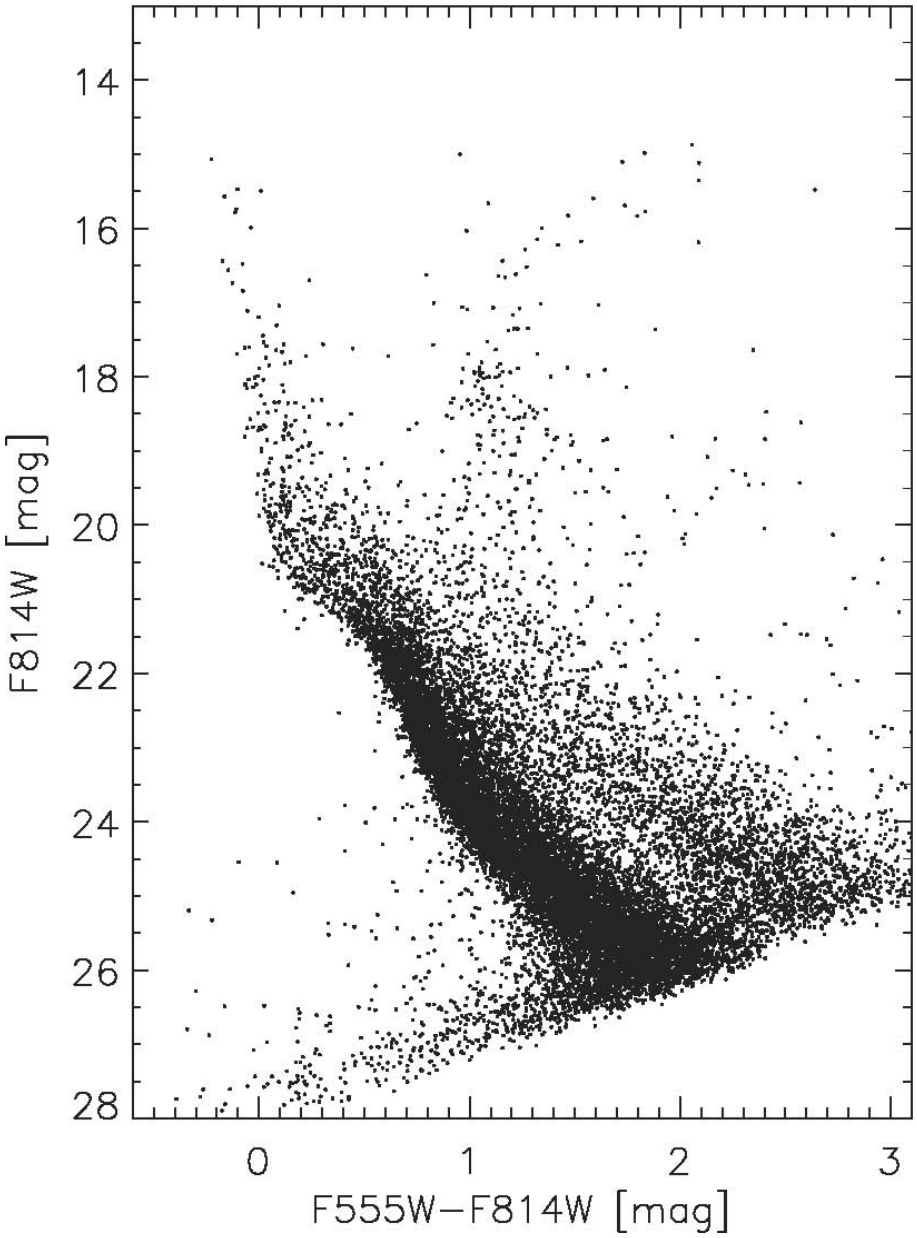

Figure 2.1 $F555W - F814W$, $F814W$ Color-Magnitude Diagram of the entire LH 95 region, according to the updated photometric catalog, which includes about 900 stars more, recovered by visual inspection of the sources rejected in the photometric study of Gouliermis et al. (2007). It is worth noting that, besides a dense main-sequence population, this CMD is characterized by a remarkable number of PMS stars at faint magnitudes and red colors, as indicated in Gouliermis et al. (2007).

Table 2.1. Sample from the photometric catalog of all stars found in the region of LH 95 with HST/ACS imaging

#	R.A. (J2000.0)	DECL. (J2000.0)	$F555W$ (mag)	σ_{555} (mag)	$F814W$ (mag)	σ_{814} (mag)
1	05 37 06.04	−66 21 37.15	14.839	0.001	15.066	0.001
2	05 37 19.26	−66 21 07.88	15.956	0.001	15.001	0.001
3	05 36 59.26	−66 21 20.66	15.406	0.001	15.570	0.001
4	05 37 15.12	−66 21 44.39	15.503	0.001	15.494	0.001
5	05 37 05.62	−66 21 35.39	15.372	0.001	15.473	0.001
6	05 36 49.60	−66 23 26.16	16.930	0.003	14.873	0.001
7	05 37 05.53	−66 21 59.65	15.632	0.001	15.740	0.001
8	05 37 04.53	−66 22 01.02	15.670	0.001	15.783	0.002
9	05 37 14.29	−66 22 52.00	15.951	0.001	15.990	0.001
10	05 36 56.68	−66 21 10.40	16.828	0.001	15.102	0.001
11	05 36 53.49	−66 21 55.55	17.183	0.002	15.595	0.001
12	05 36 59.67	−66 22 02.10	16.813	0.001	14.982	0.001
13	05 37 01.86	−66 22 35.65	16.752	0.002	15.663	0.001
14	05 36 57.29	−66 21 49.03	16.267	0.001	16.440	0.001
15	05 36 53.06	−66 22 11.28	16.610	0.001	16.736	0.002
...	...	...	...	...	...	...

Note. — Magnitudes are given in the Vega system. Units of right ascension are hours, minutes, and seconds, and units of declination are degrees, arcminutes, and arcseconds. The spatial resolution of the ACS/WFC is $0.05''$.

In this work we enhance the photometric catalog of stars derived in Gouliermis et al. (2007) by searching for eventually missing objects, especially in the low-mass PMS regime. Photometry was obtained using the ACS module of the package DOLPHOT[2] (Ver. 1.0). The selection of stars in our original photometry was based on the quality parameters estimated for each detected source by the package. However, objects which are actual stars may have been rejected as spurious detections in crowded regions, especially in the presence of a non-uniform background due to nebular emission, as well as in the neighborhood of very bright sources. Therefore, we considered the catalog with all the rejected sources and we performed a visual inspection of each of them on the original ACS FITS images constructed with `Multidrizzle`. With this process we recovered about 900 additional stars. The updated photometric catalog of the association LH 95 includes in total 17,245 stars. A sample of this catalog is shown in Table 2.1. The corresponding CMD is shown in Fig. 2.1. Typical uncertainties of our photometry as a function of the magnitude for both filters are given in Figure 2.2 (left), for both the "system" and the "field" ACS pointings.

2.2.1 Completeness

The completeness of the data is evaluated by artificial star experiments with the use of lists of almost 400,000 artificial stars created with the utility *acsfakelist* of DOLPHOT for each of the observed areas of the system and the field. This utility enables to add stars of given magnitudes to all the frames simultaneously, searching for a detection in none, one, or both photometric bands. In this way it is possible to derive automatically a 2-dimensional completeness function for both color ($F555W - F814W$) and magnitude $F555W$ or $F814W$. Considering that at any given faint magnitude in one band the color term covers a range of up to 2 mag, as shown in the CMD of Figure 2.1, allowing the magnitude in the other band and therefore the completeness to vary significantly, this two-dimensional approach is necessary for an accurate treatment of the completeness of our data. Therefore, we define with our artificial star technique the 2D completeness as a function of ($F555W - F814W$) and $F814W$, by computing the ratio of the detected sources over the total added stars in a grid of equally spaced bins 0.25 mag wide in ($F555W - F814W$) and and 0.5 mag in $F814W$.

Such completeness maps have been constructed for both the system and the field,

[2]DOLPHOT is an adaptation of the photometry package `HSTphot` (Dolphin, 2000). The software and its documentation can be obtained from `http://purcell.as.arizona.edu/dolphot/`.

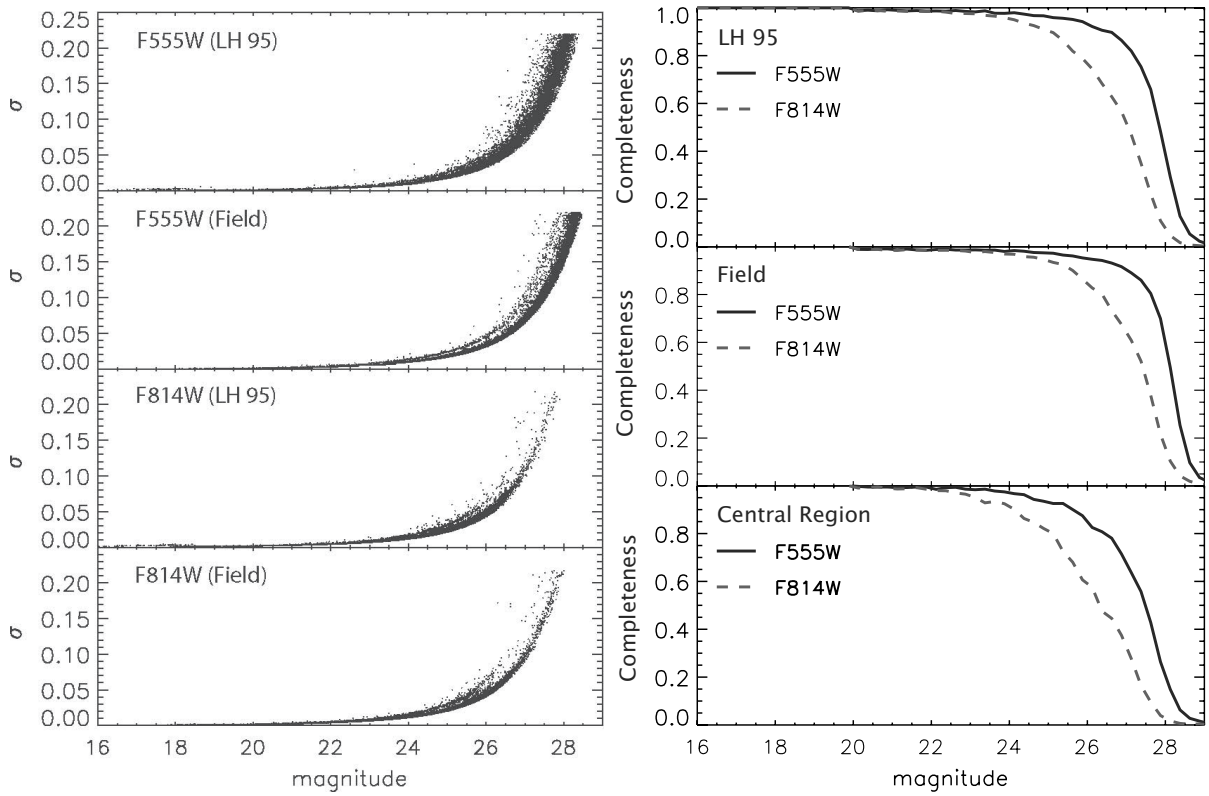

Figure 2.2 *Left panel*: distribution of the photometric errors, for both the F555W and F814W band for the LH95 system and the LMC field. *Right panel*: completeness of our photometry in the entire observed areas of both the system (top) and the field (middle), as well as for the *central region* of the association LH 95 (see Section 2.3.2).

enabling, via interpolation, an accurate determination of the actual completeness at any given point of the CMD. The right panel of Figure 2.2 shows the completeness function in both bands for both the system and the field (top and middle respectively). The completeness is found to vary with location, and therefore different regions in the observed field of view are characterized by different completeness functions according to their crowding. In the bottom panel of the figure we show the completeness as a function of magnitude for the central region of the association, as it is defined in Section 2.3.2. It is remarkably lower than that in the entire field of view, due to higher crowding of faint stars and overdensity of the bright ones.

To avoid further contamination by spurious objects in our catalog, which could have been included through additional stars, we trimmed the data set used in this work excluding sources with $V > 28.5$ mag or $I > 28$ mag. At these magnitude limits stars are faint enough to be well below any reasonable completeness limit. The completeness in the "system" CMD at V=28.5 mag and I=28 mag is less than 1%. Consequently, their

removal does not affect the quality and completeness of our data.

2.3 The Pre-Main Sequence Population of LH 95

2.3.1 Field subtraction

The observed stellar population in the area of the association LH 95 is naturally contaminated by the general field population of LMC. Therefore, in order to study the stellar members of the association alone, and in particular its PMS stars, the field contamination should be removed. In our case, having at our disposal photometry in only two bands, the possibility to distinguish if a given star is a true member or not is limited, but a statistical approach can provide accurate results.

We use a Monte Carlo technique, which considers that a star belongs to the cluster or the field with a probability, which depends on the local density in the same part of each CMD (of system and field). In order to maximize the statistical accuracy of the result, two iterations are applied. First, the field subtraction is applied to the entire observed field of view centered on the system, enabling to study the spatial distribution of the LH 95 stars and to isolate the boundaries of the association. After that, the study is limited on this subregion of the frame, and another field subtraction is carried out on the central region providing an accurate estimate of the membership of the sources included.

Specifically, for the first iteration we consider each star in the catalog of the system and we select an elliptical region in the CMD of the system centered on the position of this star, and the same region in the CMD of the field. Each such region is being chosen with semi-axes $\Delta I = 0.5$ mag and $\Delta(V-I) = 0.17$ mag. This particular size has been chosen as to be wide enough to include a considerable number of stars, and still small enough to achieve a considerably high resolution in the resulting CMD. We compute the probability of each star in the area of the system to belong to the field as:

$$P = A \cdot \frac{N_{\rm fld}}{N_{\rm sys}} \cdot \frac{C_{\rm sys}}{C_{\rm fld}} \tag{2.1}$$

where $N_{\rm sys}$ and $N_{\rm fld}$ are the numbers of stars included in the elliptical region of the CMD of the system and the field respectively. $C_{\rm sys}$ and $C_{\rm fld}$ are the completeness factors, for system and field, measured for exact position of the considered star in the CMD, as explained in Section 2.2.1. A is a normalization factor which takes into account differences in the field stellar density between the two regions. From repeating measurements in different parts of the area of the field and that of the system we found that on average the field includes

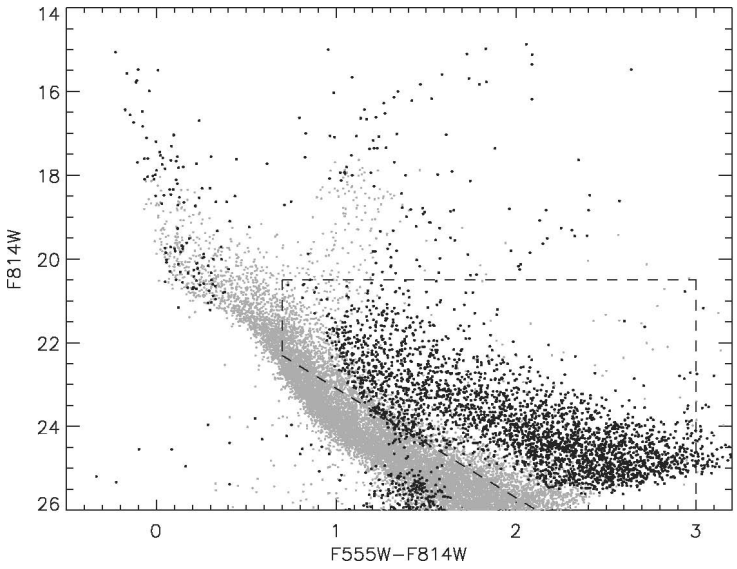

Figure 2.3 $F555W - F814W$, $F814W$ Color-Magnitude Diagram (CMD) of the entire observed area around LH 95. The stars which are identified as members of the system alone and not of the field of the LMC based on the first field-subtraction iteration (see Section 2.3.1) are plotted with thick symbols. The dashed line sets the limits of the loci in the CMD of the PMS alone. The spatial distribution of these stars has revealed the existence of young stellar subgroups within the association (Gouliermis et al. (2007); see also Section 2.3.2).

systematically ~ 1.3 times more main sequence stars than LH 95. Therefore, considering that both areas cover equal surfaces, we set $A = 0.77$. According to Eq. 2.1, when $P \geq 1$ the star is considered to be a field star and it is removed; $P = 0$ means that there are no field stars in the field CMD in the elliptical neighborhood of the star and therefore it is considered a member of the association. When $0 < P < 1$ the star is randomly kept or rejected as a member star with a probability equal to P.

The result of the first field-subtraction iteration, applied to the entire LH 95 field of view is shown in Fig. 2.3, where stars flagged to belong to the association are plotted by black dots. As shown in Gouliermis et al. (2007), it is evident that the PMS population belongs entirely to LH 95, while all lower main sequence stars turn out to belong to the LMC field. The upper main sequence (UMS) shows an overabundance of stars in the area of the system, demonstrating the presence of the corresponding population in the association itself.

2.3.2 Topography of the PMS Stars

In this section we study the spatial distribution of the PMS stars in the area of LH 95, as an indication of the places where star formation occurs. For this purpose, we construct surface density maps of the whole area by counting the stars identified as system members after applying the Monte Carlo removal of the field contamination as described in Section 2.3.1. Since we are interested in the PMS cluster properties, we considered only the PMS population, as selected in the region of the CMD shown in Figure 2.3.

The star counts are performed by dividing the whole ACS field of view into a grid of 50×50 elements, each corresponding to a size of ~ 85 pixels ($\simeq$ 1pc), and by counting the (field-subtracted) PMS stars in each of them. The selection of the specific grid-element size, which corresponds to the "resolving efficiency" of the detection of stellar concentrations, was chosen, after several experiments, as the most appropriate for revealing the smallest concentrations with a physical meaning.

In order to remove from this map eventual noise, we applied a smoothing on the density map with a kernel of size $\sim$ 2.5pc $\simeq$ 200 pixels. The majority of the PMS stars is found to be located within a compact region $\sim 1' \times 2'$, with a density well above the threshold of 3σ, where σ is the standard deviation of the background surface density. The derived two-dimensional density map is shown in Figure 2.4 (left), where the 3σ density limit, corresponding to the first (lower) isopleth, is chosen to define the statistically significant concentration of the PMS population of the association LH 95.

From here on, we refer to the region confined by the 3σ density isopleth of Figure 2.4 as the *central region* of LH 95, and we focus our subsequent analysis on the stellar population included within the boundaries of this region, as the most representative of LH 95. In Figure 2.4 (left) can be seen that within the central region there are smaller substructures characterized by a higher projected density of PMS stars. We select the three most prominent ones, isolating circular areas within the central region as shown in Figure 2.4 (right). We refer to these substructures as *subcluster A*, *B* and *C* respectively. The positions and sizes of the selected circular regions around the subclusters, shown in Figure 2.4 (right), are given in Table 2.2 with those for the whole central region. We measure the total mass, $M_{\rm tot}$, included in each stellar concentration, assuming that all systems follow a mass function similar to the standard Galactic field IMF (Kroupa, 2002), and extrapolating their stellar content down to 0.08 $M_\odot$. We then estimate the stellar density, ϱ, and the disruption time, $t_{\rm d}$, of each cluster following the method by Gouliermis

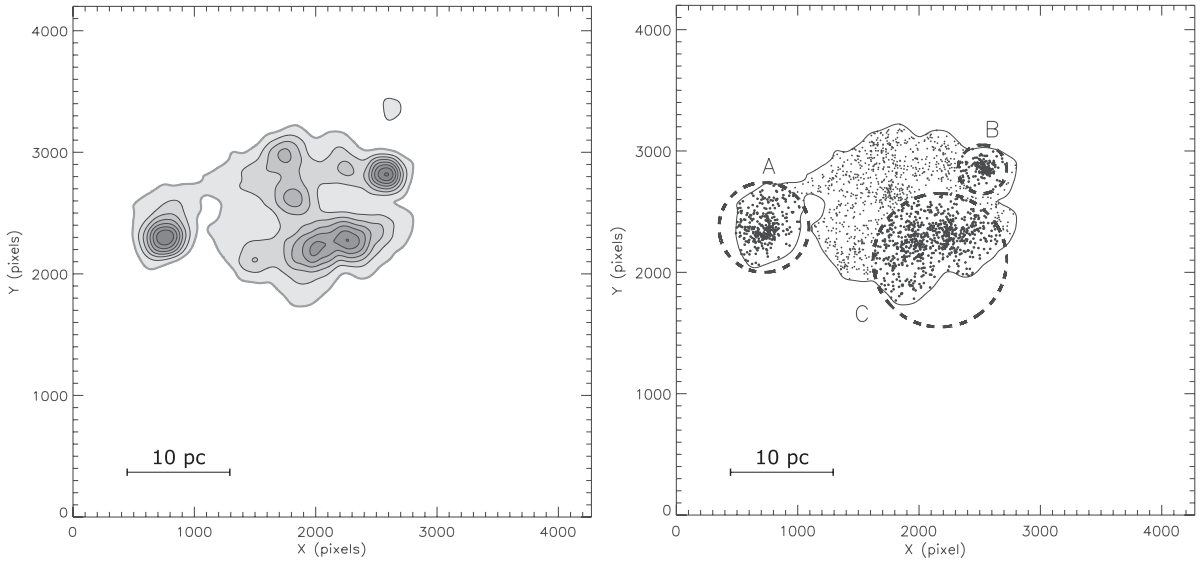

Figure 2.4 *Left panel:* Isodensity contour map of the area of the system constructed from star counts of the PMS stars alone. Isopleths are drawn in steps of 1σ, where σ corresponds to the standard deviation of the background density, starting from the 3σ level. This level defines the limits chosen for the selection of the stars used for the construction of the CMD of the central part of the area of the system shown in Figure 2.5 (left and right panels). This map demonstrates that, as we found in Gouliermis et al. (2007), PMS stars are concentrated in few compact subgroups within the association. These density peaks in the PMS stars coincide with those of the Upper Main Sequence (UMS) stars (Gouliermis et al., 2007), suggesting that these subgroups contain fully populated IMFs. Units are in pixels on the ACS drizzled frame. *Right panel:* Positions of the three most prominent concentrations (subclusters) of PMS stars, which appear as the densest substructures of the main part of the association LH 95.

et al. (2002, their section 6). The latter is given as (Spitzer, 1958):

$$t_{\rm d} = 1.9 \times 10^8 \varrho \left(\frac{\rm M_\odot}{\rm pc^3} \right) \ \ \text{years} \ . \tag{2.2}$$

Moreover, the dynamical status of a stellar system is defined by two additional timescales, the *crossing* and the *two-body relaxation* time (Kroupa, 2008), which are given as:

$$t_{\rm cr} \equiv \frac{2r_{\rm \,h}}{\sigma} \quad \text{and} \quad t_{\rm relax} = 0.1 \frac{N}{\ln N} t_{\rm \,cr} \tag{2.3}$$

respectively. The three-dimensional velocity dispersion of the stars in the cluster, σ, is given as

$$\sigma = \sqrt{\frac{\rm G M_{\,tot}}{\epsilon r_{\rm h}}} \ , \tag{2.4}$$

where ϵ is the star formation efficiency (SFE) and $r_{\rm h}$ the half-mass radius of the cluster.

Table 2.2 Characteristics of the *Central Region* (LH 95) and its three subclusters

	RA (J2000.0)	DEC (J2000.0)	Size (pc)	$r_{\rm h}$ (pc)	$M_{\rm tot}$ (10^3 $M_\odot$)	ϱ ($M_\odot$ pc^{-3})	$t_{\rm d}$ (100 Myr)	$t_{\rm cr}$ (Myr)	$t_{\rm relax}$ (Myr)
LH 95	5 37 06.50	−66 22 03.50	33.5	6.5	2.37	0.47	0.9	6.4	433.0
A	5 37 15.25	−66 21 40.87	8.7	1.7	0.33	1.28	2.4	2.2	26.9
B	5 36 59.78	−66 21 36.88	4.7	0.8	0.19	2.70	5.1	0.9	6.7
C	5 37 03.96	−66 22 09.73	12.9	3.0	0.98	1.11	2.1	3.1	95.5

In order to make a rough estimation of the aforementioned timescales for the subclusters and the whole central region of LH 95, we apply the formulas of Eq. 2.3.

The SFE in several nearby Galactic gas-embedded clusters has been found to range typically from 10% to 30% (Lada & Lada, 2003) or 20% to 40% (Kroupa, 2008), value which increases with time while the gas is removed. However, the average age of the system is 4 Myr (see §2.5), slightly greater than the typical time necessary to remove most of the gas (Lada & Lada, 2003). Therefore, and taking into account the very low optical extinction (see §2.3.2), LH 95 should be considered as an emerging cluster, meaning that it should be at the process of separation from the parental cloud. Furthermore, according to Wilking & Lada (1983), a high SFE is required for a bound young cluster to emerge from its parental cloud. As a consequence, we consider a value of $\epsilon \simeq 0.4$ as more adequate for our system. We derive, thus, values of σ of the order of 2 km s^{-1} for our objects and we provide the additional estimated structural parameters for each system also in Table 2.2. We find that the crossing time for the whole region is greater than the age of the system, and this is quite consistent with the observed subclustering of the system.

From a comparison between the characteristics of the subclusters and the central region, as they are given in Table 2.2, one can see that there is a significant fraction of mass outside the immediate regions of the subclusters. This can also be seen in the maps of Figure 2.4, where a prominent population of PMS stars is easily distinguished away from the subclusters, spread in the area among them within the central region. We estimate that the fraction of *distributed* stellar mass over the total corresponds to $\sim 40\%$, with the remaining 60% being *clustered*. This fraction of distributed PMS stars in LH 95 is consistent with statistical analysis of several Galactic nearby star-forming regions that predict $\lesssim 60\%$ (see review by Allen et al., 2007). However, it is not clear if this distributed population is the result of the star formation or a merging process. Detailed simulations do predict that subclusters may merge to form a larger one (e.g. Fellhauer et al., 2006), but our data do not allow us to verify if this takes place in LH 95. In any case, the stellar density and disruption time of all considered systems, including

the whole central region, show that all are rather compact and none of them is under disruption. Subclusters A and B, located at the east and west of the central region, are particularly compact and roughly spherical shaped, while subcluster C, close to the southern limit of the central region, presents a more elongated and extended distribution of PMS stars. This subcluster corresponds to the visibly prominent main part of the association (see Figure 1 in Gouliermis et al. 2007).

2.3.3 LH 95 Central region

For the detailed study of the PMS population in LH 95, while minimizing the contamination by other stars, we focus on the central region of the system. Specifically, we consider the entire population included in the central region and we apply, for a second time, the Monte Carlo technique for field subtraction, taking into account the ratio between the surface of the observed LMC field and that of the *central region*.

It should be noted that this second application of the field subtraction technique to the central region is not equivalent of simply isolating the stars, which are found to be located within the boundaries of the region after the first iteration of the Monte Carlo subtraction.

Naturally, the central region has a higher density of system stars (specifically PMS stars), and therefore a lower relative contamination by field stars. Consequently, the actual fraction of stars which are marked to be field stars is lower, reducing the probability of (statistically probable) wrong membership assignments. The number of field stars included in the elliptical region of the CMD $N_{\rm fld}$ is computed based on the photometry in the entire field and scaled according to the area occupied by the LH 95 central region, which we found to be $\sim$ 12.6% of the total ACS field of view.

The result is shown in Figure 2.5, where we plot the CMDs of the whole population included within the boundaries of the central region (left panel), the one of the whole area of the field, sampled randomly and downscaled according to the area coverage of the central region (central panel), and the corresponding CMD of the central region after the field contribution has been removed (right panel). From this figure it is evident that the observed stellar population of the low main sequence (LMS) can be entirely considered as field population. On the other hand the association has a prominent upper main sequence (UMS) component, and all pre-main sequence stars, easily distinguished by redder colors, are solely present in LH 95 alone. Furthermore, the second application of our

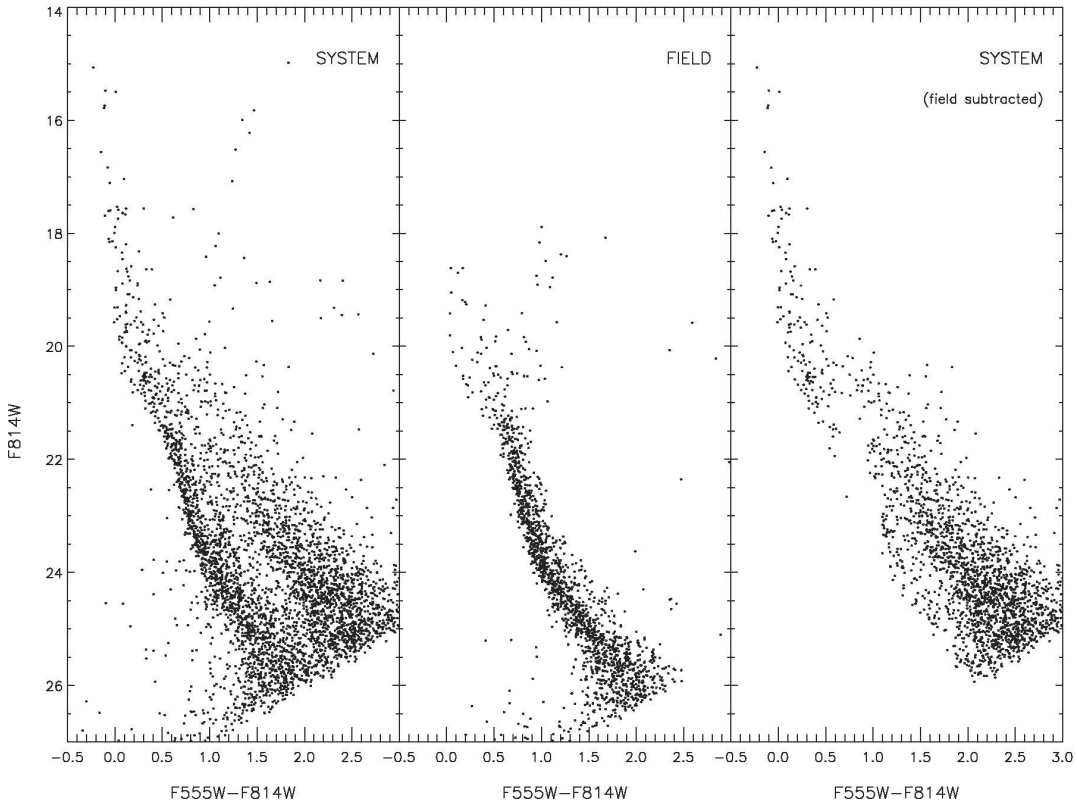

Figure 2.5 Left: CMD of all stars observed in the central part of the area of the system. This part was selected as the most representative of the association based on star counts (§ 3.2; Figure 2.4). Middle: CMD of the corresponding part of the area of the field, which was used for the decontamination of the CMD of the system from the contribution of the field stellar population. Right: CMD of central area of the system after the field subtraction was applied with the use of an advanced Monte Carlo method (§ 3.1). This CMD highlights the UMS and PMS stars as the prominent stellar populations of the association LH 95, demonstrating its youthfulness.

field subtraction technique, limited to the central region, allows us to reduce considerably the contamination by objects not located in the PMS and UMS parts of the CMD, which are still present as residuals from the first application of the method on the entire field of view (Figure 2.3).

In the CMDs of Figure 2.5 can be noted that the field population has a tighter sequence than the PMS population, which may indicate an age-spread among the PMS stars of LH 95 (see also Figure 2.7). Indeed, the locations of low-mass PMS stars in the CMD of young stellar systems of our Galaxy often show a widening, which may be evidence for an age-spread in the system (e.g. Palla & Stahler, 2000). However, several characteristics

of these PMS stars (being T Tauri stars), such as variability and circumstellar extinction, can cause considerable deviations of their positions in the CMD (Sherry et al., 2004), which may be misinterpreted as an age-spread. As a consequence, detailed simulations of the characteristics of PMS stars are required to quantify the effect of these characteristics on their positions in the CMD and to conclude on any true age-spread (Hennekemper et al., 2008) with the use of population-synthesis techniques.

In the following sections we focus our study on the isolated, field subtracted population in the LH 95 central region, shown in Figure 2.5 (right).

2.3.4 Interstellar Extinction

With photometry available only in two bands it is not possible in general to measure the visual extinction A_V independently for every star of the system. It is, however, possible to perform a statistical approximation obtaining the average value of reddening as well as its distribution. For this purpose we consider the UMS stars ($I \leq 20.0$ mag) in the central part of LH 95, after performing field subtraction, and we compare the position observed in the CMD to that expected according to the Padova grid of evolutionary models in the ACS photometric system (Girardi et al., 2002). Considering that LH 95 is a very young association ($\tau \lesssim 10$ Myr) we assume that all UMS stars have a age equal to the youngest available isochrone in the Padova models, $\log \tau = 6.6$ for a metallicity of $Z = 0.008$ (typical value for the LMC; Kontizas et al. 1993) and distance modulus $m - M = 18.41$ mag, compatible with several distance measurements for the LMC, available in the literature (e.g. Alcock et al. (2004)).

For every star we compute the intersection between the reddening vector and the isochrone, and we obtain, thus, the reddening value in terms of $E(F555W - F814W)$. Since the ACS photometric system is slightly different from the standard Johnson-Cousins system, we compute the exact reddening parameters for our ACS bands using the typical galactic extinction law of Cardelli et al. (1989), parameterized by a value of $R_V = A_V/E(B-V) = 3.1$. We consider a set of template spectra taken from the NextGen catalog (Hauschildt et al., 1999), and we apply the extinction curve with an arbitrary A_V which we choose to be equal to 1, and we measure the extinction A_{F555W} and A_{F814W} by means of integration of the original and reddened spectra within the ACS filter profiles. In this way we compute $R_{F555W} = A_{F555W}/E(F555W - F814W) \simeq 2.18$ and $R_{F814W} = A_{F814W}/E(F555W - F814W) \simeq 1.18$.

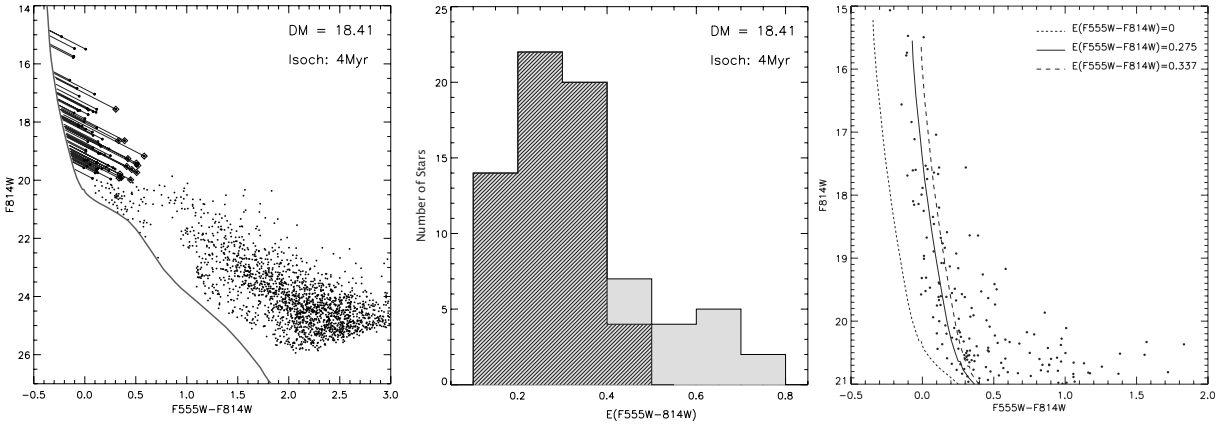

Figure 2.6 Determination of the reddening in the region of LH 95. *Left:* The field subtracted stellar population within the central area of LH 95 with the isochrone model for $\log_{10}\tau = 6.6$ and the corresponding individual reddening vectors of the upper main sequence stars overlayed. Square symbols represent objects with $(V-I) > 0.3$ mag, which may be considered as candidate Herbig Ae/Be stars, due to their highly reddened colors. *Middle*: Distributions of the measured reddening for all UMS stars (filled histogram) and excluding candidate Herbig Ae/Be (darker histogram). *Right*: UMS CMD showing the Girardi et al. (2002) isochrone for $E(F555W-F814W) = 0$ and with the mean reddening from the distributions shown in the central panel applied.

The derived reddening distribution, shown in Figure 2.6 (*middle*), appears to have a tail extended to higher values (filled histogram). This tail appears due to a number of UMS objects, which show a high color excesses. Taking into account all objects, including the ones with high color excess, the average reddening has a value $E(F555W-F814W) \simeq 0.34$ mag, corresponding to an optical extinction of $A_V = 1.56$. However, these red objects are being suggested to be Herbig Ae/Be (HAeBe) stars (Gouliermis et al., 2002). Such stars of intermediate mass, aged between 1 and 10 Myr, occupy the faint end of the UMS with $17.5 < F814W < 20$ mag. Being in their pre-main sequence phase, they have an intrinsic color higher than that of MS stars in the same luminosity range. Consequently, if indeed these are not MS but HAeBe stars, which is possible due to the youthfulness of the system, then the derived reddening would be biased toward higher values.

We estimate the mean reddening without considering these stars (darker histogram in Figure 2.6 - *middle*) and we derived a lower mean value of $E(F555W - F814W) \simeq 0.275$ mag, corresponding to an optical extinction of $A_V = 0.6$ mag. In Figure 2.6 (*right*) both values are applied to the 4 Myr isochrone model (the youngest available in the grid of models by the Padova Group). From this figure it is evident that the difference between the two values is not dramatic, producing more or less the same shift of the model in the

CMD. As a consequence, and in order to avoid any biases due to the presence of young stellar objects in LH 95, we consider an optical reddening of $E(F555W - F814W) \simeq 0.3$ mag as the most representative for the region. We repeated the construction of the reddening distributions shown in Figure 2.6 (middle) and the determination of the mean reddening values using different isochrones, spanning an age range between 4 and 7 Myr and assuming different distances varying by 0.2 mag around the assumed distance modulus. We found that the mean reddening remains practically unchanged within 0.02 mag, a difference small enough to confirm the accuracy of our estimation.

2.4 The PMS models

In the last decades several theoretical models for the pre-main sequence stellar evolution have been computed. Some of the most popular, for PMS masses above the hydrogen burning limit, are the models of Siess et al. (2000), Palla & Stahler (1999), D'Antona & Mazzitelli (1994, 1997) and Swenson et al. (1994). These models are generally expressed in terms of physical quantities, such as the effective temperature and the total bolometric luminosity, describing the evolution of stars in the HR diagram. However, one of the primary aims of stellar evolution theory is the explanation of the observed photometric data of stars in order to extract their masses and ages from their magnitudes and colors, and therefore a conversion between physical and observable quantities of the models is required. Such a conversion is specifically described by Siess et al. (2000), who include the transformation between $T_{\rm eff}$ and L to colors and magnitudes in the $UBVRI$ Cousins system and $JHKL$ infrared bands for their models based on empirical transformation valid for MS dwarfs.

As we have shown in Chapter 1, these transformations are incorrect for young stars, due to their different surface gravity than that of MS stars. We have also shown how magnitude and colors computed from synthetic photometry show a better agreement with the data for low mass PMS stars in Orion, although the atmosphere models present some uncertainties for cool, young stars. In the case of LH 95, since the association is older than the Orion Nebula Cluster (see Figure 2.7), the surface gravity of its members is closer to that of MS stars. Moreover, our photometry does not reach masses as low as for the ONC data described in Chapter 1. As a consequence, the inaccuracy of the atmosphere models we have already discussed will not affect significantly our results for LH 95. Thus, we use synthetic photometry to convert evolutionary models from the theoretical to the

observational plane, in order to derive the stellar parameters of the LH 95 members.

Among the different families of evolutionary models for intermediate-mass and low-mass stars, only those of Siess et al. (2000) are computed for the LMC metallicity; therefore we consider their isochrones and evolutionary tracks. We convert them into absolute magnitudes with the same technique described in Section 1.6.1, assuming Kurucz (1993) models for $T_{\rm eff} > 8000$ K and and NextGen models (Hauschildt et al., 1999) for lower temperatures. We consider for the atmosphere models the LMC metallicity [M/H]$= -0.3$.

2.5 The Initial Mass Function

The mass function (MF) is defined as the number distribution of stars as a function of mass. While a general observational approach measures the so called *Present Day Mass Function* (PDMF), a cornerstone for understanding how stars form is the *Initial Mass Function* (IMF), which is the mass distribution according to which stars are born. For a pre-main sequence population younger than the time required by the most massive stars to disperse it, or to evolve into post-MS evolutionary phases, the observed mass function coincides with the IMF.

Generally, the IMF is parameterized as follows:

$$\xi(M)\ {\rm d}M \propto M^{-(1+x)} \tag{2.5}$$

namely, approximating it with a power law (e.g. Salpeter, 1955) or with a series of power laws, with exponents changing in different mass ranges (Scalo, 1986; Kroupa, 2002). In this section we describe the "average" IMF derived for the stellar populations of the *central region* of LH 95, as it has been defined in Section 2.3.2.

The $F555W - F814W$, $F814W$ CMD of Figure 2.5 (right panel) is shown again in Figure 2.7, with our observable PMS evolutionary tracks (left panel) and three indicative PMS isochrones (right panel), computed in Section 2.4, overlayed. In the right panel of the figure the ZAMS from our grid of models is also plotted along with the youngest MS isochrone from the Padova grid of evolutionary models (Girardi et al., 2002) corresponding to $\log\tau \simeq 6.6$. Both isochrones fit to each other very well demonstrating that the bright MS stars of LH 95 have ages of $\lesssim$ 4 Myr. As far as the PMS stars of LH 95 concerns, their positions in the CMD correspond to an age-spread that covers ages between $\sim$ 1.5 and 10 Myr according to our PMS models. A simple statistics on the distribution of the ages of these PMS stars, based on their CMD positions, results to a normal distribution of ages

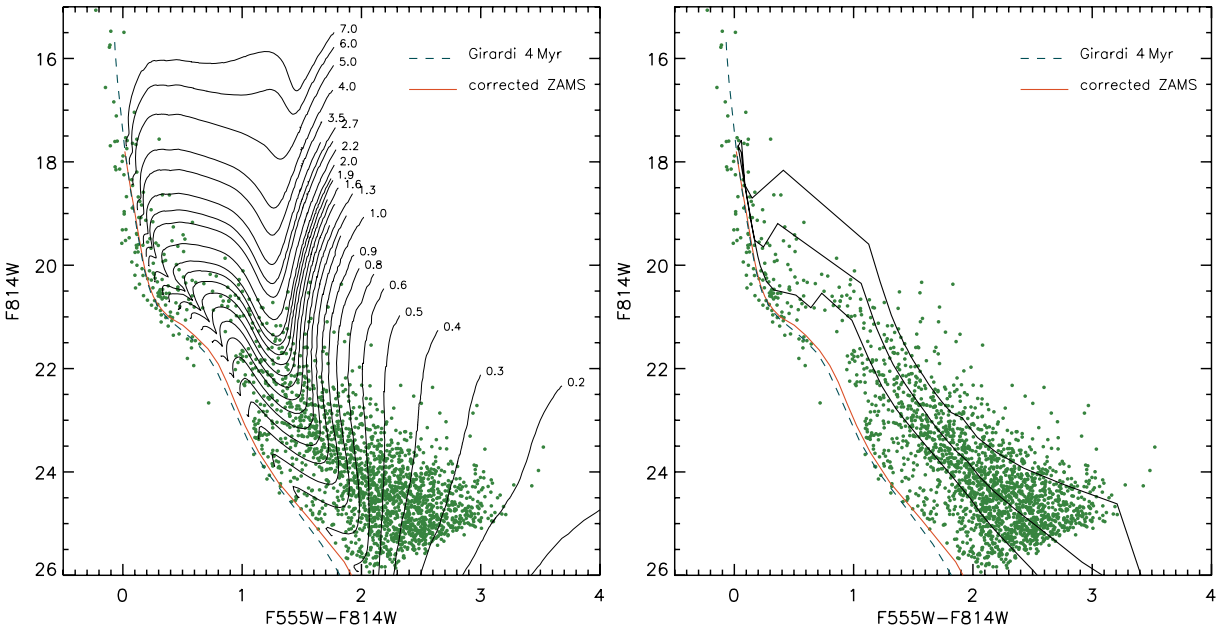

Figure 2.7 The CMD of the cluster area of LH 95 with PMS evolutionary tracks (left) and isochrones (right) overlayed for a distance modulus $m - M = 18.41$ mag and a mean reddening of $E(F555W - F814W) = 0.275$ mag (see Section 2.3.4). The PMS tracks and the corresponding PMS isochrones and ZAMS are computed by us for the *ACS* filter system, and for the metallicity of the LMC (Section 2.4). The 4 Myr isochrone for evolved MS stars is from the Padova grid of evolutionary models (Girardi et al., 2002). The comparison of this isochrone with our ZAMS demonstrates that it practically corresponds to the youngest MS populations. The selected PMS isochrones overlayed in the right panel have ages of 1.5, 4 and 10 Myr. The central, 4Myr, corresponds to the the mean age of the observed PMS stars, where the other two delimit the 1σ width of the broadening of these stars in the CMD.

which peaks at about 4 Myr. However, if this age-spread is true or not can be the subject of debate, as we discuss in Section 2.3.3. Therefore, based on the PMS population of LH 95 we define an indicative age for LH 95 of $\log \tau = 6.6 \pm 0.4$. Corresponding PMS isochrones for ages of 1.5, 4 and 10 Myr from our grid of observable PMS models are overlayed on the CMD in the right panel of Figure 2.7. A comparison of this age, which also represents the individual subclusters of LH 95, with the corresponding dynamical crossing time, estimated in Section 2.3.2, shows that all subclusters, as well as the whole central region have an age comparable to their crossing times, indicating that these systems are under 'mixing' process if not already 'mixed' and therefore we probably do not observe them close to their initial morphology.

2.5.1 Construction of the IMF

Based on our new set of PMS models computed above for the ACS photometric bands and the average LMC metallicity ($Z \sim 0.008$), we assigned a value of mass to all the stars identified in the region of LH 95, by comparing our observed data with the evolutionary tracks of these models. For this comparison we assumed a distance modulus of $m - M = 18.41$ mag, and an average reddening of $E(F555W - F814W) = 0.275$ mag, as it is derived in Section 2.3.4. According to Figure 2.7, our photometry reveals PMS stars with masses as low as 0.2 $M_{\odot}$. Our sample, though, as we discuss later, is complete for masses down to $\simeq 0.43$ $M_{\odot}$. For the PMS stars we assign a mass measurement to each observed star according to their positions in the CMD by interpolating between the PMS evolutionary tracks shown in Figure 2.7.

The position of the brightest main sequence stars is not covered by our PMS evolutionary models, limited for masses below $7M_{\odot}$. Therefore, we derive the masses of these stars directly from the Padova 4 Myr isochrone – already used for the determination of the average reddening in Section 2.3.4 – shifted in the direction of the reddening vector to reach individually each one of these stars. The good agreement between this Padova isochrone and the corrected ZAMS from the Siess models is evident from Figure 2.7. While we deredden the most massive MS stars according to their individual position in the CMD, their mass estimation is based solely on photometry. A more accurate estimation of the mass for massive stars certainly requires spectroscopy, because for such hot stars the broad-band colors are degenerate (Massey et al., 1995), and naturally this effect may influence the mass estimation for the brightest MS stars in our sample and the corresponding IMF. We discuss the influence of the use of photometry alone to the slope of the derived IMF in §2.5.2.

With the masses of both the MS and the PMS stars in our sample available the construction of their IMF is in principle straightforward, by binning the stars according to their masses and fitting the derived distribution. However, there are considerations, which affect the construction and interpretation of the IMF, and which should be taken into account. We discuss these issues below.

(i) An important issue to be considered is *the decontamination process of the stellar sample* in the region of the association from the field populations. The Monte Carlo method for the field subtraction, as applied in Section 2.3.3, is based on probabilities and therefore it is a stochastic process. As a consequence, the number

of stellar members of the system, which are counted in an arbitrary mass bin is not determined in an unambiguous manner. Moreover, the statistical significance of this number is not determined by the fraction of stars considered as system members over the total number of stars, but it depends also on the probability that *all* the observed stars in the bin are system members. This dependence affects specifically the MS populations with $19 \lesssim m_{\rm F814W}/{\rm mag} \lesssim 22$, which as it is shown in Figure 2.5 are well mixed with field populations, implying a higher uncertainty in the determination of the fraction of system members. In the faint part of the CMD, system and field populations are in general well distinguished, and therefore the uncertainties in the numbers of PMS stars that are true system members are insignificant. However, there is an important possibility that a fraction of the binary sequence, evident in the CMD for the LMC field population (see Figures 2.5 and 2.7), contaminates the selected sample of PMS star-members of the system. We consider this bias and report on its effect in Section 2.5.2

(ii) *The fitting process of the IMF.* Typical linear regression methods, which are used for obtaining a functional form of an observed IMF, such as the χ^2-method, consider the presence of measurement errors and are based on the assumption that the uncertainty associated with each point follows a Gaussian distribution. However, in this case the uncertainty in the number of counts within a mass bin is the overall effect of both the Poissonian error that naturally comes from the counting process, and the uncertainty that arises from the field subtraction, as discussed above. Although the first can be well approximated with a Gaussian for large n, the latter depends on the positions of stars and tracks in the CMDs. Moreover, in the high mass regime, where the number statistics is poor, the Poissonian error cannot be treated as Gaussian, requiring the asymmetry of the distribution to be taken into account.

(iii) *The completeness-correction process.* In the low-mass regime corrections for the incompleteness of the stellar sample are required to estimate the actual number of stars. However, given the width of the low-mass evolutionary tracks in the CMD shown in Figure 2.7 and the 2-dimensional variation of the completeness itself in the CMD (in both magnitudes and colors; see Section 2.2.1), this correction is not unique for all the stars counted in a considered mass bin.

We construct the system IMF of the association LH 95, with a special care in addressing the above issues, as follows. We first determine a grid of logarithmic mass bins, for which we choose variable width in $\log(M)$, that increases from 0.04 dex at low masses to 0.25 dex for the higher masses. The counting of the stars is made in variable-sized bins because such bins yield very small biases, which are only weakly dependent on the number of stars, in contrast to uniformly binned data (Maíz-Apellániz & Úbeda, 2005). For each $i^{\rm th}$ bin a number of stars N_i is derived. In order to achieve a statistically correct sampling of points for the constructed IMF, we simulate for each bin the probability distribution expected for every N_i with a sample of 1000 points randomly selected from a Poisson distribution with mean N_i.

We then consider the position in the CMD of all the stars in each bin, and we compute for each star its completeness C (the ratio between the number of sources detected and the total number of sources) as a function of both magnitude *and* color according to the completeness measurements described in Section 2.2.1, for the central region of LH 95. Let us consider the jth star counted in the ith bin. The star is located in a specific position of the CMD, where completeness is C_j, meaning that the total number number of stars corresponding to j is simply $1/C_j$. Consequently, for the total number of stars counted in the bin, N_i, the completeness correction is:

$$F_i = \frac{\sum_j^{N_i} \frac{1}{C_j}}{N_i} \tag{2.6}$$

which is a quantity ≥ 1.

We multiply our Poissonian sample associated with each $i^{\rm th}$ bin by F_i, and we divide by the width of the bin in order to express numbers in units of number of stars per solar mass[3]. In order to take into account the additional error introduced by the stochasticity of the Monte Carlo field subtraction (Section 2.3.3), we iterate the technique of field removal 200 times, each time repeating the procedure explained in the previous paragraphs, namely, counting the N_i number of stars in each $i^{\rm th}$ bin, sampling a Poisson random population associated with it, and computing and applying the completeness correction.

The outcome of this approach is that for each mass bin, instead of a single point-error combination, we have a population of 200,000 random IMF points, derived according to

[3]It is worth-noting that the completeness correction should be applied *after* simulating the Poisson distribution, and not before. For example, if one star of 25% completeness is counted into the $i^{\rm th}$ bin, the true number of sources associated with the N_i sample is 4, with an uncertainty of $\sqrt{1} * 4 = 4$ and not $\sqrt{4} = 2$.

the true statistical distribution of the expected number of stars in the bin. Clearly, the mean and the standard deviation of each of these distributions represent the IMF data points and error bars. The main advantage of this technique is that we override the non-Gaussian behavior of the mass bin error bars. Specifically, now for every mass bin we do not have one point associated with an error that cannot be treated by the regression theory, but a numerous set of points with no uncertainties associated with them, and consequently with arbitrary equal weights for all mass bins. Naturally, this allows a more accurate fitting of the mass function.

In Figure 2.8 we visualize the concept of this approach. For every mass bin the set of random points, representing the distribution of the expected $\xi(M)$ is drawn with tiny colored dots. In this plot an artificial spread along the x-axis (a random Gaussian shift with $\sigma = 1/8$ of the bin width) is introduced to better highlight the distributions along the $y-$axis. The black dots with error bars show the average and standard deviation of each sample of points. The derived numbers are reliable for $M \gtrsim 0.35$ $M_{\odot}$, whereas for the lower masses (the first five mass bins from the left) the completeness corrections are not sufficient. This limitation is evident from the CMD of Figure 2.7, where it can be seen that for the evolutionary tracks for very low masses ($M \lesssim 0.35$ $M_{\odot}$), the completeness is extremely low, so that no stars can be detected, limiting the ability to recover the true number distributions for such masses.

2.5.2 IMF model fitting

A commonly used procedure to derive the functional form of an observed IMF is to fit a predefined function to the individual numbers of stars originally counted per mass bin taking into account the corresponding counting errors. However, in our case, we have simulated the statistical distribution of $\xi(M)$ per mass bin taking into account the additional errors due to incompleteness and field subtraction. Within our statistical approach we perform 200 repetitions of the Monte Carlo field subtraction method and for each of them we map the Poissonian statistics 1000 times. The outcome is a nonanalytical probability distribution for each mass bin that represents the true expected statistical uncertainties due to the issues discussed in §2.5.1. This process provided a large sample of 200,000 points per mass bin, and naturally the best-fitting function can be derived more accurately with the use of these data, rather than the original 14 bins. The only assumption that we make is that the functional form of the IMF of LH 95 can be correctly

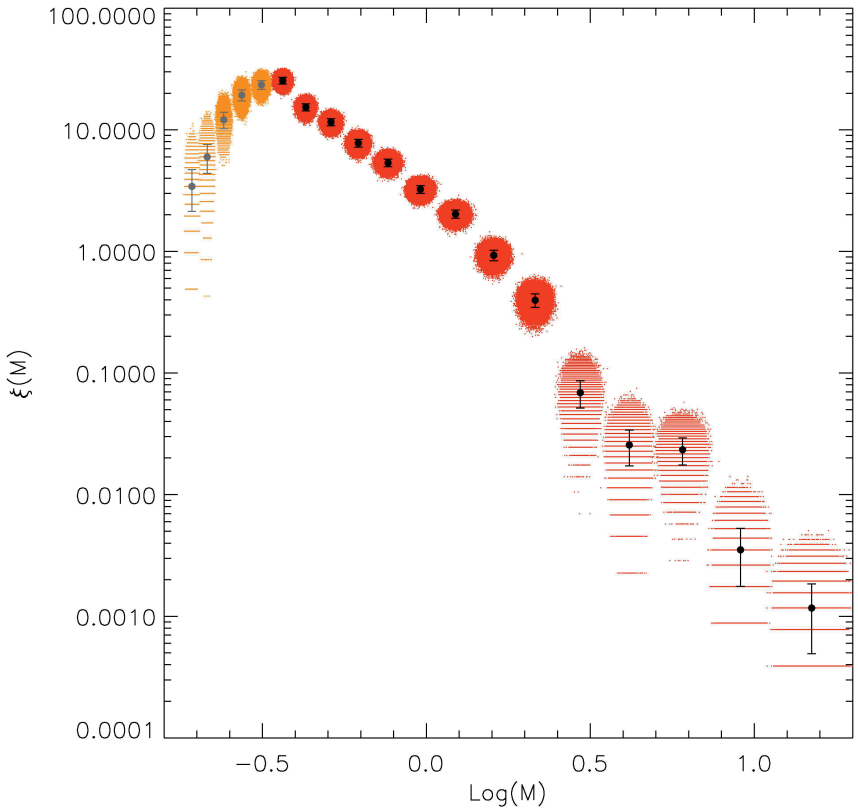

Figure 2.8 System IMF plot of LH 95, which demonstrates our method for treating the distribution of the expected number of stars per mass bin according to uncertainties due to counting, incompleteness and field subtraction. Each mass bin is represented by the distribution along the $y-$axis of a set of 200,000 randomly selected points, which map the true statistical uncertainties of star counts. An additional Gaussian spread with $\sigma = 1/8$ of the bin width along the $x-$axis has been artificially added for each bin to better highlight the behavior of the individual distributions. The asymmetry of the statistical distributions especially for the high-mass end of the IMF is demonstrated by the droplike shape of the distributions. The very-low mass end (light-gray points) appears to drop due to the limitation of our completeness correction technique in CMD regions where no stars are detected. Units of the IMF are number of stars per solar mass per pc^2 .

represented by power laws, according to the parameterization given in Eq. (2.5), and therefore we search for the best multiple power law which may reproduce our data. As seen in Figure 2.8 the IMF seems to be more shallow for the low masses ($M \lesssim 1$ M$_\odot$) than for intermediate and high masses, implying that it could be reproduced by a two-phase power law. We investigate, however, whether a two-phase power law is sufficient or a three-phase power law, such as that proposed by Scalo (1998), is required to represent our IMF.

In order to find the best-fit of two- and three-phase power laws to our IMF we applied a Levenberg-Marquard nonlinear least square minimization technique (Levenberg, 1944; Marquardt, 1963). For this fit we consider only the mass bins of the IMF for which the completeness correction allowed us to reconstruct the actual number of stars, meaning for $\log(M/\mathrm{M}_\odot) > -0.5$. The slopes of the power laws, as well as the position of the break points along the abscissa are the free parameters of our fit algorithm. All 200,000 points of each mass bin are considered of equal weight. However, since a two-phase power law is a sub-case of the three-phase power law, the sum-of-squares of the latter is always lower. Therefore, the results of the fit algorithm for each case are normalized in a rigorous manner by performing the so-called statistical "F test".

This test compares the relative increase in the residual sum of squares by reducing the complexity of the model with the relative increase of degrees of freedom, namely, the differences between the number of data points and the free parameters. Factor F is, thus, computed as

$$F = \frac{\frac{RSS_2 - RSS_3}{p_3 - p_2}}{\frac{RSS_3}{n - p_3}} \tag{2.7}$$

where RSS_2 and RSS_3 are the residual sum of squares for the two- and three-phase power law best-fit models, $p_2 = 4$ and $p_3 = 6$ are the corresponding number of free parameters, and n the total number of points, which, in our case, is the effective number of considered mass bins (14) and not the total number of variables used in the fit (200,000 $\times$ 14), given that the additional multiplicity has been introduced to map the non Gaussian errors. Typically, if the simpler model is valid (which means that there is no need to add parameters), then $F \simeq 1$, whereas if the complex model represents the distribution better, then $F \gg 1$. We obtain $F = 1.15$. The probability, P, that the null hypothesis, which is "the improvement found adding additional parameters is solely due to chance" (or "the simpler model is good enough") should be rejected is given by the value of the

cumulative *Snedecor's F* distribution with $(p_3 - p_3, n - p_3)$ degrees of freedom. In our case it is $P = 0.65$, while, generally, a value of $P > 0.95$ is required to state with sufficient significance, that the complex model is better. Under these circumstances, we conclude that our system IMF is best approximated by a two-phase power law.

We compute the uncertainty associated with this result, by utilizing a sampling technique. For each mass bin we pick randomly one out of the 200,000 points from the corresponding distribution of $\xi(M)$ in that bin, and we perform a two-phase power law fit as described above, obtaining the two measurements for the slope, and the point $(\log M, \log \xi(M))$ where the change of the slope occurs. After repeating this process for a substantial amount of times, we obtain a statistically significant sample for the values of the two slopes and the point of change, and consequently the relative confidence level of our fit. Figure 2.9 shows the result of our fit to the system IMF of LH 95. The best two-phase power law fit is shown as a solid line, while the uncertainty of this fit is demonstrated by the gray shaded areas for confidence of 95% (dark gray) and 99% (light gray) respectively. In Table 2.3 we give the system IMF slopes x and their uncertainties with the corresponding mass ranges. The 1σ error in the determination of the break point is 0.07 dex.

Another bias that should be considered in the construction of the system IMF of LH 95 is the possible contamination of our selected sample of PMS stars by a binary sequence of the LMC field MS population, discussed in Section 2.5.1. In order to quantify the effect of this bias we select this part of the CMD and remove the corresponding stars. Specifically, we remove all stars bluer than the borders defined by the points (F555W−F814W, F814W) = (0.9, 22.9), (1.65, 24.3) and (2.2, 26.9) on the CMD. The number of these stars changes according to the stochastic Monte Carlo field subtraction; on average they count to 82 members, less than 4% of the selected PMS population. Then, we reapply the analysis described in Section 2.5.1 and 2.5.2 for the construction and model-fitting of the system IMF. We find that this new IMF does not differ significantly from the one shown in Figure 2.9, and its shape is not different from that described with the slopes of Table 2.3. Specifically, this IMF has 99%-confidence slopes $x \simeq 1.16$ for $-0.5 < \log(M/\mathrm{M}_\odot) < 0.04$, and $x \simeq 2.03$ for $\log(M/\ \mathrm{M}_\odot) > 0.04$, indistinguishable from the slopes of Table 2.3. Our analysis on the subclusters of LH 95 showed that the contamination of our sample by a MS binary sequence does not alter also the shape of their individual system IMFs, with slopes as well indistinguishable from those given in Table 2.4.

Table 2.3. The slope of the system IMF of the association LH 95

mass range	x	$\sigma_{95\%}$	$\sigma_{99\%}$
$-0.5 < \log(M/\mathrm{M}_\odot) < 0.04$	1.05	$^{-0.20}_{+0.15}$	$^{-0.29}_{+0.20}$
$\log(M/\mathrm{M}_\odot) > 0.04$	2.05	$^{-0.28}_{+0.39}$	$^{-0.32}_{+0.53}$

Note. — A Salpeter (1955) IMF would have a slope of $x = 1.35$.

The lack of spectroscopy and the use of broad-band photometry alone for the mass estimation of massive MS stars is found to lead to steeper IMF slopes (Massey et al., 1995), and this may affect the overall intermediate- and high-mass slope of the IMF of LH 95. However, considering that in their analysis Massey et al. (1995) show that this effect is significant for stars more massive than 15 $\mathrm{M}_\odot$, the only mass bin in our IMF that can be biased is the most massive one, comprising stars with $11 \lesssim M/\mathrm{M}_\odot \lesssim 20$. In addition, the IMF derived from photometry alone for high-mass stars in star-forming regions of the Magellanic Clouds *is found to be also quite shallow and not steep*, and within the observed IMF slope variations in such regions (see discussion in §2.6.2). Under these circumstances, the corresponding uncertainty in our derived system IMF slope due to the use of photometry alone should not be expected to be larger than those given in Table 3.

2.6 Discussion

The IMF constructed in the previous section is the most complete extragalactic system IMF down to the subsolar regime derived so far. Specifically, our correction for incompleteness in the derivation of $\xi(M)$ actually provides a reliable IMF down to $M \simeq 0.43 M_\odot$, as discussed in §2.5.1. Probably, the most interesting result concerning this IMF is the change in its slope, which we verified statistically for stars in the the subsolar mass range. The IMF slope, x, decreases for these stars by one unit. An analogous behavior is generally found in related studies in the Galaxy. Comprehensive studies which summarize the

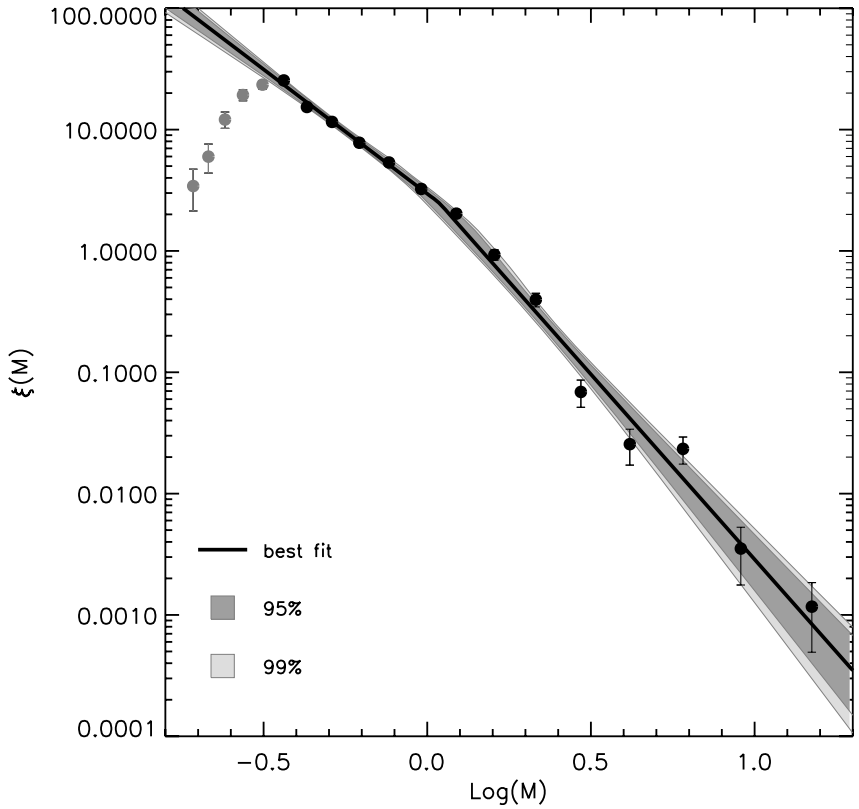

Figure 2.9 The system IMF of the association LH 95. The best two-phase power law fit derived in Section 2.5.2 is drawn with a solid line, while the shaded areas represent the 95% and 99% confidence uncertainties in the slope determination and the break point. Units of the IMF are logarithmic number of stars per solar mass per pc^2. The corresponding IMF slopes and their uncertainties are given in Table 2.3.

average properties of the galactic IMF are those of Scalo (1986), revisited in Scalo (1998) and Kroupa (2001, 2002). The latter investigations are rather complete, since they cover stellar mass distributions in a wide mass range, from brown dwarfs with $M \sim 0.01 M_{\odot}$ to the most massive stars. According to Kroupa (2002), the IMF slope x (Eq. 2.5) changes from $x = -0.7$ in the substellar mass range, to $x = 0.3$ for masses between 0.08 $M_{\odot}$ and 0.5 $M_{\odot}$, $x = 1.3$ for 0.5 $M_{\odot} < M < 1$ $M_{\odot}$, and $x = 1.7$ for stars of higher masses. This IMF is generally characterized as the Galactic average, in the sense that it is reasonably valid for different regions of the Galaxy. A comparison between the system IMF we construct here for LH 95 and that of Scalo (1998), as well as the universal IMF of Kroupa (2001) and the average Galactic IMF of Kroupa (2002), is shown in Figure 2.10. We scaled all other IMFs to match our mass distribution at $\log(M/M_{\odot}) = -0.3$. In Figure 2.10 an overall agreement between the various IMFs is quite evident.

The mass limit of the breaking point in our system IMF (~ 1 $M_{\odot}$) coincides with the "standard Galactic field IMF", which has been reported to have a change of slope at $1 M_{\odot}$ (Kroupa, 2002), in agreement also with the knee of the IMF derived by Scalo (1998). In addition, there is a second knee in the Kroupa IMF, which occurs at the lower mass-limit of 0.5 $M_{\odot}$. Since we cannot constrain the system IMF below $0.43 M_{\odot}$ we do not identify this second knee. The slope of our IMF for stars with $M \gtrsim 1$ $M_{\odot}$ falls within the range of slopes found by both Scalo and Kroupa. This is in line with the recent finding that the system IMF is essentially equal to the stellar IMF for intermediate and massive stars (Weidner et al., 2008). Our system IMF, however, is somewhat steeper, as an indication of a bottom-heavy IMF, but the use of photometry alone for the estimation of the masses for the brightest stars ($M \gtrsim 15$ $M_{\odot}$) may bias the slope to steeper values (see §2.5.2). As far as the slope of our IMF in the subsolar regime is concerned, it is found slightly more shallow than that of these authors. Specifically, our IMF is by $\Delta x = 0.1$ - 0.3 more shallow than the stellar IMF (as seen from the theoretical α-plots of Kroupa, 2001), making the resulting stellar IMF for LH 95 indistinguishable to the Galactic-field stellar IMF (e.g. Kroupa, 2002). It should be noted that both Scalo and Kroupa IMFs extend down to masses as low as the hydrogen burning limit ($M \simeq 0.08$ $M_{\odot}$), well below our detection limit. In general, one can conclude that the system IMF we derive for LH 95 is in agreement with the average galactic IMF in the entire mass range we studied, from 0.43 $M_{\odot}$ to ~ 20 $M_{\odot}$.

The high-mass IMF of LH 95 was constructed earlier from direct CCD imaging in BVR with the 1-m telescope at Siding Spring Observatory by Gouliermis et al. (2002).

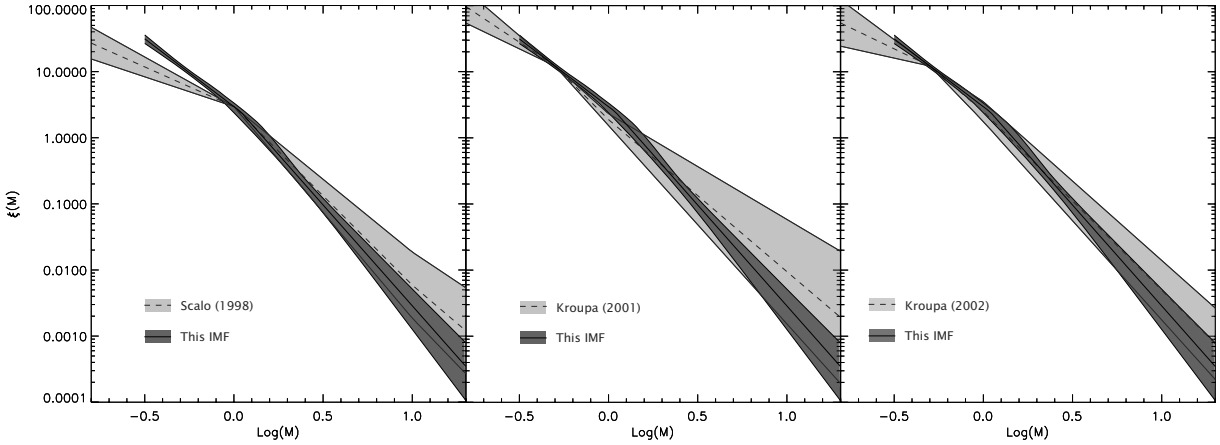

Figure 2.10 Comparison between the derived LH 95 system IMF and the average IMF of Scalo (1998) (left), Kroupa (2001) (middle), as well as the universal IMF of Kroupa (2002) (right).

These authors provide the field-subtracted completeness-corrected IMF of the system for stars with masses down to ~ 2 M$_\odot$, and they find that this IMF can be fitted with a single power law with slope $x = 1.2 \pm 0.3$ for stars with masses up to about 17 M$_\odot$. This result indicates a more shallow slope x than what we found for intermediate and high mass stars ($x = 2.05$). However, in our analysis we included masses as low as $1M_\odot$, extending the mass range investigated in Gouliermis et al. (2002). Indeed, if we exclude the mass bins from 1 to 2 M$_\odot$ ($0 < \log(M/\mathrm{M}_\odot) < 0.3$) from our analysis we derive a more shallow value for x for the intermediate- and high-mass stars. The effect of a steeper IMF for the mass range between 1 and 2 M$_\odot$ is evident in Figs. 2.8 and 2.9. After excluding stars of $M < 2$ M$_\odot$ from the considered stellar sample and performing a single power law fit on the resulting $\xi(M)$, we find an IMF slope of $x \simeq 1.55$, comparable to that of Gouliermis et al. (2002).

Concerning our derived IMF for the central region of LH 95 it is important to assess the accuracy of our findings, in relation with the possible sources of uncertainties. One of the most important error sources normally comes from the incomplete stellar samples. However, in our case we consider the completeness as it has been derived from artificial star tests in the central part of LH 95, where the crowding is higher (Figure 2.2b), and we performed rigorous corrections for incompleteness taking into account variations of completeness for all stellar positions in the CMD. As far as the very-low mass stars is concerned, we do not consider those with $M \lesssim 0.35$ M$_\odot$, where our completeness correction is limited.

2.6.1 Stellar Binarity

An important source of uncertainty in the construction of the IMF is also the presence of unresolved binaries. Unresolved binarity, can modify the shape of the observed mass function so that it appears more shallow than what it actually is. For this reason, we stress that the IMF reported in Table 2.3 must be considered as the *system* IMF of our region, and not a *stellar* IMF as which one refers when the effect due to binarity is removed. Clearly it is not possible to correct this effect without the knowledge of the actual binary fraction of the studied population, but one can estimate the overall effect on the final mass distribution. Sagar & Richtler (1991) applied Monte Carlo simulations on artificial stellar populations, in order to investigate the change in the mass function slope Δx due to binarity for stars in the mass range $2 < M/M_{\odot} < 14$. These authors found that the result depends on both the binary fraction f and the original slope x_0 of the mass function. Specifically, for an original slope $x_0 = 1.5$ and a binary fraction $f = 0.5$ Sagar & Richtler (1991) found a slope change $\Delta x \simeq 0.34$, while for $x_0 = 0.5$ and $f = 0.5$, $\Delta x \simeq 0.5$. On the other hand, Kroupa et al. (1991) in their investigation on the low-mass IMF in the solar neighborhood, showed that binaries can make a major effect in mass function determinations below 1 $M_{\odot}$. Consequently, the expected changes in the slope due to unresolved binarity may introduce uncertainties in the derived slopes given in Table 2.3, but not large enough to justify the intrinsic change of slope that we observe in our IMF for LH 95 at 1 $M_{\odot}$. In any case, as discussed by Kroupa (2002), most of the studied mass functions in the literature are not corrected for binarity, mostly due to the high uncertainty in the binary fraction. The Galactic IMF derived by (Kroupa, 2001, 2002), however, has been corrected for unresolved multiple systems. A more recent study of the binary effect on the massive-star IMF by Weidner et al. (2008) shows that a power law IMF is not significantly affected even by large numbers of unresolved binaries or higher order multiples.

In order to analyze the effect of unresolved binarity in the measured slope of the system IMF in the subsolar regime, we apply a Monte Carlo technique adopted from the work of Sagar & Richtler (1991) and Kroupa et al. (1991, 1993). For this method we assume a predefined set of functions for the IMF, and in order to be consistent with those we find for the system IMF, as well as with the Galactic IMF of Kroupa (2002), we consider three-phase power laws with break points at 0.3 $M_{\odot}$ and 1 $M_{\odot}$. We limit our mass samples in the stellar regime with $M > 0.08$ $M_{\odot}$. We let the slopes x_1, x_2, x_3 within

the three selected mass ranges to change respectively in the range $-1 < x_1 < 1.5$ for $0.08 < M/\mathrm{M}_\odot < 0.3$, $0 < x_2 < 2$ for $0.3 < M/\mathrm{M}_\odot < 1$ and $1 < x_3 < 2$ for $M/\ \mathrm{M}_\odot > 1$. For each of these mass distributions, we generate a sample of 50,000 stars positioned in the CMD along our 4 Myr PMS isochrone (corresponding to the age of the system). We assume binary fraction, f, between 0 and 1, and we randomly pair couples of stars from the simulated distributions. We then compute the new position in the CMD of these binary systems and assign new masses as if they were single stars. The out-coming mass distributions are fitted with a 3-phase power law imposing the same position of the break points.

We isolate the models for which the derived system IMF in the range $0.3 < M/\mathrm{M}_\odot < 1$ is compatible with the one measured for LH 95 within the confidence interval of the latter. Naturally there are multiple solutions, given the lack of knowledge about the actual IMF of LH 95, its shape at lower masses, and the binarity fraction appropriate for this system. However, we can constrain the uncertainties due to unresolved binarity in our measured slope, x_2, for the subsolar regime $0.3 < M/\mathrm{M}_\odot < 1$. The IMF slope within this mass range is mainly affected by the value of f. If we assume x_1 to be that of the Galactic-field IMF, the slope x_2 in this mass range changes by $\Delta x_2 \simeq 0.45$ for $f = 1$. This change decreases to $\Delta x_2 \simeq 0.35$ for $f = 0.6$, and $\Delta x_2 \simeq 0.25$ for $f = 0.4$.

A change in the original IMF for masses larger than solar does not affect our results by more than $\Delta x_3 = 0.1$, whereas changing the slope at very low masses ($0.08 < M/\mathrm{M}_\odot < 0.3$) affects significantly the slope x_2, diminishing it when x_1 becomes much steeper or shallower than the value of Kroupa (2002) IMF. Even in this case, the effect is always less than $\Delta x_3 = 0.2$. Therefore, we conclude that for a reasonable binary fraction of $f \simeq 0.5$, unresolved binarity can bias our IMF slope, x, in the subsolar regime on average by no more than 0.3 units. As a consequence unresolved binarity does not affect significantly the measured IMF for LH 95 within the estimated errors, and thus the corrected stellar IMF for LH 95 remains indistinguishable from the Galactic IMF.

2.6.2 Metallicity effects

Recent findings suggest that variations in the metallicity of a star-forming cloud might cause variations in the IMF slope for stars with masses $M < 0.7\ \mathrm{M}_\odot$, in the sense that Galactic regions with higher $[Fe/H]$ appear to produce more low-mass stars (Kroupa, 2002). This is further supported by the measured IMF in Galactic open clusters (Barrado

y Navascués et al., 2001), globular clusters (Piotto & Zoccali, 1999) and old and relatively metal-poor thick disk stars (Reylé & Robin, 2001). Kroupa (2002) proposes a systematic metallicity dependence of the IMF exponent of the form $x \approx 0.3 + \Delta x[Fe/H]$, where $\Delta x \approx 0.5$. If we apply this dependence to the LMC, for which $[Fe/H] \simeq -0.4$, we find that the slope of the average IMF in the LMC for masses $M < 0.7$ M$_\odot$ should be flattened to the value $x \approx 0.1$. The flattening of the IMF of the LMC general field for stars with $M < 0.7$ M$_\odot$ has been discussed by Gouliermis et al. (2006a), who found only indications of such a change in the IMF slope, because of observational limitations. Our data, on the other hand, being deeper, show a constant IMF slope in the low-mass regime down to the detection limit of $M \simeq 0.43$ M$_\odot$ with no indication of flattening for $M < 0.7$ M$_\odot$. Consequently, we cannot verify any metallicity dependence of the subsolar IMF in the LMC, at least based on the formula of Kroupa (2002). Considering that this result is based on a single stellar system, more studies of low-mass populations in the Magellanic Clouds may provide a better constraint on any systematic metallicity dependence of the low-mass IMF.

As far as the high-mass regime is concerned, while the IMF of LH 95 seems to be steeper than that derived from ground-based observations by Gouliermis et al. (2002), our analysis (§2.6) shows that if we consider only stars more massive than 3 M$_\odot$ the IMF of LH 95 has a Salpeter-like slope, comparable to that of Gouliermis et al. (2002). While, as discussed in §2.5.2, the use of photometry alone leads to steeper IMFs, there are several photometric studies of associations in the LMC, which derive *a high-mass IMF that is not steeper, but more shallow* than the typical Salpeter IMF (e.g. Hill et al., 1994; Oey, 1996; Dolphin & Hunter, 1998). Taking into account all available studies for the intermediate- and high-mass stars with $M \gtrsim 7$ M$_\odot$, both spectroscopic *and* photometric (e.g. Massey et al., 1989a,b; Hill et al., 1994; Massey et al., 1995; Hill et al., 1995; Massey & Hunter, 1998) one can see that the corresponding IMF slopes in star-forming regions of the LMC are found clustered around the value $x \approx 1.5$, similar to the Galactic average IMF. The system IMF we derive here for LH 95 for stars within the same mass limits does not differ significantly from this value. Extensive studies have also shown that the high-mass IMF is independent of metallicity in the Galaxy and the Magellanic Clouds (see review by Massey, 2003), and our results also suggest a weak metallicity dependence of the high-mass IMF, providing further support to its universality, in the sense that the *average* IMF of a galaxy seems to be independent from environmental factors, and that any individual stellar system is not expected to share the exact IMF. Indeed, the standard

galactic IMF, as presented by, e.g., Scalo (1986) and Kroupa (2002), is the average over a set of systems, each of them showing slightly different mass distributions.

2.6.3 Variability of the IMF within LH 95

The clustering behavior of the PMS stars in LH 95 is discussed in Section 2.3.2, where three high concentrations of such stars within the main body of the system are identified as the subclusters of the association LH 95 (given the names cluster A, B and C respectively). In order to study how the IMF may vary from one subcluster to the other, and how the IMF of each individual concentration of PMS compares to the "overall" IMF of the system, we constructed the IMF for each of the three subclusters.

We applied the same method used in §2.5.1 and 2.5.2, isolating each time the regions of the subclusters, as shown in Figure 2.4b, iterating the Monte Carlo field subtraction, computing the distribution of number of stars in mass bins and correcting for incompleteness. For the model fitting, we used the same Levenberg-Marquard technique, with the difference that, in this case, we constrained the position of the break point between the two power laws to be the same as for the general IMF, namely, at $\log(M/M_{\odot}) = 0.04$. This choice is reasonable considering that we are mainly interested in eventual changes in the derived slopes of the IMF.

The constructed IMF for each subcluster is shown in Figure 2.11. The overall IMF for the whole system is also overlayed, after it is normalized in order to match the subclusters' best-fit on the break point. In each case the IMF for the subsolar masses is the same as the general IMF, as discussed in §2.6 for the entire system of LH 95. Moreover, the derived two-phase models that fit the IMF of each subcluster and the corresponding uncertainties, given in Table 2.4, are compatible to that of the overall IMF given in Table 2.3.

The IMF constructed for each subcluster in LH 95 suggests that the mass distribution of the PMS stars in this association does not vary much with location. Moreover, the spatial distribution of the intermediate- and high-mass stars within the whole of the system does not show any indication that the system is mass segregated. On the other hand if the individual subclusters are considered, the more massive stars do occupy the central parts of each of them, providing clear evidence that mass segregation in LH 95 probably occurs in rather small clustering scales.

According to recent results by Weidner & Kroupa (2006) on the integrated galaxial stellar IMF, the overall IMF of a composite system should be steeper than the one it

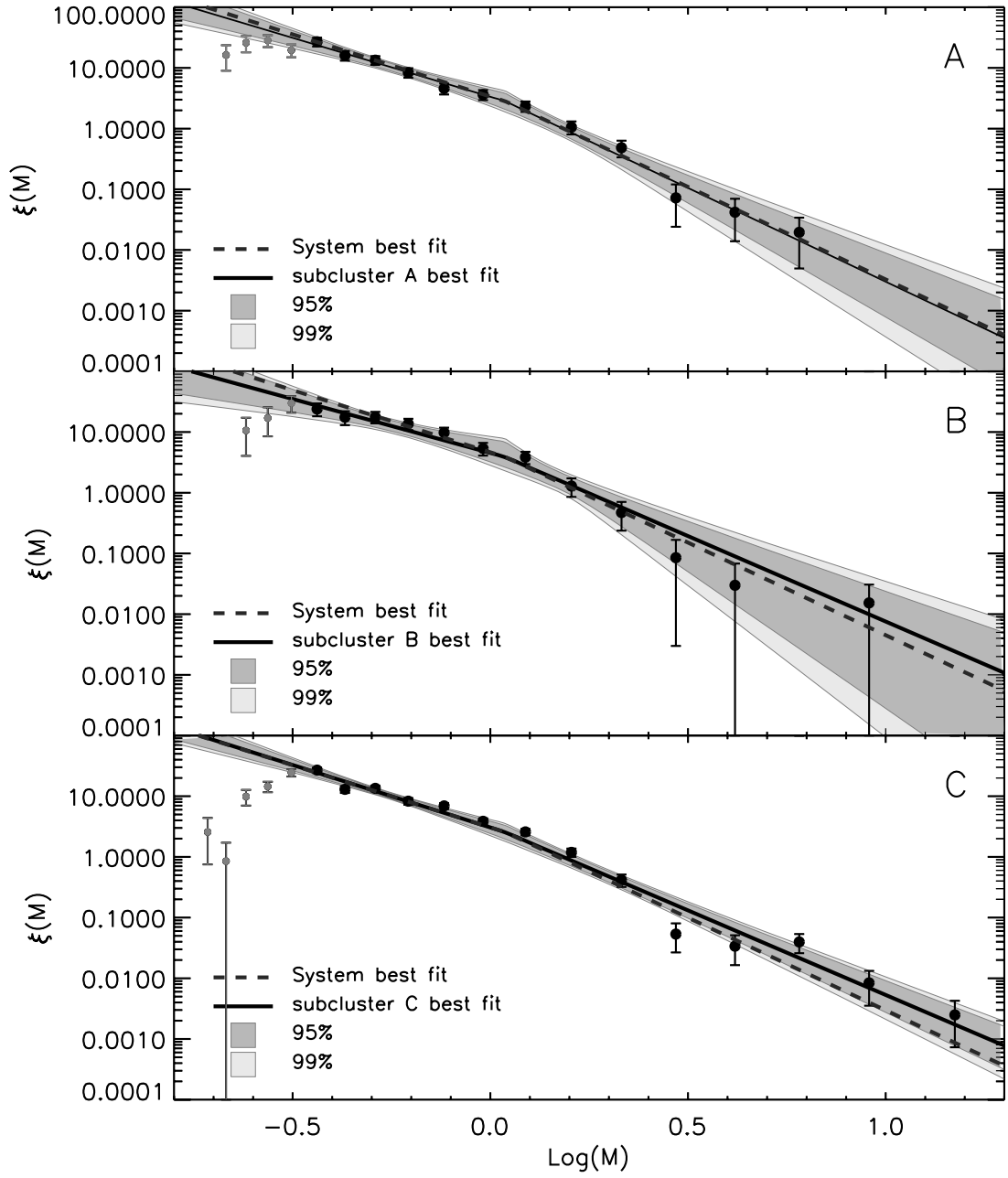

Figure 2.11 Measured mass function for the 3 subclusters of LH 95, as they are defined in Table 2.2 and shown in Figure 2.4b. The method used for the determination of the best-fitted two-phase power law is analogous to that applied for the entire central region of LH 95, except for the fact that here we constrain the break point to be the same derived for the global IMF, at $\log(M) = 0.04$. The overall $\xi(M)$ of LH 95 is overlayed as a dashed line.

Table 2.4. IMF slopes and uncertainties for the three subclusters of LH 95

	$-0.5 < \log(M/M_\odot) < 0.04$	$\log(M/M_\odot) > 0.04$
subcluster A	$0.94^{-0.40}_{+0.41}$	$2.09^{-0.55}_{+0.70}$
subcluster B	$0.78^{-0.77}_{+0.53}$	$1.82^{-0.60}_{+1.71}$
subcluster C	$1.05^{-0.35}_{+0.33}$	$1.79^{-0.29}_{+0.36}$

Note. — slopes are in terms of x according to Equation 2.5, uncertainties are 95% confidence intervals.

would have if it was not composite, in the intermediate- and high-mass regime. Taking into account the fact that LH 95 is resolved into at least three individual subclusters (§2.3.2), it may be considered as a scaled-down case of the scenario of these authors, and therefore as a composite system. It should be noted that also this may explain the somewhat steep slope of the IMF we derive for LH 95.

Chapter 3

A New Method for the Assessment of Age and Age Spread of Pre-Main Sequence Stars in Young Stellar Associations of the Magellanic Clouds[1]

3.1 Introduction

As we discussed in the previous chapter, the Magellanic Clouds are well suited environments for the study of resolved star formation. From the observational point of view, the difficulty in detecting and resolving singular low-mass stars – which requires high spatial sensitivity such as that of the Hubble Space Telescope – is counterbalanced by exceptional advantages which simplify in the analysis of the observed population. The main advantages are a lower interstellar extinction compared to similar studies in the Galaxy, and the relative ease membership assignment, guaranteed by the absence of a significant relative distance spread in the population of the host galaxy.

In Chapter 2 we utilize the deepest optical photometry ever obtained for a cluster of the LMC to derive the IMF of LH 95 down to ~ 0.4 $M_{\odot}$. In this chapter, based on the same dataset, we study the problem of age and age spread.

PMS stars remain in the contraction phase for several times 10 Myr, and therefore they are chronometers of star formation and its duration. However, the estimate of stellar ages in the PMS regime from photometry is not without difficulties. This is because the

[1]**The research presented in this chapter has been published, as a refereed paper, in Da Rio et al. (2010b)**

observed fluxes are affected by several physical and observational effects. While these stars are optically visible, they are still surrounded by gas and dust from their formation, typically in circumstellar disks. Irregular accretion, due to instabilities in these disks, produces variability in the brightness of these stars. Moreover, PMS sources exhibit periodic fluctuations in light produced by rotating starspots. The variable nature of PMS stars dislocates them from their theoretical positions in the CMD. This effect in addition to observable biases, such as crowding and unresolved binarity, results in a broadening of the sequence of PMS stars in the CMD. As a consequence the measurement of the age of the host system and any intrinsic age spread, which may indicate continuous star formation, cannot be derived from simple comparisons of PMS isochrones with the observed CMD. This problem is particulary critical for our understanding of the star formation processes in every region. In particular, Naylor (2009) showed that neglecting unresolved binaries may lead to an underestimation of the age of a young cluster of a factor 1.5-2. Concerning the star formation duration, the apparent luminosity spread in the CMDs, if not disentangled from a possible intrinsic age spread, leads to an overestimation of the star formation timescale.

With spectroscopic and variability surveys with HST in star-forming regions of the MCs being practically impossible, the only way to disentangle the age and the duration of star formation in such regions from the rich samples of PMS stars is with the application of a statistical analysis, from a comparison between the observed CMDs and simulated ones.

In this study we present a new maximum-likelihood method, for the derivation of the ages of PMS stars and the identification of any age spread among them. We apply our method to the rich sample of PMS stars detected with ACS in LH 95 to determine the age of the stars from their positions in the CMD in a probabilistic manner, accounting for the physical and observational biases that affect their colors and magnitudes. We present new evolutionary models in Section 3.2. In order to achieve the most accurate results we further refine our previous selection of PMS stars members of the system in Section 3.3. In Section 3.4 we construct modeled 2D density distributions of PMS stars in synthetic CMDs by applying the considered observational and physical biases to the evolutionary models, and we apply our maximum-likelihood technique for the derivation of the age of the system. In Section 3.5 we use our method to investigate the existence of an age spread in LH 95, and we discuss our findings in Section 3.6.

3.2 Description of the evolutionary models

For the purposes of our study we calculate a set of evolutionary models for PMS stars with the use of the FRANEC (Frascati Raphson Newton Evolutionary Code) stellar evolution code (Chieffi & Straniero, 1989; Degl'Innocenti et al., 2008). Opacity tables are taken from Ferguson et al. (2005) for $\log T[K] < 4.5$ and Iglesias & Rogers (1996) for higher temperatures. The equation of state (EOS) is described in Rogers et al. (1996). Both opacity tables and EOS are calculated for a heavy elements mixture equal to the solar mixture of Asplund et al. (2005). Our models are then completely self-consistent, with an *unique* chemical composition in the whole structure.

The value of the mixing length parameter, α, has been chosen by fitting a solar model, obtained to be $\alpha = 1.9$. Helium and metal content of the models are those best representative for the LMC, i.e. $Y = 0.25$ and $Z = 0.01$ respectively. The evolutionary tracks have been calculated for a range of masses between 0.2 and 6.5 $M_{\odot}$. We have interpolated a dense grid of isochrones from the evolutionary tracks, which covers ages from 0.5 to 200 Myr, with steps of 0.1 Myr below 10 Myr, with steps of 0.5 Myr between 10 and 20 Myr, with steps of 1 Myr between 20 and 50 Myr isochrones, and with steps of 5 Myr above 50 Myr. For ages $\tau < 1.6$ Myr the isochrones do not reach the main sequence (MS) for the highest masses in our sample, while at $\tau \sim 50$ Myr the models cover also post-MS evolutionary phases for intermediate masses.

The evolution of light elements (Deuterium, Lithium, Beryllium and Boron) is explicitly included in this version of FRANEC code. Deuterium burning plays an important role in the very early stages of PMS evolution for stars with $M \lesssim 0.6$ M$_{\odot}$. For these stars the energy provided by the D$(p,\gamma)^3$He reaction is able to slow down the contraction in the initial part of the Hayashi track. This can be seen in Figure 3.1, where it can be seen that the low-mass end of the PMS isochrones is bent toward higher luminosities a for ages younger than ~ 5 Myr.

In order to explore the dependance of our findings on the assumed models, the consideration apart from FRANEC of additional families of PMS evolutionary models (e.g., D'Antona & Mazzitelli, 1994; Baraffe et al., 1997; Palla & Stahler, 1999) would be justified. However, the majority of the available grids of models are not available for low metallically populations like those in the LMC. The grid of PMS evolutionary models by Siess et al. (2000) is the only one that has been computed also for a subsolar value of metallicity $Z = 0.01$ and covers the mass range which is interesting to us, from the

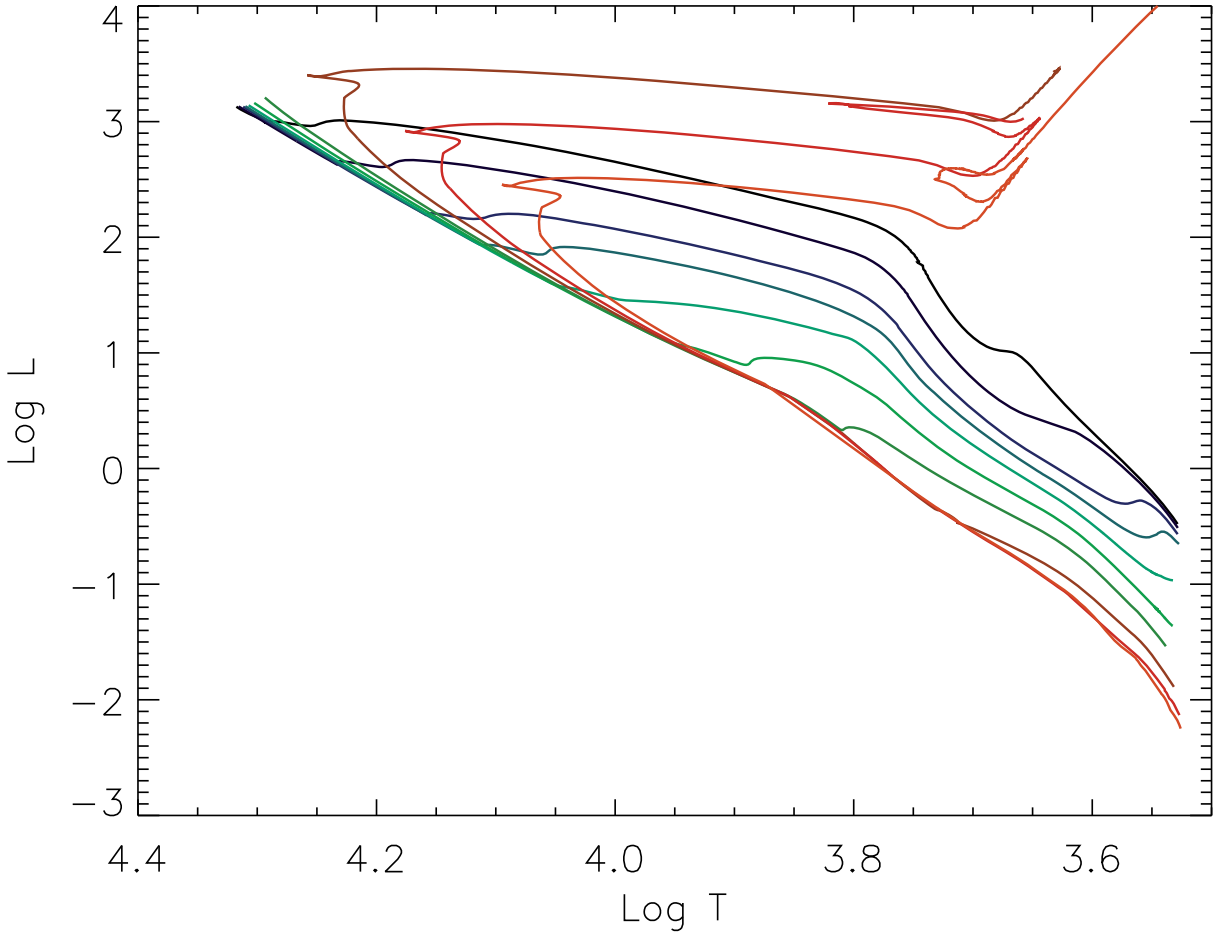

Figure 3.1 A sample of isochrones computed by us using the FRANEC code. The shown isochrones correspond to ages of 0.5, 1, 2, 3, 5, 10, 20, 50, 100 and 200 Myr.

hydrogen burning limit of ~ 0.1 $M_\odot$ to the intermediate-mass regime with $M \lesssim 7$ $M_\odot$. As a consequence, in our subsequent analysis we consider both FRANEC and Siess et al. (2000) models. We will refer to the latter simply as the *Siess* models.

3.2.1 Synthetic Photometry

In order to compare our photometry with the evolutionary models, we convert them from the physical units ($T_{\rm eff}$, $\log L_{\rm bol}$) into absolute magnitudes in the HST/ACS photometric system, by means of synthetic photometry on a grid of atmosphere models. As discussed thoroughly in Chapter 3, the surface gravity dependence in the computation of optical colors for PMS stars must be accounted for, especially in the low-mass regime. Since atmosphere models are generally expressed in terms of $T_{\rm eff}$ and $\log g$, synthetic photometry provides a precise consideration of the color dependence on surface gravity, allowing to

isolate one unique spectrum as the best representative of the stellar parameters for each point in a theoretical isochrone.

The choice of a reliable atmosphere grid is critical for cool stars (Chapter 2), whose spectral energy distributions (SEDs) are dominated by broad molecular bands. Moreover, these spectral features are gravity dependent, and since the stellar surface gravity varies during PMS contraction, optical colors are age dependent for young stars. In Chapter 3 for the derivation of the IMF of LH 95 we utilized the NextGen (Hauschildt et al., 1999) synthetic spectra to convert the theoretical Siess models into colors and magnitudes, extended with the Kurucz (1993) grid for the highest temperatures ($T_{\rm eff} > 8000$ K). While our ACS photometry of LH 95 in Chapter 3 includes PMS stars down to ~ 0.2 $M_{\odot}$, the detection incompleteness could not be corrected for masses below ~ 0.4 $M_{\odot}$. Therefore, the IMF derived in Chapter 3 was constructed for masses down to ~ 0.4 $M_{\odot}$. However, in the present study on the age of LH 95 and the age distribution of its low-mass PMS stars, the whole sample of detected stars down to ~ 0.2 $M_{\odot}$ can be used. Therefore we want to refine the atmosphere models we adopt to compute intrinsic colors for the very low stellar masses.

Baraffe et al. (1998) show that NextGen models cannot reproduce empirical solar-metallicity V vs $(V-I)$ color-magnitude diagrams for main sequence populations. The problems set in for $(V-I) \gtrsim 2$, which corresponds to $T_{\rm eff} \lesssim 3600$ K, and can be attributed to shortcomings in the treatment of molecules. In particular, Allard et al. (2000) illustrate that the main reason for the failure of NextGen spectra in matching the optical properties of late-type stars is the incompleteness of the opacities of TiO lines and water. In that work they present new families of synthetic spectra (AMES models) with updated opacities, and discuss the comparison with optical and NIR data, finding a good match with empirical MS dwarf colors from the photometric catalog of Leggett (1992).

In Chapter 2, in our analysis of a multi-color optical survey of the Orion Nebula Cluster down to the hydrogen burning limit, we show that, for young, M-type stars: a) the optical colors are bluer than those of MS dwarfs at the same temperature; b) intrinsic colors obtained from synthetic photometry using AMES spectra better reproduce the observed colors; c) for late M-type stars the AMES colors are even slightly bluer than the observed sequence, needing an additional correction based on the empirical data. As we show later on, the predicted colors from NextGen models are even bluer than the AMES ones for young stars. Moreover, the correction to the AMES colors proposed in Chapter 1 is critical for temperatures below our detection limit. As a consequence, we are

confident that for the analysis presented in this work, the AMES models are in any case more appropriate than the NextGen, and their still present uncertainties do not play a significant role when used on our LH 05 photometry.

Unfortunately the AMES library is available only for solar metallicity, and therefore we proceed by performing an approximation that provides the best estimate of the correct magnitudes and colors for M-type stars with metallicity $Z = 0.01$. In conclusion, we perform synthetic photometry on the evolutionary models considered here by applying the technique presented in Chapter 2 by making use of three families of synthetic spectra: (a) NextGen, for a LMC metallicity of $Z \simeq 0.01$, (b) NextGen for solar metallicity $Z = 0.02$, and (c) combined NextGen for $T_{\rm eff} > 5000$ K and AMES for $T_{\rm eff} < 5000$ K for solar metallicity. For $T_{\rm eff} > 8000$ K all three used grids are extended using Kurucz (1993) spectra.

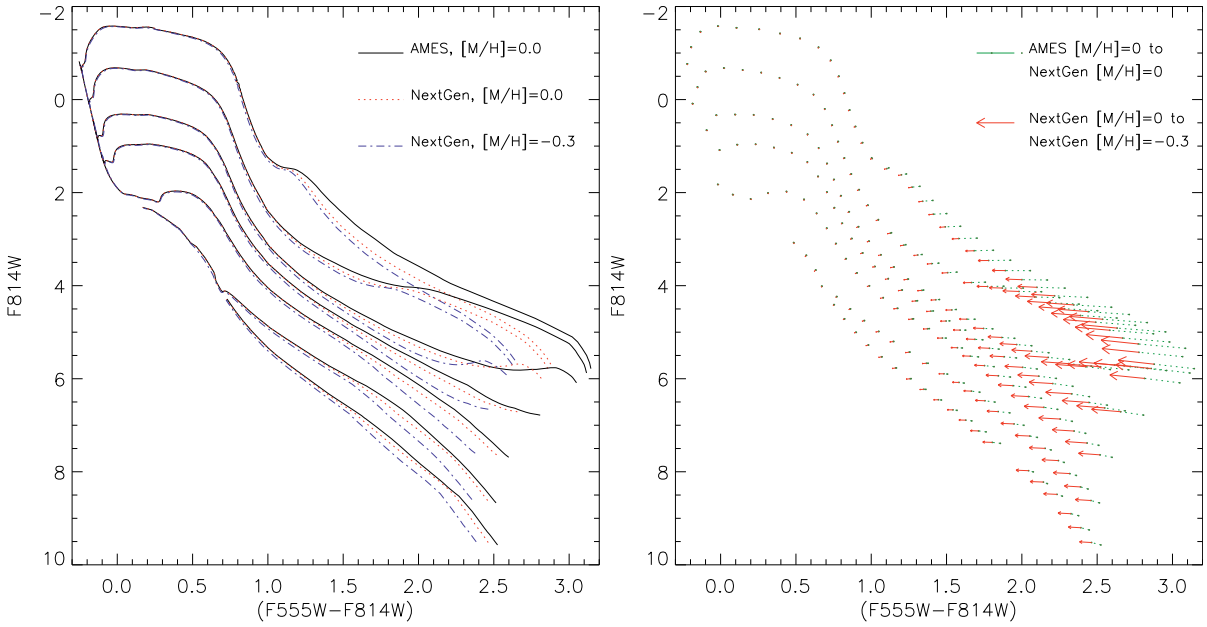

Figure 3.2 *Left panel:* CMD showing our FRANEC isochrones for ages of 0.5, 1, 3, 5, 10, 30, 100 Myr converted into the ACS photometric system using the solar metallicity atmosphere models from the AMES library (*solid line*), the NextGen models of solar metallicity (*dashed lines*) and the same of LMC metallicity $Z = 0.01$ (*dot-dashed lines*). *Left panel:* Representation of the displacements in the CMD of identical points on the evolutionary models caused by changing the three grids of atmosphere models used.

Results of our transformations are shown in Figure 3.2(*left*) for a number of FRANEC isochrones with ages spanning from 0.5 to 100 Myr. In this figure it is shown that while

the dependence of colors on the used synthetic spectra is negligible for low color-terms that correspond to high $T_{\rm eff}$, the offset increases for late spectral types and young ages. In particular, the more "correct" AMES atmospheres are up to 0.2 mag redder than the NextGen ones for the same metallicity, and a decrease of [M/H] by a factor of two (from the solar to LMC metallicity) leads to a similar offset toward bluer colors.

In order to estimate the magnitudes and colors of AMES-transformed isochrones for the LMC metallicity, we compute the displacement produced by changing the metallicity from $Z = 0.02$ to $Z = 0.01$ with the use of the NextGen spectra for every point of every isochrone. These displacements are represented with arrows in Figure 3.2(*right)*. They can be considered as a fairly good approximation of the real change in the observed colors and magnitudes in relation to $T_{\rm eff}$ and $\log g$, caused by the decrease of metallicity. Therefore, we apply the same offset, point by point, to isochrones transformed with the use of AMES spectra with solar metallicity, in order to derive their counterpart isochrones for $Z = 0.01$.

Figure 3.3 shows a sample of Franec isochrones transformed to the observable plane with the use of the AMES spectra library extrapolated to the LMC metallicity plotted over the CMD of LH 95. A distance modulus of $m-M = 18.41$ mag and average extinction of $A_V = 0.6$ mag, derived in Chapter 3, are applied to the isochrones. The PMS stars of LH 95, roughly following the 5 Myr isochrone, exhibit a wide apparent spread that spans from the youngest ages available in the models to the main sequence.

3.3 Field subtraction refinement

Our observations of the control field $2'$ away from LH 95 with setup identical to those of the system allowed us in Chapter 3 to perform a thorough statistical removal of the contamination of the observed population by the stars of the local LMC field, on the verified basis that there are no PMS stars in the LMC field. Indeed, this method provided a sufficiently clean CMD of the PMS cluster-members of LH 95 (shown in Figure 3.3). However, there is an anomalous presence of a small number of sources in the field-subtracted CMD located between the general PMS population and the MS. These sources can be seen in Figure 3.3 located in the neighborhood of the 100 and 30 Myr isochrones. In Chapter 3 we hypothesized the origin of these contaminants as a binary sequence of the field MS population, and we demonstrated that their removal does not affect the shape of the derived IMF.

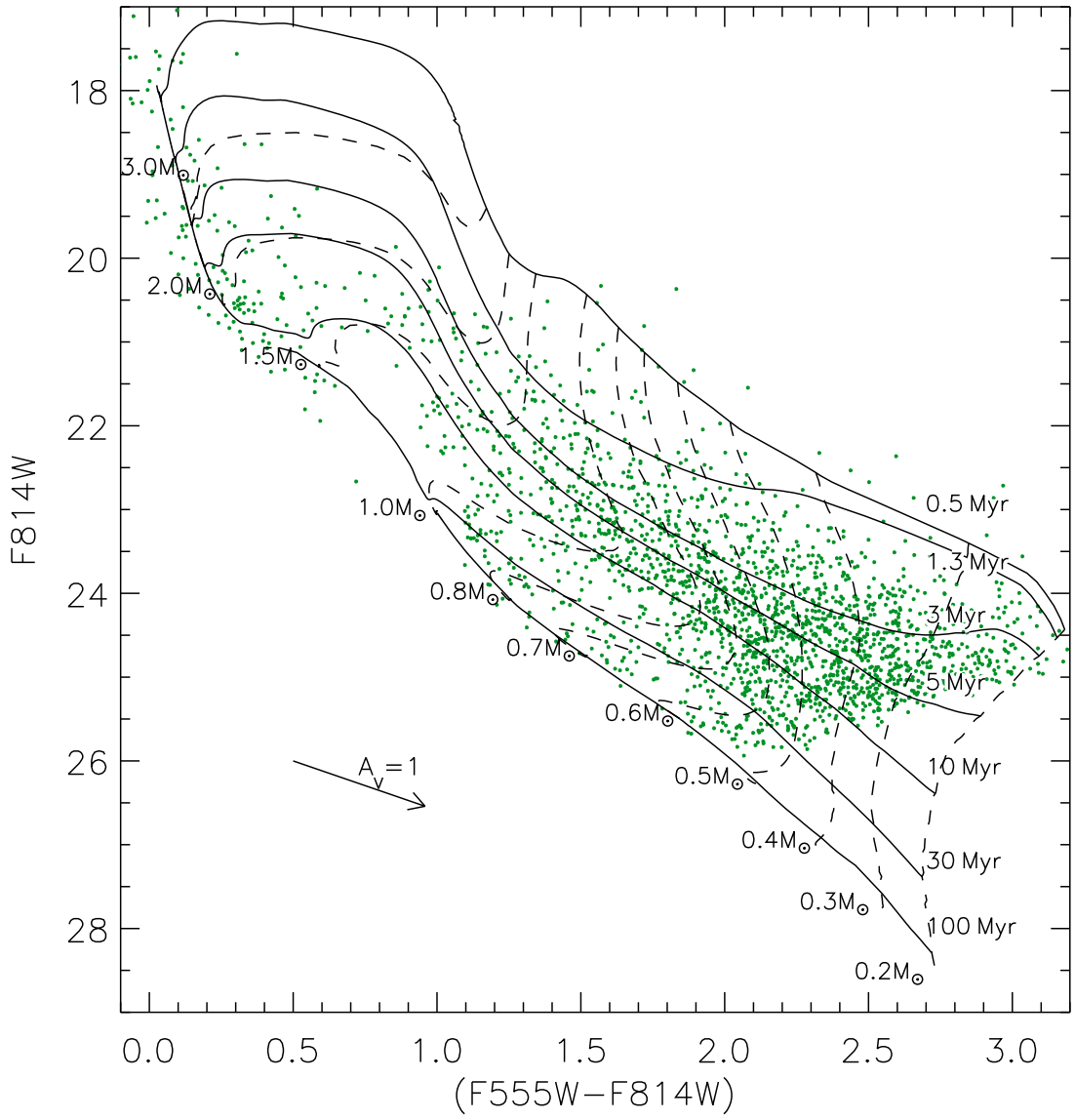

Figure 3.3 The stellar population of LH 95 with, overlaid, the FRANEC models converted into observable colors and magnitudes by extrapolating the results of the AMES model atmospheres for $Z = 0.01$.

However, for the present study, which focuses on the identification of any age distribution among PMS stars, the nature of these sources and their membership should be reevaluated. In order to study the spread of the field MS in the CMD of both LH 95 and the control field, we construct the Hess diagram of the complete stellar sample observed in the area of the association before any field subtraction. We bin the stars in the color- and magnitude-axis of the CMD and smooth the counts with a Gaussian kernel of 0.05 mag in $m_{555} - m_{814}$ and 0.16 mag in m_{814}. We repeat this process to construct the Hess diagram of the control field. The constructed Hess diagrams are shown in Figure 3.4. An important difference between the field population covered in the area of LH 95 and that in the control field is that LH 95 is embedded in the HII region named LHA 120-N 64C (or in short N 64C, Henize, 1956) or DEM L 252 (Davies et al., 1976), and therefore the reddening of the background field stars in the area of the system should be somewhat higher than those in the control field. However, a comparison of the Hess diagrams of Figure 3.4 shows that there is no significant variation of the field population between the two areas, and therefore the appearance of the nebula does not seem to affect significantly the field MS. This suggests that the LMC field population is mainly distributed in foreground with respect to LH95. Nevertheless, a small fraction of field stars could be located behind the nebula, and be affected by a larger extinction.

In order to test this possibility and further eliminate the sample of PMS cluster-members from potential field MS contaminants, we consider diagonal cross-sections of width 0.33 mag in the direction defined by the line $m_{814} = -1.92 \times (m_{555} - m_{814})$, and we fit with Gaussians the distributions of the stars along each of these strips. A sum of two Gaussian distributions is considered for the fit of the CMD of LH 95 and a single Gaussian for that of the control field. The centers and standard deviations, σ, of the best-fitting Gaussians are drawn over the Hess diagrams of Figure 3.4. We compare the σ of the best-fitting Gaussians to the MS, as a measurement of the broadening of the MS, between the CMD of LH 95 and that of the control field in Figure 3.5, where we plot σ for each selected strip as a function of the corresponding average luminosity. In this figure can be seen that σ and therefore the MS broadening are systematically smaller in the control field than in LH 95, in agreement to what we discussed above. This difference demonstrates quantitatively that the contamination of the CMD of LH 95 by field stars cannot be 100% removed, and this applies mostly to the reddest part of the field MS in the area of LH 95 due to higher reddening. As a consequence we further remove from the sample of cluster-member sources those that fall blueward of the minima between the

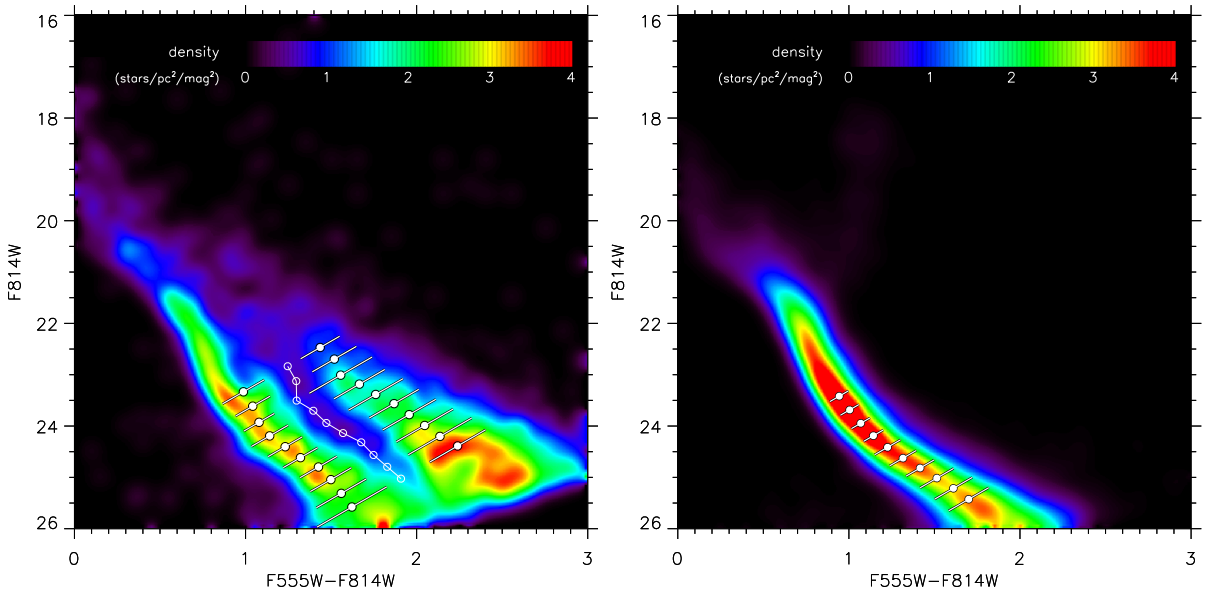

Figure 3.4 *Left*: Hess diagram of the stellar density in the area of LH 95, with no field subtraction. There are two distinct stellar sequences apparent, the MS attributed to the LMC field and the native PMS population. The results of the simultaneous fit of two Gaussians along diagonal cross-sections are drawn, using filled circles to indicate the centers of the Gaussians for every strip, open circles for the minima between them, and white lines following the directions of the strips for the standard deviations of the Gaussians. *Right*: The same as in the left panel for the area of the control field. This CMD demonstrates the complete lack of any PMS population in the local LMC field, making the distinction of the true PMS stellar-members of LH 95 quite straightforward. A single Gaussian is used to fit the MS of this CMD along identical cross-sections as for LH 95.

two gaussian fits of the CMD of LH 95, shown in Figure 3.4(*left*). This second selection border is drawn on the CMD of the area of LH 95 in Figure 3.6; we prolong this border at lower and higher luminosities, as shown with a dashed line in Figure 3.6. At the faint end a linear extrapolation in the CMD is chosen; for the bright end we arbitrarily define a cut in order to remove a handful of stars at $I \sim 22$ mag, undoubtedly located on the MS. There are 162 stars, which we consider to be field subtraction remnants, plotted with gray dots to the left of the MS border in Figure 3.6. These sources will be excluded from our subsequent analysis.

We stress that, despite the improvement of this field subtraction refinement with respect to that of Chapter 3, some uncertainty in the membership assignment on the tail of the distributions (close to the cut shown in Figure 3.6) is still present. This effect, which

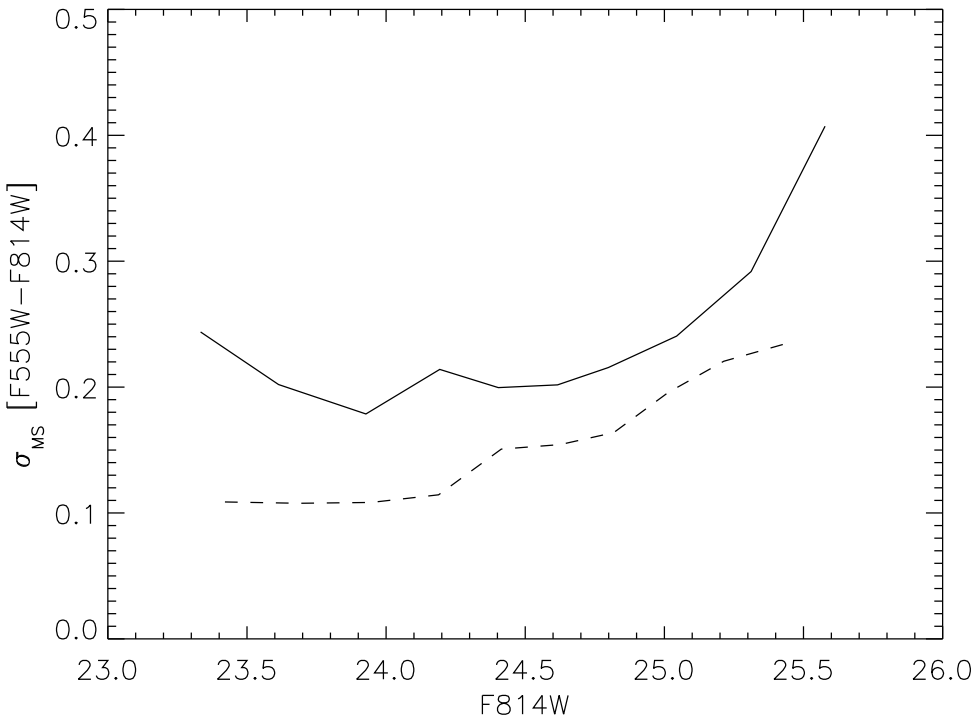

Figure 3.5 CMD broadening of the MS in color as a function of luminosity for the area of LH 95 (solid line) and the control field (dashed line). The smaller broadening of the MS in the control field than in LH 95 demonstrates that field stars could not be completely removed within the application of the statistical field-subtraction in Chapter 3. Here we refine our selection of true stellar-members for LH 95, based on the results of Gaussian fits to the distribution of the MS in the field and the system.

might affect the distribution of the oldest stars, should not be significant. The population, within the central region, considered MS field is about as numerous as that considered part of the young system (1904 and 1942 stars respectively). As a consequence, the number of young members erroneously removed being too blue should be roughly compensated by a similar number of MS stars redder than the minima between the two gaussian (Figure 3.4). This guarantees that the number of old PMS members of stars is fairly accurate, but could lead to an underestimation of the ages of some of those. In any case, since in this work we demonstrate a significant age spread for LH95, this fact would just reinforce our findings.

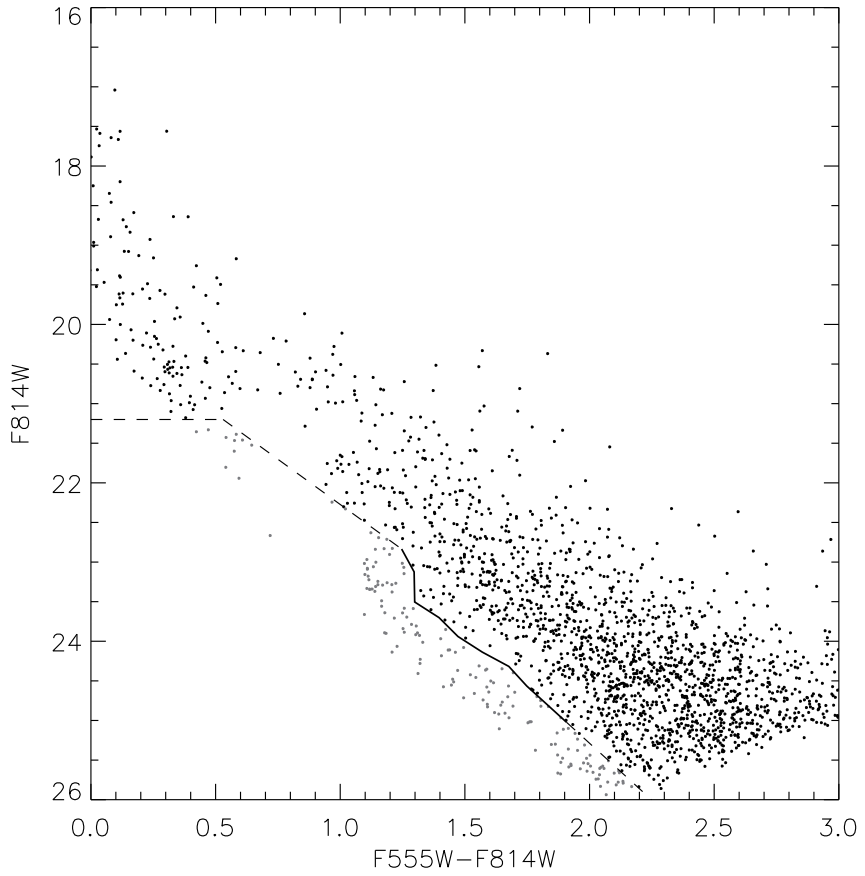

Figure 3.6 Refinement of the removal of the field contamination in the CMD of LH 95. The drawn solid line follows the minima of the best-fitting Gaussians to the MS and PMS stellar distributions before any field subtraction (see Figure 3.4*left*), showing that the bluest sources of the population clearly belong to the MS. The dashed line is our chosen continuation of the previous, at higher and lower luminosities. Sources located to the blue of this MS border and its extensions (dashed lines) are excluded from our analysis as true field-members.

3.4 Age determination of PMS stars

In this section we apply our new maximum-likelihood technique for the derivation of the ages of the PMS stars of LH 95 from their photometry. This method allows the determination of the age of a PMS star from its position in the CMD in a probabilistic manner, accounting for the physical and observational effects that affect the colors and magnitudes of all observed PMS stars.

In order to estimate the age of a young stellar system when only photometry is available, it is common practice to simply overlay a set of isochrones to the CMD and, by interpolation, assign an age to all the members. This approach, however, can lead to inaccurate results (Gouliermis et al., 2010). This is because every star is scattered from its original position in the CMD by a number of factors, and specifically by photometric errors, differential reddening, unresolved binarity, stellar variability, non-photospheric excess due to accretion, and scattered light from circumstellar material.

These effects, when not accounted for, bias the observed age distribution, both increasing the observed spread and systematically shifting the mean cluster age. These factors can be disentangled *only* on the basis of individual stars, which is the case when spectroscopic measurements are available for all stars. However, such observations on large numbers of stars are not technically feasible, and photometric observations are the most appropriate for collecting data on vast stellar numbers, like in the case of LH 95. In this case, a convenient way to estimate the overall effect of observational and physical biases to the original CMD positions of PMS stars is to compare the observed data with synthetic CMDs, which are constructed by the application of these biases to one or more theoretical PMS isochrones. There are some examples of such an approach presented in the literature, especially for the investigation of the relation between the observed luminosity spread and the true age spread among PMS star-members of young stellar systems (e.g., Burningham et al., 2005; Jeffries et al., 2007; Hennekemper et al., 2008; Hillenbrand et al., 2008).

In this context, Naylor & Jeffries (2006, hereafter NJ06) presented a rigorous approach to derive the age of young stellar systems accounting for photometric errors and binarity. They present a maximum-likelihood method for fitting two-dimensional model distributions to observed stellar CMDs. In their application, the two-dimensional models are probability density distributions in the CMD, obtained by applying binarity to a PMS isochrone of a given age, considering that the model representing a coeval population

in the CMD is not a line – like a theoretical isochrone – but a 2D density distribution. There are several advantages in the application of this approach. First, it enables one to account rigorously for the photometric errors in both color and magnitude when the fit is performed. Second, binarity is considered in the fitting process itself. Finally, this method allows the evaluation of its goodness-of-fit.

In the present study we further develop the method of NJ06, by extending its application to a realistic case of a PMS population, including in the computation of the two-dimensional models not only binarity, but also variability, crowding, and differential extinction.

3.4.1 From isochrones to density distributions in the CMD

As in NJ06, we wish to construct a stellar density distribution in the CMD for every age in the considered set of evolutionary models. This distribution represents the probability for a star of an assumed age to be found at a given point in the CMD. We consider the two families of evolutionary models (FRANEC and *Siess*) that we converted into magnitudes in the HST/ACS photometric system in Section 3.2.1. For every considered age, we populate the appropriate isochrone with $5 \cdot 10^6$ simulated stars. We assume the IMF of LH 95 derived in Chapter 3 and correct it for binarity. The change in the measured IMF slopes caused by binarity was already investigated in Chapter 3, through a Monte-Carlo simulation. Here we adopt these results, summarized in Table 3.1. We found that the IMF for intermediate and high-mass stars ($M > 1$ M$_\odot$) is almost insensitive on binaries, whereas for low-mass stars, the slope changes of up to 0.4 units adding an increasing fraction of unresolved binaries. Neglecting binaries leads to a shallower measured IMF.

Table 3.1 IMF slopes corrected for binarity, as a function of binary fraction

f	x ($M < 1M_\odot$)	x ($M \geq 1M_\odot$)
0.0	1.05	2.05
0.2	1.20	2.05
0.4	1.30	2.05
0.5	1.35	2.1
0.6	1.40	2.1
0.8	1.45	2.1

For smaller masses, not having a direct measurement of the IMF in LH 95, we assume

a value $x = 0.3$ compatible with the Kroupa (2001) IMF. This value was also assumed in Chapter 3 to compute the binarity-corrected IMF slopes reported in Table 3.1. It is worth noting that small changes in the slope of the assumed IMF do not influence significantly the ages for single stars derived using our method (see Section 3.4.2), but could affect the evaluation of the goodness-of-fit (Section 3.5) we use to determine the age spread.

After simulating a population of stars for every age, (for the two families of evolutionary models, and all the binary fractions f reported in Table 3.1, we displace with a random process the stars in the CMD according to the dictations of several factors. They are discussed below.

(i) Rotational variability: We simulate statistically the variation of magnitudes in the F555W and F814W bands due to variability caused by stellar rotation. We consider the results of Herbst et al. (2002). These authors surveyed the PMS population of the Orion Nebula Cluster (ONC) in the I-band over 45 nights, obtaining the light curves for $\sim$ 1500 candidate members. We consider their catalog of peak-to-peak variations. A single imaging of a young stellar system, like LH 95, statistically measures the flux of variable stars in random phases of their variation. Considering, at this point, variability only due to dark spots on the stellar surface, the measured fluxes are equal or fainter than those predicted if no variability is considered. Therefore, if we assume for simplicity sinusoidal light curves, the statistical distribution of I-band variations for a star with a measure peak-to-peak $\Delta I_{\rm max}$ is the distribution of $\Delta I_{\rm max} \cdot (\sin x + 1)/2$ with $0 < x < 2\pi$. We compute this for every star of the catalog of Herbst et al. (2002) and combine the derived distributions. The result, shown in Figure 3.7a, is the observed I-band variation distribution that we assume as valid for a single epoch photometry in a young stellar system. The peak at very low ΔI is mainly due to the large fraction of stars not showing significant rotational variability. We displace the brightness in the F814W filter of each of the simulated stars along each isochrone by a value randomly drawn from this distribution.

The amplitude of the $V-$band variation due to dark spots is generally larger than in I, and the ratio between the two depends, in general, on the temperature of the star-spot, on the temperature of the photosphere, and the filling factor of the spot. According to the results of Herbst et al. (1994), the ratio $\alpha = \Delta I/\Delta V$ spans from 0.39 to 0.88. The variations in the two bands should be correlated if the observations were close to co-temporal. In our photometry, however, V and I observations were

taken separately, one 4 days after the other. According to Herbst et al. (2002), the rotational period distribution of T-Tauri stars is bimodal, with a peak at $P \sim 2$ days and another at $P \sim 8$ days. Even considering the longest periods, the time delay of our observations covers about half period. As a consequence, we cannot consider the $V-$ and $I-$band variations to be correlated. We therefore simulated the $V-$band variation distribution from the $I-$band one, multiplying each of the simulated I values for a factor $1/\alpha$, where α was randomly chosen within the range 0.39-0.88. Then these V variations were applied randomly (regardless ΔI) to all the simulated stars.

(ii) Accretion: On-going accretion from the circumstellar disk onto the stars also affects the observed fluxes. In the optical wavelength range, two components contribute to the accretion excess: an optically thin emission generated in the infalling flow, and an optically thick emission from the heated photosphere below the shock (Calvet & Gullbring, 1998). The optically thin emission is characterized by a line-dominated spectrum, similar to that of a HII region; in particular the bright Balmer emission is commonly used to derive mass accretion rates for PMS stars (e.g., De Marchi et al., 2010). In $V-$ and $I-$ band the optically thick emission dominates, producing an excess, in spectroscopy referred to as "veiling", analogous to the presence of a hot spot on the stellar photosphere. For a given accreting star, the spectrum and intensity of the excesses may vary with time, due to both variations in the mass accretion, and stellar rotation.

In order to model the overall effect of accretion on a large sample of low-mass stars, we utilize the results of Chapter 2. In this work the stellar population of the Orion Nebula Cluster was studied from multi-band optical photometry and spectroscopy. In particular, for every star, the veiling excesses were determined from the comparison of the observed colors with the intrinsic ones, after modeling the color displacements caused by accretion and extinction. For the ONC, the authors find about 60% of the members showing evidences of accretion veiling. We consider this stellar sample, and restrict to the mass range $0.3\mathrm{M}_{\odot} \leq M \leq 3\mathrm{M}_{\odot}$, relevant to our study. Then, we displace each of the simulated stars for every isochrone of an amount ΔV and ΔI equal to the veiling of a randomly chosen Orion member from Chapter 2. An example of the distribution of displacements in color and magnitude is shown in Figure 3.7b.

We stress that, statistically, the effect of variability in the mass accretion is already included in the results of Chapter 2; this is because their observation produced a "snapshot" of the veiling excesses for $\sim$ 1000 members at a given time. It could be argued that the members of LH 95, with an average age about twice as older as Orion, could be affected by less veiling than for the Galactic cluster, since mass accretion decreases with stellar age (Sicilia-Aguilar et al., 2006). With no direct measurements of accretion in LH 95 we are unable to accurately constrain the real distribution of veiling excesses for our region. Nevertheless, there are evidences (e.g., Romaniello et al., 2004; De Marchi et al., 2010) suggesting that accretion lasts longer in the Magellanic Clouds, because of the lower metallicity. Because of this we are confident that the distribution of V and I excesses we assumed could be appropriate for LH 95. Future measurements of mass accretion in our region (e.g., from Hα photometry) could help to better constrain this parameter.

(iii) Binarity: For every isochrone, we associate pairs of stars from the simulated sample. This is done randomly, but allowing only configurations within a mass range, defined by constraining the mass ratio to be a flat distribution from 0.2 to 1 (Woitas et al., 2001), and do not allow binary systems to form with mass ratio < 0.2. We let the binary fraction be a free parameter, and compute different sets of two-dimensional models for different choices of its value. This is because, as we discuss later in detail, the assumed binary fraction influences significantly the derived ages, and therefore we present and compare findings obtained with different choices of this parameter. We assume a unique binary fraction and mass ratio distribution for the whole PMS mass-range. In principle high-mass stars are known to have both higher binary fraction and higher binary mass ratio than intermediate and low-mass stars (e.g., Lada, 2006; Zinnecker & Yorke, 2007). However, this does not affect our treatment, since in our analysis of stellar ages we only consider PMS stars and not the 'evolved' high-mass MS stars of LH 95.

(iv) Differential extinction: In Chapter 3 we derived the extinction distribution for LH 95, measuring the reddening of the upper main-sequence (UMS) from the ZAMS. In that work not all the UMS were considered to derive the A_V distribution, but some of the reddest were removed, since we suspected them to be Herbig Ae/Be stars. The average extinction is quite low, equal to $A_{555} \simeq 0.6$ mag, and the its distribution spans from $A_{555} = 0$ to $A_{555} \simeq 1$. We use the relation $A_{555}/A_{814} = 1.85$,

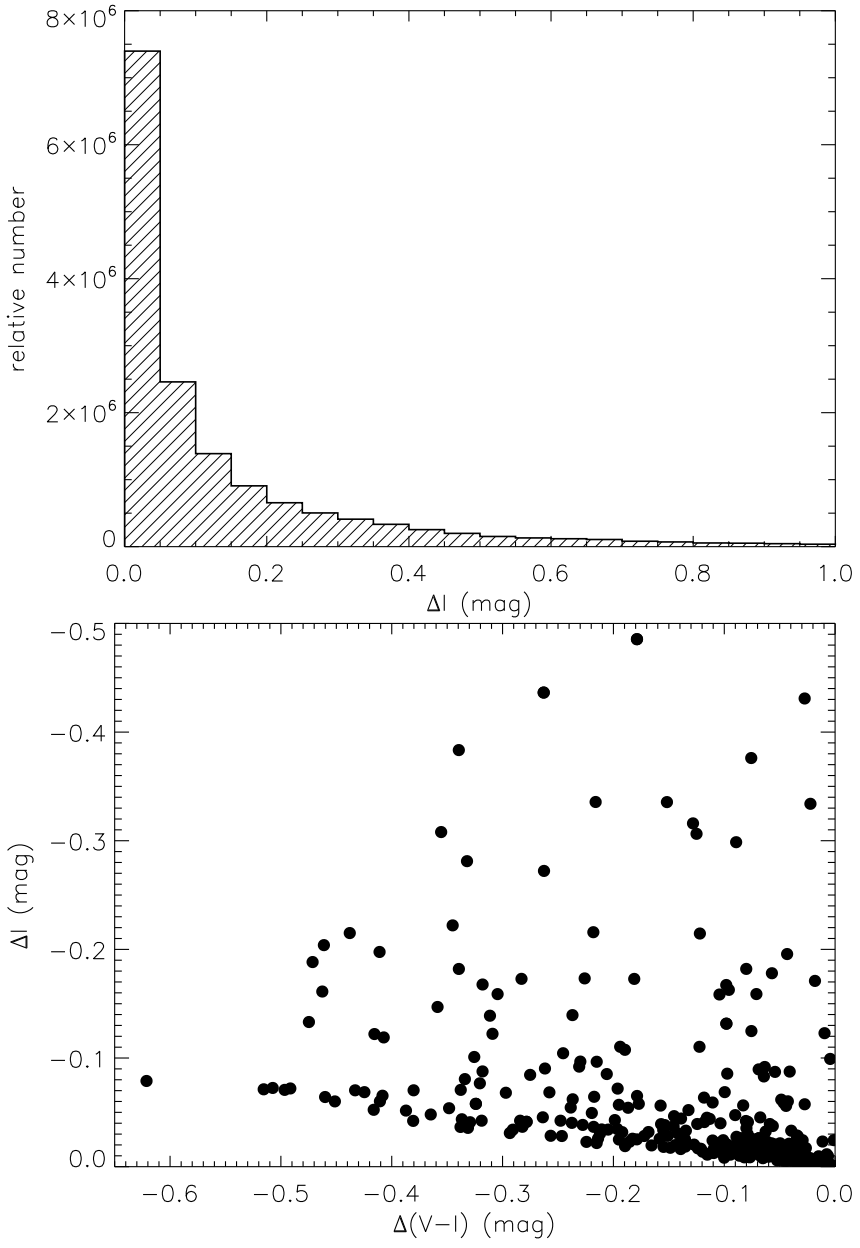

Figure 3.7 *Upper panel:* Distribution of the expected $m_{814}-$band variation due to dark spots and stellar rotation in single epoch photometry, obtained from the peak-to-peak distribution of Herbst et al. (2002). *Lower panel:* Displacements in color and magnitude caused by accretion veiling, from the findings of Chapter 2.

as it was computed in Chapter 3 for the ACS photometric system, using the extinction law of Cardelli et al. (1989). In our simulations we apply a random value of extinction to each star, drawn from the real measured A_{555} distribution of LH 95.

(v) Source confusion: LH 95 is a loose association, not centrally concentrated, which comprises at least 3 subclusters of somewhat higher stellar densities. As a consequence, source confusion due to crowing does not play a dominant role. Nevertheless, we include in our simulations a 5% source confusion, by adding the flux of this fraction to sources regardless of their assumed binarity, i.e., by allowing for random confusion also between binaries and between binaries and isolated stars. We stress that, since this additional pairing is done randomly, because of the IMF the modeled source confusion is also magnitude dependent, favoring the disappearance of faint systems.

For the computation of the 2D stellar densities we do not include photometric errors as additional sources of spread. While the aforementioned biases, which we include in the simulations, can be considered as part of *the model*, the photometric errors are part of *the data*, which the model is fitted to, and therefore photometric uncertainty will be consider later in the fitting process (Section 3.4.2).

It should be finally noted that the constructed 2D distributions are not re-normalized to, e.g., a total integral of 1, because isochrones of different ages have different maximum mass. Instead, we use the same sample of 5 million simulated stars with masses drawn from the assumed IMF and we consider only the fraction included within the limits of each isochrone. In this manner, although the total number of synthetic stars changes slightly among different 2D distributions, the number of stars per mass interval is constant. In other words, since our method to assign stellar ages and determine the cluster age is based on relative comparison of probabilities, an overall normalization of all the models is completely unnecessary.

In Figure 3.8 we show an example of the result of the application of our simulations to a 2 Myr isochrone from the *Siess* family of models. In this figure it is evident that the CMD-spread of a 'perfect' coeval PMS stellar population, produced by the biasses discussed above, can generate an observed dislocation of the stars of more than 1 mag in luminosity and up to 1 mag in color. The bifurcation seen at the faint end of the simulated distribution is an effect of binarity. This is due to the fact that the evolutionary models do not cover masses lower than 0.1 $M_{\odot}$. As a consequence our random selection of binary

pairs is unable to simulate binaries with the second component below this limit. This effect does not alter the results of our analysis, because, as it is seen in Figure 3.8, our photometry does not reach these masses.

3.4.2 Derivation of stellar ages. The single star case.

In this section we use statistics to address the issue of deriving *the most likely age of a single PMS star, for which the only information is its measured brightness and the corresponding photometric errors*. Specifically, we derive the age of each star in our catalog using a maximum-likelihood method by comparing the observed position of each star in the CMD with a complete set of simulated 2D stellar distributions, constructed from theoretical isochrones with the method described above. Each of these simulated distributions provides an estimate of the probability of finding a star in a specific CMD location, providing that we know its age. In Section 3.4.4 we will then generalize this approach to derive the best age of the entire cluster, considering all the measured stars simultaneously.

In practice, if the photometric errors were zero, the most likely age would be that of the modeled distribution that gives the highest probability in the CMD position of the star. In reality, since there are errors in the measured m_{555} and m_{814} magnitudes of the star, the observed position of the star in the CMD is also probabilistic, defined by the gaussian distributions of the photometric errors. Therefore, if we consider a star observed in the position (V_i, I_i) on the CMD and a model stellar distribution of a given age t, for every point (V_j, I_k) of the CMD-space there are two probabilities that should be specified: a) the probability, defined by the 2D model, that a star of age t is located in (V_j, I_k), and b) the probability, defined by the Gaussian distributions of the photometric errors, that the star we observe in (V_i, I_i) is instead located in (V_j, I_k) but displaced by the photometric errors. The product of these two probabilities, integrated over the entire CMD-space, provides the likelihood that the considered star has an age equal to t. This likelihood, normalized on all the possible ages, represents the exact probability that the star has an age between t and $t + \mathrm{d}t$.

Since the photometric errors in the color-magnitude space are correlated, we apply this method in the magnitude-magnitude plane. Mathematically, we define the likelihood $L_i(t)$ for the $i-$th star in our sample as function of the age t as:

$$L_i(t) = \int_{V,I} \rho(V, I, t)\ U_i(V - V_i, I - I_i)\mathrm{d}V\,\mathrm{d}I \tag{3.1}$$

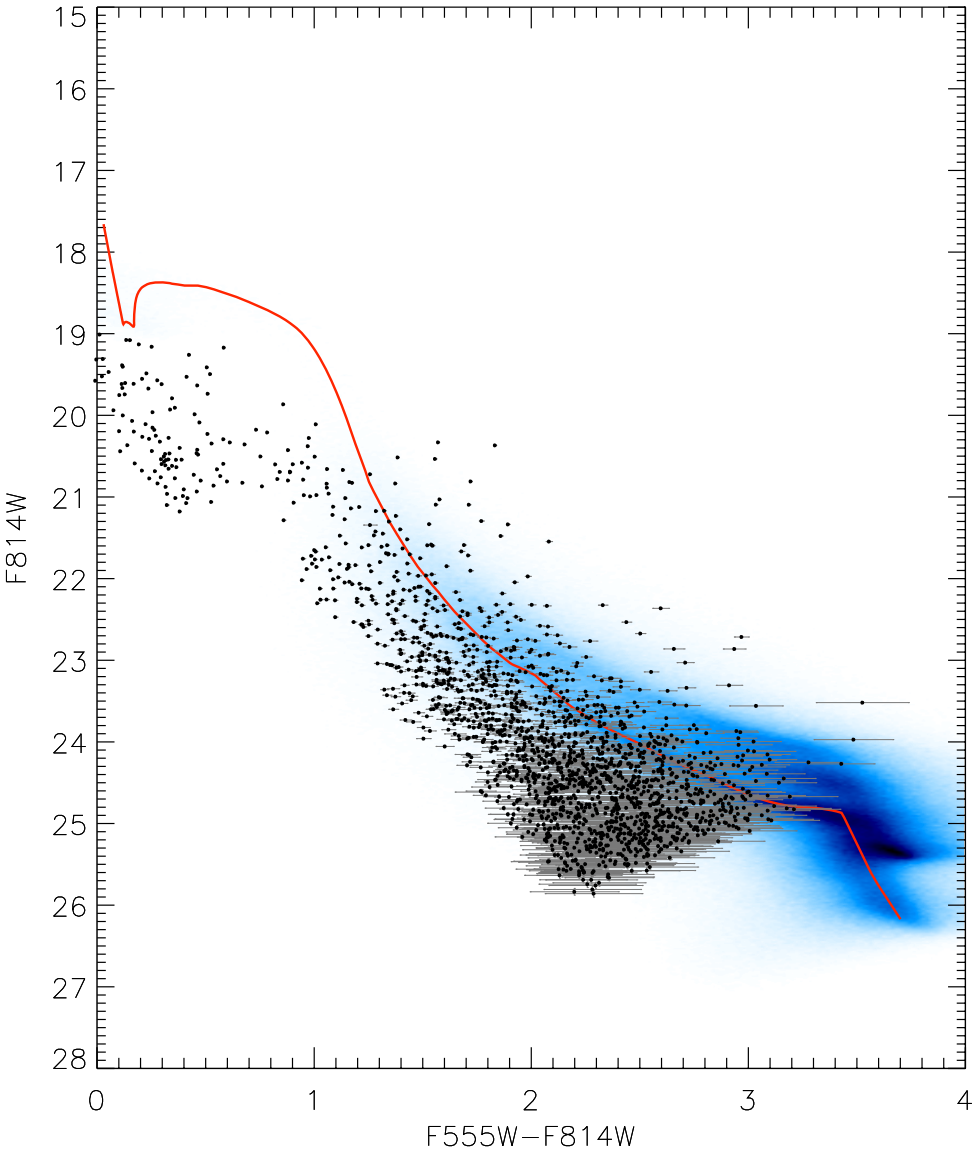

Figure 3.8 Example of a 2 Myr isochrone from the *Siess* models, which is converted into a 2D density CMD distribution (blue contour), after the application of binarity (for an assumed binary fraction $f = 0.5$), accretion, variability, differential extinction and crowding, as described in Section 3.4.1. The original isochrone is overlaid with the red line. The dots are the stars of our photometry with error bars indicating the 1σ photometric errors. An average reddening of $E(V - I) = 0.275$ mag, typical for LH 95 (Chapter 3), is applied.

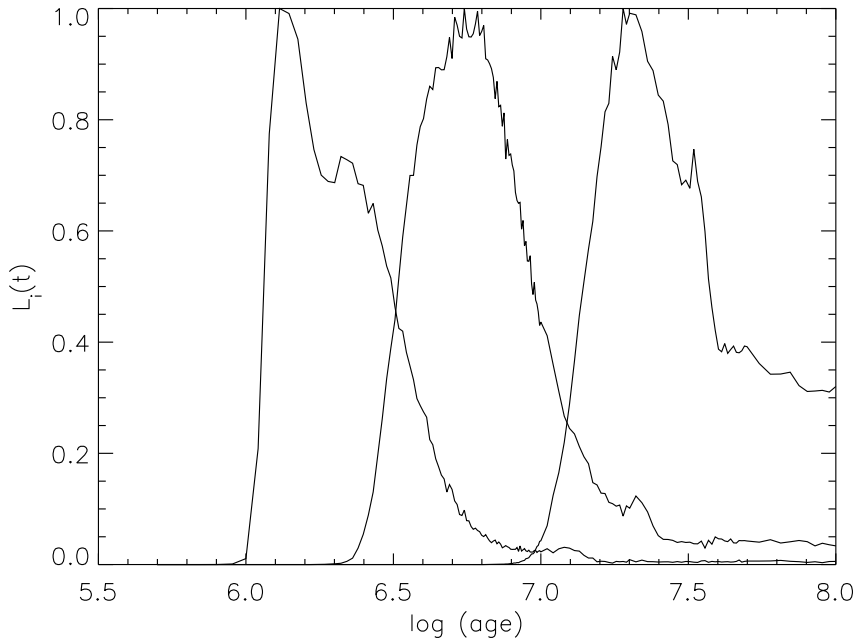

Figure 3.9 Example of likelihood functions, $L_i(t)$, for 3 stars from our photometric sample. The maxima of the functions indicate the assigned best-fit ages for the sources, equal to 1.3, 5.5 and 19 Myr respectively in this example.

where $\rho(V, I, t)$ is the surface density computed from the isochrone of age t, and

$$U_i(V - V_i, I - I_i) = \frac{1}{2\pi\sigma_{V_i}\sigma_{I_i}} e^{-\left[\left(\frac{V-V_i}{\sigma_{V_i}}\right)^2 + \left(\frac{I-I_i}{\sigma_{I_i}}\right)^2\right]} \tag{3.2}$$

is the 2D Gaussian representing the photometric error of the $i-$th star.

In Figure 3.9 we show an example of the likelihood function $L_i(t)$ computed numerically for three stars in the LH 95 catalog, assuming 2D models obtained from the FRANEC grid and assuming a binary fraction $f = 0.5$. The age assignment for every star is performed by maximizing $L_i(t)$. For example, the three stars whose $L_i(t)$ functions are shown in Figure 3.9, will have most probable ages of 1.3 Myr, 5.5 Myr and 19 Myr.

In order to estimate the accuracy in the age determinations, we isolate for every likelihood function the range, in $\log(t)$ that includes 68% of the area under the curve, in analogy with the $\pm 1\sigma$ interval for a normal distribution. Since for some stars the shape of $L_i(t)$ is highly skewed, we choose to define the limits of the interval to delimit identical areas of 34% of the total to the left and to the right from the peak of the distribution. We then call ϵ the width of the range, in units of $\log(t)$. Indicatively, if a $L_i(t)$ were normal, $\sigma(t)$ would be equal to $\epsilon/2$.

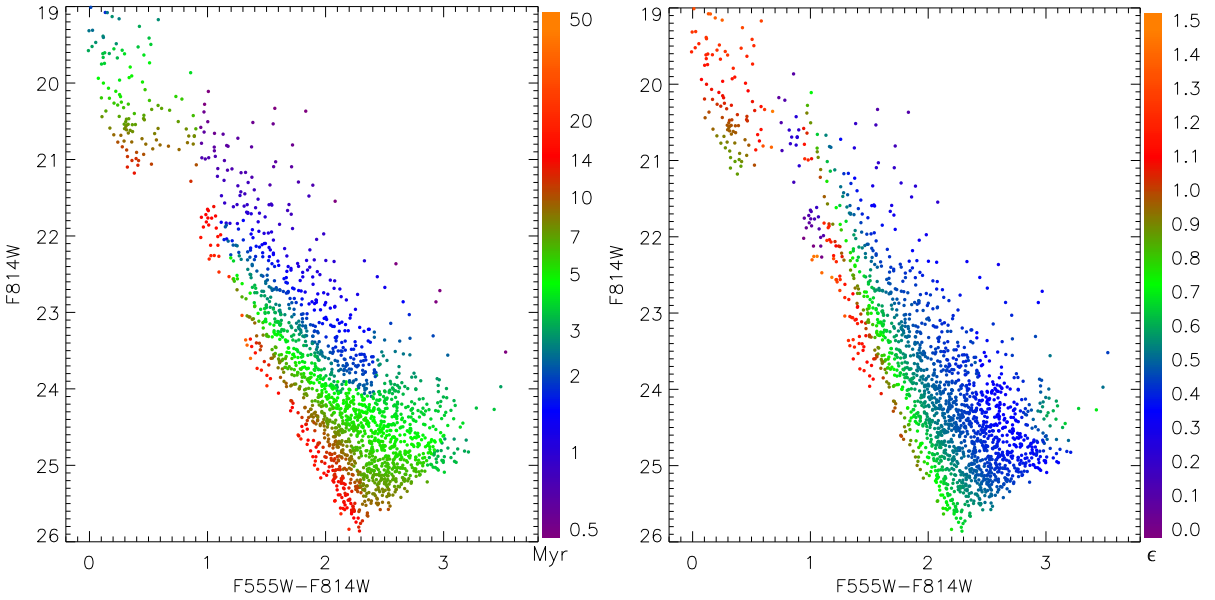

Figure 3.10 *Left*: Color-magnitude diagram with the PMS stars color-coded according to their individual ages derived with our maximum-likelihood method. The model distributions were derived with the use of theoretical isochrones from the FRANEC family of models. The assumed binary fraction is $f = 0.5$. *Right*: The same CMD with the stars color-coded according to their ϵ parameter (see Section 3.4.2).

Figure 3.10(*left*) shows the derived best-fit stellar ages in the CMD, assuming the evolutionary models of FRANEC and a binary fraction $f = 0.5$. In Figure 3.10(*right*) we show the corresponding variation of ϵ along the CMD. It is evident that, whereas the age assignment turns out to be relatively precise in the PMS regime, for higher masses, close to the PMS-MS transition ($m_{814} \lesssim 21$) the uncertainty increases up to $\epsilon \simeq 1.5$ dex. This is due to the fact that PMS isochrones of different ages are closer to each other in this range, and tend to overlap in the MS regime. The higher values of ϵ on the blue side of the sequence are also due to the fact that theoretical isochrones of ages $\gtrsim 10$ are also close to each other, since PMS evolution is significantly slower for these ages than for younger stages of PMS contraction.

We compare the distributions of the best-fit ages for our photometric sample changing the binary fraction and the original family of evolutionary models. This is shown in Figure 3.11, where we also indicate the average age for each distribution. It this figure is evident that increasing the binary fraction leads to the prediction of older ages. This confirms the findings of Naylor (2009). Indeed, a higher fraction of binary systems produces a simulated 2D distribution shifted toward higher luminosities, hence older measured ages. Passing from $f = 0$ to $f = 0.8$, we predict a difference in age of up to 0.2 dex (which is

60% older ages.).

In the same figure we also overlay the distribution of ages computed only by interpolation between theoretical isochrones, without the addition of any observational and physical bias except for the average extinction of LH 95. In this case we find that the average age is higher than that derived from our statistical method assuming $f = 0$. This is due to the effect of dark spots and accretion. The first biases the predicted luminosities toward fainter values; the second toward brighter luminosities and bluer colors. In particular, the color effect caused by veiling affects more the position in the CMD than the increase in the fluxes, requiring an older isochrone to fit the observed sequence.

In conclusion, we find that, in the derivation of stellar ages for a young PMS cluster, neglecting binaries leads to an underestimation of the ages, neglecting variability and accretion to an overestimation of those. The two effect counterbalance, in our case, for a binary fraction $f = 0.5$ and assuming star-spot and accretion values from the 2 Myr Orion Nebula Cluster.

3.4.3 Spatial variability of stellar ages

As we have shown in Chapter 2, LH 95 is not a centrally concentrated cluster. It presents 3 main concentrations of PMS stars, named in our previous work "subcluster A, B, C", located respectively at the eastern, western, and southern edges of LH95. They include about half of the stellar population of the region, while the rest of the population is distributed over the area between the three. Since the projected distance between the stellar clumps is quite large (15 - 20 pc), it could be plausible that star formation did not occur simultaneously all over the entire region, but sequentially. A Galactic example of such scenario can be found in the Orion complex (Briceño, 2008), where different populations, from 2 to 10 Myr old, are distributed over a similar range of distances.

We investigate if the stellar sub-groups in LH95 present different average ages, in order to rule out the possibility that the measured broad age distribution for the entire region (Figure 3.11) is simply due to a superposition of populations with different ages, instead of the effect of observational biases and, maybe, a real age spread. To this purpose, we isolate the members in the three subclusters, using the same selections as in Chapter 3. Then we consider the distribution of ages limited to each of the three subregions, in comparison with that of the entire LH 95. This is illustrated in Figure 3.12. It is evident that, in each region, the distributions are very similar, spanning from less than 1 Myr to

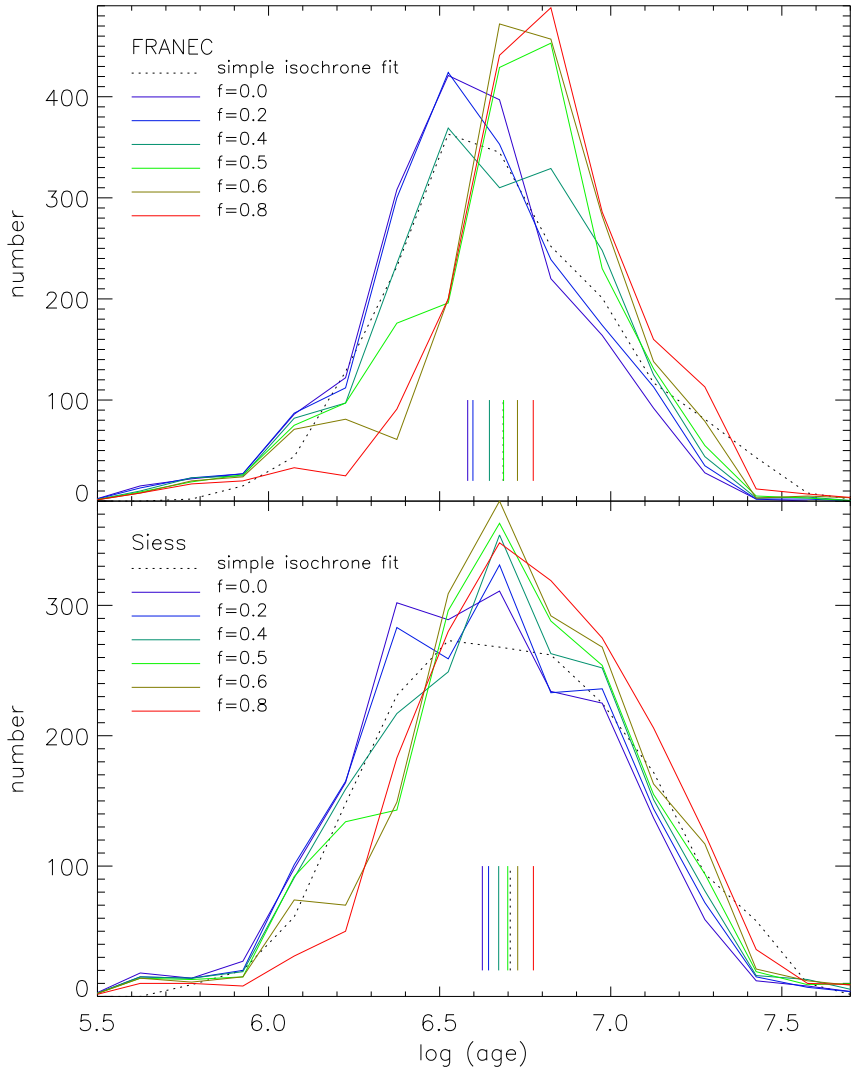

Figure 3.11 Distribution of maximum-likelihood stellar ages for the LH 95 members, computed using 2D CMD distribution models, based on FRANEC (upper panel) and *Siess* (lower panel) evolutionary models. We assume different binary fraction values f from 0.0 to 0.8. For each family of isochrones, we also show the distribution of ages computed only by interpolation of isochrones in the CMD, without accounting for physical and observational biases (black lines) . The vertical lines (colored appropriately) in each panel indicate the mean value of the age for each plotted distribution.

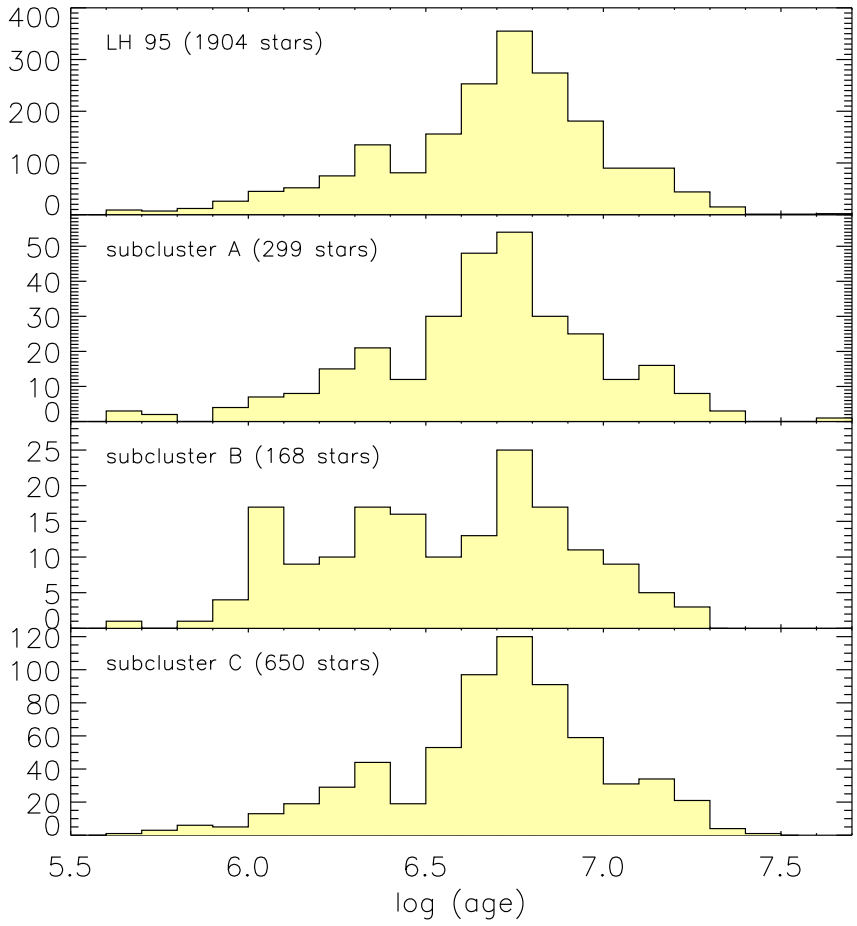

Figure 3.12 Comparison between the age distribution of the entire region and the three denser sub-clusters, for FRANEC evolutionary models and $f = 0.5$.

25 Myr, with a peak at ∼5 Myr. The only evident anomaly is an overabundance of young members for sub-cluster B. However, this group of stars encloses the densest concentration of PMS stars in the whole region, with more than 150 star within ∼ 2 pc. Because of this, stellar confusion due to crowding should be particularly dominant in this area, producing a number of overluminous stars due to unresolved superposition, and, thus, a fraction of apparently younger members. This is, however, not a problem for the analysis of the cluster age (Section 3.4.4). In our CMD modeling (Section 3.4.1) we have purposefully included the effect of crowding affecting 5% of members. The overabundance of young stars in subcluster B is caused by about 40 stars, which are ∼ 2% of the total stellar sample.

Considering this, we exclude the presence of any spatial variations of the ages in LH 95.

Despite the irregular density of stars and the relatively large size of the region, LH95 must have formed as a whole, in a unique episode of star formation.

3.4.4 Age of the entire cluster

In section 3.4.2 we derived the most likely age for every star in the sample. Here we derive the best-fit age for the entire stellar system. In a similar way as in NJ06, we compute this age by maximizing the "global" likelihood function $L(t) = \prod_i L_i(t)$. To compute $L(t)$ we restrict our treatment to the stellar sample with $22 \leq m_{555} \leq 27$. In particular, we want to eliminate any biases introduced by detection incompleteness, which would lead to the detection at the faint-end of more young bright members than old faint ones. The detection completeness reaches $\sim 90\%$ at $m_{555} = 27$ (Chapter 3), and we consider this threshold as a reasonable limit for our analysis here. We stress that, as in Naylor (2009), we could include the detection completeness function in the 2D models derived in Section 3.4.1, and then recover the implied cluster properties using our maximum likelihood procedure considering all the stars. In this way, we could test for bias also as a function of our chosen completeness limit. Nevertheless, considering the large stellar sample we have at disposal, we prefer to limit out analysis on the luminosity range where we that detection incompleteness does not affect our photometry. In this way we remove any additional uncertainty in the cluster age caused by a possible inaccuracy of the measured completeness function.

In addition, we do not include in the analysis the bright members of both the MS and the PMS-MS transition, for two reasons: 1) as shown in Figure 3.10(*right*), the accuracy of the age estimation for these sources is poor, and 2) these sources have very small photometric errors, which means that the 2D Gaussian distribution representing the errors (Eq. 3.2) goes to zero very fast in the neighborhood of the specific CMD loci, and so does $L_i(t)$. Such very small values of $L_i(t)$ would dominate the product $\prod L_i(t)$, biasing the resulting global likelihood function. From a mathematical point of view this effect is legitimate, because it only means that during the fit the data points with the smallest uncertainties dominate the statistics. However, in practice if the observational errors are much smaller than the intrinsic uncertainty of the models (in our case, the uncertainty in the theoretical evolutionary model computation and the modeling of the scattering) a strict application of the former can lead to unrealistic results.

In Figure 3.13 we show the derived $L(t)$ functions, in logarithmic units, for both

	FRANEC	Models	*Siess*	Models
f	age (Myr)	$\log L_{\max}$	age (Myr)	$\log L_{\max}$
0.0	2.8	2615.26	3.0	2492.16
0.2	3.0	2578.42	3.3	2456.14
0.4	3.6	2548.63	3.6	2431.42
0.5	3.9	2533.37	3.8	2415.62
0.6	4.1	2517.49	4.0	2398.78
0.8	4.4	2492.71	4.3	2377.05

FRANEC and *Siess* isochrones and different choices of binary fraction f. The plateau at old ages, in comparison to the cut-off at young ages, is due to the fact that old isochrones tend to be closer to each other and closer to the sequence of PMS stars observed in the CMD than the young isochrones. As a consequence, the 'distance' from a given star, in units of σ of the photometric errors, is on average lower for the older isochrones than for the younger, resulting to higher probabilities for the former.

Results of our analysis are given in Table 3.4.4, where we show the ages at the peak of each $L(t)$, as well as the associated values of likelihood for each choice of parameters. Our analysis also shows that the best-fit age is very sensitive to the assumed binary fraction, consistently with what we found in Section 3.4.2 analyzing the distribution of ages for single stars. as it increases of up to 60% with increasing binarity (depending on the considered isochrone models). The peak values of $\log L(t)$ given in Table 3.4.4 do not have an absolute meaning, given the arbitrariness of the normalization of the 2D density models $\rho(V, I, t)$.

In Figure 3.14 we show again the observed CMD, with the best-fit 2D density models from FRANEC (*left*) and *Siess* (*right*) grids of isochrones superimposed for $f = 0.5$, for the luminosity range we considered in our analysis. The two models are very similar, with FRANEC producing a slightly over-density at the reddest end of the considered magnitude range.

From Figure 3.14, it is evident that an additional spread, besides that modeled in the 2D density distribution, is evident in our data. In particular, there are observed members at the sides of the sequence which may not be well modeled by the simulated distributions for a single cluster age. This may be indicating of an additional age spread in LH95. In the next sections we study this possibility.

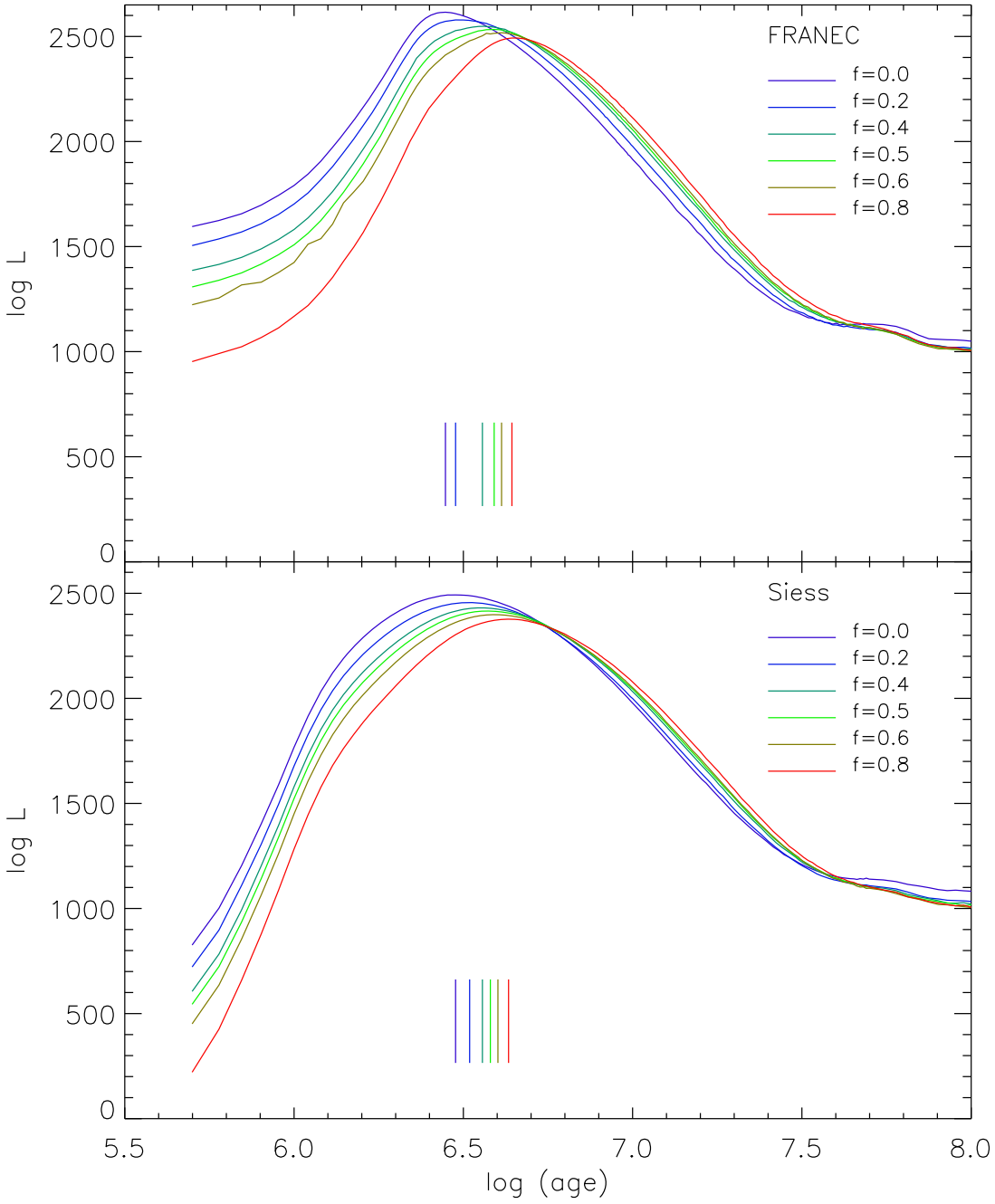

Figure 3.13 Global likelihood functions $L(t)$, derived from the simultaneous fit of the the 2D stellar distribution models to all PMS stars in our photometric sample with $22 < m_{555} < 27$ based on FRANEC (upper panel) and *Siess* (lower panel) evolutionary models. We assume different binary fraction values f from 0.0 to 0.8. The vertical lines (colored appropriately) in each panel indicate the age of the maxima of each curve.

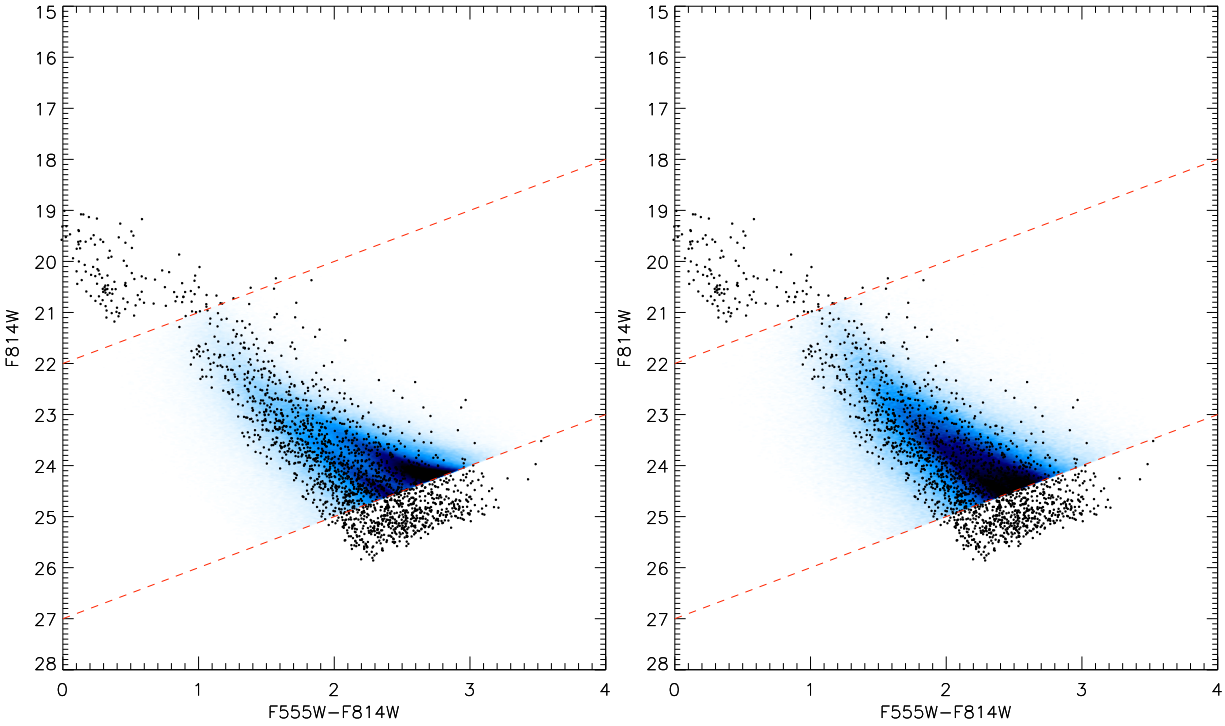

Figure 3.14 The observed CMD with the 2D density models that provide the best fit to the observed sequence of PMS stars, assuming binarity of $f = 0.5$ for the FRANEC (*left panel*, age 3.9 Myr) and the *Siess* (*right panel*, age 3.8 Myr) family of evolutionary models. The dashed lines denote the subsample of the photometry used in this analysis. For clarity, only the portion of the 2D models within this luminosity range is shown.

3.5 Age spread of PMS stars in LH 95

3.5.1 Verification of an age spread

In the previous section we have determined the average age of LH 95 isolating the 2D model that provides the best fit to the observed sequence, for two families of theoretical evolutionary models. In this section we wish to investigate whether the spread of the PMS stars in the observed CMD is wider or not than that of the simulated 2D density distributions as they are produced by accounting for the sources of CMD-broadening discussed in Section 3.4.1, *after we additionally apply the photometric uncertainties*. If indeed the observed CMD broadening of PMS stars is wider than the synthetic derived from a single isochrone, under the hypothesis that we do not have underestimated the sources of apparent luminosity spread in the CMD, this would suggests the presence of a *real* age spread in LH 95. The method applied in this section, described below, also allows us to qualify the goodness of our fit.

This method can be compared to a standard χ^2 minimization, in which the best fit model is obtained by minimizing the χ^2, and this value is then compared to the expected distribution of χ^2 given the degrees of freedom. A measured χ^2 which significantly exceeds the expected distribution indicates a poor fit, while a value too low suggests that the fit is suspiciously good, which is the case, e.g., of overestimated errors. In our statistical framework, the procedure is qualitatively similar, with two main differences: i) since the measured $\log L(t)$ is maximized, a poor fit is found when the measured value is lower than expected; ii) the expected distribution of $\log L(t_{\text{best-fit}})$ is not analytical but can be derived numerically. In general, this distribution varies for different assumed 2D models, and depends on the number of data points.

We compute the expected distribution of $\log L$ as follows. We consider the two best-fit 2D models shown in Figure 3.14, limiting ourselves, for the moment, to the case of an assumed binary fraction $f = 0.5$. We limit the model to the same range used to derive the cluster age ($22 \leq m_{555} \leq 27$), and simulate a population of stars randomly drawn from the distribution of the model itself, as numerous as the LH 95 members in the same luminosity range. We consider each of the simulated stars, and displace its position in the CMD by applying the average photometric error measured in its immediate CMD area. In particular, for each simulated source we consider the 60 observed stars closer to it in the magnitude-magnitude plane. Then we randomly assign the photometric error of one of these 60, with a weight proportional to the inverse of the distance in magnitudes. We then apply the same method described in Section 3.4.4 to the simulated population, deriving $\log L$. We iterate this procedure 100 times, each time randomly simulating a different population of test-stars from the same best-fit 2D model. In this way we obtain 100 values of $\log L$ describing the *expected distribution* of this variable for the considered model, which is compared to the *measured* value computed for the observed sequence of PMS stars.

For the two models shown in Figure 3.14, i.e., the FRANEC 3.9 Myr and the *Siess* 3.8 Myr models for $f = 0.5$, we obtain predicted $\log L$ values of 2739 ± 20 and 2473 ± 19 respectively ($\pm 1\sigma$ interval). In comparison, the measured values of 2533 and 2416 (see Table 3.4.4) are significantly lower, at $\sim -10\sigma$ and -3σ from the expected values. This implies that the observed sequence *cannot originate from the best-fit models by additionally applying photometric errors*, but that the stars tend to be statistically located in regions of the CMD where the 2D model has lower density ρ (see Eq. 3.1), and hence a lower average $\log L_i$ for the stars. For guidance, the low density regions of the 2D

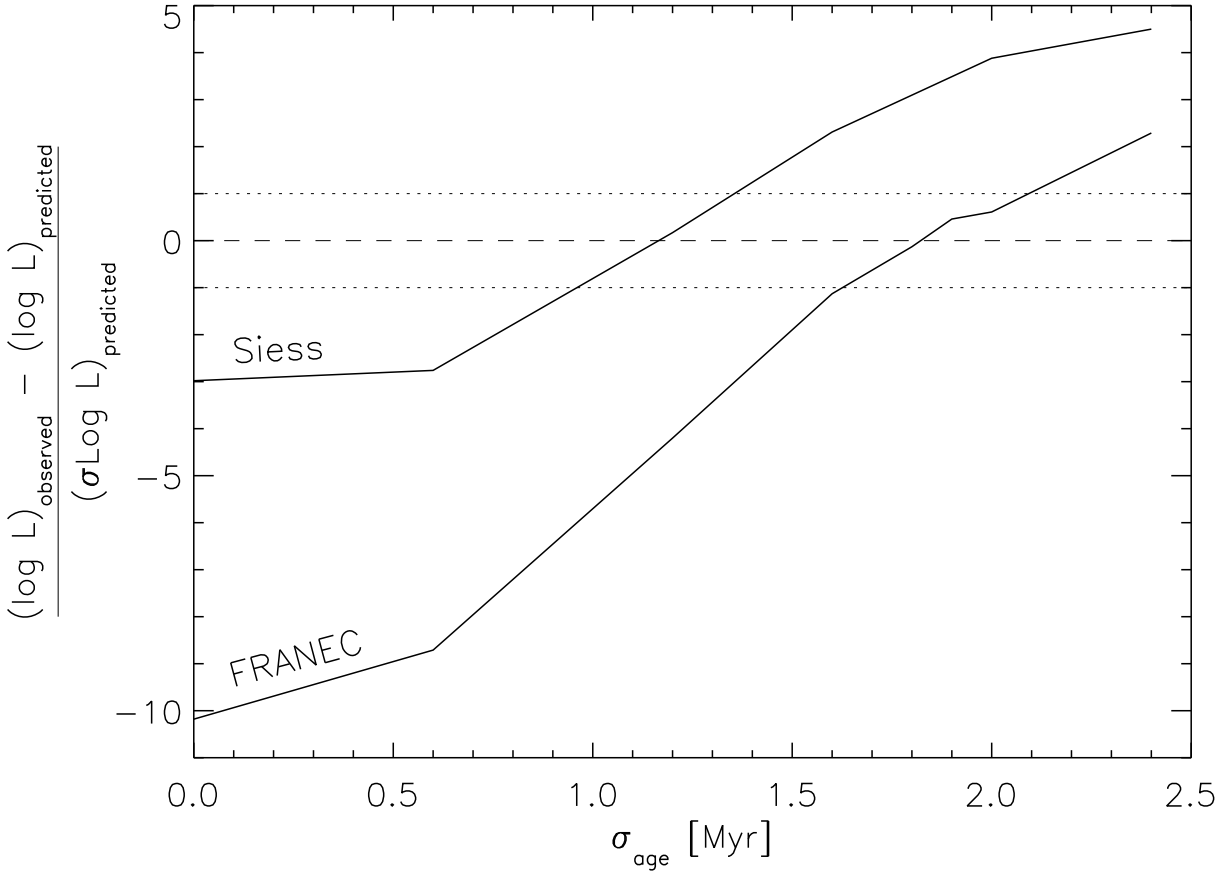

Figure 3.15 Comparison between the measured value of log-likelihood and the predicted one, in units of standard deviation of the latter, as a function of the age spread.

models in Figure 3.14 are those indicated with lighter blue colors, i.e., at high luminosity, where the IMF predicts fewer members, and at both sides along the 2D distribution in the CMD, at large distance from the peaks of the 2D sequence itself. Since the IMF we use to compute the 2D models has been derived from the actual observed data, we exclude the possibility that the low measured value of $\log L$ is due to an overabundance of intermediate mass stars in comparison to low-mass stars. As a consequence, our results suggest that the observed sequence of PMS stars in the CMD *is broader than that predicted by the 2D model for a single age*. There are two possible interpretations for this: a) LH 95 is formed by a coeval population, and the extra spread in the observed CMD is due to additional sources of apparent broadening in the CMD besides those we have included in our models; b) LH 95 hosts a real age spread among its PMS stars. From hereafter we will assume the second possibility, and, under the validity of our modeling, we determine the age spread of the population.

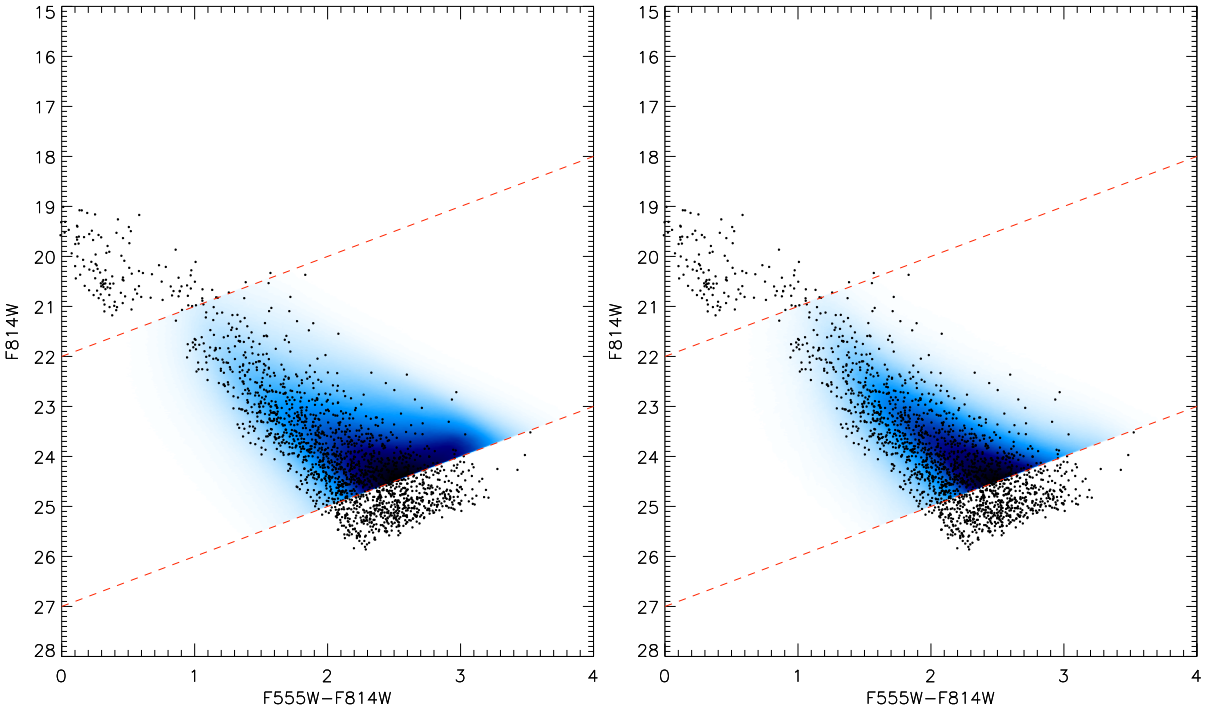

Figure 3.16 The observed CMD with the 2D density models that provide the best fit to the observed sequence of PMS stars, including an intrinsic age spread, for an assumed binarity of $f = 0.5$. *Left*: The model obtained from FRANEC isochrones, with an average age of 3.8 Myr and a Gaussian age spread of $\sigma_{\rm age} = 0.18$ Myr. *Right*: The model obtained from *Siess* isochrones, with an average age of 3.9 Myr and $\sigma_{\rm age} = 0.12$ Myr. The dashed lines denote again the subsample of the photometry used in the analysis.

3.5.2 Evaluation of the age spread

In order to quantify the age spread we include in our construction of the 2D model distributions, apart from the sources of CMD-broadening of PMS stars previously considered (Section 3.4.1), also a distribution in ages. Specifically, we consider the best fit age previously measured for the cluster (Table 3.4.4) along with a Gaussian distribution of ages peaked at the best fit age with standard deviations varying from $\sigma_{\rm age} = 0.1$Myr to $\sigma_{\rm age} = 3$ Myr. We construct, thus, broader 2D model distributions by essentially adding together different single-age models, computed in Section 3.4.1, each weighted according to the Gaussian distribution. For each value of $\sigma_{\rm age}$ we compute the $\log L$ from our data on the newly constructed 2D model, as well as the expected distribution of $\log L$, from simulated stars drawn from the model, as described above. We stress that the expected distribution of $\log L$ is not unique, but varies for each assumed value of $\sigma_{\rm age}$, being derived from the 2D model computed for the exact value of $\sigma_{\rm age}$

For every value of $\sigma_{\rm age}$ we compare the "observed" $\log L$ (i.e. derived from the data) with the predicted one. As mentioned earlier, if the first is significantly smaller than the second, it indicates a poor fit; viceversa, a significantly larger value implies a suspiciously good fit, analogous to a $\chi^2 \lambda\lambda 1$. The standard deviation of the predicted $\log L$ distribution allows us to quantify these differences in a meaningful way. This is simplified by the fact the predicted $\log L$ is normally distributed, due to the central limit theorem, since $\log L$ is the sum over a large sample of stars of the individual single-star likelihoods $\log L_i$.

In Figure 3.15 we present the difference between the observed and predicted $\log L$, normalized on the width of the predicted distribution, as a function of the assumed age spread $\sigma_{\rm age}$, for the two families of evolutionary models and assuming $f = 0.5$. The values of $\sigma_{\rm age}$ for which the difference in the y-axis is zero provide the best-fit value of the age spread, the and the projection on the x-axis of the $\pm 1\sigma$ (dotted lines in the Figure), the associated uncertainty. We find that, for FRANEC models the measured age spread is $\sigma_{\rm age} = 1.8$ Myr (FWHM$\simeq$ 4.2 Myr), while for Siess models this decreases to $\sigma_{\rm age} = 1.2$ Myr (FWHM$\simeq$ 2.8 Myr). In both cases the uncertainty in $\sigma_{\rm age}$ is about 0.2 Myr.

The observed CMD, with the best-fit 2D density models from FRANEC (*left*) and *Siess* (*right*) grids of isochrones superimposed is shown again for $f = 0.5$ in Figure 3.16, but with the best-fit 2D models constructed by including the measured age spread of 0.5 dex. In this figure is evident how the model density probabilities now follow quite nicely the observed broadening of the PMS population of LH 95, within the magnitude range $22 \leq m_{555} \leq 27$, which is considered for the evaluation of the age and age spread of the system. The difference of these plots with those of Figure 3.14, where the best-fit 2D models were constructed assuming coeval PMS populations, is significant. By adding an age spread, the model distributions in the CMD now reproduce well the observed sequence.

Our method predicts a 50% higher age spread assuming FRANEC models than assuming Siess models, and the difference is larger than the uncertainties of each of two values. This is a consequence of the particular shape of the FRANEC young isochrones for the lowest masses, where the modeling of the deuterium burning leads to a brighter predicted luminosity. This can be seen already in the original isochrones in the H-R diagram (Figure 3.1), and is responsible for the over-density seen in both Figure 3.14a and 3.16a at $V - I \sim 3$ and $I \sim 24$. In this region of the CMD the models predict more stars than actually observed, regardless the assumed age spread. Since the observed population statistically populates more the positions of the CMD where the density of the 2D models

Table 3.2 Age and age spread for different binary fractions

	FRANEC Models		*Siess* Models	
f	age (Myr)	$\sigma_{\rm age}$ (Myr)	age (Myr)	$\sigma_{\rm age}$ (Myr)
$f = 0.4$	3.6	1.4 ± 0.2	3.6	1.0 ± 0.2
$f = 0.5$	3.8	1.8 ± 0.2	3.9	1.2 ± 0.2
$f = 0.6$	4.1	2.3 ± 0.25	4.0	1.4 ± 0.2

is lower, the measured likelihood turns out to be smaller than the predicted one even for the "right" age spread. This leads to an overestimation of the value of $\sigma_{\rm age}$.

We remark that this is a general behavior of the method we have proposed: our technique may overestimate the overall age spread. This occurs in the case where the isochrones do not follow the observed sequence, but have a systematically different shape with respect to it. In fact, the condition we imposed to constrain the measured $\sigma_{\rm age}$ is based on the requirement that our data and a simulated population of test stars obtained from the best 2D density model (including an age spread) produce similar values of "global" likelihood $\log L$. If the 2D models have a shape which strongly differs from the observed sequence, the model would never reproduce the data, but there will be always an assumed value of age spread which leads to similar values of likelihood as for the observed sample. In this case, the derived age spread might be higher than the real one. As we discuss in the next section, we can quantify any systematic differences in the shape of the isochrones with respect to the data, and estimate the correct age spread, by analyzing the age properties of the population in smaller luminosity ranges.

We investigated how the assumed binary frequency f affects the derived age spread. We have assumed $f = 0.4$ and $f = 0.6$ and reapplied the method described above. We stress that, although we previously described our results for a larger range of assumed binary ratios, in the mass range relevant for our study, the value of f is not expected to differ much from 50% (Lada, 2006). The results are presented in Table 3.2. We find that a higher fraction of binaries leads to a larger derived age spread, and, in contrast, a lower f to a shorter $\sigma_{\rm age}$. Both the results are a consequence of the dependence of the average cluster age as a function of f: given that the distance between consecutive isochrones decreases with age. A given spread in the CMD results in a larger age spread if the central isochrone is older, and viceversa.

Table 3.3. Variation of ages and age-spreads with luminosity for assumed binarity $f = 0.5$

magnitude range	FRANEC Models age (Myr)	FRANEC Models σ age spread (Myr)	*Siess* Models age (Myr)	*Siess* Models σ age spread (Myr)
$22 \leq m_{555} \leq 23$	0.9	2.2 ± 0.7	1.0	2.8 ± 0.7
$23 \leq m_{555} \leq 24$	1.4	1.7 ± 0.5	1.8	2.4 ± 0.9
$24 \leq m_{555} \leq 25$	2.6	0.6 ± 0.6	2.7	0.9 ± 0.8
$25 \leq m_{555} \leq 26$	3.6	0.8 ± 0.4	3.6	0.6 ± 0.4
$26 \leq m_{555} \leq 27$	4.6	1.0 ± 0.2	4.7	0.0 ± 0.8

3.5.3 Luminosity-dependence of the age and age spread

We want to verify the presence of systematic changes of both age and age spread with luminosity. This effect, which can be caused by uncertainties in the theoretical evolutionary models, as well as in our modeling of the broadening effects in the CMD, can lead to an overestimation of the measured age spread. To demonstrate this dependence we divide the photometric sample in the considered magnitude range of $22 \leq m_{555} \leq 27$ into five sub-ranges 1 mag wide each, and we repeat the method described in Section 3.4.4 to derive the best-fit age within each subsample. We then apply the method of Section 3.5 to derive the corresponding age-spreads, simulating a family of 2D models with different assumed $\sigma_{\rm age}$ around the average age measured for each magnitude interval.

The results are given in Table 3.3, again for both the FRANEC and *Siess* families of evolutionary models for an assumed binary fraction $f = 0.5$. We find a clear variation of both average age and measured age spread with luminosity. In particular, for the bright members, close to the PMS-MS transition, which correspond to masses in the range $1 \lesssim M/\mathrm{M}_{\odot} \lesssim 2$, the derived ages are systematically younger than those for fainter luminosities (and lower masses). The differences in age are of the order of 4 Myr. Also, the measured age spread tends to be significantly larger than the average one for bright stars, and smaller for the lowest masses. In particular, for $22 \leq m_{555} \leq 23$ the age spread derived with our method is larger than $\sigma = 2.5\ Myr$, corresponding to an FWHM exceeding 5 Myr. Considering the very young ages measured in this luminosity interval, and the fact that, for our modeling, the minimum age included in our simulation is

0.5 Myr, this finding implies that the best-fit age distribution for the luminous part of the PMS sequence is highly skewed, with a peak at $\sim 1\ Myr$ and a broad tail toward older ages. On the other hand, for the faintest end of our stellar sample, our method finds that a more modest age spread is needed to produce a simulated distribution of stars as broad as the observed sequence.

The differences in the derived age spreads as a function of luminosities may be due to an incorrect modeling of the 2D isochrones we have used. In particular, some of the broadening effects we included in the model might be mass-dependent. For example, variability and accretion might affect more the brightest members, and less the smallest masses, whereas we assumed identical distributions of these effects along the entire mass range. Considering our results, and averaging the age spreads at different luminosities, the average age spread for the entire stellar sample, derived in Section 3.5.2 should be a fairly well approximation of the real spread.

If we trust our models, the age-luminosity dependance we measure implies that stars in the low-mass regime have been formed some Myr *before* the intermediate-mass members. However, this is not what is observed in young Galactic 1-2 Myr-old associations, where no evidence of highly biased IMF are found (Hartmann, 2003). An explanation for this age difference among different stellar masses is the assumed binarity. An overestimated binary fraction can lead to overestimation of the age for the low-mass stars, because the large numbers of unresolved low-mass binaries produce systematically wider modeled distributions of low-mass stars in the synthetic CMDs. We have investigated this effect by computing the average age in the five selected magnitude intervals (as those in Table 3.3), but with 2D modeled distributions constructed assuming no binaries ($f = 0$). While in this case the mass-age dependance reduces, *it does not vanish*, with a reduced variation in the derived ages of the order of 1 Myr. Naturally, this is an extreme case since such a very low binary fraction is not realistic, but unfortunately the true binary fraction in the considered mass ranges cannot be directly resolved at the distance of the LMC[2].

We have investigated more in detail if the mass-age correlation we have found can be a biased result to an inaccuracy in the modeling of the 2D isochrones. In particular, since the effect caused by accretion veiling is the most uncertain among those we have considered (mostly because of the lack of mass accretion estimates for LH 95), we have tried to redo the entire analysis presented in this chapter excluding accretion from our modeling. In case of no accretion, we find that the age of the cluster is older (of the order

[2]At the distance of the LMC, 1 ACS/WFC pixel corresponds to ~ 2400 AU.

of 6 Myr, depending on the other parameters), the age spread is larger (several Myrs), and still, there is consistent mass-age correlation, with the very-low mass stars systematically older than the intermediate-mass stars.

Taking into account the above, and if we assume that indeed such a dependence of age with mass should not be observed, as in Galactic young clusters, we can attribute the observed dependence of age with mass to an inaccuracy of the PMS models we have utilized. Actually, the inconsistency between the ages predicted by the FRANEC and *Siess* isochrones suggests that the PMS stellar modeling is still far from completely reliable. For a metallicity close to solar, typical of the Galaxy, several studies have been presented to constrain the evolutionary models based on empirical isochrones (e.g., Mayne et al., 2007). Certainly new data that sample different young associations and clusters in the metal-poor environment of the MCs will be exceptionally useful to test the agreement of data with the PMS models also for lower metallicities.

3.6 Discussion

We stress that our results on the age determination of LH 95 and the evidence for an age spread in the system are valid under the assumption of the correctness of the sources of spread in the CMD considered in our models (Section 3.4.1). It should be noted that having included, apart from photometric uncertainties, several important biasing factors, namely *differential reddening*, *stellar variability*, *accretion binarity* and *crowding*, our modeling technique is more accurate than similar previous studies, which completely neglect these biases. Using our models, we cannot reproduce the observed sequence assuming a coeval population, but an additional spread in age is measured. Nonetheless, as we have shown, our results are very sensitive on the assumptions used to model observed populations in the CMD. In particular, changes in the assumed binary fraction alter significantly both the average cluster age and the derived age spread. Also, as discussed previously, the overall effect of accretion veiling influences both this quantities. For our modeling, we assumed accretion and variability measurements from the Orion Nebula Cluster. If on-going accretion in LH 95 is weaker than we assumed, for instance because of an earlier disruption of the circumstellar disks caused by the flux of the early-type stars present in the region (3 of which are O-type stars, see chapter 4) or simply because of the older age, the measured age would turn out be older and the age spread larger that the results we have presented.

Slow star formation scenarios have been proposed based on both observational and theoretical evidence (Palla & Stahler, 2000; Palla et al., 2005; Tan et al., 2006); the loose, not centrally concentrated geometry of LH 95, and its relatively low stellar density and mass (see Chapter 2) would be compatible with a slow conversion of gas into stars (Kennicutt, 1998). Unfortunately, the absence of dynamical information on our region, as well as a precise estimate of the gas mass do not allow us to infer much about the past evolution of LH 95.

On the other hand, additional unconsidered effects that can displace PMS stars in the CMD may still be present and affect the derived age spread; we briefly discuss them here. The presence of circumstellar material can cause star light to be scattered in the line of sight direction (e.g. Kraus & Hillenbrand, 2009; Guarcello et al., 2010). This effect may either increase the observed optical flux with respect to that of the central star, or reduce it, if the central star is partially obscured by the circumstellar material. This scenario, however, requires both the presence of a significant circumstellar environment and a particular geometrical orientation, so, if present, would affect only a fraction of the stars in a cluster. In any case, as shown in Guarcello et al. (2010), stars observed in scattered light appear significantly bluer than the PMS sequence. If such sources are present in our photometric catalog, they would affect only the old tail of our age distribution, or even be excluded as candidate MS field stars. Thus, we are confident that neglecting this effect should not affect significantly our findings. Another unconsidered effect that could bias the measured age spread is that presented by Baraffe et al. (2009). Under certain conditions, if a star accretes a significant amount of material it cannot adjust its structure quickly enough, so appears underluminous for a star of its mass. This effect will have a memory, which may persist for several Myr according to the authors, and will cause some young stars to appear older than they are. This would also cause an additional apparent spread in the H-R diagram even in case of a coeval population. The scenario proposed by Baraffe et al. (2009), however, requires episodes of vigorous mass accretion, with a high $\dot{M}$. With no direct measurements of accretion in LH 95, and no information about the past history of accretion, as a function of mass, we are unable to estimate if this scenario could play any role in our region, and if so, to what extent.

Chapter 4

The high mass population of LH 95

4.1 Introduction

In the two previous chapters, we have studied the stellar population of the young association LH 95, based on deep V and I observations with the Advanced Camera for Surveys onboard the Hubble Space Telescope. In particular, in Chapter 2 we have isolated the cluster population from the field, and we have derived the IMF down to the subsolar regime. In Chapter 3 we determined the age and age distribution of the system with a statistical approach based on the distribution in the CMD of the low-mass and intermediate-mass stars.

Despite the large luminosity (and mass) range spanned by our ACS observations, as we mentioned in Chapter 2, our stellar sample is not complete to the high-mass end, since 5 of the brightest stars appeared saturated in the HST imaging. Moreover, as we have already discussed, optical photometry alone is insufficient for an accurate derivation of the stellar parameters in the high-mass range ($M \gtrsim 8$ M$_\odot$). This is because this type of stars, characterized by a high $T_{\rm eff}$, emit a large fraction of their flux in the UV wavelength range; as a consequence, the optical bands are in Rayleigh regime, and the observed colors tend to be independent on $T_{\rm eff}$. This problem has been evident in Chapter 3, where, using our method, we demonstrated that the assessment of the ages for massive stars, based on our photometry, turned out to be highly uncertain.

For this reason, we perform a spectroscopic follow-up of the brightest members of LH 95, in order to construct the H-R diagram for the massive end of the population. To this purpose, optical spectra are acquired, and these data are complemented with existing BVR photometry obtained from ground based observations of LH 95, from Gouliermis et al. (2002). The main aims of this work are two: 1) To complete the IMF derived in

Chapter 2 for the highest masses, in order to create the most complete extragalactic IMF ever obtained. 2) To analyze the physical parameters of the high-mass stars (masses and ages), in order to verify, in this mass range, evidences of age spread, in relation to the work we have presented for the low mass stars in Chapter 3.

This chapter is organized as follows: in Section 4.2 and 4.3 we present the observations and the data reduction; in Section 4.4 we classify the stars based on their spectral features. In Section 4.5 we derive the H-R diagram for the five brightest stars, and we derive their masses and ages. A discussion on the accuracy of the results, and the assessment of an age spread are presented in Section 4.6. Finally, in Section 4.7 we derive the high-mass IMF in LH 95, and discuss the relation between the most massive star and the mass of the stellar system.

4.2 The Observations

For our spectroscopic follow-up, we selected the brightest sources in LH95, which are all saturated in the HST/ACS frames used in our previous two chapters. We consider the BVI ground-based photometric catalog of LH 95 from Gouliermis et al. (2002). It is characterized by a larger field of view (FOV), a significantly shallower detection limit, and a poor spatial resolution compared to our ACS imaging. Nevertheless, this catalog provides BVI photometry for all the bright sources within the star forming; based on this data we exclude the bright stars with significantly red colors, as field RGB stars. The remaining (5 upper main-sequence stars), have been selected for follow-up, and are indicated for ease with the letter A,B,C,D,E. Figure 4.1a displays the 5 targets over the color-composite image from ACS/WFC observations. Figure 4.1b shows the CMD from the photometric catalog of Gouliermis et al. (2002), highlighting the stars within the ACS FOV and the 5 targets.

The observations have been carried out with the Fibre-fed, Extended Range Èchelle Spectrograph (FEROS) at the 2.2 m MPG/ESO telescope located at the ESO La Silla Observatory, Chile. The spectrograph has a resolution of $R = 48,000$ and a wavelength coverage of 3600 - 9200$\mathring{A}$ (Kaufer & Pasquini, 1998). The spectrograph is fed by two fibres of 2.0 arcsec in aperture providing simultaneous spectra of object plus either sky or one of the two calibration lamps (wavelength calibration and flat-field). Given that for our purposes the wavelength calibration is not critical (such as, for instance, in the case radial velocity measurements), we used the OBJSKY setup, acquiring in parallel to the targets

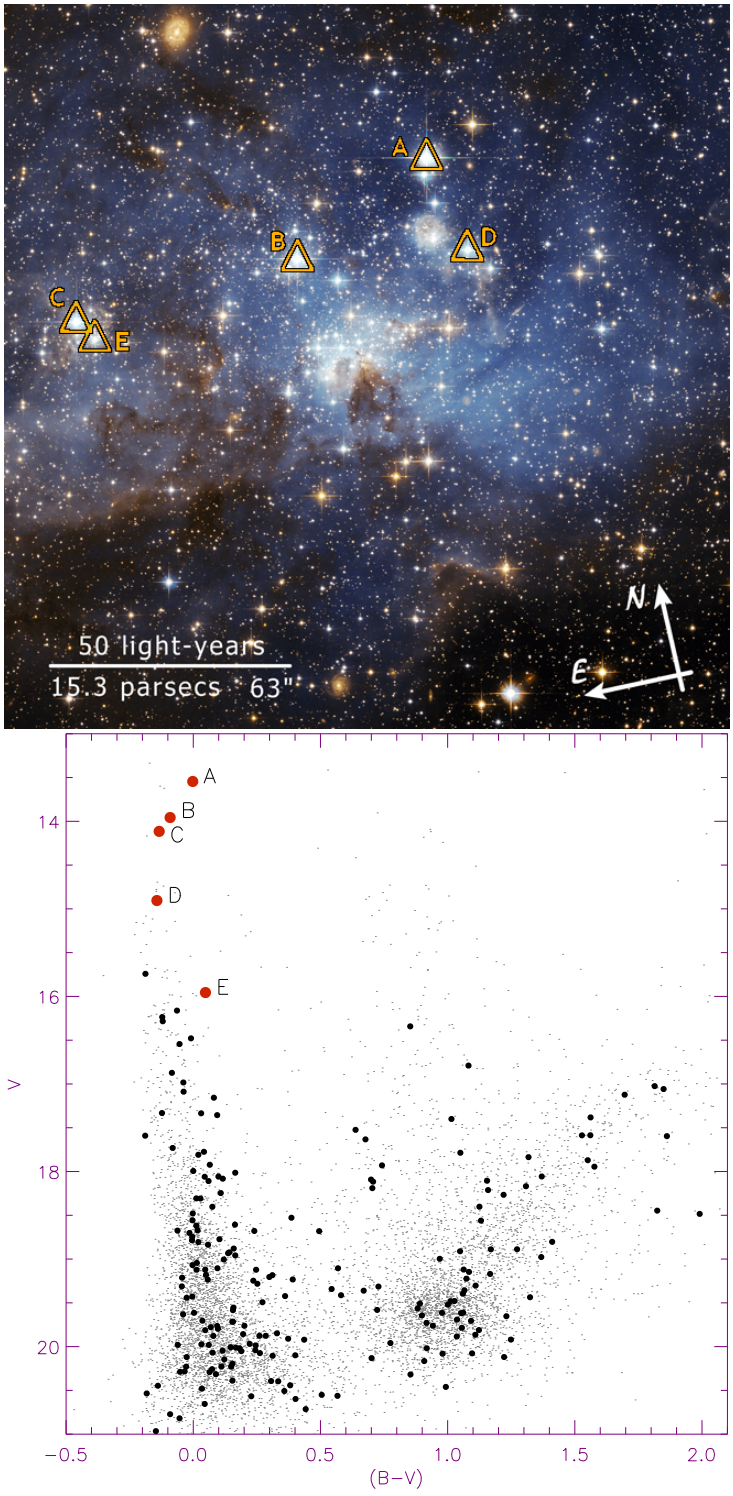

Figure 4.1 Upper panel: The location of the 5 targets for spectroscopy, on the color-composite image from ACS/WFC observations in the filters F555W and F814W (V- and I-equivalent) of the LMC association LH 95 *Image credit: NASA, ESA and D. A. Gouliermis (MPIA).* Lower panel: CMD from the Gouliermis et al. (2002) photometric catalog. Thick dots indicate sources located within the ACS FOV. The 5 selected targets for spectroscopy are denoted with red dots.

a position of the sky separated by 2.9 arcmins. The necessary calibration acquisitions – for image and wavelength calibration – have been carried out before each observing night.

Observations were carried out in two epochs: November 2008 and January 2009. Spectra of standard stars were taken twice during the observing nights, at different airmasses. Our aim was to monitor the atmospheric extinction as a function of wavelength and airmass as well as the overall response of the instrument, in order to absolutely calibrate the continuum of the brightest LH 95 members and derive an accurate unbiased determination of their interstellar reddening. Unfortunately, the non photometric conditions and the variability of atmospheric extinction behavior in short time scale during our run strongly affected our the capability to perform such correction in an accurate way.

The final layout of the observations is presented in Table 1. Multiple observations of the same targets have been taken in order to detect and remove cosmic rays. The repetitions of targets D and E during the second observing epoch has been chosen in order to increase the SNR of the two faintest sources in our sample.

4.3 Data Reduction

For each spectrum the basic data reduction has been performed by using the online pipeline, which produces 39 orders of one-dimensional spectra and combine them together in a single spectrum performing a wavelength calibration. For each spectrum the relative sky emission was subtracted. Having at disposal a unique 1D spectrum for each exposure, we combine the spectra of identical targets removing cosmic rays as follows. For each spectrum we correct the differences in the continuum shape introduced by changes in airmass and atmospheric extinction. This is done first isolating each continuum using a median filter with a width of 400 wavelength elements ($12\mathring{A}$), and fitting a high-order polynomial to the ratio between the continuums. This step also normalizes the relative fluxes of different spectra in case of non uniform exposure time for the different repetitions. Then cosmic rays are detected as peaks, on one of the spectra but not on the others, at at least 3σ from the average noise. This is measured in a $2\mathring{A}$ neighborhood of each wavelength point. The cosmic rays are thus masked, and the spectra are combined using a weighted average that takes the relative exposure times into account. Finally, the co-added spectra were normalized to the interpolated continuum, to facilitate feature recognition and comparison to spectral atlases. For spectral classification, the original spectra were also degraded to a resolution of $1\mathring{A}$.

Table 1. Layout of the observations

ID	ID2 (G02)	alternative name	RA ((J2000.0))	Dec ((J2000.0))	V	exposure time (s)	airmass	epoch
A	9136	Sk -66 170	05:36:58.945	-66:21:16.130	13.17	3600	1.31	Nov
						1000	1.35	Nov
						1500	1.39	Nov
						1200	1.26	Jan
						1200	1.25	Jan
B	9141	Sk -66 172	05:37:05.553	-66:21:34.950	13.58	1200	1.30	Nov
						900	1.32	Nov
C	9143	Sk -66 174	05:37:15.723	-66:21:38.355	13.74	900	1.27	Nov
						900	1.28	Nov
D	18		05:36:58.007	-66:21:42.613	14.53	1000	1.25	Nov
						1000	1.26	Nov
						1800	1.26	Jan
						1800	1.28	Jan
E	85		05:37:15.129	-66:21:44.304	15.58	1400	1.28	Nov
						1400	1.31	Nov
						1400	1.34	Nov
						1800	1.31	Jan
						1800	1.35	Jan

Note. — ID2 (second column) are catalog numbers of Gouliermis et al. (2002). ID3 (third column) are the Sanduleak (1970) identification numbers

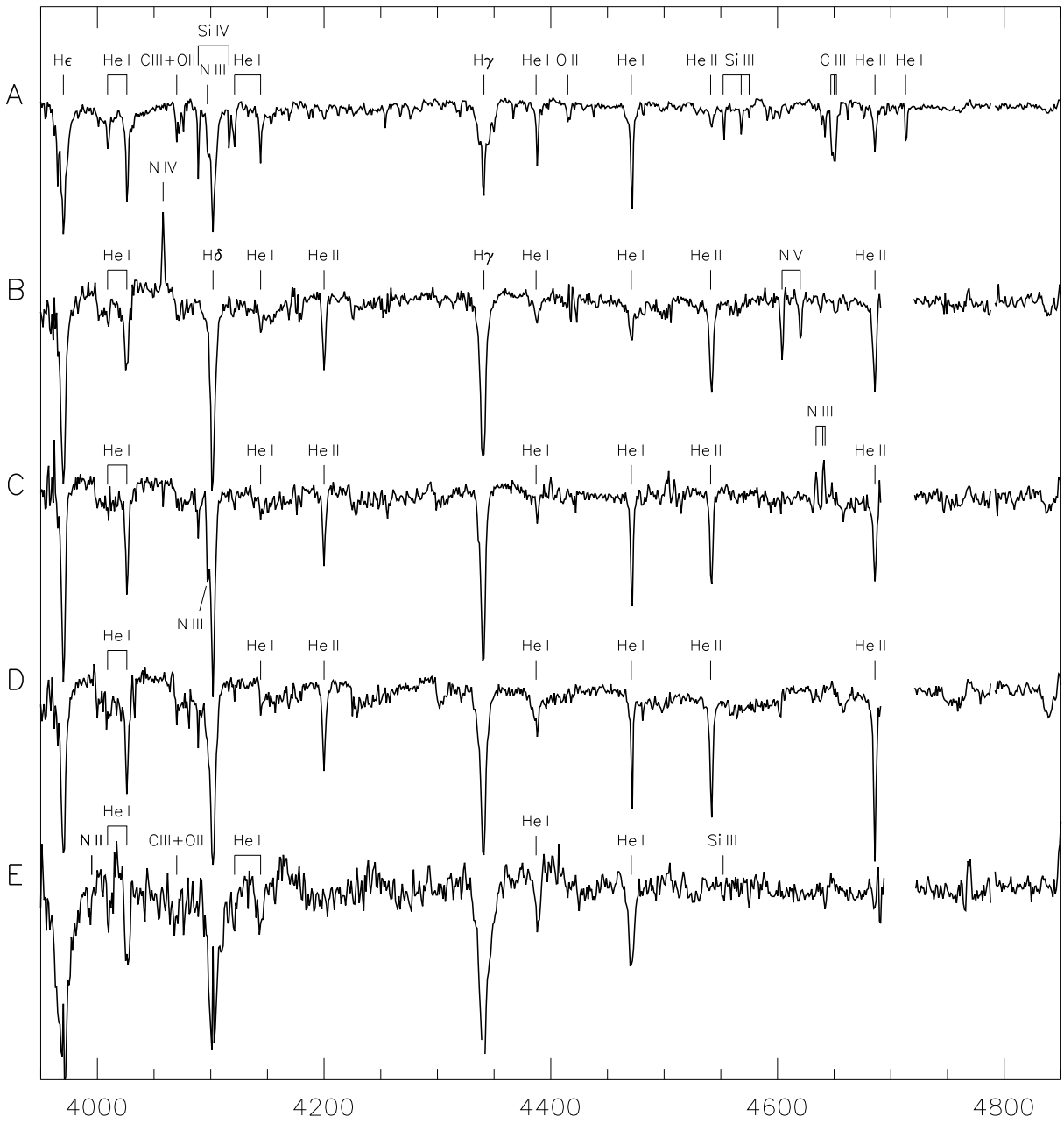

Figure 4.2 Reduced spectra for the 5 targets, covering the violet-blue range of the spectrum, relevant for spectral classification of early-type stars. Units are wavelength (in $\mathring{A}$). The main stellar lines we have identified in the spectra are indicated as well. The features identified in the spectra are: He I $\lambda\lambda 4009, 4026, 4121, 4144, 4387, 4471, 4713$; He II $\lambda\lambda 4200, 4541, 4686$; C III/O II $\lambda 4070$; Si IV $\lambda\lambda 4089 - 4116$; Si III $\lambda\lambda 4552 - 4568 - 4575$; N II $\lambda 3995$; N III $\lambda\lambda 4097, 4634 - 4640 - 4642$; N IV $\lambda 4058$; N V $\lambda\lambda 4604 - 4620$; O II $\lambda 4415$; C III $\lambda\lambda 4647 - 4650 - 4652$.

The result, in the violet-blue wavelength range, is presented in Figure 4.2. In this plot the spectra are blue shifted of an amount $\delta\lambda/\lambda = 10^{-3}$, to correct for the approximate common value of radial velocity $v_r \simeq 300$ km/s we have determined for these members of LH 95 from the spectra themselves. For the four faintest sources, we have removed manually the portion of the spectra at $4695\mathring{A} \leq \lambda \leq 4720\mathring{A}$, where an artifact affecting the 16th dispersion order introduces an unreal excess in the measured flux, systematically dominant for faint targets. We checked that the He II λ4686 line is not affected by this artifact, being located at the red end of the previous dispersion order. This artifact does not appear in the spectra of bright sources. This is why we do not detect it in the spectrum of star A.

4.4 Spectral classification

We perform spectral classification by comparison of the reduced spectra with spectral atlases. In particular we used the atlas of Walborn & Fitzpatrick (1990), which contains an abundant selection of early type stars, providing a very finely grained coverage of the two-dimensional classification of the OB spectral types, as well as the atlases of OB type stars of Walborn et al. (1995) and Walborn et al. (2002).

star A According to the photometry of Gouliermis et al. (2002), this star is the brightest source in the region ($V \sim 13.5$ mag), and with a total exposure time exceeding 2 hours we were able to reach a high SNR.

The ratio between He I λ4471 and He II λ4541, together with the ratio Si III λ4552/Si IV λ4089 indicate it as a B0.2 type star. For what concerns the luminosity class, this spectrum shows some inconsistencies. The significant strength of the Si IVlines suggests a very luminous star, also supported by the low metallicity of the LMC, but, the He II λ4686 line should disappear in a B0.2 giant or supergiant, suggesting a luminosity class IV or V. As a consequence we assign a compromised giant luminosity class to this source, which is then classified as **B0.2 IIIp**

star B This star is the only one in our sample that was previously classified spectroscopically. It was classified by Walborn et al. (1995) as an O3 III(f*), and then reclassified in Walborn et al. (2002) as **O2 III(f*)**, with evidence in support of a composite system with a later OB-type star. From our spectrum we confirm this classification. The primary criterion which indicates an O2-type star is the presence

of a strong N IV λ4058 emission, without any N III λ4640 emission. The presence of the N V $\lambda\lambda 4604-4620$ absorption line indicates a luminous star ($\leq$ III), and the He II λ4686 in absorption excludes a supergiant. According to Walborn et al. (2002), the spectrum is a composite including an unresolved later type star, because of the detection of the He I λ4471. In our spectrum (see Figure 4.1) we also clearly detect He I λ4387, which did not appear in Walborn et al. (1995) spectrum, and this, thus, further supports the composite nature of this spectrum.

star C According to the ratio between He II λ4541 and He I λ4471 (which should be equal in strength for an O7 star) this is a O7.5 star. The presence of N III $\lambda\lambda 4634-4640-4642$ emission is typical of a luminous star of such spectral type, and its moderate strength suggest a II(f) luminosity class. The strength of the N III λ4097 absorption is also supportive of a bright giant. However, the strength of the He II λ4686 absorption indicates a luminosity not higher than class III. As a consequence we classify this star as **O7.5 III(f)**, and we infer that the atypical strength of the N lines could be due to a nitrogen enrichment.

star D The ratio between He II λ4541 and He I λ4471 indicates this star as an O6.5 star, and the presence of the strong He II λ4686 absorption, typical of main-sequence O-type stars, leads to the identification of this star as an **O6.5 V** type.

star E Given the strength of the He I lines and the absence of He II this is an early-B star. The strength of Si IV and Si III, together with the absence of Si II $\lambda\lambda 4128-4130$ indicate a B1.5 star. The additional presence of the N II $\lambda\lambda$3995 suggests a luminous star, but not superluminous given the absence in our spectrum of several indicators of such (e.g., strong O II lines). Therefore we assign a spectral type **B1.5 III**.

We assume an uncertainty in the assigned spectral types of 0.5 subtype for stars A-D and 1 subtype for star E.

4.5 The H-R diagram

In order to derive the stellar parameters of the stars, we construct the H-R diagram of these sources, using both the spectroscopic information described above, and the photometry of Gouliermis et al. (2002).

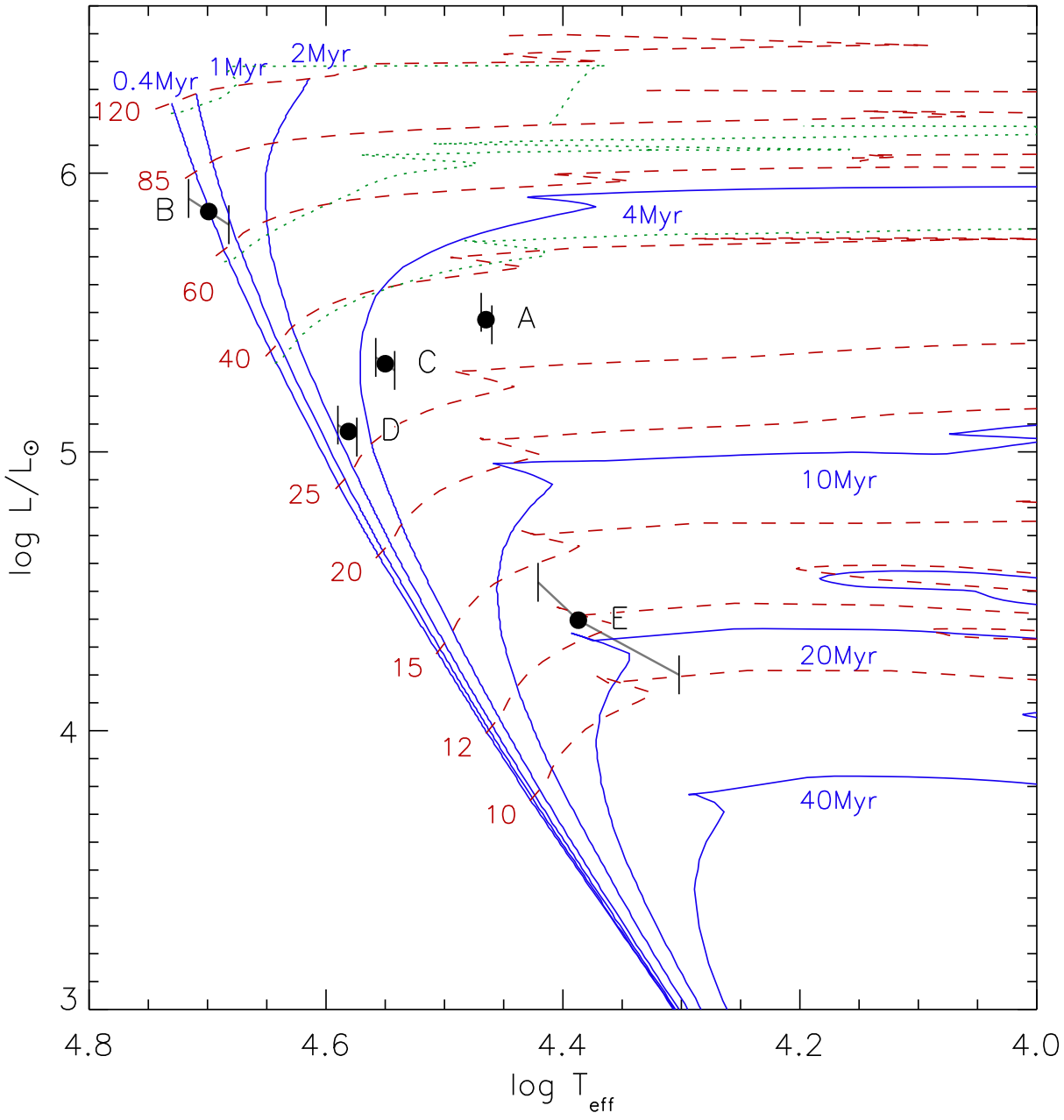

Figure 4.3 H-R diagram of the selected targets, together with evolutionary tracks for initial masses between 10 and 120 $M_\odot$ (dashed lines) and isochrones for ages between 0.4 Myr and 40 Myr (solid lines) from the Geneva models of Schaerer et al. (1993) for LMC metallicity. The dotted lines are evolutionary models for stars with rotation, for masses of 40, 60 and 120 $M_\odot$ and LMC metallicity, from Meynet & Maeder (2005).

We derive the effective temperature of the stars from their spectral types. To this purpose, we consider appropriate temperature scales for early-type stars with LMC metallicity. A number of spectral type - $T_{\rm eff}$ conversions can be found in the literature, covering different ranges of the parameter space. The derivation of such relation usually relies on the modeling the stellar spectra, which are then compared to observational criteria, such as, presence of spectral lines and line ratios, which define spectral types and luminosity classes. The stellar atmosphere modeling is particular challenging in particular for O-type stars, requiring several ingredients such as non-LTE treatment, spherical expansion due to stellar winds, and line blanketing to take into account the effects of metals in the atmospheric structure and emergent spectrum (Martins et al., 2005). These studied showed a clear dependance of the temperature scale on luminosity class, with luminous stars being colder than dwarfs at a given spectral type. In addition, Massey et al. (2005) found evidence for a systematic change in the temperature scale with metallicity. They collected high SNR optical and UV spectra of a sample of O-type stars in the Galaxy and in the two Magellanic Clouds and derived $T_{\rm eff}$ via modeling, finding that SMC O-type stars are systematically hotter than Galactic stars at the same spectral type. LMC stars follow an intermediate temperature scale between the two, as expected by their metallicity. In agreement with previous works, they find lower $T_{\rm eff}$ for supergiants (luminosity class I), while no significant difference are measured between giants and dwarfs (III and V).

We, therefore, adopted the Massey et al. (2005) LMC scale, covering the O3-O9.5 range, for the late O-type stars in our sample. O2 type stars are not explicitly provided a temperature; however, their sample includes two LMC O2 III stars, for which they assign a lower-limit $T_{\rm eff}$ = 48000 K, and two O2 V with temperatures between 51000 K and 55000 K. We therefore assign to our O2 III star a $T_{\rm eff}$ = 50000 K $\pm$2000 K, value which is compatible with the Massey V+III scale extrapolated to O2-type, also in agreement with other O2 LMC giant stars (e.g., Evans et al., 2010). For the two early B-type stars, we adopt the temperature scale of Bessell et al. (1998), which matches very well the Massey scale at B0. We highlight that for B-type stars, the uncertainties in the spectra modeling become less prominent: this is supported by the fact that all the recent temperature scales for O-type stars (e.g., Vacca et al., 1996; Martins et al., 2005; Massey et al., 2005), while they present significant differences at higher $T_{\rm eff}$, they are in agreement with each other at the O-B transition, with a predicted $T_{\rm eff} \simeq$ 30000 K. Moreover, in the B-type range we do not expect any significant metallicity dependence in the $T_{\rm eff}$ scale, since such variations determined by Massey et al. (2005) become smaller towards late O-types and vanish at

Table 4.1. Derived stellar parameters

$T_{\rm eff}$ (K)	BC_V (mag)	A_V (mag)	$\log L/L_\odot$
29170^{+270}_{-330}	$-2.816^{-0.066}_{+0.046}$	0.880 ± 0.174	$5.474^{+0.026\pm0.07}_{-0.018\pm0.07}$
50000^{+2000}_{-2000}	$-4.433^{-0.118}_{+0.118}$	0.644 ± 0.174	$5.862^{+0.047\pm0.07}_{-0.047\pm0.07}$
35480^{+660}_{-650}	$-3.407^{-0.057}_{+0.060}$	0.464 ± 0.174	$5.316^{+0.023\pm0.07}_{-0.024\pm0.07}$
38110^{+800}_{-610}	$-3.620^{-0.058}_{+0.050}$	0.433 ± 0.174	$5.073^{+0.023\pm0.07}_{-0.020\pm0.07}$
24380^{+1990}_{-4330}	$-2.430^{-0.340}_{+0.490}$	0.982 ± 0.174	$4.396^{+0.136\pm0.07}_{-0.196\pm0.07}$

Note. — the first error in $\log L/L_\odot$ represents the propagation of the uncertainty in $\log T_{\rm eff}$ (and consequently in BC), the second error represent the propagation of the uncertainty in M_V.

B0.

To derive the bolometric luminosities of our stars, we have to correct our V magnitudes for extinction, and apply bolometric corrections for the given stellar temperature. We estimate the extinctions by measuring the $E(B-V)$ color excess from the Gouliermis et al. (2002) photometry. The intrinsic $(B-V)_0$ colors we assume are from Martins & Plez (2006) for O-type stars, and from Bessell et al. (1998) for B-type stars. We stress that, since O-type stars are well into the Rayleigh-Jeans regime for optical wavelength, the intrinsic colors are hardly sensitive on $T_{\rm eff}$. According to Martins & Plez (2006), $(B-V)_0$ decreases only from 0.28 mag to 0.26 mag in the entire spectral class, with differences due to luminosity of less than 0.01 mag. Subsequently, we expect that also metallicity variations would not affect the intrinsic (B-V) color. For the two early-B stars in our sample we consider the intrinsic colors of Bessell et al. (1998), assuming a surface gravity of $\log g = 4.0$. According to that work, for the $T_{\rm eff}$ of early B-type stars, changes of surface gravity of more than 1 dex cause very small variations of $(B-V)_0$, of the order of 0.01 mag. As a consequence, uncertainties in the luminosity classes we assign to sources

A and E are not expected to bias in any way the assumed intrinsic colors of the two stars, hence, subsequently, the derived optical extinction.

We used the color excess $E(B-V)$ to derive extinction A_V assuming the average LMC reddening parameter $R_V = 3.41 \pm 0.06$ (Gordon et al., 2003), slightly higher than the typical the Galactic one of $R_V = 3.1$ (Cardelli et al., 1989). The photometric errors in B and V from Gouliermis et al. (2002) are negligible, given the high luminosity of the 5 bright members of LH 95. Nevertheless, we add a constant 0.035 mag uncertainty to every star in each band, representing a reasonable precision for the photometric calibration of that work; in this way the the derived $E(B-V)$ has an error of 0.05 mag. We convert the de-reddened V_0 magnitude into absolute M_V magnitudes removing the distance modulus $dm = 18.41$ (Chapter 2).

To convert absolute magnitudes into total stellar luminosity $\log L/L_\odot$ we consider bolometric corrections BC_V. For O-type stars we use the relation from Massey et al. (2005): $BC = 27.99 - 6.90 \cdot \log T_{\rm eff}$. Clearly, as for the intrinsic colors, they find the BCs to be mainly dependent on temperature, and independent on luminosity. Furthermore, their BCs are in good agreement with the analogous relations derived from previous works (e.g., Vacca et al., 1996). Comparison of this relation with the BCs of Martins et al. (2005), yield differences below 2%. For the BCs of the B-type stars, we use again the work of Bessell et al. (1998).

With all the ingredients, we derive the bolometric luminosity simply from $\log L/L_\odot = 0.4 \cdot (M_{\rm bol,\odot} - M_V - BC_V))$, where $M_{\rm bol,\odot} = 4.75$ is the bolometric absolute magnitude of the sun. In Table 4.1 we report the derived temperatures and luminosities of the five stars. Figure 4.3 shows the position of the members in the H-R diagram, as well as the errors due to both $T_{\rm eff}$ uncertainties (diagonal error bars) and photometry (vertical error bars hats).

In the same plot we overlay a set of Geneva evolutionary models for the LMC metallicity ($Z = 0.008$). These are taken from Schaerer et al. (1993) and are computed assuming no stellar rotation. In general, stellar rotation plays an important role in the evolution of massive stars (Maeder & Meynet, 2000), enhancing mass loss, introducing anisotropies and inducing transport of angular momentum and mixing of chemical elements in radiative zones. These effects influence the modeling of the evolution in the H-R diagram (Meynet & Maeder, 2000); however they are mostly critical for the evolved stages of massive stellar evolution, influencing the Wolf-Rayet phases (Meynet & Maeder, 2003) and the final pre-supernova stages (Hirschi et al., 2004). Unfortunately at present no complete

set of evolutionary models with rotation and LMC metallicity is available, spanning the entire range of masses of high-mass stars. Nevertheless, in Figure 4.3 we also show three evolutionary tracks from Meynet & Maeder (2005), computed for Z=0.008 and including stellar rotation assuming v_{ini} = 300 km/s for masses of 40, 60 and 120 $M_{\odot}$; for clarity we have not plotted the evolved staged for these masses. From the comparison between the two families of tracks, it is evident that, given the position in the H-RD of our five stars, assuming non-rotating models does not affect significantly the stellar parameters we derive.

Hence, we utilize the grid of Schaerer et al. (1993), and assign masses and ages to our stars by means of interpolation. The evaluation of the uncertainties associated to these parameters, for every star, requires particular attention. As shown in Figure 4.3, the errors in $\log T_{\rm eff}$ and $\log L$ are correlated and asymmetric. Moreover, the probability for the star to be measured in different positions of the HRD within the error may not be constant. This is the case of source E: its measured $\log T_{\rm eff}$ and $\log L$ are located just over the H-exhaustion point of the evolutionary models (the turn-around feature evident for all the isochrones and tracks of Figure 4.3 at $\log T \sim 4.4$). In the HRD, the speed of stellar evolution is much faster after the H-exhaustion than before. Thus, the chance of detecting a star at colder temperatures than this point is significantly lower than that of detecting a star at hotter temperatures. We take into account this effect to normalize our results, utilizing the speed of evolution in the HRD as a prior.

We proceed with a Monte Carlo simulation as follows. First we derive a map in the HRD representing the relative rapidity of stellar evolution. To this purpose, we interpolate the original grid of isochrones and tracks of Schaerer et al. (1993) onto a dense grid characterized by a uniform spacing in mass and age. For each of these points in the new grid, the relative speed of evolution is proportional to the inverse of the distance, on the same track, between neighboring points at younger and older ages than that of the considered point. This distance depends on the assumed metric: we choose a linear scale for both axis of the HRD; since we are interested in the relative variation of evolution speed between different points in the HRD, the units chosen in both axis to derive the distance between points are arbitrary and equivalent. Then, for each of our five stars, we generate a well populated number of synthetic stars distributed within the errors shown in Figure 4.3. We assume a flat distribution in $\log T$, with an equal number of stars on both sides from the central temperature, and a Gaussian distribution in $\log L$, maintaining the correlation between the two quantities (the diagonal error bars) as shown in Figure 4.3.

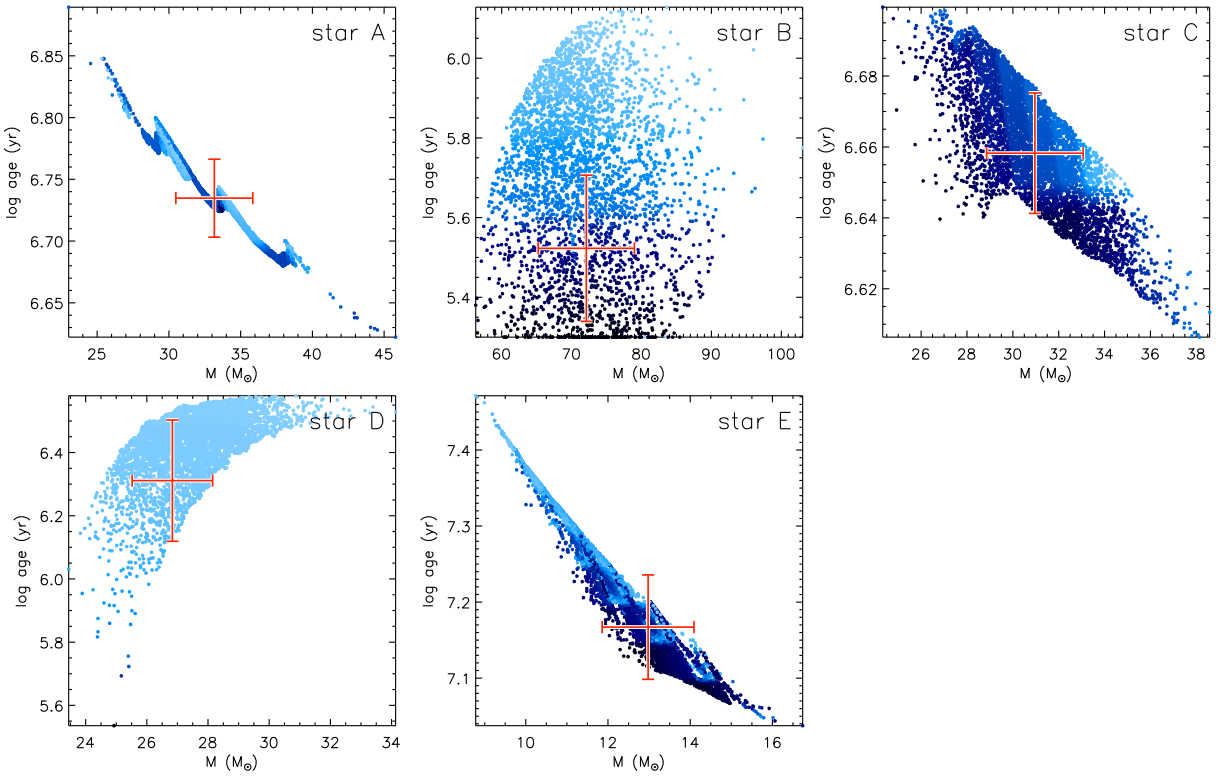

Figure 4.4 Illustration of the MC method to derive the stellar mass and age as well as the associated uncertainties, accounting for the evolution speed in the HRD as a weighting quantity. For every star, the dots represent the transformation in the mass-age plane of the simulated population of stars within the error bars in the HRD. The color is proportional (from dark to light blue) to the rapidity of evolution in the HRD. The crosses represent the derived mean parameters, weighted according to the inverse of the rapidity of evolution.

For each of these simulated stars, we assign masses and ages by interpolation on the grid of models, as well as the exact value of relative speed of evolution. Finally, we derive the best mass and age, as well the uncertainty on these quantities, using a weighted statistics from the simulated population inside the errors. The weight is, naturally, the inverse of the evolutionary rapidity, proportional to the probability of detecting a star with the stellar parameters of each point. The findings are illustrated in Figure 4.4, where, for each of the five stars, we show the distribution in the mass-age place of the simulated stars within the errors of the HRD position, color-coded according to the weight.

In Table 4.2 we summarize the results for the five stars, reporting the best age, mass and uncertainties. The importance of our method to weight the derived stellar parameters on the evolution time scales is evident for stars B and E. For star B, the method tends to favor a slightly younger age than the central age of $\sim$ 0.4 Myr, while its mass is not

Table 4.2. Derived masses and ages

	mass ($M_\odot$)	age (Myr)
A	33.2 ± 2.7	5.43 ± 0.41
B	72.1 ± 6.9	0.33 ± 0.18
C	31.0 ± 2.1	4.55 ± 0.18
D	26.8 ± 1.3	2.05 ± 1.14
E	13.0 ± 1.1	14.7 ± 2.5

significantly affected. For star E, the uncertainty in the HRD leads to a highly correlated uncertainty in the mass-age plane, predicting either a younger, more massive star, or an older, less massive object; however, the latter case is less probable than the first, because of the much rapid stellar evolution. This leads to estimate a most likely mass of $M = 13$ $M_\odot$, a larger value than the central mass that can be estimated neglecting the errors in the HRD (see Figure 4.3, the measured $\log T$ and $\log L$ for star E overlap the 12 $M_\odot$ stellar track).

4.6 Discussion on the derived ages and masses

4.6.1 Stellar multiplicity

The stellar parameters we derived in the previous section might be biased by the presence of unresolved companions. In fact the majority of the early type stars are expected to be formed in binary systems (Lada, 2006), with a binary fraction of the order of $60 - 100\%$ (Zinnecker & Yorke, 2007). Given the distance of the Magellanic Clouds, the possibility of resolving binary systems is very limited based on ground based observations[1]. Our HST/ACS observations, characterized by a significantly better spatial resolution, can not improve this, since the brightest stars, as mentions, are highly saturated.

For star B, as we discussed in Section 4.4, there is evidence, from the spectrum, supporting the presence of an unresolved object, of later spectral type, superimposed to the star. For the other sources, we are unable to confirm stellar multiplicity based on our spectroscopy. For stars A, D and E, for which our spectroscopic observations were

[1] At the distance of the LMC, 1" corresponds to 50,000 AU

performed in two epochs separated by $\sim$ 2 months, we have attempted to detect evidence of binarity looking for radial velocity variations.

To compute the stellar radial velocities, we used a cross-correlation technique Baranne et al. (e.g., 1996). Each stellar spectrum was cross-correlated with a numerical template that has been built from the stellar spectrum itself by selecting certain spectral lines. For this propose we rejected blended absorption lines. We used 6 absorption lines for A and obtained an accuracy $\sim$2 km/s per measurements. A similar accuracy was also obtained for D and E where we selected 4 absorption lines. While we observed no significant radial-velocity variation in star A and E during the two epoch (November 2008 and January 2009), we detected a linear trend in the radial-velocity variation of D during this observation time window. The RV variation between the second (January 2009) and the first epoch (November 2008) is $\sim$9 km/s. This RV variation can be caused by the stellar activity or the presence of an unseen stellar companion.

We discuss how the possibility that our five stars are unresolved systems may affect the derived masses and ages. We assume the presence of two unresolved stars and we distinguish two cases.

1) The optical luminosity of the companion is significantly smaller than that of the primary: in this case, both the measured spectral type and the optical magnitude are representative of the primary, and thus also the position of the star in the HRD. The presence of the companion, therefore, does not alter the derived parameters of the primary, but affects only the completeness of the stellar sample.

2) The optical luminosity of the companion is comparable with that of the primary. In this case, we further distinguish two possibilities. *a)* The two stars have identical spectral type; together with the same optical luminosity, this implies that they are identical companions, with the same mass and age. They would be located in the HRD at the same $T_{\rm eff}$ we have determined through spectroscopy, and 0.3 dex fainter in $\log L$. *b)* The two stars have different spectral types. Since we have assumed similar optical luminosities, the spectral type we have determined from spectroscopy will be, roughly, the average of the individual spectral types of the two stars. This scenario, however, would be unrealistic. This is clarified in Figure 4.5, where we simulate this effect on star C. Two companions with identical optical luminosity but $T_{\rm eff}$ respectively hotter and colder than that we have assumed for this source would be located in symmetric positions in the HRD with respect to the case of identical companions (open circle). Considering the shape of the isochrones in the HRD, however, this would lead to a significant difference of age among the two

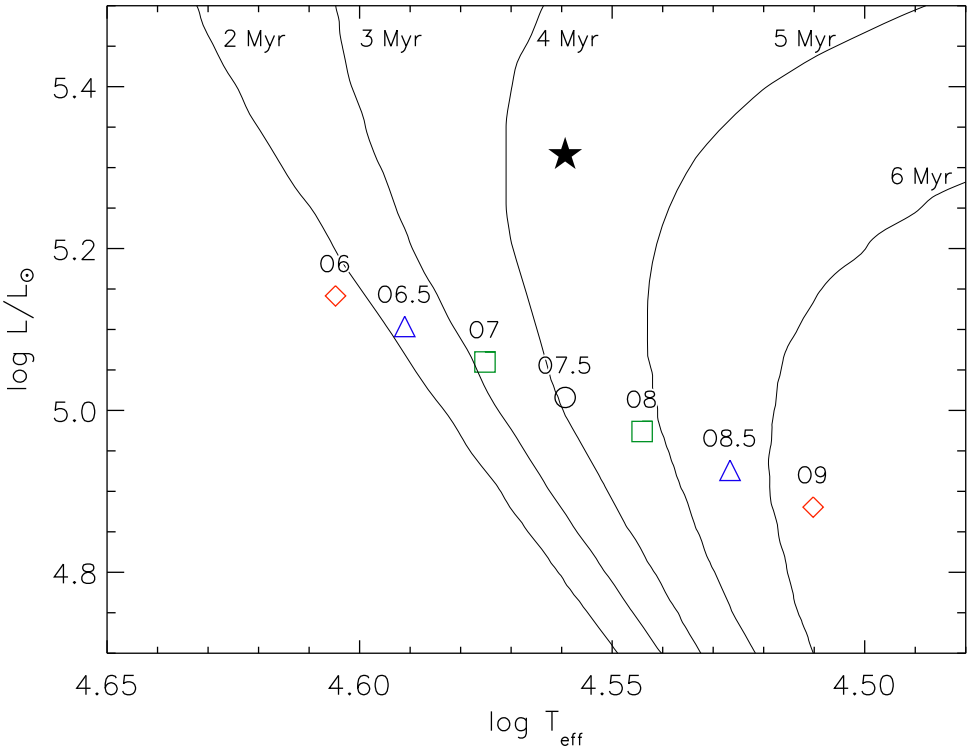

Figure 4.5 Example of how the presence of un unresolved binary system, in the case *2b* (two companions of similar optical luminosity, but different spectral types, *see text*) would bias the derived position of the star C in the HRD. Instead of the derived parameters for this star assumed single (black star), two companions would be individually located on symmetric locations (O7+O8, O6.5+O7.5, O6+O9) at both sides from the average spectral type for this source. The diagonal alignment is caused by the increasing BC with temperature. Schaerer et al. (1993) isochrones for ages 2-6 Myr are overplotted.

companions, even for a small difference in their spectral type. Given the youthfulness of LH 95, and the fact that its age is comparable with the crossing time of the region (see Chapter 2), dynamical evolution should not have altered significantly the binarity properties of the systems at the time they have formed; moreover, since LH 95 is a loose system, crowding should not affect significantly the photometry, leading to the detection apparent, unbound, binary systems. Therefore we are expecting that if some of the massive stars we study in this work are in multiple systems, the components should be nearly coeval, and this cannot be reproduced in the case we are investigating.

We conclude that the only plausible scenarios are 1) or 2a), which is that in case of unresolved massive binaries, either one component is unseen, but without biasing the derived stellar parameters of the primary, or the two stars have nearly identical mass and

age, each of them 0.3 dex underluminous than what we have estimated in the previous section. The important result, here, is that in both cases, at least the derived $T_{\rm eff}$ cannot change significantly from that we have derived.

An interesting case is that of star B, the most massive and also youngest source in our sample. From our spectroscopy, we have found evidence of an unresolved, colder, companion, which, according to our considerations of above, should not alter its derived parameters. We stress that an additional equal-mass companion to star B cannot be the case. Decreasing the bolometric luminosity of this source by a factor of 2 would shift this source outside of the parameter space spanned by the evolutionary models, being too faint and hot than even a Zero-Age MS massive star.

4.6.2 Evidence for an Age Spread

Our findings show that there is a spread in the derived ages for the most massive stars. This results is in agreement with what we derived in Chapter 3, studying the age and age spread of low-mass population of LH 95 from a statistical analysis of the field subtracted optical CMD. In that work, we found that the average age of the system is about 4 Myr, with a confirmed age spread that is compatible with a gaussian distribution with σ = 1.2 Myr. In Figure 4.6 we present the derived age distribution for the low-mass end of the population, compared to the derived ages for the 5 massive members analyzed here. In this plot we are preliminary assuming the ages obtained neglecting unresolved binarity, which is also the case of having binary companions faint enough not to alter the derived age of the primary (see Section 4.6.1).

From Figure 4.6, it is evident that three of our sources (stars A, C and D) have an age compatible with the low-mass age distribution. In fact, the average age for these object is exactly 4 Myr. On the other hand, sources B and E are significantly away from the population. Star E shows a significantly large age than that of the cluster. However, this is the faintest source of our sample with the largest uncertainties. Also, it is located in a particularly crowded sub-cluster (see Figure 4.7), and thus we do not exclude that stellar confusion might have contributed to alter the derived parameters.

We have computed how the presence of unresolved equal-mass binaries for these four source, which is the limiting case of the highest bias in the HRD position of the members, affects the age and age distribution. We find that star E becomes even older, which would confirm the peculiarity of its derived parameters. On the other hand, stars A would turn

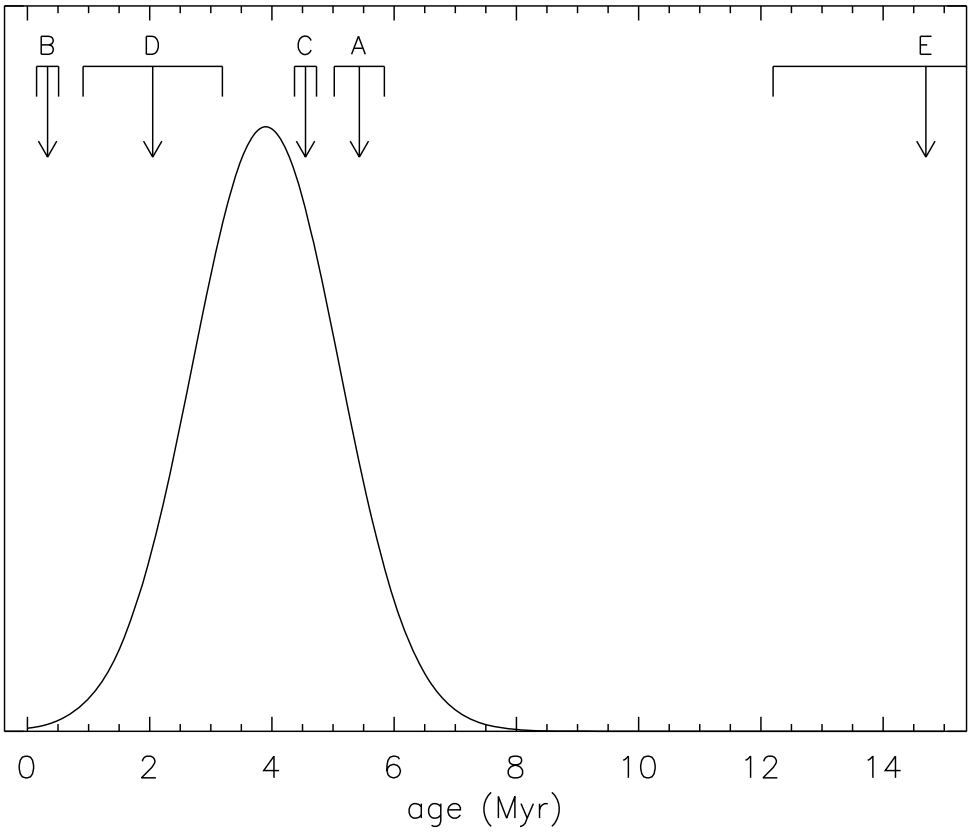

Figure 4.6 The age distribution we derived in Chapter 3 for LH 95 (gaussian distribution) from the analysis of the low-mass population. The arrows, with error bars, indicate the ages and uncertainties of the five massive stars.

out to be 1.4 Myr older, star D 1.7 Myr younger, and star C would have about the same age as if it is not a multiple system. For these three sources, then, the average age remains compatible with that of the low-mass stars even in case of unresolved binarity, and the measured age spread increases even more.

The most interesting case, on the other hand, is that of source B, the most massive star of the system. We find that its age is significantly younger than the others, and at 3σ from the age distribution of the entire cluster, with a relatively small uncertanty. As we mentioned in Section 4.6.1, given its position in the HRD, we exclude that this is an equal-mass binary system, since it is already located at the blue edge of the evolutionary models. We do detect from the analysis of the spectrum a contamination from a later-type star, whose flux should be lower than that of the hot primary. In any case, if we have slightly underestimated the luminosity of this source, the derived age for source B would be even younger than that we derived, whereas its mass would not change significantly. The nature of this source is, therefore, peculiar: a ~ 70 $M_{\odot}$ star formed in

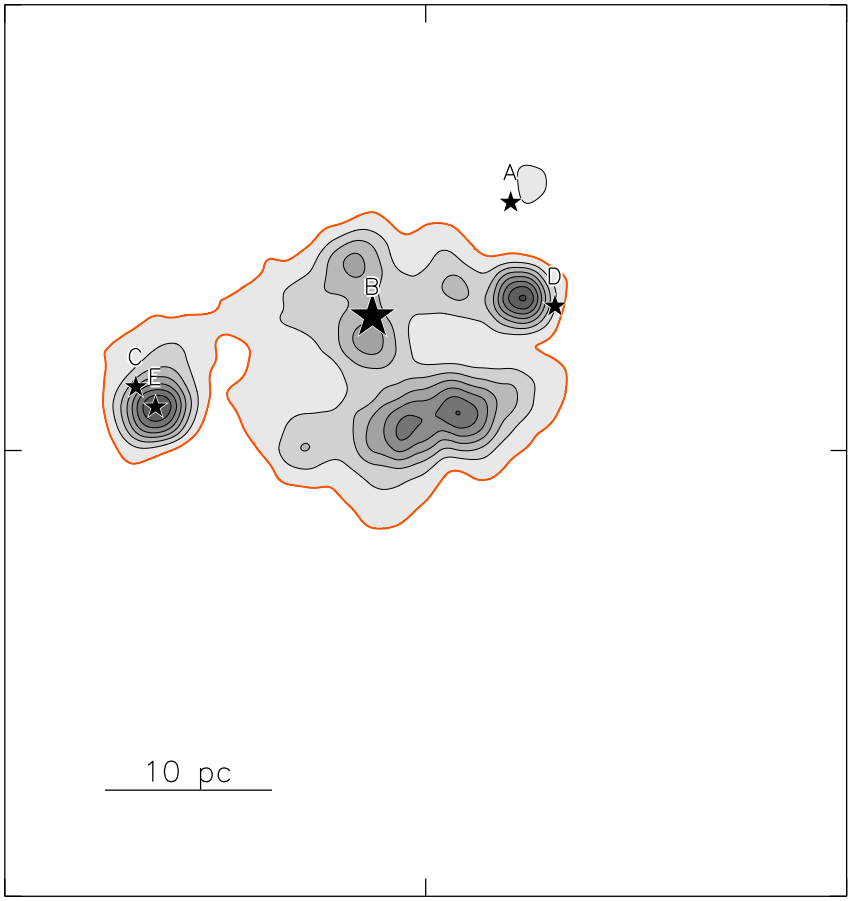

Figure 4.7 Projected spatial positions of the 5 sources presented in this study, compared to the spatial density distribution of PMS stars derived in Chapter 2

our system after the entire star formation process, which originated the stellar population in LH 95 in the entire mass-range, already occurred. As seen in Figure 4.7, the sources is located, in projection, very close to the center of the system, but in a region characterized by a relatively low stellar density, in comparison with the three main subclusters (see Chapter 2 for the characterization of these stellar aggregates). Also, in Chapter 3, we found that there is no spatial variation of both average age and age spread of low-mass stars throughout the entire region. We could hypothesize different scenarios to justify the presence of a late-born massive star in LH 95. If the original location where source B was born coincides with the actual position, its formation could have been triggered by the surrounding population of massive stars. However, there are two problems with this scenario: first, it would be difficult to justify how a massive clump was prevented to collapse in the central part of the system for ~ 3 Myr, when massive star formation was

taking place in the surrounding region; second: the low-mass population in the immediate vicinity of source B does not show evidence of a younger age than the rest of the region, so the massive star would have formed in isolation. Another hypothesis is that source B has not formed in the present position. In fact, 10-25% of the O-type stars are runaway, (Blaauw, 1961; Poveda et al., 1967; Gies & Bolton, 1986), ejected from their birthplace by dynamical interaction. Considering a typical ejection velocity of 40–100 km/s, and given the age of source B of the order, at most, of 0.5 Myr, it could have then formed about 20-50 pc away from the actual position, which means (see Figure 4.7) still in the vicinity of the rest of the system. From an analysis of the spectrum, we do not detect any radial velocity variation of source B with respect to the other massive stars. However, with no proper motion estimates, we are unable to measure the actual velocity of this source, and therefore confirm that it is a runaway star.

4.7 The high-mass IMF

In Chapter 2 we derived the IMF of LH 95, down to the subsolar regime, based on ACS V and I photometry. We found that the IMF is well approximated by a two-phase power law, with a break point at $\sim 1 M_{\odot}$. For larger masses we measured a slope $\alpha = 3.05$[2], whereas for low-mass star the slope decreased to $\alpha = 2.05$. In that work, as mentioned, the five stars studied here were not included, due to saturation in the ACS frames. In this section we complete the IMF previously derived for the high-mass end.

We consider then the masses estimated derived in Chapter 2, limiting to the sources with $M > 2\ M_{\odot}$. We stress that in Chapter 3 we refined the background subtraction that was assumed in Chapter 2, removing an additional small fraction of sources that were candidate to be still MS stars belonging to the LMC field. As we stated, this did not alter the shape of the derived IMF, and furthermore, all the stars in the second field subtraction refinement have an estimate mass $< 2\ M_{\odot}$. Thus, the refinement of the field subtraction we performed in Chapter 3 is irrelevant for the derivation of the massive IMF. In this mass range, and including the new five stars, the sample is constituted by 110 members.

To derive the mass distribution, we utilize the method suggested by Maíz-Apellániz & Úbeda (2005). In this work the authors discuss the biases in the computation of an IMF introduced by the binning process. They find that assuming a constant bin size can lead to misleading results, due to the correlation between the number of stars per bin

[2]In these units, the Salpeter (1955) slope is $\alpha = 2.35$

(higher for lower masses) and the assigned weights (from the Poisson statistics). Instead, they show how to circumvent this problem by assuming a variable bin size, in order to have an equal number of sources in each bin. They also find that, in this case, the bias is almost independent on the assumed number of stars per bin, and remains low also for 1 star in each bin. We therefore choose the latter option, in order to maintain as possible the statistical information from the five massive stars studied in this work.

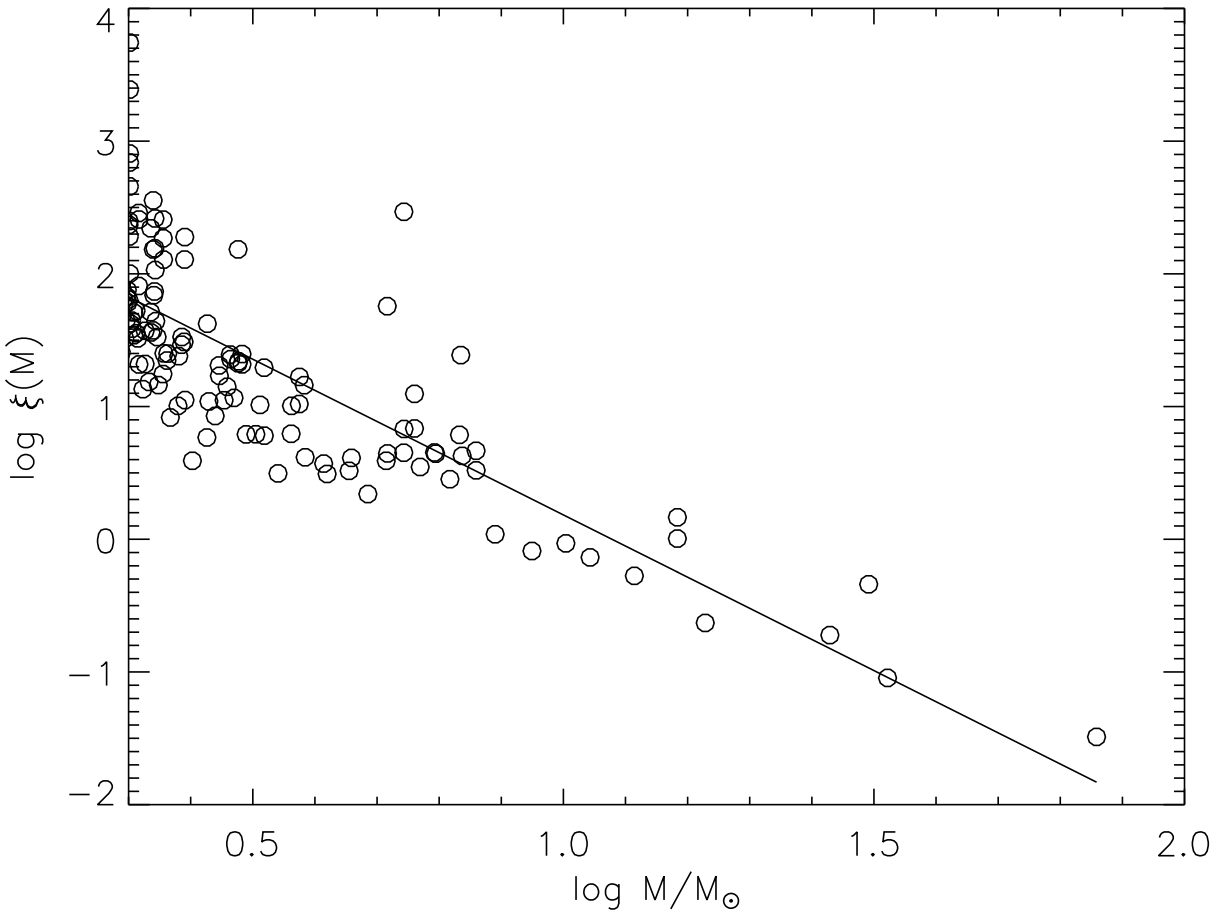

Figure 4.8 Initial mass function for LH 95, limited to the mass interval $M > 2$ M$_\odot$. We utilize open dots for clarity, but the points represent an histogram, with variable bin size, containing one star in each bin. The line represents the best fit of the data.

We proceed as follow: we sort all the members according to their mass. For every star we define the limits of the bin which contains only that star; these are chosen to be the mean (in log units) between the mass of the star and, respectively, the preceding and following one. For the most and least massive stars in the sample, the upper and lower boundaries of the bins are chosen to be symmetric from the actual mass of the star. The value of the mass distribution in each bin is then simply the number of stars per bin (1

by definition) divided by the width of the bin. The result is illustrated in Figure 4.8. One advantage of the binning method we used is that the weights are identical for each source. In fact, the uncertainty associated to each mass bin is represented by a Poisson distribution with $\theta = 1$, with a scaling factor equal to the size of the bin. This scaling factor of the error bar, however, is equal to the IMF value in that point. This implies that, expressing the IMF in logarithmic units on the y-axis, as in Figure 4.8, all the error bars are identical. As a consequence, we can neglect the errors in the fit of the IMF, and a standard linear regression can be used. We find that our IMF is well fitted by a power low with $\alpha = 2.32 \pm 0.14$, i.e., a Salpeter IMF. In particular, the new slope turns out to the shallower than that we previously derived without the most massive stars included in this work.

4.7.1 The relation between the most massive star and the cluster mass

The correlation between the mass of the most massive star in a cluster, $m_{\rm max}$, and the stellar mass of an entire cluster, M_{ecl}, has been long investigated both through empirical studies and analytical modeling (e.g., Larson, 2003; Oey & Clarke, 2005; Weidner & Kroupa, 2004; Weidner et al., 2010). Its importance is fundamental for several applications: in particular it allows to understand what is the upper mass limit for the formation a star; it also enables one to investigate whether or not newborn massive stars in star clusters are randomly drawn from the IMF.

In Chapter 2 we derived an estimate of the stellar mass in LH 95, based on the derived IMF extended to the masses below our detection limit. In the central region of LH95, where the study of the population was limited (delimited by the outermost contours of Figure 4.7), we estimated a total stellar mass of $M_{ecl} \sim 2.37 \cdot 10^3$ M$_\odot$. Accounting for the newly added massive stars, we have $M_{ecl} \sim 2.5 \cdot 10^3$ M$_\odot$. Furthermore, considering unresolved binarity and a small fraction of diffuse low-mass stars outside the central region, we estimate a total cluster mass in the range $M_{ecl} \sim 3.0$–$3.5 \cdot 10^3$ M$_\odot$. We utilize the model relation $m_{\rm max}$ vs. M_{ecl} from Weidner & Kroupa (2004), derived assuming a maximum stellar mass of 150 M$_\odot$ and a the Kroupa (2001) IMF. We stress that the assumed stellar upper mass limit does not affect significantly our analysis, given that LH 95 population is not enough populated to reach masses as high as $\sim$ 150 M$_\odot$. Moreover, as we discussed in Chapter 2, the low mass population of the region follows the Kroupa IMF once the unresolved binarity is accounted for, and the high-mass IMF derived in this work also

agrees with it. Therefore the model assumptions are fully consistent with our stellar system. The Weidner & Kroupa (2004) model relation predicts a $m_{\rm max} \simeq 70$ M$_\odot$ for $M_{ecl} = 3 \cdot 10^3$ M$_\odot$, and $m_{\rm max} \simeq 80$ M$_\odot$ for $M_{ecl} = 3.5 \cdot 10^3$ M$_\odot$. These values are in very good agreement with our mass estimate of ~ 72 M$_\odot$ for star B, suggesting that the high-mass population of LH 95 is compatible with a random sampling of stellar masses from its IMF.

Our finding, on the contrary, is in contrast with the empirical determinations of $m_{\rm max}$ in clusters of different mass. As Weidner et al. (2010) point out, carrying out a collective research of cluster masses and maximum stellar mass, there is evidence that the observed $m_{\rm max}$ is statistically lower than that predicted, along the entire range of M_{ecl}, suggesting the presence of additional mechanisms preventing the formation of the most massive stars in a cluster. Moreover, the authors find that, in particular, the observed relation has a plateau for clusters with M_{ecl} in the range 10^3 – $4 \cdot 10^3$ M$_\odot$, where the observed $m_{\rm max} \sim 25$ M$_\odot$, well below the predicted value. Thus, LH 95 would be in agreement with the maximum mass observed in clusters if our most massive star would not be part of the system. This fact, together with the very young age for this star (see Section 4.6.2), further suggests a peculiar nature for this star, which, as we already hypothesized, might be a runaway object born in the vicinity of LH 95.

Conclusions

I summarize here the main results of the work described in this thesis.

In Chapter 1, I present a new analysis of the Orion Nebula Cluster based on ground-based multiband photometry as well as spectroscopy. I produce a catalog in the U B, V, I, TiO ($\sim 6200\mathring{A}$) and Hα bands with the Wide Field Imager at the 2.2 m MPG/ESO telescope at La Silla. I define a spectro-photometric index, that I name [TiO] index, from the fluxes in $V-$, $I-$ and TiO $6200\mathring{A}$, and, comparing it with the spectral atlas of ONC members of Hillenbrand (1997), I find and present a correlation between the two quantities in the M-type stars range. This allow me to classify 217 new stars, whose spectral type is now presented. From the analysis of the observed color-color diagrams, I find evidence that the intrinsic photospheric colors for the ONC differ from those of main-sequence dwarfs in the M-type regime, but they are shifted toward bluer colors, in a similar way as predicted by atmosphere models assuming $\log g$ values from a PMS isochrone, but of an amount that I calibrated empirically limiting to the known members with modest extinction and no accretion detected from Hα photometry. I study the effects in the observed optical colors caused by on-going accretion; I develop a method that, based on three bands, allows one to disentangle accretion excess and extinction. This enables me to improve significantly the derivation of the extinctions for all the members with known spectral type. I derive the bolometric luminosities for ~ 1000 members and position them the HRD, down to the hydrogen-burning limit. The revised lower distance than previously assumed leads to systematically lower luminosities; this is compensated for in M-type stars, where we predict higher L, caused by higher measured extinctions for late-type stars. Using the evolutionary models, I assign ages and masses to all the members. I extract the age distribution of the ONC members, and find an average age for the ONC of $2-3$ Myr, older than previously assumed. I also confirm the evidence of an age spread in Orion. I find the mass-age correlation, evidenced by some previous studies, is not a real, being due to inaccuracy of some families of evolutionary models, and a bias

from the source detection incompleteness. I derive the IMF of our sample, corrected for detection incompleteness down to the hydrogen burning limit; the IMF turns out to be model-dependant and presents a turn-over at $M \simeq 0.2$ M$_\odot$.

In Chapter 2 I present a comprehensive investigation of the stellar populations of the star-forming association LH 95, located on the north-western edge of the super-giant shell LMC 4 in the Large Magellanic Cloud, using deep V and I HST/ACS photometry. I select the area of the cluster, and isolate its young population performing a statistical subtraction of the LMC field population. The PMS stars within the association are found to be mostly concentrated in three distinctive subclusters, providing evidence of the existence of stellar subgroups within a single association. I estimate the dust extinction and correct for it the photometry, and I compute the masses of all the members of the system, using a new conversion of PMS evolutionary models accounting for the gravity dependence of optical colors. The stellar sample reaches masses as low as ~ 0.2 M$_\odot$. I derive the system IMF of the system, corrected for incompleteness. I detect a change in the slope of the IMF (the "knee" of the IMF) for masses lower than 1 M$_\odot$. The IMF slope is found to be $x = 1.05^{-0.20}_{+0.15}$ in the subsolar regime, and $x = 2.05^{-0.28}_{+0.39}$ at intermediate and high masses. This IMF, once corrected for unresolved binarity, is statistically compatible, within the studied mass range, with the average Galactic IMF. As a consequence, I cannot consider the metallicity difference between the LMC ($Z = 0.008$) and the Galaxy important enough for a significant change in the IMF slope. I find no significant differences in the shape of the overall IMF of LH 95 from that of each of the three individual PMS subclusters of the association.

In Chapter 3 I focus on the age and age distribution of LH 95, based on the same dataset used in Chapter 2. I develop a maximum-likelihood method to derive the age of the system accounting simultaneously for photometric errors, unresolved binarity, differential extinction, accretion, stellar variability and crowding. The application of the method is performed in several steps: First, a set of PMS isochrones is converted to two-dimensional probability distributions in the magnitude-magnitude plane; one model distribution is constructed for every considered age. A well populated ($N > 10^6$ stars) synthetic population is thus created by applying the aforementioned sources of displacement in the CMD – except for photometric errors – to the isochrone for each chosen age. A maximum-likelihood method is then applied to derive the probability, for each observed star to have a certain age, taking its photometric uncertainty into account. The multiplication of the likelihood functions of all the stars provides an age probability function

for the entire cluster, from where the most probable age of the cluster is derived. The application of this method on LH 95 relies on the derived IMF and reddening distribution for the system, as previously derived. I also assume distributions of the variations in both V and I caused by accretion and variability due to dark spots by utilizing my results for the Orion Nebula Cluster. I study the model age-dependent probability distributions using two sets of evolutionary models, that by Siess et al. (2000), for the metallicity of the LMC, and a new grid computed for the same metallicity. I find that the age determination is very sensitive to the assumed evolutionary model and binary fraction; the age of LH 95 is found to vary from ∼2.8 Myr to ∼4.4 Myr, depending on these factors. Assuming $f = 0.5$, the average binary fraction in our mass range, the best-fit age of the system derived for this binary fraction is determined to be of the order of 4 Myr. Despite the sparse and clumpy spatial distribution of PMS stars in LH 95, I find no evidence of systematic variations of age with location. The statistical method allows me to disentangle any *real* age spread from the apparent CMD-spread caused by the physical and observational biases which dislocate the PMS stars from their theoretical positions in the CMD. I find that LH 95 hosts an overall age spread well modeled by a Gaussian distribution with $FWHM = 2.8 - 4$ Myr.

In Chapter 4, finally, I use ground-based optical spectroscopy and photometry to study the high-mass population of LH95. I derive effective temperatures and bolometric corrections of the five brightest sources of the cluster. I measure their masses, in the range 13–72 $M_{\odot}$, and their ages. This allows me to complete the IMF in the high-mass range; this turns out to be shallower than that derived excluding the most massive stars, and in agrement with the Galactic IMF. The ages and age spread of the massive stars is in agreement with that derived in Chapter 3 for the low-mass stars, with the exception of our most massive star. This is found to be significantly younger than the rest of the cluster, suggesting a different nature for its formation. We hint to the possibility that this star is a runaway object, born in the vicinity of LH 95. The peculiarity of the most massive stars is also supported by the comparison of its mass with that of the entire cluster. Whereas this is in agreement with a random sampling from a Salpeter IMF, Galactic cluster of similar mass as that of LH 95 tend to present a smaller value of mass for the most massive star.

In conclusion, this work presents several useful results. From the point of view of the characterization of young PMS clusters, I present a new study of the ONC, one of the most studied Galactic star forming regions, improving over the results of previous works.

I also carry out the first extensive study of a PMS association in the LMC – deriving the IMF, the age, and age spread of the members – down to the low-mass stellar regime.

I also present several novelties for what concerns the derivation of stellar parameters for PMS stars. I describe a method to perform spectral classification of cool stars based on narrow-band photometry. I demonstrate that the photospheric colors of PMS stars, at a given effective temperature, differ from those of MS dwarfs. I show how to evaluate, and correct for, the effect of on-going accretion on the derived colors and magnitudes. Also, I describe how to test the validity of the spectral type to temperature conversions. Although this meticulous approaches can be carried out, to derive the stellar parameters of single members, having at disposal an extensive dataset, I show how to model several of these effects statistically, to derive accurate results for a PMS regions in the case that only photometry in two bands is available.

Future prospects

The study I have presented, naturally suggests a number of future developments, applications, and some open questions. I will briefly summarize the principal ones.

- *Extension of the complete characterization of the ONC down to the substellar regime.*
  A natural continuation of my work in the ONC is its extension to the BDs regime. In particular, a deeper, multi-band photometric survey of the region is already available (the already mentioned HST/ACS catalog from the Orion HST Treasury Program). The independent $T_{\rm eff}$ estimate, needed to derive the stellar parameters, can be obtained from both spectroscopic surveys in the literature, and exploiting my tested methods based on narrow-band photometry.

- *Characterization of the optical veiling caused by on-going accretion.*
  In the work I presented, I studied the effect of accretion in the optical colors and magnitudes. This was accomplished by modeling a typical accretion spectrum, and computing the broadband excesses as a function of $T_{\rm eff}$ and $L_{\rm accr}/L_{\rm tot}$. Most likely, the problem is more complicated than this. The shape of the accretion spectrum can vary from star to star, and this has not been studied in great detail so far. An extensive spectral survey of accreting stars, in order to disentangle the accretion spectrum, can allow me to test the accuracy of a simulated accretion spectrum,

and, if needed, add an additional parameter related to the shape of the optical continuum. Then, having at disposal multi-band optical photometry, one will be able to disentangle all these quantities from the photospheric parameters and the dust extinction, improving the derivation of physical parameters for PMS stars based on photometry. The understanding of the statistical contribution of veiling excess, for PMS stars of different masses, ages, and at different wavelength, is critical to understand the observed broadening of optical CMDs (see Chapter 3).

- *Statistical characterization of all the biasing effects to the observed colors and magnitudes of PMS stars.*
  Related to the point above, other effects are known to modify the observed photometry of PMS stars. The main are the presence of stars seen in scattered light, and stellar variability, both due to accretion and dark spots. A statistical analysis of the overall effect of these biases on the observed CMD for a PMS region has never been carried out. This is fundamental to improve our understanding on the age and age spread of young clusters.

- *Study of low-mass PMS cluster in the Magellanic Clouds.*
  In this work I have shown the advantages, for the understanding of PMS cluster, of the study of such regions in the Magellanic Clouds. In this context, LH 95, so far, is the only region in which the PMS population has been studied to the lowest stellar masses, a luminosity limit where it is possible to assign memberships solely based on the location of the detected stars in the CMD. This study should be extended to other star forming regions in the MCs (reaching the same, or deeper, detection limit), providing a more complete snapshot of star formation in different environments. Moreover, the observational characterization of low-mass PMS stars in these regions, can be now extended to other wavelengths. In particular, deep, high resolution imaging in the near infrared, is needed to characterize the properties of circumstellar disk, in comparison with analogous regions of the Galaxy. Very deep photometry in $U-$band and $H\alpha$ are also required, together with the characterization of the disk properties, to measure accretion rates for low-mass star. This will allow one to test if (as suggested by recent researches), mass accretion may last longer in low metallicity environment.

- *...and beyond...*

  The study of low-mass stars in the Magellanic Clouds is still, unfortunately, limited by the spatial resolution and sensitivity of the telescopes. As of now, the Hubble Space Telescope provides the optimal performances to accomplish this observational study, enabling one to detect sources down to almost the H-burning limit. From ground-based observatories, these performances are hardly equalled using adaptive optics (AO). Nevertheless, present instrumentation is yet insufficient to extend this research to lower stellar masses and in the brown dwarf regime. In the next decade, future space and ground-based observatories, such as, first the *James Webb Space Telescope* (JWST), and, then, the *European Extremely Large Telescope* (E-ELT) will enable a significant improvement in the study of low mass stellar objects outside the Galaxy. In particular, the Near Infrared Camera (NIRCam) designed for JWST will provide, in the NIR, excellent sensitivity and slightly better spatial resolution than the optical detectors now available on the HST. These capabilities will be ideal for the characterization of very-low mass stars and brown dwarfs in the MCs. A subsequent improvement from the observational point of view will be achievable with the E-ELT. This observatory will be equipped with several instrument designed for both optical and NIR imaging and spectroscopy. The use of Multi-Conjugated Adaptive Optics (MCAO) will allow one to reach unmatchable spatial resolution, down to a few mas. As a consequence, the E-ELT will not only improve the study of resolved stellar populations in the MCs, but also open to the study of the intermediate-mass and low-mass stars in the Local Group. The most suitable of such targets will be the Andromeda Galaxy M31. This galaxy is located at a distance from us $\sim$ 13 times larger than that of the LMC. As a consequence, in order to perform a similar research in M31 as the study of LH 95 I presented in this thesis, a spatial resolution at least 13 times higher than that of ACS (i.e., $\sim$ 4 mas) and a sensitivity $\sim 13^2$ times higher (i.e., achievable with a 30m class telescope) are required; both this requirements are matched by the E-ELT and its instruments. Thus, the ability of studying resolved, young, low-mass populations in another galaxy will guarantee an exceptional progress in our understanding of the star formation processes and the properties of the IMF.

Acknowledgements

I am most indebted to my supervisors, Dimitrios A. Gouliermis and Thomas Henning, for their patience, expertise and always present supervision, and for the freedom they also granted me to pursue my research interests. I want to express a particular appreciation to Dimitrios for his care and for being a good collaborator and friend.

I offer my sincerest gratitude to Massimo Robberto, for his guidance and for inspiring me through his example and friendship.

Many thanks to all my other collaborators: Lynne Hillenbrand, Keivan Stassun, Francesco Palla, David R. Soderblom, Nino Panagia, Mario Gennaro, Boyke Rochau, Anna Pasquali, Johny Setiawan, Luca Ricci, Gaetano Scandariato. Without them this work would not have been as good as it is. Thank you very much for the fruitful and pleasant collaborations.

I acknowledge the financial support from the German Aerospace Center (DLR), which funded my PhD program through grant 50 OR 0401. I also thank IMPRS Heidelberg and the Max-Planck Institute for Astronomy for the opportunity I was offered, and for additional financial support.

Finally, I am grateful to my family for their support, encouragement and *love*, and to all the friends I had the privilege to know over the years.

Bibliography

Alcock, C., et al. 2004, AJ, 127, 334

Alencar, S. H. P., & Basri, G. 2000, AJ, 119, 1881

Ali, B., & Depoy, D. L. 1995, AJ, 109, 709

Allard, F., & Hauschildt, P. H. 1995, ApJ, 445, 433

Allard, F., Hauschildt, P. H., & Schwenke, D. 2000, ApJ, 540, 1005

Allard, F., Hauschildt, P. H., Alexander, D. R., Tamanai, A., & Schweitzer, A. 2001, ApJ, 556, 357

Allard, F., Guillot, T., Ludwig, H.-G., Hauschildt, P. H., Schweitzer, A., Alexander, D. R., & Ferguson, J. W. 2003, Brown Dwarfs, 211, 325

Allen, L. E., & Strom, K. M. 1995, AJ, 109, 1379

Allen, L., et al. 2007, Protostars and Planets V, 361

Alonso, A., Arribas, S., & Martínez-Roger, C. 1999, A&AS, 140, 261

Ambartsumian, V. A. 1947, In *Stellar Evolution and Astrophysics, Armenian Acad. of Sci.*

Appenzeller, I., & Mundt, R. 1989, A&AR, 1, 291

Asplund, M., Grevesse, N., & Sauval, A. J. 2005, Cosmic Abundances as Records of Stellar Evolution and Nucleosynthesis, 336, 25

Bally, J., O'Dell, C. R., & McCaughrean, M. J. 2000, AJ, 119, 2919

Baraffe, I., Chabrier, G., Allard, F., & Hauschildt, P. H. 1997, A&A, 327, 1054

Baraffe, I., Chabrier, G., Allard, F., & Hauschildt, P. H. 1998, A&A, 337, 403

Baraffe, I., Chabrier, G., Allard, F., Hauschildt, P. 2001, From Darkness to Light: Origin and Evolution of Young Stellar Clusters, 243, 571

Baraffe, I., Chabrier, G., & Gallardo, J. 2009, ApJL, 702, L27

Baranne, A., et al. 1996, A&AS, 119, 373

Barrado y Navascués, D., Stauffer, J. R., Bouvier, J., & Martín, E. L. 2001, ApJ, 546, 1006

Bergin, E. A., Snell, R. L., & Goldsmith, P. F. 1996, ApJ, 460, 343

Bertin E., Mellier Y., Radovich M., Missonnier G., Didelon P., Morin B., 2002, ASPCS , 281, 228

Bertout, C. 1989, ARA&A, 27, 351

Bessell, M. S., Castelli, F., & Plez, B. 1998, A&A, 333, 231

Bica, E. L. D., & Schmitt, H. R. 1995, ApJS, 101, 41

Bica, E. L. D., Schmitt, H. R., Dutra, C. M., & Oliveira, H. L. 1999, AJ, 117, 238

Binney, J., & Merrifield, M. 1998, Galactic astronomy / James Binney and Michael Merrifield. Princeton, NJ : Princeton University Press, 1998. (Princeton series in astrophysics)

Blaauw, A. 1961, BAIN, 15, 265

Bohlin, R. C. 2007, The Future of Photometric, Spectrophotometric and Polarimetric Standardization, 364, 315

Bouchet, P., Lequeux, J., Maurice, E., Prevot, L., & Prevot-Burnichon, M. L. 1985, A&A, 149, 330

Brandl, B., Brandner, W., Eisenhauer, F., Moffat, A. F. J., Palla, F., & Zinnecker, H. 1999, A&A 352, L69

Brandner, W., Clark, J. S., Stolte, A., Waters, R., Negueruela, I., & Goodwin, S. P. 2008, A&A, 478, 137

Briceño, C., Hartmann, L., Hernández, J., Calvet, N., Vivas, A. K., Furesz, G., & Szentgyorgyi, A. 2007, ApJ, 661, 1119

Briceño, C. 2008, Handbook of Star Forming Regions, Volume I, 838

Burningham, B., Naylor, T., Littlefair, S. P., & Jeffries, R. D. 2005, MNRAS, 363, 1389

Caldwell, J. A. R., & Coulson, I. M. 1986, MNRAS, 218, 223

Calvet, N., & Hartmann, L. 1992, ApJ, 386, 239

Calvet, N., & Gullbring, E. 1998, ApJ, 509, 802

Cardelli, J. A., Clayton, G. C., & Mathis, J. S. 1989, ApJ, 345, 245

Chabrier, G. 2003, PASP, 115, 763

Chieffi, A., & Straniero, O. 1989, ApJS, 71, 47

Chlebowski, T., & Garmany, C. D. 1991, ApJ, 368, 241

Cohen, M., & Kuhi, L. V. 1979, ApJS, 41, 743

Cole, A. A. 1998, ApJL, 500, L137

Comerón, F., Spezzi, L., & López Martí, B. 2009, A&A, 500, 1045

Costero, R., & Peimbert, M. 1970, Boletin de los Observatorios Tonantzintla y Tacubaya, 5, 229

Currie, T., et al. 2010, ApJS, 186, 191

D'Orazi, V., Randich, S., Flaccomio, E., Palla, F., Sacco, G. G., & Pallavicini, R. 2009, A&A, 501, 973

D'Antona, F., & Mazzitelli, I. 1994, ApJS, 90, 467

D'Antona, F., Mazzitelli, I. 1997, Memorie della Societa Astronomica Italiana, 68, 807

D'Antona, F., & Mazzitelli, I. 1998, Brown Dwarfs and Extrasolar Planets, 134, 442

Da Rio, N., Robberto, M., Soderblom, D. R., Panagia, N., Hillenbrand, L. A., Palla, F., & Stassun, K. G. 2010a, ApJ, *in press.* (arXiv:1008.1265)

Da Rio, N., Gouliermis, D. A., & Gennaro, M. 2010b, ApJ, *in press.* (arXiv:1009.0006)

Da Rio, N., Gouliermis, D. A., & Henning, T. 2009a, ApJ, 696, 528

Da Rio, N., Robberto, M., Soderblom, D. R., Panagia, N., Hillenbrand, L. A., Palla, F., & Stassun, K. 2009b, ApJS, 183, 261

Davies, R. D., Elliott, K. H., & Meaburn, J. 1976, MEMRAS, 81, 89

De Marchi, G., Panagia, N., & Romaniello, M. 2010, ApJ, 715, 1

Degl'Innocenti, S., Prada Moroni, P. G., Marconi, M., & Ruoppo, A. 2008, APSS, 316, 25

Dolphin, A. E., & Hunter, D. A. 1998, AJ, 116, 1275

Dolphin, A. E. 2000, PASP, 112, 1383

Elmegreen, B. G. 2007, ApJ, 668, 1064

Evans, C. J., et al. 2010, ApJL, 715, L74

Fellhauer, M., Kroupa, P., & Evans, N. W. 2006, MNRAS, 372, 338

Ferguson, J. W., Alexander, D. R., Allard, F., Barman, T., Bodnarik, J. G., Hauschildt, P. H., Heffner-Wong, A., & Tamanai, A. 2005, ApJ, 623, 585

Ferland, G. J., Korista, K. T., Verner, D. A., Ferguson, J. W., Kingdon, J. B., & Verner, E. M. 1998, PASP, 110, 761

Flower, P. J. 1996, ApJ, 469, 355

Getman, K. V., Feigelson, E. D., Grosso, N., McCaughrean, M. J., Micela, G., Broos, P., Garmire, G., & Townsley, L. 2005, ApJS, 160, 353

Gies, D. R., & Bolton, C. T. 1986, ApJS, 61, 419

Girardi, L., Bertelli, G., Bressan, A., Chiosi, C., Groenewegen, M. A. T., Marigo, P., Salasnich, B., Weiss, A. 2002, A&A, 391, 195

Girardi, L., et al. 2008, PASP, 120, 583

Gordon, K. D., Clayton, G. C., Misselt, K. A., Landolt, A. U., & Wolff, M. J. 2003, ApJ, 594, 279

Gouliermis, D., Keller, S. C., de Boer, K. S., Kontizas, M., & Kontizas, E. 2002, A&A, 381, 862

Gouliermis, D., Brandner, W., & Henning, Th. 2006a, ApJL, 636, L133

Gouliermis, D. A., Dolphin, A. E., Brandner, W., & Henning, Th. 2006b, ApJS, 166, 549

Gouliermis, D. A., Henning, Th., Brandner, W., Dolphin, A. E., Rosa, M., Brandl, B. 2007, ApJL, 665, L27

Gouliermis, D. A., et al. 2010, in the Proceedings of the 41st ESLAB Symposium: The Impact of HST on European Astronomy, 71

Guarcello, M. G., Damiani, F., Micela, G., Peres, G., Prisinzano, L., & Sciortino, S. 2010, arXiv:1006.3813

Gullbring, E., Calvet, N., Muzerolle, J., & Hartmann, L. 2000, ApJ, 544, 927

Gunn, J. E., & Stryker, L. L. 1983, ApJS, 52, 121

Hartmann, L. 2003, ApJ, 585, 398

Hauschildt, P. H., Baron, E., & Allard, F. 1997, ApJ, 483, 390

Hauschildt, P. H., Allard, F., Baron, E. 1999, ApJ, 512, 377

Henize, K. G. 1956, ApJS, 2, 315

Hennekemper, E., Gouliermis, D. A., Henning, Th., Brandner, W., & Dolphin, A. E. 2008, ApJ, 672, 914

Herbig, G. H., & Terndrup, D. M. 1986, ApJ, 307, 609

Herbst, W., Herbst, D. K., Grossman, E. J., & Weinstein, D. 1994, AJ, 108, 1906

Herbst, W., Bailer-Jones, C. A. L., Mundt, R., Meisenheimer, K., & Wackermann, R. 2002, A&A, 396, 513

Herczeg, G. J., & Hillenbrand, L. A. 2008, ApJ, 681, 594

Hill, R. J., Madore, B. F., & Freedman, W. L. 1994, ApJ, 429, 204

Hill, R. S., Cheng, K.-P., Bohlin, R. C., O'Connell, R. W., Roberts, M. S., Smith, A. M., & Stecher, T. P. 1995, ApJ, 446, 622

Hillenbrand, L. A. 1997, AJ, 113, 1733 (H97)

Hillenbrand, L. A., & Hartmann, L. W. 1998, ApJ, 492, 540

Hillenbrand, L. A., Strom, S. E., Calvet, N., Merrill, K. M., Gatley, I., Makidon, R. B., Meyer, M. R., & Skrutskie, M. F. 1998, AJ, 116, 1816

Hillenbrand, L. A., & Carpenter, J. M. 2000, ApJ, 540, 236

Hillenbrand, L. A., Carpenter, J. M., & Feigelson, E. D. 2001, From Darkness to Light: Origin and Evolution of Young Stellar Clusters, 243, 439

Hillenbrand, L. A., Bauermeister, A., & White, R. J. 2008, 14th Cambridge Workshop on Cool Stars, Stellar Systems, and the Sun, 384, 200

Hillenbrand, L. A. 2009, IAU Symposium, 258, 81

Hirota, T., et al. 2007, PASJ, 59, 897

Hirschi, R., Meynet, G., & Maeder, A. 2004, A&A, 425, 649

Iglesias, C. A., & Rogers, F. J. 1996, ApJ, 464, 943

Jeffries, R. D., Oliveira, J. M., Naylor, T., Mayne, N. J., & Littlefair, S. P. 2007, MNRAS, 376, 580

Jeffries, R. D. 2007, MNRAS, 381, 1169

Johnson, H. L. 1967, ApJL, 150, L39

Jones, B. F., & Walker, M. F. 1988, AJ, 95, 1755

Joy, A. H. 1949, ApJ, 110, 424

Kaufer, A., & Pasquini, L. 1998, proc. SPIE, 3355, 844

Kennicutt, R. C., Jr. 1998, ApJ, 498, 541

Kenyon, S. J., et al. 1994, AJ, 107, 2153

Kenyon, S. J., & Hartmann, L. 1995, ApJS, 101, 117

Kirkpatrick, J. D., Kelly, D. M., Rieke, G. H., Liebert, J., Allard, F., & Wehrse, R. 1993, ApJ, 402, 643

Kirkpatrick, J. D. 2008, 14th Cambridge Workshop on Cool Stars, Stellar Systems, and the Sun, 384, 85

Koenigl, A. 1991, ApJL, 370, L39

Kontizas, M., Kontizas, E., & Michalitsianos, A. G. 1993, A&A, 269, 107

Koornneef, J. 1982, A&A, 107, 247

Kraus, A. L., & Hillenbrand, L. A. 2009, ApJ, 704, 531

Kroupa, P., Gilmore, G., & Tout, C. A. 1991, MNRAS, 251, 293

Kroupa, P., Tout, C. A., & Gilmore, G. 1993, MNRAS, 262, 545

Kroupa, P. 2001, MNRAS, 322, 231

Kroupa, P. 2002, Science, 295, 82

Kroupa, P. 2008, in The Cambridge N-body Lectures, S. Aarseth, C. Tout, R. Mardling (eds), Lecture Notes in Physics Series, Springer Verlag (arXiv:0803.1833)

Kurucz, R. 1979, ApJS, 40, 1

Kurucz, R. 1993, ATLAS9 Stellar Atmosphere Programs and 2 km/s grid. Kurucz CD-ROM No. 13. Cambridge, Mass.: Smithsonian Astrophysical Observatory, 1993., 13

Lada, C. J., & Lada, E. A. 2003, ARA&A, 41, 57

Lada, C. J. 2006, ApJL, 640, L63

Landolt, A. U. 1992, AJ, 104, 340

Larson, R. B. 2003, ASP Conf. Ser.Vol. 287, Galactic Star Formation Across the Stellar Mass Spectrum. Astron. Soc. Pac., San Francisco, p. 65

Leggett, S. K. 1992, ApJS, 82, 351

Levenberg, K. 1944, The Quarterly of Applied Mathematics 2, 164

Lucas, P. W., & Roche, P. F. 2000, MNRAS, 314, 858

Luck, R. E., Moffett, T. J., Barnes, T. G., III, & Gieren, W. P. 1998, AJ, 115, 605

Lucke, P. B. & Hodge, P. W. 1970, AJ, 75, 171

Luhman, K. L. 1999, ApJ, 525, 466

Luhman, K. L., Rieke, G. H., Young, E. T., Cotera, A. S., Chen, H., Rieke, M. J., Schneider, G., & Thompson, R. I. 2000, ApJ, 540, 1016

Luhman, K. L., Stauffer, J. R., Muench, A. A., Rieke, G. H., Lada, E. A., Bouvier, J., & Lada, C. J. 2003, ApJ, 593, 1093

Maeder, A., & Meynet, G. 2000, ARA&A, 38, 143

Maíz-Apellániz, J. 2004, PASP, 116, 859

Maíz Apellániz, J., & Úbeda, L. 2005, ApJ, 629, 873

Maíz-Apellániz, J. 2007, The Future of Photometric, Spectrophotometric and Polarimetric Standardization, 364, 227

Marks, M., Kroupa, P., & Baumgardt, H. 2008, MNRAS, 386, 2047

Marquardt, D. 1963, SIAM Journal on Applied Mathematics 11, 431

Martins, F., Schaerer, D., & Hillier, D. J. 2005, A&A, 436, 1049

Martins, F., & Plez, B. 2006, A&A, 457, 637

Massey, P., Silkey, M., Garmany, C. D., & Degioia-Eastwood, K. 1989a, AJ, 97, 107

Massey, P., Parker, J. W., & Garmany, C. D. 1989b, AJ, 98, 1305

Massey, P., Lang, C. C., Degioia-Eastwood, K., & Garmany, C. D. 1995, ApJ, 438, 188

Massey, P., & Hunter, D. A. 1998, ApJ, 493, 180

Massey, P. 2003, ARA&A, 41, 15

Massey, P., Puls, J., Pauldrach, A. W. A., Bresolin, F., Kudritzki, R. P., & Simon, T. 2005, ApJ, 627, 477

Mayne, N. J., Naylor, T., Littlefair, S. P., Saunders, E. S., & Jeffries, R. D. 2007, MNRAS, 375, 1220

Menten, K. M., Reid, M. J., Forbrich, J., & Brunthaler, A. 2007, A&A, 474, 515

Meynet, G., & Maeder, A. 2000, A&A, 361, 101

Meynet, G., & Maeder, A. 2003, A&A, 404, 975

Meynet, G., & Maeder, A. 2005, A&A, 429, 581

Meyer, M. R., Calvet, N., & Hillenbrand, L. A. 1997, AJ, 114, 288

Muench, A. A., Lada, E. A., Lada, C. J., Alves, J. F. 2002 ApJ, 573, 366

Muzerolle, J., Hartmann, L., & Calvet, N. 1998, AJ, 116, 455

Muzerolle, J., Calvet, N., & Hartmann, L. 1998, ApJ, 492, 743

Naylor, T., & Jeffries, R. D. 2006, MNRAS, 373, 1251 (NJ06)

Naylor, T. 2009, MNRAS, 399, 432

Nota, A., et al. 2006, ApJL, 640, L29

Oey, M. S., & Clarke, C. J. 2005, ApJL, 620, L43

Oey, M. S. 1996, ApJS, 104, 71

Palla, F., Randich, S., Pavlenko, Y. V., Flaccomio, E., & Pallavicini, R. 2007, ApJL, 659, L41

Palla, F., Randich, S., Flaccomio, E., & Pallavicini, R. 2005, ApJL, 626, L49

Palla, F., & Stahler, S. W. 2002, ApJ, 581, 1194

Palla, F., & Stahler, S. W. 2000, ApJ, 540, 255

Palla, F., & Stahler, S. W. 1999, ApJ, 525, 772

Pei, Y. C., Fall, S. M., & Hauser, M. G. 1999, ApJ, 522, 604

Piotto, G., & Zoccali, M. 1999, A&A, 345, 485

Portegies Zwart, S. F., McMillan, S. L. W., & Gieles, M. 2010, AA&A, 48, 431

Poveda, A., Ruiz, J., & Allen, C. 1967, Boletin de los Observatorios Tonantzintla y Tacubaya, 4, 86

Preibisch, T., Brown, A. G. A., Bridges, T., Guenther, E., & Zinnecker, H. 2002, AJ, 124, 404

Prosser, C. F., Stauffer, J. R., Hartmann, L., Soderblom, D. R., Jones, B. F., Werner, M. W., & McCaughrean, M. J. 1994, ApJ, 421, 517

Rebull, L. M., Hillenbrand, L. A., Strom, S. E., Duncan, D. K., Patten, B. M., Pavlovsky, C. M., Makidon, R., & Adams, M. T. 2000, AJ, 119, 3026

Reggiani, M., Robberto, M., Da Rio, N., Ricci, L., Soderblom, D. R., 2010, *in preparation*

Reylé, C., & Robin, A. C. 2001, A&A, 373, 886

Ricci, L., Robberto, M., L., Soderblom, D. R., 2008, AJ, 163, 2136

Robberto, M., Song, J., Mora Carrillo, G., Beckwith, S. V. W., Makidon, R. B., & Panagia, N. 2004, ApJ, 606, 952

Robberto, M., et al. 2005, AJ, 129, 1534

Robberto, M., Soderblom, D. R., Scandariato, G., Smith, K., Da Rio, N., Pagano, I., & Spezzi, L. 2010, AJ, 139, 950

Rochau, B., Brandner, W., Stolte, A., Gennaro, M., Gouliermis, D., Da Rio, N., Dzyurkevich, N., & Henning, T. 2010, ApJL, 716, L90

Rogers, F. J., Swenson, F. J., & Iglesias, C. A. 1996, ApJ, 456, 902

Romaniello, M., Panagia, N., Scuderi, S., & Kirshner, R. P. 2002, AJ, 123, 915

Romaniello, M., Robberto, M., & Panagia, N. 2004, ApJ, 608, 220

Sabbi, E., et al. 2008, AJ, 135, 173

Sagar, R., & Richtler, T. 1991, A&A, 250, 324

Salpeter, E. E. 1955, ApJ, 121, 161

Sandstrom, K. M., Peek, J. E. G., Bower, G. C., Bolatto, A. D., & Plambeck, R. L. 2007, ApJ, 667, 116

Santos, N. C., Melo, C., James, D. J., Gameiro, J. F., Bouvier, J., & Gomes, J. I. 2008, A&A, 480, 889

Scalo, J. M. 1986, Fundamentals of Cosmic Physics, 11, 1

Scalo, J. 1998, The Stellar Initial Mass Function (38th Herstmonceux Conference), 142, 201

Schaerer, D., Meynet, G., Maeder, A., & Schaller, G. 1993, A&AS, 98, 523

Schmalzl, M., Gouliermis, D. A., Dolphin, A. E., & Henning, Th. 2008, ApJ, 681, 290

Schmidt-Kaler, T. 1982, in Landolt-Bornstein, Group VI, Vol. 2, ed. K.-H. Hellwege (Berlin: Springer), 454

Sherry, W. H., Walter, F. M., & Wolk, S. J. 2004, AJ, 128, 2316

Shu, F., Najita, J., Ostriker, E., Wilkin, F., Ruden, S., & Lizano, S. 1994, ApJ, 429, 781

Sicilia-Aguilar, A., et al. 2005, AJ, 129, 363

Sicilia-Aguilar, A., Hartmann, L. W., Fürész, G., Henning, T., Dullemond, C., & Brandner, W. 2006, AJ, 132, 2135

Siess, L., Forestini, M., Dougados, C. 1997, A&A, 324, 556

Siess, L., Dufour, E., Forestini, M. 2000, A&A, 358, 593

Slesnick, C. L., Hillenbrand, L. A., & Carpenter, J. M. 2004, ApJ, 610, 1045

Smith, N., Bally, J., Shuping, R. Y., Morris, M., & Kassis, M. 2005, AJ, 130, 1763

Spezzi, L., Alcalá, J. M., Frasca, A., Covino, E., & Gandolfi, D. 2007, A&A, 470, 281

Spitzer, L. Jr. 1958, ApJ, 127, 17

Stassun, K. G., Mathieu, R. D., Mazeh, T., & Vrba, F. J. 1999, AJ, 117, 2941

Stetson, P. B. 1987, PASP, 99, 191

Swenson, F. J., Faulkner, J., Rogers, F. J., & Iglesias, C. A. 1994, ApJ, 425, 286

Tan, J. C., Krumholz, M. R., & McKee, C. F. 2006, ApJL, 641, L121

Vacca, W. D., Garmany, C. D., & Shull, J. M. 1996, ApJ, 460, 914

Vandame, B., PhD thesis, Nice University, 2004

van den Berg, M., Stassun, K. G., Verbunt, F., & Mathieu, R. D. 2002, A&A, 382, 888

VandenBerg, D. A., & Clem, J. L. 2003, AJ, 126, 778

Walborn, N. R., & Fitzpatrick, E. L. 1990, PASP, 102, 379

Walborn, N. R., Lennon, D. J., Haser, S. M., Kudritzki, R.-P., & Voels, S. A. 1995, PASP, 107, 104

Walborn, N. R., et al. 2002, AJ, 123, 2754

Walborn, N. R., et al. 2010, AJ, 139, 1283

Weidner, C., Kroupa, P., & Bonnell, I. A. D. 2010, mnras, 401, 275

Weidner, C., Kroupa, P., & Maschberger, T. 2009, MNRAS, 393, 663

Weidner, C., & Kroupa, P. 2006, MNRAS, 365, 1333

Weidner, C., & Kroupa, P. 2004, mnras, 348, 187

Westerlund, B. 1961, PASP, 73, 51

Westerlund, B. E. 1997, The Magellanic Clouds (Cambridge: Cambridge Univ. Press)

White, R. J., & Hillenbrand, L. A. 2005, ApJL, 621, L65

Wilking, B. A., & Lada, C. J. 1983, ApJ, 274, 698

Woitas, J., Leinert, C., Köhler, R. 2001, A&A, 376, 982

Zinnecker, H., & Yorke, H. W. 2007, ARA&A, 45, 481